



MONASH University

**Engineering Sensors to Investigate the Intracellular
Trafficking of Nanomaterials**

Laura Ina Selby

Bachelor of Science (Chemistry)

Master of Engineering (Chemical)

A thesis submitted for the degree of *Doctor of Philosophy* at
Monash University in 2018
Monash Institute of Pharmaceutical Sciences

I. Copyright notice

© Laura Selby 2018

I certify that I have made all reasonable efforts to secure copyright permissions for third-party content included in this thesis and have not knowingly added copyright content to my work without the owner's permission.

II. Abstract

Nanoparticles have been proposed as drug carriers to overcome limitations associated with traditional delivery methods. By encapsulating cargo such as drugs, proteins or nucleic acids inside nanomaterials and targeting them to specific cells, issues such as degradation, poor solubility and off-target effects can potentially be avoided. To engineer materials for a desired therapeutic outcome, we must develop a better understanding of how cells and nanomaterials interact. However, this requires improving on currently available tools to examine the critical steps involved in the intracellular trafficking of nanomaterials. This thesis addresses the limitations in the sensitivity of fluorescence measurements in flow cytometry through development of an algorithm to improve data analysis and the development of three fluorescent sensors to determine the amount of material internalised, where it is trafficked to within the cell and if it can escape from endo/lysosomal vesicles to deliver the cargo to the cytosol.

Flow cytometry has become a routine method in the examination of bio-nano interactions. However, this type of analysis is limited by weak particle fluorescence or low particle binding numbers. This causes the fluorescence histograms of the treated cells to overlap significantly with that of the untreated cells, making it difficult to assess the effect of the nanoparticles. To overcome this, an algorithm that uses the mathematical process of deconvolution on fluorescence histograms to identify the cells within the sample that have had a response was developed. The detection of small changes in nanoparticle association with cells that otherwise would be missed by currently available methods is demonstrated.

The capacity of nanoparticles to be internalised into cells is critical for their use in drug delivery. To probe this, a fluorescent sensor that uses click chemistry to specifically quench extracellular fluorescence was developed. By quenching the fluorescence of material on the outside of the cell and leaving the intracellular signal unaffected, the amount of material taken up can be quantified. The sensor effectively quantified the internalisation of a range of protein sizes (15 – 150 kDa) and was shown to be compatible with additional fluorescent markers as the quenching interaction is specific to the compatible click group.

Following internalisation into the cell, nanoparticles often become trapped in endosomes and lysosomes. As many applications require delivery of cargo to the cytosol or nucleus, it is necessary to

determine if the nanoparticles can effectively induce endosomal escape. This is commonly achieved by examining the colocalisation of fluorescent markers by fluorescence microscopy. However, the results from this type of analysis can be difficult to interpret. To overcome this, a quenched probe that interacts with a commercially available enzyme (SNAP-tag) tagged onto points of interest within the cell and fluoresces on activation was synthesised. This sensor was able to detect the delivery of cargo to the cytosol and nucleus using a common transfection reagent by flow cytometry and fluorescence microscopy. The system was also able to detect the presence a protein in proximity to its receptor on the cell surface.

The potential of a second endosomal escape sensor was also investigated that avoided the need for transfection of cells. The sensor was composed of a 27-mer fluorescently labelled and 21-mer quencher labelled DNA duplex that is activated in the presence of the mRNA for glyceraldehyde 3-phosphate dehydrogenase, a sequence known to be expressed in the cytosol. Although the sensor responded to the target sequence in solution, the low copy number mRNA sequences in cytosol resulted in a poor signal-to-noise ratio, limiting its use.

Overall, this thesis demonstrates the design, synthesis and validation of several methods to probe how cells process different nanomaterials and proteins. The algorithm developed and the synthesis of the fluorescent sensors adds to the collection of tools available to nanomaterial scientists and cell biologists to assist in in the design of carriers for drug delivery and in our understanding of how cells function.

III. Publications During Enrolment

- (1) **Selby, L. I.**; Cortez-Jugo, C. M.; Such, G. K.; Johnston, A. P. R. Nanoescapology: Progress toward Understanding the Endosomal Escape of Polymeric Nanoparticles. *Wiley Interdiscip. Rev. Nanomedicine Nanobiotechnology* **2017**, e1452.
- (2) Wong, A. S. M.; Czuba, E.; Chen, M. Z.; Yuen, D.; Cupic, K. I.; Yang, S.; Hodgetts, R. Y.; **Selby, L. I.**; Johnston, A. P. R.; Such, G. K. pH-Responsive Transferrin-pHlexi Particles Capable of Targeting Cells *in Vitro*. *ACS Macro Lett.* **2017**, 315–320.
- (3) **Selby, L. I.**; Kongkatigumjorn, N.; Such, G. K.; Johnston, A. P. R. Flow Cytometry: HD Flow Cytometry: An Improved Way to Quantify Cellular Interactions with Nanoparticles. *Advanced Healthcare Materials*, 2016, 5, 2332.
- (4) Mann, S. K.; Czuba, E.; **Selby, L. I.**; Such, G. K.; Angus, P.; Johnston, R. Quantifying Nanoparticle Internalization Using a High Throughput Internalization Assay. *Pharm. Res.* **2016**, 33, 2421–2432.

IV. Thesis Including Published Works Declaration

I hereby declare that this thesis contains no material which has been accepted for the award of any other degree or diploma at any university or equivalent institution and that, to the best of my knowledge and belief, this thesis contains no material previously published or written by another person, except where due reference is made in the text of the thesis.

This thesis includes 2 original papers published in peer reviewed journals and 3 submitted publications. The core theme of the thesis is the design of sensors to study the behaviour of nanomaterials in cells. The ideas, development and writing up of all the papers in the thesis were the principal responsibility of myself, the student, working within the Faculty of Pharmacy and Pharmaceutical Sciences under the supervision of Dr. Angus Johnston. The inclusion of co-authors reflects the fact that the work came from active collaboration between researchers and acknowledges input into team-based research.

Student signature:



Date: 09/02/2018

The undersigned hereby certify that the above declaration correctly reflects the nature and extent of the student's and co-authors' contributions to this work. In instances where I am not the responsible author I have consulted with the responsible author to agree on the respective contributions of the authors.

Main Supervisor signature:



Date: 09/02/2018

In the case of Chapters 1 and 2, my contribution to the work involved the following:

Thesis Chapter	Publication Title	Status	Nature and % of student contribution	Co-author name(s) Nature and % of Co-author's contribution	Co-author(s), Monash student Y/N
1	Nanoescapology: Progress toward Understanding the Endosomal Escape of Polymeric Nanoparticles	Published	70% - Wrote section on mechanisms and detection methods of endosomal escape, compiled and edited the manuscript.	Cortez-Jugo, C. (10%) – Wrote section on lipid nanoparticles. M.; Such, G. K. (10%) – Wrote section on pH responsive particles. Johnston, A. P. R. (10%) – Wrote section on endosomal escape peptides, proof read and edited manuscript.	No
2	HD Flow Cytometry: An Improved Way to Quantify Cellular Interactions with Nanoparticles	Published	70% - Assisted in writing the MATLAB script, conducted CellTracker flow cytometry experiments, analysed the data, wrote and edited the manuscript.	Kongkatigumjorn, N. (5%) – Synthesised nanoparticles and provided data for analysis. Such, G. K. (5%) – Desiged nanoparticles and experiments. Johnston, A. P. R. (20%) – Assited with MATLAB script and experimental design. Also proof read and edited the manuscript. Prodcuded the table of contents image.	No

I have renumbered sections of submitted of published papers in order to generate a consistent presentation within the thesis.

V. Acknowledgments

First and foremost, I would like to express my sincerest gratitude to the NanoMB group. I am incredibly grateful to my supervisor Dr. Angus Johnston for his encouragement and belief in my abilities. His dedication and leadership make the NanoMB a truly wonderful research team to be a part of. I would like to extend a special thanks to our post-doctoral fellow Dr. Daniel Yuen and research assistants Moore Chen, Ewa Czuba, Sarah Mann and Haiyin Liu for their tireless efforts in maintaining the lab and willingness to give up their time to share their knowledge with others.

From Monash University, I would like to thank Dr. Jason Dang and Dr. Kade Roberts for their assistance with liquid chromatography and mass spectrometry, Sandy Fung and Cameron Nowell for lending their expertise in flow cytometry and microscopy and research project staff Karen Drakatos and Karen McConalogue. I would also like to thank Assoc. Prof. Bim Graham's research group for sharing their experience and knowledge with me. I am grateful to Dr. Luigi Aurelio for his patience while teaching me organic synthesis and to Josh Conner for always having the time to help out.

I would also like to thank Dr. Georgina Such and her research group at The University of Melbourne as well as my panel members Prof. Chris Porter, Dr. Michelle Halls, Prof. Colin Pouton, and Dr. Nicholas Veldhuis for their involvement in my project and invaluable advice over the time of my candidature. In addition, I would like to thank Nachnicha Kongkatigumjorn for her nanoparticle synthesis. I am extremely grateful to my husband James Selby for his constant love and companionship and thank him for believing in me. I would like to thank my fantastic parents Ina Messig and Barry FitzGerald for their emotional and financial support during my PhD and to my sister Audrey FitzGerald and mother-in-law Christine Selby for their help over this time. I am also appreciative of the continuous company and friendship provided by my cat Montii.

Finally, I gratefully acknowledge Monash University and the ARC Centre of Excellence in Convergent Bio-Nano Science and Technology for their support and the opportunities they have provided throughout my PhD.

VI. Table of Contents

I.	Copyright notice	1
II.	Abstract	2
III.	Publications During Enrolment	4
IV.	Thesis Including Published Works Declaration	5
V.	Acknowledgments	7
VI.	Table of Contents	8
	Chapter 1. Introduction	10
	1.1 Summary.....	11
	1.2 Manuscript for It's what's on the Inside That Counts: Methods for Investigating the Uptake and Recycling of Proteins and Nanoparticles	12
	1.3 Published manuscript for Nanoescapology: progress toward understanding the endosomal escape of polymeric nanoparticles	24
	1.4 Purpose of the Research	47
	Chapter 2. HD Flow Cytometry: An Improved Way to Quantify Cellular Interactions with Nanoparticles	48
	2.1 Summary.....	49
	2.2 Published Manuscript and Supporting Information	50
	Chapter 3. Quantifying Cellular Internalisation with a Fluorescent Click Sensor	75
	3.1 Summary.....	76
	3.2 Manuscript for Quantifying Cellular Internalisation with a Fluorescent Click Sensor and Supporting Information	77
	3.3 Introduction.....	99

3.4 Results and Discussion.....	102
3.5 Conclusions.....	115
3.6 Materials and Methods.....	116
3.7 References.....	121
Chapter 4. SNAPSwitch: A Molecular Sensor to Quantify Endosomal Escape and Cellular Localisation	124
4.1 Summary.....	125
4.2 Manuscript and Supplementary Information	126
Chapter 5. Oligonucleotide Switches for Quantifying Endosomal Escape	
Efficiency	155
5.1 Summary.....	156
5.2 Introduction.....	157
5.3 Results and Discussion.....	165
5.4 Conclusions.....	186
5.5 Materials and Methods.....	186
5.5 References.....	195
Chapter 6. Summary and Future Directions	200
6.1 Main Findings and Future Directions.....	201
6.2 Overall Summary.....	204
6.3 References.....	205

Chapter 1. Introduction

1.1 Summary

Nanomaterials have gained substantial attention due to their potential for addressing problems associated with traditional drug delivery. Encapsulating or conjugating therapeutics to carriers improves drug solubility and imparts protection to delicate cargo such as proteins, peptides and nucleic acids that would otherwise degrade while circulating around the body. In addition, the carriers can be modified with targeting groups to increase accumulation in specific cell types. To design nanomaterials for a biological objective requires a thorough understanding of the bio-nano interface. This requires answering the following questions: how much material gets inside the cell, where is it trafficked to and can it reach the intended subcellular destination?

As an introduction, this chapter contains two manuscripts reviewing the cellular processing of nanomaterials. To deliver drugs into the cell requires the carrier be taken up, most commonly by endocytosis. The first section of this chapter describes current methods for quantifying internalisation and highlights the significant advantages of sensors in this endeavour. Although therapeutics may be active in the cytosol, many do not reach this destination. The escape of cargo from endocytic vesicles to the cytosol following uptake is currently considered to be a major bottleneck in intracellular delivery by nanomaterials and is the focus of the second part of this chapter. The current understanding of nanoparticle endocytosis and intracellular trafficking is reviewed. Methods for determining the location of nanoparticles within the cell and for the detection of endosomal escape are also described. Finally, the current state in polymeric nanoparticles engineered for inducing escape is covered.

It's What's on the Inside That Counts: Methods for Investigating the Uptake and Recycling of Nanoparticles and Proteins

L. I. Selby^{a,b} and A. P. R. Johnston^{a,b*}

Received 00th January 20xx,
Accepted 00th January 20xx

DOI: 10.1039/x0xx00000x

www.rsc.org/

Many applications of nanomedicines depend on the therapeutic gaining access to the inside of cells. As most proteins and nanoparticles are taken up by endocytosis, delivery of drugs to the cytosol or other subcellular regions requires efficient uptake. Determining what properties are required to do this effectively is challenging and so, methods that can evaluate nanoparticle internalisation are essential. In this review, we cover the current approaches for investigating the uptake of nanoparticles and proteins into cells. We review the techniques available for detecting materials within cells and tactics for quantifying internalisation. The recent developments in sensors and their advantages over traditional assays for uptake and recycling are also highlighted.

1. Introduction

Drug delivery relies heavily on either the therapeutic target being located on the cell surface or the compound being membrane permeable. Biopharmaceuticals, including proteins, peptides and nucleic acids, have immense potential to treat a range of diseases, but the ability to deliver these molecules must be improved.^{1,2} To address this, nanoparticle systems are currently being developed to protect cargo and improve uptake in specific cells.^{3–5} As the goal is to deliver therapeutics to the inside of the cell, material that is not internalised will be ineffective for delivery to intracellular targets.

The ability to determine the extent to which a material is taken up into cells is critical. This is important for investigating what properties are required for efficient internalisation, such as the effect of size, shape and surface modifications.⁶ The effect of experimental conditions such as concentration, incubation time and how uptake changes across cell lines,⁷ or due to differences in cell media and the components of the protein corona must also be considered.⁸

Some of the techniques used to examine nanoparticle internalisation can equally be applied to study proteins, and in many cases, were originally developed for this type of analysis. Examining the uptake of proteins is vital from a mechanistic standpoint, as there are still unanswered questions regarding how particular antibodies exert their therapeutic effect.⁹ In addition, the distinction between membrane binding and passage through the endocytic network is particularly critical for antibody-drug conjugates with labile linkers.¹⁰ With an in-depth

understanding of how nanomaterials and proteins bind to and are taken up into cells, we can move towards engineering more effective drug delivery systems.

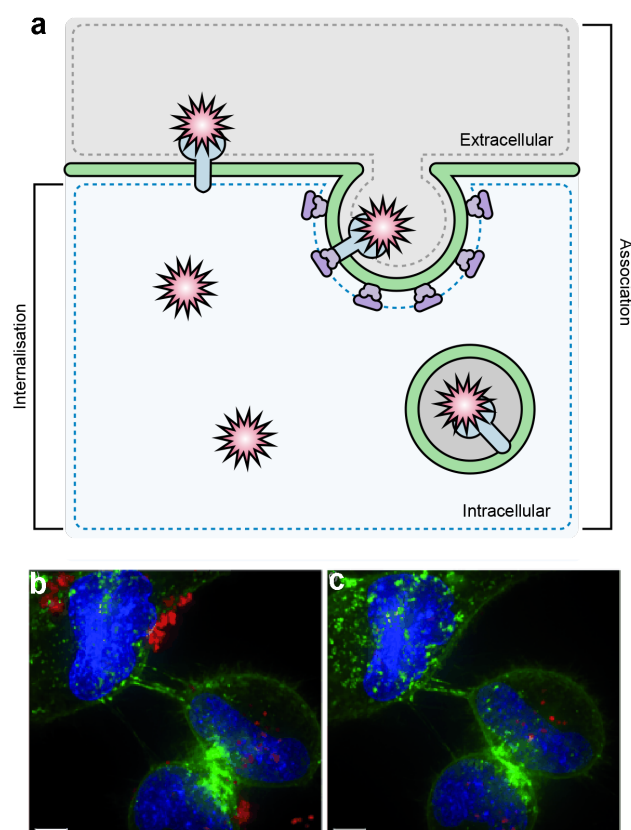


Figure 1 – The difference between association and internalisation. (a) Associated material comprises the total amount both inside and remaining attached to the surface of the cell. The definition for “internalization” refers only to material in the intracellular space. (b) Fluorescently labelled nanoparticles (red) associate with HeLa cells (top panel) with a surface stain (green) and nuclear stain (blue). (c) Removing surface fluorescence shows not all particles were internalised. Scale bar = 5 μ m. ((b) and (c) reprinted with permission from Ref 23. Copyright 2013 Wiley)

^a Drug Delivery, Disposition and Dynamics, Monash Institute of Pharmaceutical Sciences, Monash University, Parkville, Australia. E-mail: Angus.Johnston@monash.edu

^b ARC Centre of Excellence in Convergent Bio-Nano Science and Technology, Monash University, Parkville, Australia

Herein, we provide an overview of the techniques currently used to quantify internalisation with a focus on fluorescence-based methods. We highlight the desirable attributes of sensors for this purpose as well as their adaptation to study recycling.

2. Defining Uptake

The terms “uptake” and “internalisation” are both used to refer to the amount of material that has moved to the inside of the cell. However, these terms can be used incorrectly when used to describe the total amount of material “associated” with the cell (**Figure 1**).¹¹ An example is the use of flow cytometry to determine the mean fluorescence intensity (MFI) of a cell, and equate this value to uptake. The MFI represents total fluorescence emitted from the cell, and encompasses material both inside the cell and that remaining bound to the cell surface. As such, this is a measure of association, not internalisation. To precisely quantify internalisation, a method must be used to differentiate between material inside the cell and that remaining bound to the cell surface.

Aside from the amount of material taken up, the mechanism of internalisation is often also of interest. Multiple mechanisms exist for material to enter the cell. Of these, the most well-characterised is clathrin-dependent endocytosis, although clathrin-independent mechanisms are also important.¹² In this process, adaptor proteins and clathrin are recruited to draw in the membrane and form a vesicle which is eventually cut off from the cell surface by dynamin.¹³ Following internalisation, vesicles from both clathrin-dependent and independent endocytosis are rapidly trafficked to early endosomes which sort the incoming material into different pathways such as on to late endo/lysosomes or into recycling pathways.¹⁴ Following internalisation, endocytic compartments acidify.¹⁵ This causes changes in the structure of some receptors and acts as a trigger to release endogenous endocytic cargo, allowing for the receptor to be recycled or degraded.^{16,17}

The question remains if the mechanism of internalisation is important in the subsequent trafficking and hence efficacy of the delivered material. In addition, while endogenous proteins are usually taken up by a characterised receptor, nanoparticles can be taken up by multiple mechanisms simultaneously¹⁸ which adds to the confusion. Inhibitors can be used to block uptake by certain pathways in order to classify the mechanism. For example, treatment of cells with sodium azide causes ATP-depletion and interferes with energy-dependent endocytosis.¹⁹ Many inhibitors are available but they do have varying levels of specificity. Some have additional carry over effects so caution is urged when interpreting results and the use of multiple methods, including genetic manipulation of the pathways is encouraged.^{20,21}

3. Halting Internalisation

Before internalisation can be quantified, further uptake must be prevented. Cooling the cells to 4°C is an effective strategy to inhibit endocytosis²² and maintain particles, proteins²³ and

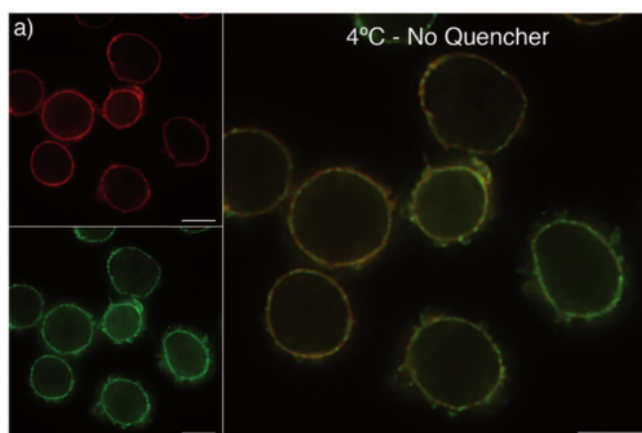


Figure 2 – Low temperature (4°C) incubation of 75 µg/mL transferrin labelled with an oligonucleotide-Cyanine 5 conjugate in CEM.NKR cells for 30 minutes results in fluorescence forming a ring of red fluorescence at the cell surface that localizes with an Alexa Fluor 488-wheat germ agglutinin conjugate. Scale bar = 10 µm. (Reprinted with permission from Ref 23. Copyright 2013 Wiley)

peptides²⁴ at the cell surface, where they appear as a ring of fluorescence (**Figure 2**). The change in temperature rigidifies the cell membrane by causing the lipids to undergo a phase transition to a crystal gel state.^{25,26} The detection of certain peptides^{27,28} and particles within cells at this temperature has been used to suggest some materials may possess the ability to directly translocate across the membrane. However, there is significant debate in the literature as to whether these results are real or are an artefact of the experimental method used.²⁹

2. Techniques for Detecting Nanomaterials in Cells

The interactions of nanomaterials and proteins with cells are typically investigated using fluorescent labels in conjunction with microscopy or flow cytometry. A method using only 3D confocal microscopy image stacks to identify the number of nanoparticles inside an individual cell has been developed using an ImageJ macro (*Particle_in_Cell-3D*).³⁰ The script uses a fluorescent membrane stain to define the inside and outside of the cell as regions of interest in three dimensions (**Figure 3**). Nanoparticles labelled with a different fluorophore can then be

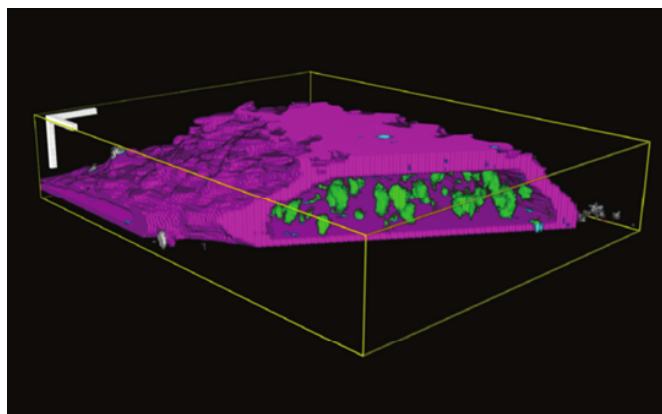


Figure 3 – A 3D representation of a cell with internalised nanoparticles from analysis with the ImageJ macro *Particle_in_Cell-3D*. (Reprinted with permission from Ref 30. Copyright 2013 Future Medicine)

assigned to one of the regions and the uptake calculated. The procedure has been demonstrated to quantify the number of 100 nm polystyrene nanoparticles per cell, and could detect how many particles were present as small aggregates. However, absolute quantification requires external calibration to determine the average intensity of an individual particle and assumes this value will not change if the particle is inside a cell.

Confocal microscopy has high resolution that can resolve the sub-cellular localisation of the materials, but is inherently low-throughput. Flow cytometry is extremely high-throughput and allows data acquisition on thousands of cells per second³¹ but gives no information about the location of the fluorescent signal. Attempts have been made to overcome these limitations through combining flow and microscopy in various ways and adapting them to quantify internalisation without the use of methods to identify internalised material.

A combined approach has been used to quantify the average number of nanoparticles per cell.³² The first step in this process is to obtain the average fluorescence intensity of an individual nanoparticle (**Figure 4a**). As the typical lower detection limit for nanoparticles by flow is around 300 – 500 nm,³³ a method was developed to obtain the fluorescence value of one particle. This was achieved by measuring the fluorescence of a series of known concentration standards in a fluorimeter and comparing them to the fluorescence of 1 μm particles (which are large enough to be detected by flow cytometry) obtained under the same conditions by both the fluorimeter and by flow cytometry to develop a calibration factor (**Figure 4b, c**). Measurements of

the total fluorescence of cells incubated with the particles was then obtained by flow cytometry (**Figure 4d-g**) and using confocal scanning laser microscopy images, the proportion of particles located inside the cell was determined by manually selecting the inside of 20 – 50 cells per sample, using wheat germ agglutinin as a cell surface marker. (**Figure 4h-k**). By combining the values obtained separately from these three instruments into Equation 1, the average number of internalised particles per cell can be calculated.

$$n \left[\frac{P_{in}}{cell} \right] = f_i \times \frac{MF_{cell} - MF_{neg\ cell}}{\left[(1 - f_i) + f_i \times \frac{1}{FR_{o/i}} \right] MF_P} \quad (\text{Equation 1})$$

Where,

$n[P_{in}/cell]$ = Average number of internalised particles per cell,
 f_i = Fraction of internalised particles, MF_{cell} = Mean, fluorescence intensity of cells incubated with particles from flow, $MF_{neg\ cell}$ = Mean fluorescence intensity of cells without particles from flow, MF_P = Mean fluorescence intensity of an individual particle and $FR_{o/i}$ = Correction factor for changes in fluorescence on internalisation

The authors also took the change in the average fluorescence intensity when the particles are internalised into account, a factor that is often not considered. However, they highlight that compensating for this is not necessary if the dye is pH

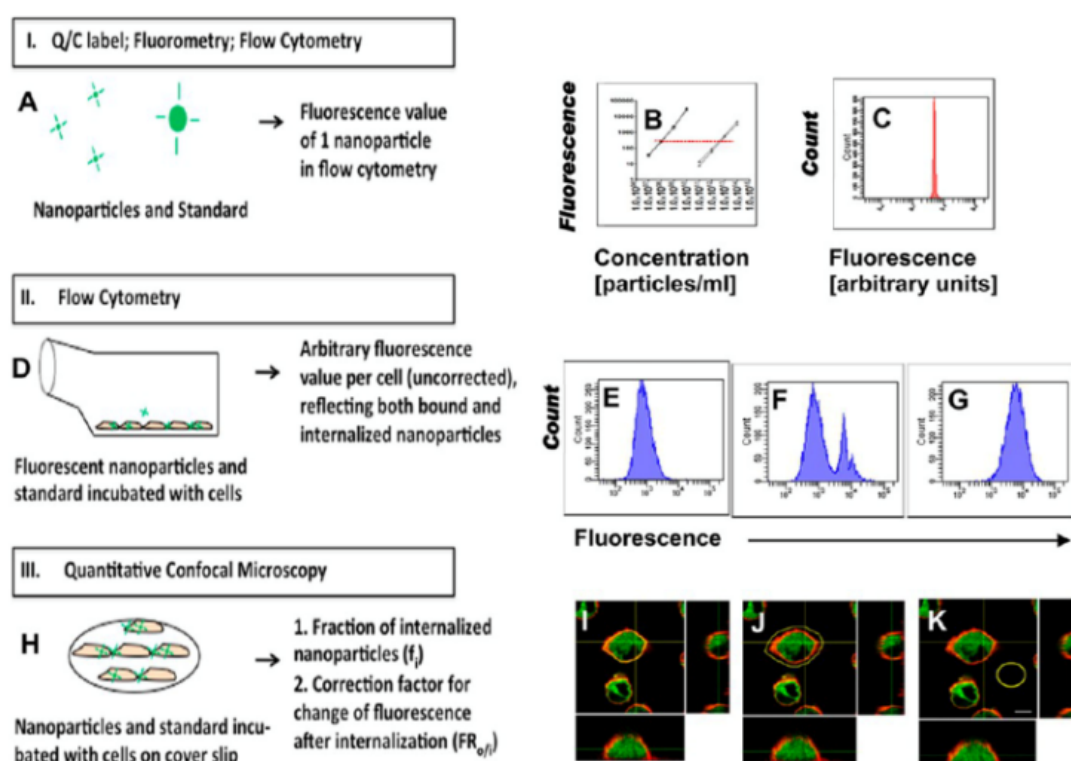


Figure 4 – Process for internalisation quantification using flow cytometry in conjunction with confocal scanning laser microscopy. (a-c) The fluorescence of one nanoparticle is determined using a fluorimeter and flow cytometry. (d-g) Cells are incubated with and without particles and the mean fluorescence intensity of the cells is determined by flow cytometry. (h-k) The fraction of the fluorescence emanating from within the cells is determined by confocal scanning laser microscopy by manually selecting the inner region, using a cell surface stain as a guide (wheat germ agglutinin). (Reprinted with permission from Ref 32. Copyright 2013 American Chemical Society)

insensitive and doing so drastically simplifies the analysis and subsequent error associated with the final value. Common dyes including the Alexa series,³⁴ cyanine fluorophores (that have not been modified for pH-responsiveness)³⁵ and tetramethylrhodamine are known for their pH insensitivity and should be used over other common dyes that display pH-responsive properties such as fluorescein³⁶ to facilitate internalisation studies. This requirement to carry out confocal microscopy still limits the throughput of this method as this is a time-consuming process. Altering experimental conditions, such as the inclusion of a panel of inhibitors would drastically increase the time needed to perform an experiment since imagining would need to be repeated for each modification.

The individual limitations of confocal microscopy and flow cytometry along with potential issues arising from the use of different protocols for non-adherent and adherent cell lines before analysis has led to the development of imaging flow cytometry (IFC).³⁷ Using this technology, the mean fluorescent intensity on a population level is available as with regular flow cytometry, but IFC also captures a microscopy image of each individual event to provide spatial information.³⁸ Software packages for IFC determine internalisation by defining a region of interest inside the plasma membrane, which is identified based on a bright field image. Internalisation is calculated by the ratio of intensity inside the region to the total intensity.³⁹ IFC is still a relatively recent development but has been used to compare uptake between two colon carcinoma cell lines with and without the receptor for a targeted antibody-functionalized polymer capsule,⁴⁰ probe internalisation of antibody-functionalised polymer capsules in dendritic cells⁴¹ and quantify lipidoid nanoparticle uptake in Kupffer cells.³⁹

4. Non-specific Methods for Removing Surface Signal

There are several methods available to non-discriminately and physically detach proteins or nanoparticles from the cell membrane. While straightforward experimentally, they also remove all surface signal which can be problematic when other fluorescent markers are used, such as for cell phenotyping. Two main methods are used to dissociate surface-bound material from the cell, the first of which is acid-washing. Particles targeted to specific receptors can exploit the natural action of pH as a trigger for dissociation between ligand and receptor to remove surface-bound material. By washing the cells in a mildly acidic solution, this dissociation can be forced. This is commonly used in the study of ligands bound to receptors^{42,43} and in the study of nanoparticle internalisation^{44,45} but does have several drawbacks. Although often targeted to a particular receptor, the particle may bind to multiple regions of the cell surface and interactions with serum constituents and the formation of the protein corona can hide targeting moieties, rendering them ineffective.⁴⁶ Acid-wash is not completely efficient in its removal of proteins from the surface, even in the case of transferrin which possesses pH-dependent receptor binding.^{23,47} In addition, this method is deleterious to cell viability.^{48,49}

The second technique to remove material bound to receptors is the use of the protease trypsin. This enzyme cleaves at the carboxyl side of both lysine and arginine residues and as such, also digests cell surface proteins.^{50,51} This is often suggested as a method to remove nanoparticles bound to receptors, but this is only the case if the particles are indeed bound to proteins. A study into the cell-line dependent internalisation of fluorescently labelled alginate-chitosan DNA complexes revealed that while treatment with trypsin drastically decreased association in both the HEK293T and COS7 cell lines by 75 – 85%, a decrease of only 15% was seen in CHO cells. This suggested that the particles were not attached to trypsin-sensitive proteins in all cell lines.⁵² Therefore, trypsin cannot reliably be used as a method to remove surface bound material.

Fluorescence remaining on the cell surface can also be non-specifically removed using the membrane impermeable dye Trypan Blue.^{53,54} It is routinely used to establish cell viability through dye exclusion assays⁵⁵ but is also used in flow cytometry and confocal microscopy to remove the fluorescence signal on the outside of the cell. It is critical the quenching dye remains excluded from the inside of the cell so the internalised fluorescence signal is unaffected. This technique has been used in multiple nanoparticle studies to investigate uptake efficiency.^{56–58} The effect of particle characteristics such as material type,⁵⁹ charge⁶⁰ and the efficacy of targeting moieties to certain receptors⁶¹ has been investigated with this quenching method. While simple to use, the non-specific quenching of trypan blue can be an issue if other fluorescent surface markers need to be used such as for immunophenotyping. Trypan blue binds to certain proteins,⁶² possesses significant fluorescence between 600 – 720 nm when excited at 488 nm^{63,64} and can increase the autofluorescence of cells by up to 2.5-fold which effects quenching efficiency and signal to noise ratio.⁶⁵

A similar method was developed that exploits electrostatic attraction to draw the quencher in towards the cell surface. By conjugating a quencher dye to the polyamine spermine, a reduction in the signal from fluorescently labelled receptors on the cell surface could be reduced by 94%.⁶⁶ Spermine is positively charged under extracellular conditions and is attracted to the anionic cell membrane. This conjugate was used to probe if low-density lipoprotein receptors internalize as oligomers. The authors initially attempted to remove the surface fluorescence using an amine-reactive succinimidyl ester-modified quencher but observed incomplete quenching effects.

Although most methods for quantifying internalisation rely on fluorescence, non-fluorescent techniques exist for certain nanoparticle compositions, such as metallic nanoparticles. Engineering sensitivity towards certain chemicals is possible so that they can then be removed through “etching.” Plasmonic silver nanoparticles can be rapidly removed with hexacyanoferrate-thiosulphate de-staining solution while gold nanoparticles can be dissolved off the cell surface with an iodine/potassium iodide solution. Etching using these chemicals is highly specific to these materials and cannot be used on other nanoparticle systems.

Analytical electron microscopy has been used with CdSe/ZnS core/shell semiconductor quantum dots in U-2OS cells to track the particles from incubation through to lysosomal accumulation with transmission electron microscopy (TEM) for individual dot counting.⁶⁷ Serial block face scanning electron microscopy (SBF SEM) has also been performed to produce a 3D image stack and was used to show the traverse of vesicles containing quantum dots towards the centre of the cell over time.

The extremely high resolution of transmission X-ray microscopy (TXM) has also been used to study internalisation by identifying nanoparticle clusters inside the cell. Using this technique, crosslinking of dextran on iron oxide nanoparticles was shown to permit uptake in HeLa and EMT-6 cells while particles with non-crosslinked surface coatings were not internalised.⁶⁸ Differences in the internalisation of polyethylene glycol coated gold nanoparticles between individual cells in the same culture and between cell lines have also been observed in a separate study.⁶⁹ The X-ray source in this method is synchrotron-based and as access to the required facilities may be difficult, this method is likely to be too costly and inconvenient for most uptake studies.

Alternatives to microscopy for quantifying the internalisation of inorganic nanoparticles that require much less specialized training and with increased throughput exist but are at the cost of spatial information. Spectroscopy techniques that analyse samples for metals have been used extensively in this field. Inductively coupled plasma-mass or atomic emission spectroscopy (ICP-MS and ICP-AES) have both been used to measure the amount of metal internalised, typically looking for iron in magnetic particles or gold.^{8,70–72} The samples are initially prepared in a similar manner as they would for flow cytometry but are then dissolved in 37% hydrochloric acid. None of this standard processing significantly removes surface bound material and further treatment is required to fully quantify what is inside the cell.

5. Sensors for Cellular Uptake

The diversity of therapeutic targets means that many particles and proteins cannot be detached from the cell surface using either acid-wash or trypsin cleavage. Sensors developed specifically to probe internalisation provide advantages to overcome these issues. An ideal internalisation sensor should be specific to a single fluorophore that can be attached to the nanoparticle or protein, easy to use, preferably without any additional wash steps and compatible with multiple instruments including flow cytometry and fluorescent microscopy. Many of the advances have come from the need for quantifying receptor and ligand internalisation in the molecular biology field but can be applied to study the uptake of nanomaterials.

The internalisation of receptors and their ligands can be tracked using pH-sensitive dyes (**Figure 5a**). These dyes sense changes in pH through groups that can be protonated at biologically relevant pH values (such as that of an endosome). This causes a change in the fluorescence properties such as the fluorescence intensity or the excitation and emission wavelengths. Some of the dyes, such as pHrodo or CypHer 5,⁷³ increase in fluorescence intensity with a decrease in pH, as experienced through endocytic trafficking. For quantification purposes, the particle must be co-labelled with a pH insensitive dye and the ratio between the two computed. This ensures high fluorescence is due to a pH drop, and not due to a high concentration of particles at a higher pH. A limitation with pH sensitive dyes is that most have some level of background fluorescence at extracellular pH, resulting in a low signal-to-noise ratio. Additionally, even if this can be overcome, they are inappropriate to study materials that are designed to reach the cytosol. Escape of material from endo/lysosomes causes the pH to return to ~ 7.5 and leads to the incorrect assumption that the material has not been internalised.

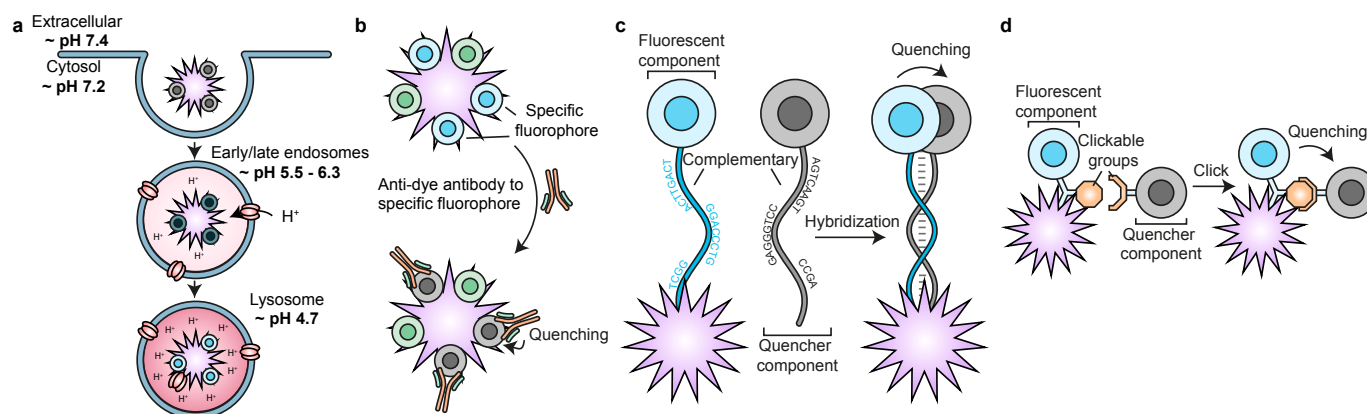


Figure 5 – Sensors for internalisation. **(a)** pH sensitive dyes – After internalisation, particles are trafficked into endosomal and lysosomal compartments where the pH changes from ~ 7.4 down to 4.7. Protonation of the dye causes a change in the emission intensity. **(b)** Anti-dye antibodies – an antibody to the specific dye on the nanoparticle is added which quenches the fluorescence. **(c)** The specific hybridisation internalisation probe (SHIP) assay – a fluorescently labelled oligonucleotide is attached to the nanoparticle. After incubation, a second oligonucleotide with a complementary sequence and with a quencher dye attached is added to hybridise to the fluorescent strand and quench extracellular fluorescence. **(d)** Click internalisation sensor – fluorescent component containing a fluorophore and click group are conjugated to the material of interest. Following internalisation, extracellular fluorescence is removed by addition of a quencher component which contains a compatible click group, allowing it to covalently attach to any material remaining on the cell surface.

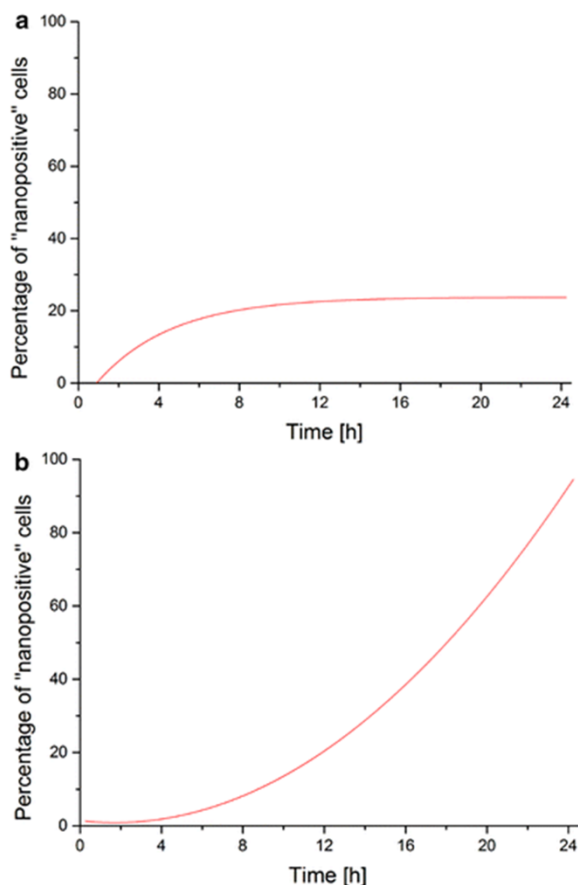


Figure 6 – Internalisation over time of iron nanowires labelled with pHrodo red in (a) HeLa cells and (b) HCT 116 cells, calculated by a modified version of CellCognition, a computational framework that uses object identification to classify cells as positive or negative for the presence of nanowires. (Reprinted from Ref 74. Copyright Margineanu et al. 2016, licensed under creativecommons.org/licenses/by/4.0/)

pH sensitive dyes have been used in conjunction with computational methods to semi-automate quantification of internalisation.⁷⁴ An open source machine-learning software called *CellCognition* was modified to identify particular phenotypes from live cell imaging movies based on manual selections by the user.⁷⁵ Using iron and nickel nanowires labelled with pHrodo red to differentiate between nanowires located inside and outside the cell, the difference in uptake between two cell lines (HCT 116 and HeLa) over time could be observed (**Figure 6a and b**). The results were in good agreement to those obtained through flow cytometry (percentage of cells positive for a pHrodo red signal) and were close to internalisation calculated by manual assignment of cell images. The authors highlight the issues of using dyes such as pHrodo to monitor internalisation, as particles adsorbed to the cell surface have some fluorescent signal. As the process is semi-automated, the only user input required is the classification of objects. This includes identifying cells through a nuclear marker and then, cells with and without particles within these objects through fluorescence in a separate channel. The analysis is limited to approximately 500 - 600 cells per image but may be useful in validating bulk measurements obtained by flow cytometry.

Aside from changing fluorescence intensity in response to pH, some dyes emit at different wavelengths depending on the protonation state of the fluorophore.⁷⁶ An example of this is seminaphtharhodafleur (SNARF) dyes which have been used to quantify the uptake of polyelectrolyte microcapsules.⁷⁷ By loading polymer capsules with SNARF–dextran conjugates and measuring the fluorescence in both the red and green channels by flow cytometry, the ratio of particles internalised was determined. Cells with particles, either adhered to the surface or internalised, display high forward- and side-scatter properties while cells without particles or particles not associated with cells are lower in both channels (**Figure 7**). However, a major limitation with this method is the inability to distinguish cells that have particles on the surface as well as inside (or both red and green fluorescence simultaneously). The authors propose this can be controlled by adding a limited number of particles to ensure association of only 1 per cell. While limiting association to one microcapsule per cell is feasible for the large particles used in the study (3–4 μm), when studying nanoparticles there are typically many nanoparticles associated with one cell.

An additional means to specifically switch off extracellular fluorescence is through antibodies generated to bind to specific fluorophores (**Figure 5b**). They are available for a selection of common dyes including Alexa Fluor 488 and fluorescein. Quenching is generally highly efficient and specific, with limited cross reactivity between antibodies targeting different dyes.⁷⁸ Although these have been used in the molecular biology field to

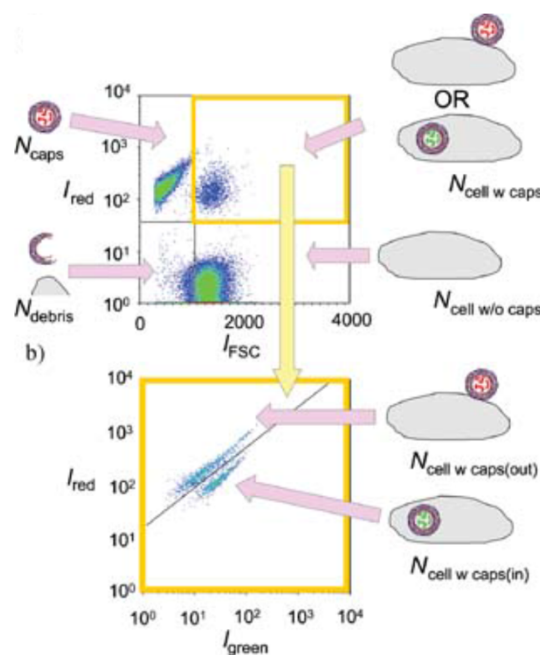


Figure 7 – pH-sensitive fluorophores used to track internalisation with flow cytometry. Internalised microcapsules can be differentiated from those bound to the surface using the red fluorescence intensity vs. forward-scatter plot. The red vs. green fluorescence intensity plot is then used to isolate cells with surface-bound particles from those with internalised particles. (Reprinted with permission from Ref 77. Copyright 2008 Wiley)

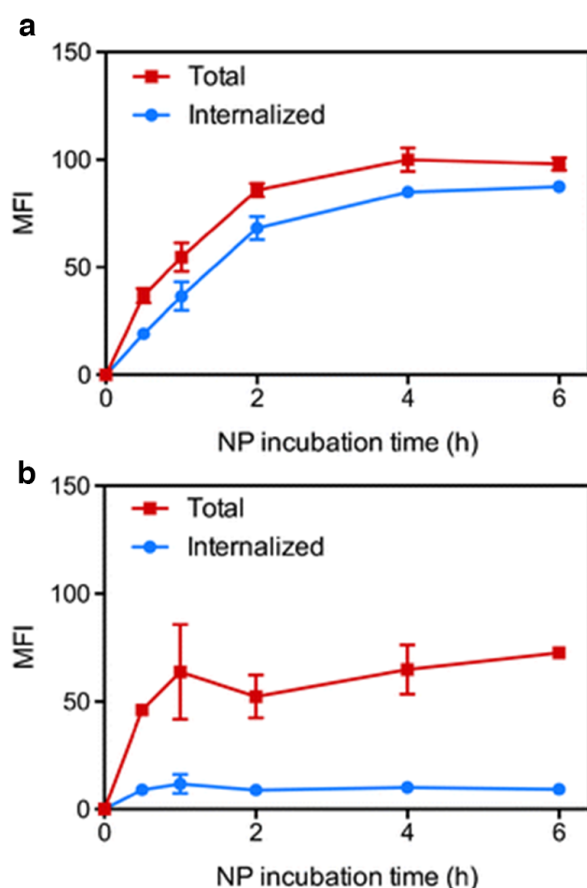


Figure 8 – Cell line-dependent internalisation kinetics of polymeric nanoparticles investigated with the Specific Hybridisation Internalisation Probe (SHIP) assay. Particles labelled with a fluorescent DNA oligonucleotide and incubated with (a) 3T3 and (b) CEM cells before analysis by flow cytometry. The mean fluorescence intensity from unquenched (red squares) and quenched (blue circles) is plotted showing the total and internalised signal respectively. (Reprinted with permission from Ref 91. Copyright 2016 Springer)

quantify the internalisation of transmembrane enzymes or of other antibodies,^{48,79} they have not yet been applied in probing the uptake of nanoparticles.

Alternatively, dual labelling with a fluorophore and quencher simultaneously has the potential to quantify the internalisation of materials that degrade once taken up into cells. This has been performed to screen the uptake and degradation of antibodies directed towards extracellular targets.⁸⁰ The fluorescence of the labelled antibodies was quenched by ~80–90% through conjugation of a quencher dye, and they regained ~70–90% of their fluorescence when treated with a proteinase and sodium dodecyl sulfate. This method requires a high degree of labelling, with up to 11 dyes molecules per antibody which may affect the binding properties of the protein/nanoparticle. It has been observed that with a dye to protein ratio as low as 1.8, the binding to the receptor is decreased and that higher degrees of labelling can result in complete inactivation of the antibody.⁸¹ In addition, digestion is required for signal to be observed, which may not occur for all materials, and if it does occur, there will be a delay between the material being internalised and the degradation occurring. This

type of assay could be used to study the internalisation of nanoparticles designed to disassemble, such as those constructed from pH-responsive materials. However, it would be inappropriate for materials that do not degrade or are recycled, such as transferrin.^{16,82}

Relying on antibody digestion or using pH responsive dyes are both indirect ways to measure internalisation. The time taken to reach endocytic vesicles with a certain pH value or that are capable of degradation is likely dependent on the properties of the material and the cell type. For example, transferrin is internalised and recycled within minutes with neither receptor or cargo experiencing degradation.^{82,83} Collagen however, was found to move from early to late endosomes after 20 minutes, followed by slow accumulation in lysosomes over 16 hours in rat liver endothelial cells.⁸⁴ The endocytosis of nanomaterials may be even more variable. A small proportion (~13%) of poly (DL-lactide-co-glycolide) particles delivered to ARPE-19 cells were found in lysosomes as early as 15 minutes after addition, with the majority taking an hour to arrive (~72%).⁸⁵ This was determined by quantifying the level of colocalisation between fluorescently labelled particles and lysosomes stained with LysoTracker, a membrane permeable and pH responsive dye that accumulates in acidic organelles.⁸⁶ In addition to the effect of probe concentration on fluorescence intensity, non-specific labelling may cause other organelles to be incorrectly identified as lysosomes, a significant limitation when using this labelling method.⁸⁷ Other material types can take longer to traffic within cells. Latex microspheres targeted to the intercellular adhesion molecule-1 took 2–3 hours to reach the lysosomes of HUVEC cells.⁸⁸ Due to the variation in time taken to each lysosomes, quenching of the extracellular surface is preferable for identifying internalised material.

To improve the specificity of quenching, only the signal of the fluorophore on the nanoparticle/protein should be removed. In addition to the previously described anti-dye antibodies, an example of a system that is capable of this is the oligonucleotide-based sensor system called the Specific Hybridisation Internalisation Probe (SHIP).²³ A fluorescently labelled oligonucleotide (FIP) is attached to a protein or particle of interest and allowed to internalise. Internalisation is stopped by reducing the temperature of the cells to 4°C and a complementary oligonucleotide labelled with a quencher can hybridise with labelled material on the cell surface (**Figure 5c**). This method was shown to have improved quenching ratios over both acid-wash and trypan blue methods.

This switchable fluorescence system has been used to highlight the critical difference between uptake and association by investigating these quantities in two different cell lines (**Figure 8**). Polymeric nanoparticles labelled with FIP and added to 3T3 or CEM cells showed that over 98% of cells in both cell lines had associated nanoparticles after 6 hours. The internalisation however was starkly different. In the 3T3 cell line, 89% of nanoparticles were internalised after 6 hours while

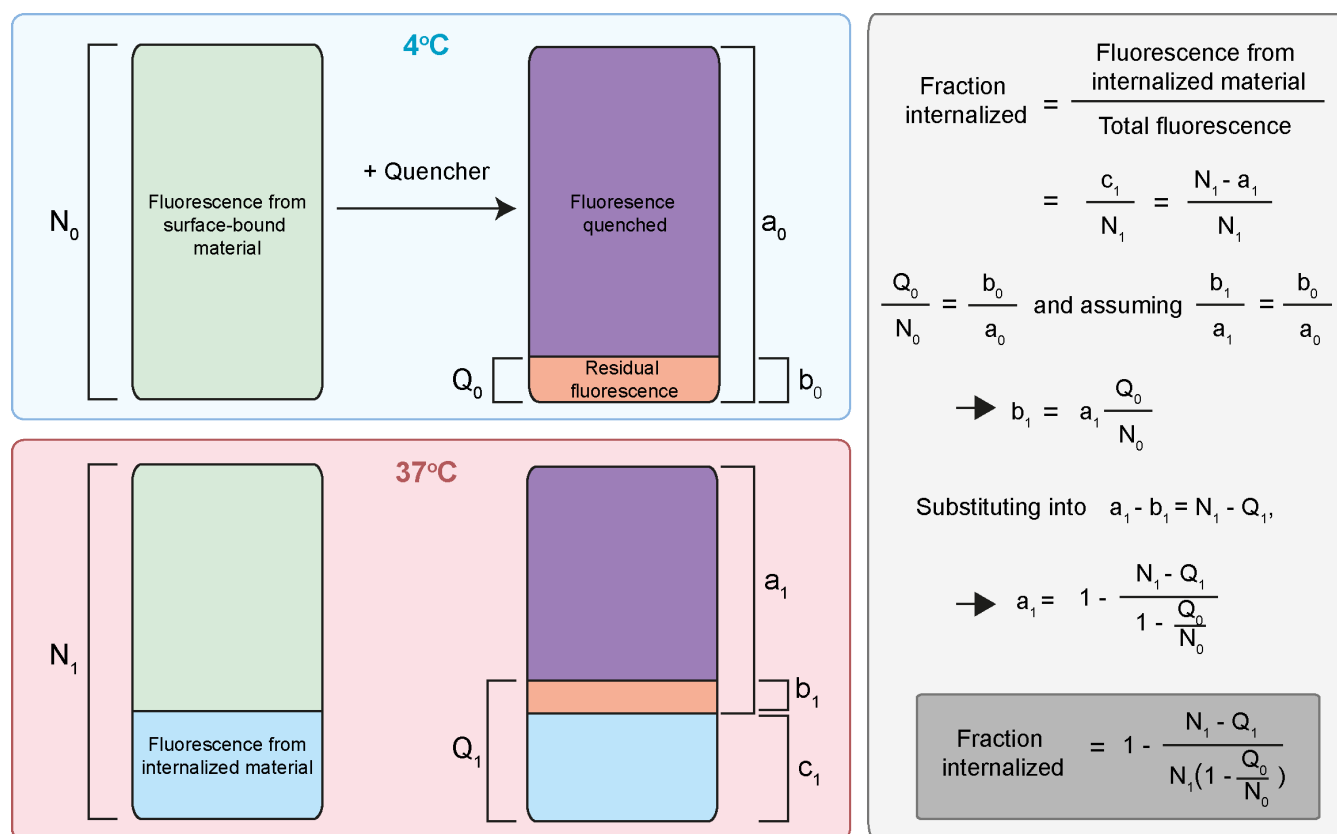


Figure 9 – Compensating for incomplete surface quenching. Flow cytometry allows for the following four fluorescence intensity values to be measured: the signal from material bound to the cell surface at 4°C (N_0), the remaining signal after quenching at 4°C (Q_0), the signal from material on the surface and inside the cell at 37°C (N_1) and the signal from material inside the cell along with the unquenchable surface component (Q_1). By defining a series of variables that describe each component of the fluorescence signal, an equation can be derived to calculate the fraction of material internalised that accounts for the quenching efficiency using only the measurable quantities from flow cytometry. (Figure modified from Ref 48)

only 20% of particles internalised in the CEM cell line. This switch is also compatible with inhibitor screening to elucidate mechanisms involved in internalisation.

More recently, a modified version of the SHIP assay was designed to decrease the size of the fluorescent label.⁸⁹ Although the original system was demonstrated to not interfere with the innate trafficking pathways of transferrin (80 kDa), the effect on smaller materials or those that carry a significant charge may not be compatible with the 10 kDa negatively charged DNA sequence. Instead of using DNA hybridisation to specifically quench surface-bound fluorescence, the rapid click-chemistry reaction between *trans*-cyclooctene (TCO) and tetrazine was used. Here, a fluorophore conjugate was synthesised to contain both a TCO group and a carboxylic acid for attachment to the material, while a compatible quencher was conjugated to a tetrazine group (**Figure 5d**). This sensor system works analogously to the SHIP assay albeit, with slightly lower quenching efficiency. The clickable sensor had comparable kinetics to the FIP assay, obtained its maximum quenching efficiency at the same concentration of quencher and matched the calculated value for the internalised quantity of transferrin. It was also demonstrated to be applicable to the study of other sized proteins including a nanobody (~14 kDa) and antibody (~150 kDa).

6. Compensating for Incomplete Surface Quenching and Low Fluorescence

The most direct way to calculate the fraction of material internalised is to compute the ratio between the quenched and total fluorescent signal. If quenching is incorrectly assumed to be 100% efficient, the resulting number is in an overestimation of the amount of material internalised. This is due to the residual surface fluorescence that cannot be quenched being included with the fluorescence intensity from the inside of the cell, artificially inflating this value. Incomplete quenching is caused by a combination of factors, including the inherent quenching efficiency of the fluorophore/quencher pair and the complicated chemical nature of cell surfaces hindering accessibility to all fluorophores.

To compensate for this phenomenon, an equation for calculating internalisation using the values obtained by flow cytometry has been derived that takes into account inefficient quenching.^{48,78} The intensity of only the material inside the cell (c_1) (**Figure 9**) is required, however this is not directly available, as the measurable quantity (Q_1) includes both the internalised component (c_1) and the residual fluorescence (b_1) from incomplete surface quenching. To determine the residual fluorescence, the quenching efficiency of the

fluorophore/quencher pair must be experimentally determined by incubating the material of interest with cells at 4°C. The fluorescence from cells under these conditions emanates from the cell surface as endocytosis is halted (N_0). When quencher is added to the sample at 4°C (Q_0), the remaining signal is the residual fluorescence (b_0). The quenching efficiency can then be determined by subtracting the ratio of the quenched to unquenched signal from 1. By assuming this ratio remains constant, the residual fluorescence can be compensated for and the amount of internalisation determined (**Figure 9**).

Analysis of internalisation by flow cytometry can also be complicated by low fluorescence due to low binding of nanoparticles or proteins to the cells. This results in significant overlap between the signal of the treated and control cells. In addition, not all cells may bind the material, resulting in the presence of two populations which can complicate analysis when the mean fluorescence intensity is used. The amount of information that can be extracted from the data can be extended using a specialized mathematical process (HD-Flow) analogous to the deblurring for microscopy images.⁹⁰ This process identifies the percentage of positive cells with greater accuracy compared to gating based on control cells. It also calculates the mean fluorescence intensity of those positive cells which allows for internalisation to be quantified on this subset independently. This method has been used to aid in determining the level of association and internalisation of polymer nanoparticles.⁹¹

7. Probing Nanoparticle Recycling

Quantifying the internalisation of nanoparticles is an important step towards understanding their cellular processing but is still only one part of the whole picture. The simple model of internalised material increasing with time is complicated by the occurrence of recycling, where endocytosed material is trafficked back to the surface of the cell. This phenomenon is just as important as internalisation but is often given less attention.^{20,92,93} When internalisation is measured at a given time point, it is useful to know if the material remaining on the cell surface was never internalised or if has been internalised and come out again. Recycling can occur rapidly after internalisation, where cargo is returned to the surface straight from the early endosome, or can take a longer route by trafficking through recycling endosomes.⁹⁴ Specific GTPases have been associated with certain recycling pathways including Rab4 with the fast pathway or Rab11 in the slow recycling case.⁸²

Due to its critical role in cell metabolism, growth and signalling as well as in immunity, many of the methods to study recycling were developed within the molecular biology field. Correlations between transfection efficiency and the amount of recycling through the Rab 11 slow recycling pathway have been demonstrated for cationic liposomes and have been shown to be related to membrane charge density.⁹⁵ This study was heavily reliant on determining colocalisation with expressed fluorescent protein fusions with the GTPases or LysoTracker and required analysis using a custom script. Similar observations

have been reported for lipid nanoparticles delivering short interfering RNA (siRNA). Nanoparticles formed with equal amounts of siRNA that had been labelled with Alexa Fluor 647 and 594 (which are a FRET pair) showed a reduction in FRET over time, suggesting rapid disassembly of the particles upon internalisation, and a slow increase of the Alexa Fluor 647 signal in the supernatant over 24 hours indicative of recycling.⁹² However, this only allows detection of complexes that have recycled and detached from the cell surface. Ideally, sensors that directly measure recycling would be preferred over colocalisation analysis and supernatant monitoring.

An approach with multiple fluorescent antibodies has been used to monitor the recycling of immune complexes bound to complement receptors in follicular dendritic cells.⁹⁶ By staining cells with green, blue then red fluorescent antibodies over three incubation periods, the behaviour of the complexes bound to the receptor can be determined by the combination of colours via confocal microscopy. However, this type of analysis is low throughput and is not compatible with high-throughput flow cytometry, as co-localisation information is required to assign the recycling state.

The SHIP assay, detailed in section 5, can also be modified to measure recycling.⁹⁷ After internalisation, surface fluorescence is specifically switched off with the complementary quencher probe at 4°C. Excess quencher probe is removed and the cells are returned to 37°C to resume trafficking. The cells are then cooled to 4°C and quenched again, removing fluorescence of any cargo that has recycled back to the surface during the subsequent incubation period. By adding quencher at different time points, the amount of material recycled to the surface can be monitored by tracking the decrease in fluorescence intensity. This method has been used to discern differences in the behaviour of the transferrin receptor in different cell lines with the presence of its natural ligand transferrin and the antibody to the receptor. While C1R cells showed limited recycling of transferrin but not the antibody, bone marrow erythroblasts recycled approximately 80% of both proteins over 24 minutes.

Enzyme tagging systems, such as the SNAP-tag, are an additional avenue to investigate recycling. The SNAP-tag is a genetically modified O⁶-alkylguanine-DNA-alkyltransferase and is routinely used to covalently label cellular proteins using a fluorescently modified version of the enzyme substrate (benzylguanine).⁹⁸ To study internalisation and recycling, this substrate has been modified to contain a cleavable disulphide linker between the benzylguanine and fluorophore (**Figure 10a**).⁹⁹ By applying the membrane impermeable reducing agent tris(2-carboxyethyl)phosphine (TCEP) to cells with labelled SNAP-tagged receptors, any fluorophores on the surface can be released while leaving the labelling of the internalised receptors unaffected. The sensor was used to demonstrate the recycling of the β_2 adrenergic receptor tagged with the SNAP protein. After initial labelling and endocytosis of surface localised receptors, fluorescence can be seen on the cell surface and within the cell (**Figure 10b, panel 1**). Adding TCEP then removed the fluorescence from the surface (**Figure 10b, panel 2**).

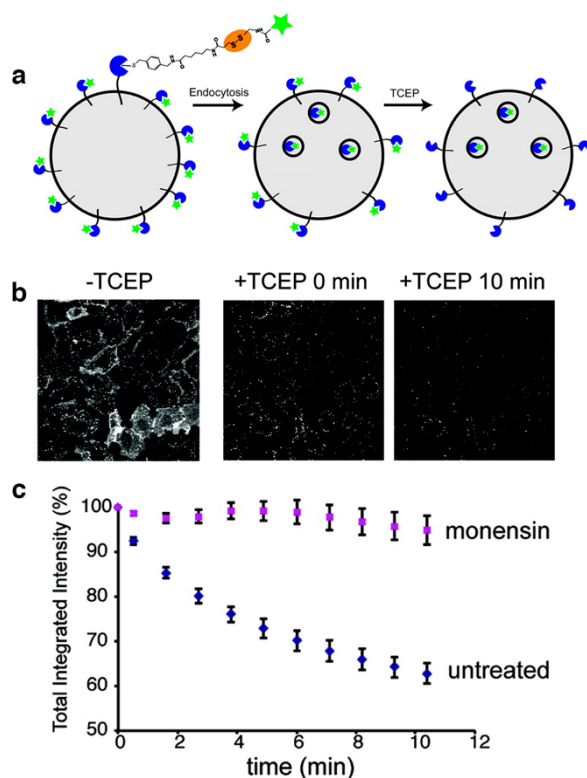


Figure 10 – Tracking recycling of the β_2 adrenergic receptor using the SNAP-tag system. (a) Releasable substrate scheme. A disulfide linker is included in between the fluorophore Alexa Fluor 488 and the benzylguanine SNAP-tag substrate which can be cleaved. Cleavage by tris(2-carboxyethyl)phosphine (TCEP) allows release of the fluorophore from SNAP-tag located on the cell surface while leaving internalised receptor unaffected (b) HEK293A cells stably expressing a fusion of the SNAP enzyme tag with the β_2 adrenergic receptor first treated with the fluorescent disulfide SNAP-tag substrate then with the reducing agent TCEP to remove surface fluorescence over time. (c) The total decrease in fluorescence over time as the receptor is recycled is prevented in the presence of a recycling inhibitor for the receptor. (Reprinted with permission from Ref 99. Copyright 2012 American Chemical Society)

Addition of more TCEP after 10 minutes further reduced the fluorescence suggesting rapid recycling of the receptors back to the cell surface (**Figure 10b, panel 3**). Treating the cells with monensin, a recycling inhibitor for the β_2 adrenergic receptor, caused the total fluorescence intensity of the cell to remain constant over 10 minutes as recycling was prevented (**Figure 10c**). Although this is currently limited to monitoring the recycling of the receptor rather than its cargo, this study highlights the potential of enzyme-tagging systems as sensors for cellular events.

8. Conclusions

We are advancing towards not only targeting nanoparticles and biopharmaceuticals to cells, but to directing them to specific subcellular spaces. The first stage of which, is cellular entry. Evaluating this event demands differentiating between material adsorbed to the cell surface from that within the cell. Many of the methods for this have not had their efficiency properly characterized. Commonly used methods such as acid-wash and trypsin may not be effective, depending on how the particles are bound to the cell membrane. The use of sensors can

drastically simplify these issues by responding specifically to changes in chemical environments such as the decrease in pH following intracellular trafficking or by giving the particles a switchable character, allowing their signal to change when they have entered the cell. Progress in this area will come from using the available sensors to achieve an appreciation of the interactions of nanomaterials with cells across multiple disciplines. This includes how association is distinct to uptake and why this critical difference changes the biological effect of a given material.

9. Conflicts of interest

There are no conflicts to declare.

10. References

- 1 S. Mitragotri, P. A. Burke and R. Langer, *Nat. Rev. Drug Discov.*, 2014, **13**, 655–672.
- 2 L. Rajendran, H.-J. Knölker and K. Simons, *Nat. Rev. Drug Discov.*, 2010, **9**, 29–42.
- 3 A. Fu, R. Tang, J. Hardie, M. E. Farkas and V. M. Rotello, *Bioconjug. Chem.*, 2014, **25**, 1602–1608.
- 4 H. Yin, R. L. Kanasty, A. A. Eltoukhy, A. J. Vegas, J. R. Dorkin and D. G. Anderson, *Nat Rev Genet*, 2014, **15**, 541–555.
- 5 M. L. Tan, P. F. M. Choong and C. R. Dass, *Peptides*, 2010, **31**, 184–193.
- 6 A. Albanese, P. S. Tang and W. C. W. Chan, *Annu. Rev. Biomed. Eng.*, 2012, **14**, 1–16.
- 7 J. Blechinger, A. T. Bauer, A. a. Torrano, C. Gorzelanny, C. Bräuchle and S. W. Schneider, *Small*, 2013, **9**, 3970–3980.
- 8 G. Maiorano, S. Sabella, B. Sorce, V. Brunetti, M. A. Malvindi, R. Cingolani and P. P. Pompa, *ACS Nano*, 2010, **4**, 7481–7491.
- 9 V. Bertelsen and E. Stang, *Membranes (Basel)*, 2014, **4**, 424–446.
- 10 P. D. Senter, *Curr. Opin. Chem. Biol.*, 2009, **13**, 235–244.
- 11 A. P. R. Johnston, *ACS Sensors*, 2017, **2**, 4–9.
- 12 M. Kirkham and R. G. Parton, *Biochim. Biophys. Acta - Mol. Cell Res.*, 2005, **1746**, 350–363.
- 13 A. Benmerah and C. Lamaze, *Traffic*, 2007, **8**, 970–982.
- 14 S. Mayor, R. G. Parton and J. G. Donaldson, *Cold Spring Harb. Perspect. Biol.*, 2014, **6**.
- 15 J. R. Casey, S. Grinstein and J. Orłowski, *Nat. Rev. Mol. Cell Biol.*, 2010, **11**, 50–61.
- 16 A. Dautry-Varsat, A. Ciechanover and H. F. Lodish, *Proc. Natl. Acad. Sci.*, 1983, **80**, 2258–2262.
- 17 E. F. Grady, A. M. Garland, P. D. Gamp, M. Lovett, D. G. Payan and N. W. Bunnett, *Mol. Biol. Cell*, 1995, **6**, 509–524.
- 18 I. a Khalil, K. Kogure, H. Akita and H. Harashima, *Pharmacol. Rev.*, 2006, **58**, 32–45.
- 19 M. Von Zastrow and B. K. Kobilka, *J. Biol. Chem.*, 1994, **269**, 18448–18452.
- 20 T.-G. Iversen, T. Skotland and K. Sandvig, *Nano Today*, 2011, **6**, 176–185.
- 21 D. Dutta and J. G. Donaldson, *Cell. Logist.*, 2012, **2**, 203–

- 208.
- 22 K. L. Goldenthal, I. R. A. Pastan and M. C. Willingham, *Exp. Cell Res.*, 1984, **152**, 558–564.
- 23 H. Liu and A. P. R. Johnston, *Angew. Chemie - Int. Ed.*, 2013, **52**, 5744–5748.
- 24 D. D. Jensen, M. L. Halls, J. E. Murphy, M. Canals, F. Cattaruzza, D. P. Poole, T. Lieu, H.-W. Koon, C. Pothoulakis and N. W. Bunnett, *J. Biol. Chem.*, 2014, **289**, 20283–94.
- 25 B. J. Wisnieski, J. G. Parkes, Y. O. Huang and C. F. Fox, *Proc. Natl. Acad. Sci. U. S. A.*, 1974, **71**, 4381–5.
- 26 Y. Ghetler, S. Yavin, R. Shalgi and A. Arav, *Hum. Reprod.*, 2005, **20**, 3385–3389.
- 27 C. L. Watkins, D. Schmaljohann, S. Futaki and A. T. Jones, *Biochem. J.*, 2009, **420**, 179–189.
- 28 C. Y. Jiao, D. Delaroche, F. Burlina, I. D. Alves, G. Chassaing and S. Sagan, *J. Biol. Chem.*, 2009, **284**, 33957–33965.
- 29 I. M. Kaplan, J. S. Wadia and S. F. Dowdy, *J. Control. Release*, 2005, **102**, 247–253.
- 30 A. A. Torrano, J. Blechinger, C. Osseforth, C. Argyo, A. Reller, T. Bein, J. Michaelis and C. Bräuchle, *Nanomedicine*, 2013, **8**, 1815–1828.
- 31 M. Rieseberg, C. Kasper, K. F. Reardon and T. Scheper, *Appl. Microbiol. Biotechnol.*, 2001, **56**, 350–360.
- 32 C. Gottstein, G. Wu, B. J. Wong and J. A. Zasadzinski, *ACS Nano*, 2013, **7**, 4933–4945.
- 33 E. J. van der Vlist, E. N. M. Nolte-'t Hoen, W. Stoorvogel, G. J. A. Arkesteijn and M. H. M. Wauben, *Nat. Protoc.*, 2012, **7**, 1311–1326.
- 34 N. Panchuk-Voloshina, R. P. Haugland, J. Bishop-Stewart, M. K. Bhalgat, P. J. Millard, F. Mao, W.-Y. Leung and R. P. Haugland, *J. Histochem. Cytochem.*, 1999, **47**, 1179–1188.
- 35 M. S. Briggs, D. D. Burns, M. E. Cooper and S. J. Gregory, *Chem. Commun.*, 2000, 2323–2324.
- 36 J. Han and K. Burgess, *Chem. Rev.*, 2010, **110**, 2709–2728.
- 37 D. A. Basiji, W. E. Ortyen, L. Liang, V. Venkatachalam and P. Morrissey, *Clin. Lab. Med.*, 2007, **27**, 653–670.
- 38 N. S. Barteneva, E. Fasler-Kan and I. A. Vorobjev, *J. Histochem. Cytochem.*, 2012, **60**, 723–733.
- 39 J. S. Dolina, S. S. Sung, T. I. Novobrantseva, T. M. Nguyen and Y. S. Hahn, *Mol Ther Nucleic Acids*, 2013, **2**, e72.
- 40 A. P. R. Johnston, M. M. J. Kamphuis, G. K. Such, A. M. Scott, E. C. Nice, J. K. Heath and F. Caruso, *ACS Nano*, 2012, **6**, 6667–6674.
- 41 J. D. Mintern, C. Percival, M. M. J. Kamphuis, W. J. Chin, F. Caruso and A. P. R. Johnston, *Adv. Healthc. Mater.*, 2013, **2**, 940–944.
- 42 A. M. Garland, E. F. Grady, D. G. Payan, S. R. Vigna and N. W. Bunnett, *Biochem. J.*, 1994, **303**, 177–186.
- 43 A. Wilde, E. C. Beattie, L. Lem, D. A. Riethof, S. Liu, W. C. Mobley, P. Soriano, F. M. Brodsky and S. Francisco, *Cell*, 1999, **96**, 677–687.
- 44 L. Au, Q. Zhang, C. M. Copley, M. Gidding, A. G. Schwartz, J. Chen and Y. Xia, *ACS Nano*, 2010, **4**, 35–42.
- 45 L. Fraser and S. F. Hamm-alvarez, *ACS Nano*, 2011, **4**, 2735–2747.
- 46 A. Salvati, A. S. Pitek, M. P. Monopoli, K. Prapainop, F. B. Bombelli, D. R. Hristov, P. M. Kelly, C. Åberg, E. Mahon and K. A. Dawson, *Nat. Nanotechnol.*, 2013, **8**, 137–43.
- S. T. Sawyer and S. B. Krantz, *J. Biol. Chem.*, 1986, **261**, 9187–9195.
- C. D. Austin, A. M. De Mazière, P. I. Pisacane, S. M. van Dijk, C. Eigenbrot, M. X. Sliwkowski, J. Klumperman and R. H. Cheller, *Mol. Biol. Cell*, 2004, **15**, 5268–5282.
- S. A. Raza Naqvi, J. K. Sosabowski, S. Ahamad Nagra, M. M. Ishfaq, S. J. Mather and T. Matzow, *Appl. Radiat. Isot.*, 2011, **69**, 68–74.
- B. Zhang, H. Shan, D. Li, Z. R. Li, K. S. Zhu, Z. B. Jiang and M. S. Huang, *Tumori*, 2012, **98**, 800–803.
- M. Ojima, K. Tsuji, K. Otabe, M. Horie, H. Koga, I. Sekiya and T. Muneta, *Osteoarthritis Cartil.*, 2016, **24**, S509–S510.
- K. L. Douglas, C. A. Piccirillo and M. Tabrizian, *Eur. J. Pharm. Biopharm.*, 2008, **68**, 676–687.
- S. C. Finemann, V. L. Bonilha, A. D. Marmorstein, E. Rodriguez-Boulan and M. M. Dyson, *Cell Biol. Commun. by Torsten N. Wiesel*, 1997, **94**, 12932–12937.
- J. Nuutila and E.-M. Lilius, *Cytometry. A*, 2005, **65**, 93–102.
- D. Cadena-Herrera, J. E. Esparza-De Lara, N. D. Ramírez-Ibañez, C. A. López-Morales, N. O. Pérez, L. F. Flores-Ortiz and E. Medina-Rivero, *Biotechnol. Reports*, 2015, **7**, 9–16.
- Y. F. Tan, R. C. Mundargi, M. H. A. Chen, J. Lessig, B. Neu, S. Venkatraman and T. T. Wong, *Small*, 2014, **10**, 1790–1798.
- S. Kakimoto, T. Hamada, Y. Komatsu, M. Takagi, T. Tanabe, H. Azuma, S. Shinkai and T. Nagasaki, *Biomaterials*, 2009, **30**, 402–408.
- A. J. Convertine, C. Diab, M. Prieve, A. Paschal, A. S. Hoffman, P. H. Johnson and P. S. Stayton, *Biomacromolecules*, 2010, **11**, 2904–2911.
- M. Ekkapongpisit, A. Giovia, C. Follo, G. Caputo and C. Isidoro, *Int. J. Nanomedicine*, 2012, **7**, 4147–4158.
- A. M. Bannunah, D. Villasaliu, J. Lord and S. Stolnik, *Mol Pharm*, 2014, **11**, 4363–4373.
- J. M. Rosenholm, A. Meinander, E. Peuhu, R. Niemi, J. E. Eriksson, C. Sahlgren and M. Lindén, *ACS Nano*, 2009, **3**, 197–206.
- J. H. Lang and E. C. Lasser, *Biochemistry*, 1967, **6**, 2403–2409.
- V. L. et al Mosiman, *Cytometry*, 1997, **30**, 151–156.
- S. Busetto, E. Trevisan, P. Patriarca and R. Menegazzi, *Cytometry*, 2004, **58A**, 201–206.
- E. S. Van Amersfoort and J. A. G. Van Strijp, *Cytometry*, 1994, **17**, 294–301.
- P. Zou and A. Y. Ting, *ACS Chem. Biol.*, 2011, **6**, 308–313.
- N. Hondow, M. R. Brown, T. Starborg, A. G. Monteith, R. Brydson, H. D. Summers, P. Rees and A. Brown, *J. Microsc.*, 2016, **261**, 167–176.
- F.-K. Huang, W.-C. Chen, S.-F. Lai, C.-J. Liu, C.-L. Wang, C.-H. Wang, H.-H. Chen, T.-E. Hua, Y.-Y. Cheng, M. K. Wu, Y. Hwu, C.-S. Yang and G. Margaritondo, *Phys. Med. Biol.*, 2010, **55**, 469–482.
- H.-H. Chen, C.-C. Chien, C. Petibois, C.-L. Wang, Y. S. Chu, S.-F. Lai, T.-E. Hua, Y.-Y. Chen, X. Cai, I. M. Kempson, Y. Hwu and G. Margaritondo, *J. Nanobiotechnology*, 2011, **9**, 14.
- S. Hou, K. N. Sikora, R. Tang, Y. Liu, Y. W. Lee, S. T. Kim, Z.

- Jiang, R. W. Vachet and V. M. Rotello, *ACS Nano*, 2016, **10**, 6731–6736.
- 71 F. X. Hu, K. G. Neoh and E. T. Kang, *Biomaterials*, 2006, **27**, 5725–5733.
- 72 Y. Zhang, N. Kohler and M. Zhang, *Biomaterials*, 2002, **23**, 1553–1561.
- 73 L. Göstring, M. T. C. Chew, A. Orlova, I. Höidén-Guthenberg, A. Wennborg, J. Carlsson and F. Y. Frejd, *Int. J. Oncol.*, 2010, **36**, 757–763.
- 74 M. B. Margineanu, K. Julfakyan, C. Sommer, J. E. Perez, M. F. Contreras, N. Khashab, J. Kosel and T. Ravasi, *J. Nanobiotechnology*, 2016, **14**, 4.
- 75 M. Held, M. H. a Schmitz, B. Fischer, T. Walter, B. Neumann, M. H. Olma, M. Peter, J. Ellenberg and D. W. Gerlich, *Nat. Methods*, 2010, **7**, 747–754.
- 76 J. E. Whitaker, R. P. Haugland and F. G. Prendergast, *Anal. Biochem.*, 1991, **194**, 330–344.
- 77 M. Semmling, O. Kreft, A. M. Javier, G. B. Sukhorukov, J. Käs and W. J. Parak, *Small*, 2008, **4**, 1763–1768.
- 78 S. Liao-Chan, B. Daine-Matsuoka, N. Heald, T. Wong, T. Lin, A. G. Cai, M. Lai, J. A. D'Alessio and J.-W. Theunissen, *PLoS One*, 2015, **10**, 1–15.
- 79 M. M. Schmidt, G. M. Thurber and K. D. Wittrup, *Cancer Immunol. Immunother.*, 2010, **57**, 1879–1890.
- 80 Y. Li, P. C. Liu, Y. Shen, M. D. Snavely and K. Hiraga, *J. Biomol. Screen.*, 2015, **20**, 869–875.
- 81 S. Vira, E. Mekhedov, G. Humphrey and P. S. Blank, *Anal. Biochem.*, 2010, **402**, 146–150.
- 82 K. M. Mayle, A. M. Le and D. T. Kamei, *Biochim. Biophys. Acta - Gen. Subj.*, 2012, **1820**, 264–281.
- 83 B. J. Iacopetta and E. H. Morgan, *J. Biol. Chem.*, 1983, **258**, 9108–9115.
- 84 T. Hellevik, I. Martinez, R. Olsen, B. H. Toh, P. Webster and B. Smedsrød, *Hepatology*, 1998, **28**, 1378–1389.
- 85 G. C. Baltazar, S. Guha, W. Lu, J. Lim, K. Boesze-Battaglia, A. M. Laties, P. Tyagi, U. B. Kompella and C. H. Mitchell, *PLoS One*, 2012, **7**, 1–10.
- 86 S. Chikte, N. Panchal and G. Warnes, *Cytom. Part A*, 2014, **85A**, 169–178.
- 87 Y. Wang, C. Wang, Y. Li, G. Huang, T. Zhao, X. Ma, Z. Wang, B. D. Sumer, M. A. White and J. Gao, *Adv. Mater.*, 2017, **29**, 1603794.
- 88 S. Muro, X. Cui, C. Gajewski, J.-C. Murciano, V. R. Muzykantov and M. Koval, *Am. J. Physiol. Cell Physiol.*, 2003, **285**, C1339–47.
- 89 L. I. Selby, L. Aurelio, D. Yuen, B. Graham and A. P. R. Johnston, 2018, **Manuscript**.
- 90 L. I. Selby, N. Kongkatigumjorn, G. K. Such and A. P. R. Johnston, *Adv. Healthc. Mater.*, 2016, **5**, 2332.
- 91 S. K. Mann, E. Czuba, L. I. Selby, G. K. Such, P. Angus and R. Johnston, *Pharm. Res.*, 2016, **33**, 2421–2432.
- 92 G. Sahay, W. Querbes, C. Alabi, A. Eltoukhy, S. Sarkar, C. Zurenko, E. Karagiannis, K. Love, D. Chen, R. Zoncu, Y. Buganim, A. Schroeder, R. Langer and D. G. Anderson, *Nat. Biotechnol.*, 2013, **31**, 653–658.
- 93 D. Hofmann and V. Mailänder, *Nanomedicine (Lond.)*, 2013, **8**, 321–323.
- H. Stenmark, *Nat. Publ. Gr.*, 2009, **10**, 513–525.
- 95 R. N. Majzoub, E. Wonder, K. K. Ewert, V. R. Kotamraju, T. Teesalu and C. R. Safinya, *J. Phys. Chem. B*, 2016, **120**, 6439–6453.
- 96 B. A. Heesters, P. Chatterjee, Y. A. Kim, S. F. Gonzalez, M. P. Kuligowski, T. Kirchhausen and M. C. Carroll, *Immunity*, 2013, **38**, 1164–1175.
- 97 C. Dumont, E. C. M. Chen, J. A. Villadangos, A. P. R. Johnston and J. D. Mintern, *Traffic*, 2016, **18**, 242–249.
- 98 A. F. Hussain, M. Amoury and S. Barth, *Curr. Pharm. Des.*, 2013, **19**, 5437–42.
- 99 N. Cole and J. Donaldson, *ACS Chem. Biol.*, 2012, **7**, 464–469.



Nanoescapology: progress toward understanding the endosomal escape of polymeric nanoparticles

Laura I. Selby,¹ Christina M. Cortez-Jugo,^{1,2,3} Georgina K. Such^{4*} and Angus P.R. Johnston^{1,2*}

Using nanoparticles to deliver drugs to cells has the potential to revolutionize the treatment of many diseases, including HIV, cancer, and diabetes. One of the major challenges facing this field is controlling where the drug is trafficked once the nanoparticle is taken up into the cell. In particular, if drugs remain localized in an endosomal or lysosomal compartment, the therapeutic can be rendered completely ineffective. To ensure the design of more effective delivery systems we must first develop a better understanding of how nanoparticles and their cargo are trafficked inside cells. This needs to be combined with an understanding of what characteristics are required for nanoparticles to achieve endosomal escape, along with methods to detect endosomal escape effectively. This review is focused into three sections: first, an introduction to the mechanisms governing internalization and trafficking in cells, second, a discussion of methods to detect endosomal escape, and finally, recent advances in controlling endosomal escape from polymer- and lipid-based nanoparticles, with a focus on engineering materials to promote endosomal escape. © 2017 Wiley Periodicals, Inc.

How to cite this article:

WIREs Nanomed Nanobiotechnol 2017, e1452. doi: 10.1002/wnan.1452

INTRODUCTION

The treatment of a wide range of diseases and the development of improved vaccines both stand to benefit from more efficient therapeutic delivery.^{1,2} Nanoparticles have the capacity to transform conventional drug delivery, with the potential to reduce side effects through targeting, improve solubility of hard to deliver drugs, and provide sustained and

controlled release of therapeutics.³ Nanoparticles also have the potential to offer protection to promising but delicate therapeutics such as nucleic acids and proteins through encapsulation.^{4,5} However, while encapsulation can protect a therapeutic from degradation before it reaches the target cell, it is also critical that it is trafficked to the site inside the cell where the drug is therapeutically active. The optimal nanoparticle size depends on the delivery application. For most applications where the nanoparticles enter the systemic circulation system, the optimal size is above 10 nm, to prevent clearance by the kidneys, and below 200 nm to enable passage through microcapillaries.⁶

Nanoparticles are typically taken up into cells via endocytosis into endosomes, and are then subsequently trafficked into acidic lysosomal compartments.⁷ The environment of the lysosome can result in significant degradation of the therapeutic cargo. Nanoparticle systems are of particular interest for the delivery of short interfering RNA (siRNA) for RNA interference (RNAi),⁸ DNA for gene therapy,⁹

*Correspondence to: angus.johnston@monash.edu; gsuch@unimelb.edu.au

¹Drug Delivery, Disposition and Dynamics, Monash Institute of Pharmaceutical Sciences, Monash University, Parkville, Victoria, Australia

²ARC Centre of Excellence in Convergent Bio-Nano Science and Technology, Monash University, Parkville, Victoria, Australia

³Department of Chemical and Biomolecular Engineering, The University of Melbourne, Parkville, Victoria, Australia

⁴Department of Chemistry, The University of Melbourne, Parkville, Victoria, Australia

Conflict of interest: The authors have declared no conflicts of interest for this article.

antigens for vaccines,¹⁰ and proteins for anticancer treatment or enzyme delivery.^{11,12} The aforementioned therapies exert their effect in either the cytosol or nucleus and hence must escape endocytic vesicles in a fundamental step known as endosomal escape. This critical event is widely considered to be the rate-limiting step or 'bottleneck' in the intracellular delivery of therapeutics using nanoparticle-based systems.^{13–15}

A variety of both natural and synthetic materials have been investigated for their potential to induce endosomal escape. Naturally occurring fusogenic or endosomolytic peptides derived from viruses^{16,17} and bacterial toxins¹⁸ have been explored as both bear the innate ability to escape the trafficking pathway as is required for their pathogenicity.^{19,20} This has created a drive for the design of synthetic peptides with similar chemical properties.^{21,22} Carbon-based materials such as fullerenes²³ and nanotubes²⁴ have been developed, along with functionalized inorganic nanoparticles including quantum dots²⁵ and nanoparticles with gold, mesoporous silica, and calcium phosphate cores.^{26,27} A significant body of work has focused on soft materials, such as liposomes and polymeric particles,^{28,29} and these materials will be the focus of this review.

A major roadblock in the development of endosomal escape materials is the lack of methods to quantify escape efficiency and subsequently the ability to determine the mechanisms behind it. Engineering nanoparticles for endosomal escape requires a fundamental understanding of how they interact with cells but our knowledge in this area is still lacking. Herein, we outline the current understanding of the cellular processing of polymeric and lipid nanoparticles and the methods for probing endosomal escape. The final section of this review focuses on the recent progress in engineering soft materials (polymers and lipids) that have demonstrated endosomal escape.

UPTAKE AND INTRACELLULAR TRAFFICKING

Internalization Mechanisms

Knowledge of nanoparticle uptake mechanisms and the subsequent trafficking within the cell is imperative if we are to design nanoparticles capable of delivering therapeutic cargo to its active site. Endocytosis is the dominant mechanism of uptake for nanoparticles into cells^{7,30,31} (Figure 1), as opposed to direct diffusion across the cellular membrane. However, fusion of nanoparticles with the plasma membrane has also been demonstrated.³⁵ Endocytosis is a broad term for

many specific endocytic pathways with individual mechanisms.³⁶ While much research has focused on clathrin- and caveolae-dependent mechanisms, growing evidence suggests that additional clathrin- and caveolin-independent pathways may play a substantial role in endocytosis.³⁷ Nanoparticles decorated with targeting moieties such as antibodies^{38,39} or specific ligands such as for the transferrin⁴⁰ or folate^{41,42} receptors aim to induce uptake, but nontargeted particles can still enter through receptor-mediated endocytosis via scavenger or G-protein-coupled receptors.⁴³ The uptake mechanism and subsequent trafficking is nanoparticle and cell line dependent, and entry into multiple pathways can occur simultaneously.³¹

It is also important to differentiate nanoparticle uptake from association. Conventional flow cytometry assays only quantify association, thus more sophisticated assays must be employed to quantify internalisation.⁴⁴ Our understanding of these the endocytosis pathways is currently quite limited, which is partly due to a lack of acceptable markers and specific inhibitors for these processes.^{7,45} Following endocytosis at the cell membrane, Rab5 (a signaling protein) binds to the cytoplasmic side of the endocytic vesicle. Rab5 then interacts with EEA1 on early endosomes, which tethers to the surface of the vesicle and draws it in to fuse with the early endosome.⁴⁶ The endocytic vesicles rapidly acidify via V-type H⁺ ATPases,⁴⁷ reducing the pH from an extracellular pH of 7.4 down to ~6.3.⁴⁸ The initial fate of clathrin- and caveolin-dependent or -independent vesicles is similar in most cell lines, with fusion to early endosomes occurring within minutes of internalization.⁴⁹ Endosomes are then either recycled back to the cell surface or continue to acidify to pH 5.5 in late endosomes and multivesicular bodies before fusion with lysosomes (pH 4.7).⁴⁸ As the major function of lysosomes is to break down incoming material, they contain a range of acid hydrolases, including proteases, nucleases, esterases, and lipases.⁵⁰ Nanoparticles that are trafficked to the lysosome are subjected to these enzymes, degrading the cargo.⁵¹ Nanoparticles can also be engineered to degrade in the presence of enzymes such as proteases⁵² and nucleases⁵³ to control the release of the cargo. Rupture of lysosomes is associated with cell death (apoptosis) through release of cathepsins and calcium ions, so timing of escape and limiting the release of proapoptotic molecules is critical.^{54,55} Therefore, the window of time between internalization into the initial vesicles and fusion with lysosomes has been targeted as optimal period for pH-responsive nanomaterials to be engineered to induce endosomal escape.^{56,57}

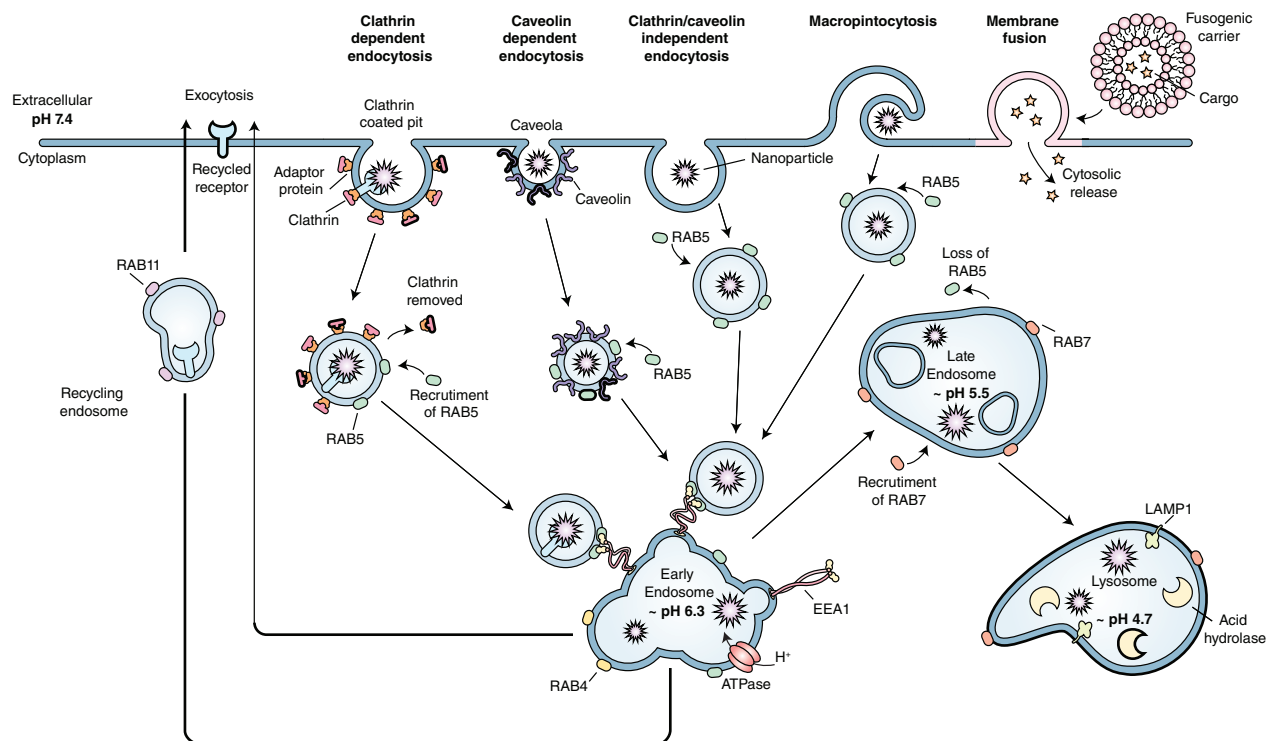


FIGURE 1 | Nanoparticles can enter cells through multiple mechanisms. Particles are taken up into vesicles coated with clathrin, caveolin, or by using a clathrin/caveolin-independent mechanism. EEA1 tethers to RAB5 on internalized vesicles and draws them into RAB5-positive early endosomes. The pH drops to ~ 6.3 and cargo is recycled to the surface or trafficked to RAB7-positive late endosomes (pH ~ 5.5). Contents are trafficked to the lysosome (pH ~ 4.7) where they are degraded by acid hydrolases. Alternative modes of entry include membrane fusion or direct translocation across the membrane, bypassing the trafficking pathway.^{32–34}

The principal method for determining the mechanism of nanoparticle internalization is treating cells with drugs that inhibit endocytic pathways. These drugs work via a variety of mechanisms, such as by affecting the formation of clathrin-coated vesicles or by blocking enzymes involved in the budding of the vesicles from the cell surface.⁵⁸ Caution is required when interpreting data from inhibitor studies, as most inhibitors show off-target effects. For example, methyl- β -cyclodextrin causes cholesterol depletion and filipin disturbs cholesterol function to inhibit caveolae-mediated endocytosis, but both drugs may also alter clathrin-mediated uptake and other clathrin-independent mechanisms for which cholesterol is required.⁴⁵

Alternatively, the colocalization of the fluorescence from particles with that from markers of particular internalization pathways such as caveolin-1 has been used to assign mechanisms. However, caveolin has also been identified to localize in late endosomes and lysosomes after it has been tagged for degradation. This can lead to incorrect assumptions over the role caveolin plays in nanoparticle internalization. The existence of ‘caveosomes’ as distinct

organelles involved in a unique caveolae-mediated trafficking pathway has previously been hypothesized; however, this is now regarded as unlikely.⁵⁹ Helenius and coworkers, the originators of the caveosome hypothesis, demonstrated in more recent work that the presence of caveolin inside endosomal compartments corresponds to ubiquitinated caveolin marked for degradation, rather than corresponding to a distinct endosomal compartment.⁶⁰ Despite these findings, there are still a number of reports in the literature relating to caveosomes playing a role in nanoparticle trafficking.

The uptake mechanism of nanoparticles has been extensively studied and shown to be highly dependent on the physical properties of the material^{61,62,63} as well as cell type.⁶⁴ The protein corona that forms from the adsorption of proteins and other biomolecules onto the surface of nanoparticles from *in vivo* circulation⁶⁵ also plays a role in cellular processing. Which proteins are adsorbed has been shown to be dependent on both the size and surface chemistry of particles.⁶⁶ In addition, the surface chemistry can disrupt proteins in the corona and change the mechanism of uptake.⁶⁷ The targeting ability to

specific receptors can also be compromised from the corona shielding access to targeting moieties.⁶⁸ Experiments testing nanoparticles are typically carried out in media supplemented with serum to simulate *in vivo* conditions and induce corona formation. However, chemical differences in the media and *in vivo* conditions can cause differences in corona formation which in turn affects cellular processing.⁶⁹

Furthermore, it has been suggested that the specific mechanism of internalization can be associated with the fate of the particles. This is exemplified by studies into polyethylenimine (PEI)-mediated gene delivery. Gabrielson and Pack suggest that PEI-mediated transfection is only highly efficient when taken up through the caveolae-dependent pathway, and when taken up by the clathrin-dependent pathway, particles were trafficked quickly to the lysosomes for degradation.⁷⁰ Rejman et al. reached a similar conclusion by demonstrating that clathrin-dependent internalized particles were trafficked to lysosomes using the inhibitors chlorpromazine and K⁺ depletion for clathrin-dependent or filipin and genistein for caveolae-dependent endocytosis.⁷¹ They also found that inhibition of the caveolae-dependent pathway stopped transfection via PEI polyplexes completely, while inhibition of the clathrin-dependent pathway had no effect.

Quantifying nanoparticle internalization is also critical, as the kinetics and level of internalization may influence endosomal escape. This requires the ability to differentiate between nanoparticles that have been internalized and those remaining bound to the cell surface. Fluorescence microscopy is commonly used to qualitatively determine internalization; however, it is inherently low throughput. Recently, confocal microscopy combined with flow cytometry has been used to increase the throughput of analysis.⁷² Internalization can also be quantified using flow cytometry by acid washing⁷³ or surface etching the cells,⁷⁴ where acidic pH or particular chemicals remove particles remaining bound to the surface. Trypan blue has been used to nondiscriminately quench cell-surface fluorescence.⁷⁵ Both these techniques are limited by removal of all surface markers, limiting the ability to phenotype different populations of cells. Alternatively, a fluorescent sensor can be incorporated into the nanoparticles that remains switched on only when the particle is internalized into the cell (specific hybridization internalization probe (SHIP) method).⁷⁶ The SHIP method has been used to demonstrate distinct differences in uptake in separate cell lines and when used in conjunction with inhibitors, can explore the mechanisms of internalization.⁷⁷ Flow cytometry assays can also be enhanced

by deconvolving flow cytometry histograms to enhance the detection of interactions that would otherwise be lost in the background noise of cell autofluorescence.⁷⁸

While there is some evidence to suggest internalization pathways play a role in the subsequent fate of the cargo, it is unclear the mechanism by which this happens. As the fate of most endocytic vesicles that bud from the plasma membrane is trafficking to an early endosome, it has not been established how the subsequent trafficking pathways are differentiated. It is possible that differences in intracellular trafficking and endosomal escape relate to interactions that occur within the endosomal compartment rather than the initial mechanism of entry. Notwithstanding, the link between the mechanism of nanoparticle uptake and successive efficacy clearly warrants further investigation, as successful targeting to a particular pathway may be the key to an improvement in delivery efficiency.

Mechanisms of Endosomal Escape

The mechanism by which endosomal escape occurs is still highly contentious. There is little consensus in the literature around the mechanism of trafficking across the endosomal membrane, and there are a number of diverse mechanisms that can be employed to induce endosomal escape (Figure 2). We have focused on three proposed strategies for inducing endosomal escape; however, it is highly likely that more than one of the mechanisms are required for efficient cytoplasmic delivery of therapeutics.

Proton Sponge Effect and Osmotic Lysis

A common strategy for inducing endosomal escape is via the proton sponge effect, which is based on the buffering effect of polymers with a pKa in a physiologically relevant range. This mechanism is often assigned to polycationic materials such as PEI⁷⁹ and poly(amidoamine) (PAMAM) dendrimers⁸¹ but is still heavily debated.^{82–84} As the polymer becomes protonated, protons are continuously pumped into the endosomes/lysosomes, necessitating the transport of chloride counter ions to maintain a charge balance. This results in a high osmotic pressure that eventually causes the endosome/lysosome to rupture (Figure 2 (a)). While in theory this is quite an elegant hypothesis, it does not provide a full explanation for endosomal escape. Not all polymers that buffer within the pH 5–7 range are capable of inducing endosomal escape, and efforts to engineer polymers with an enhanced buffering capacity within a physiologically relevant range have not resulted in an increased

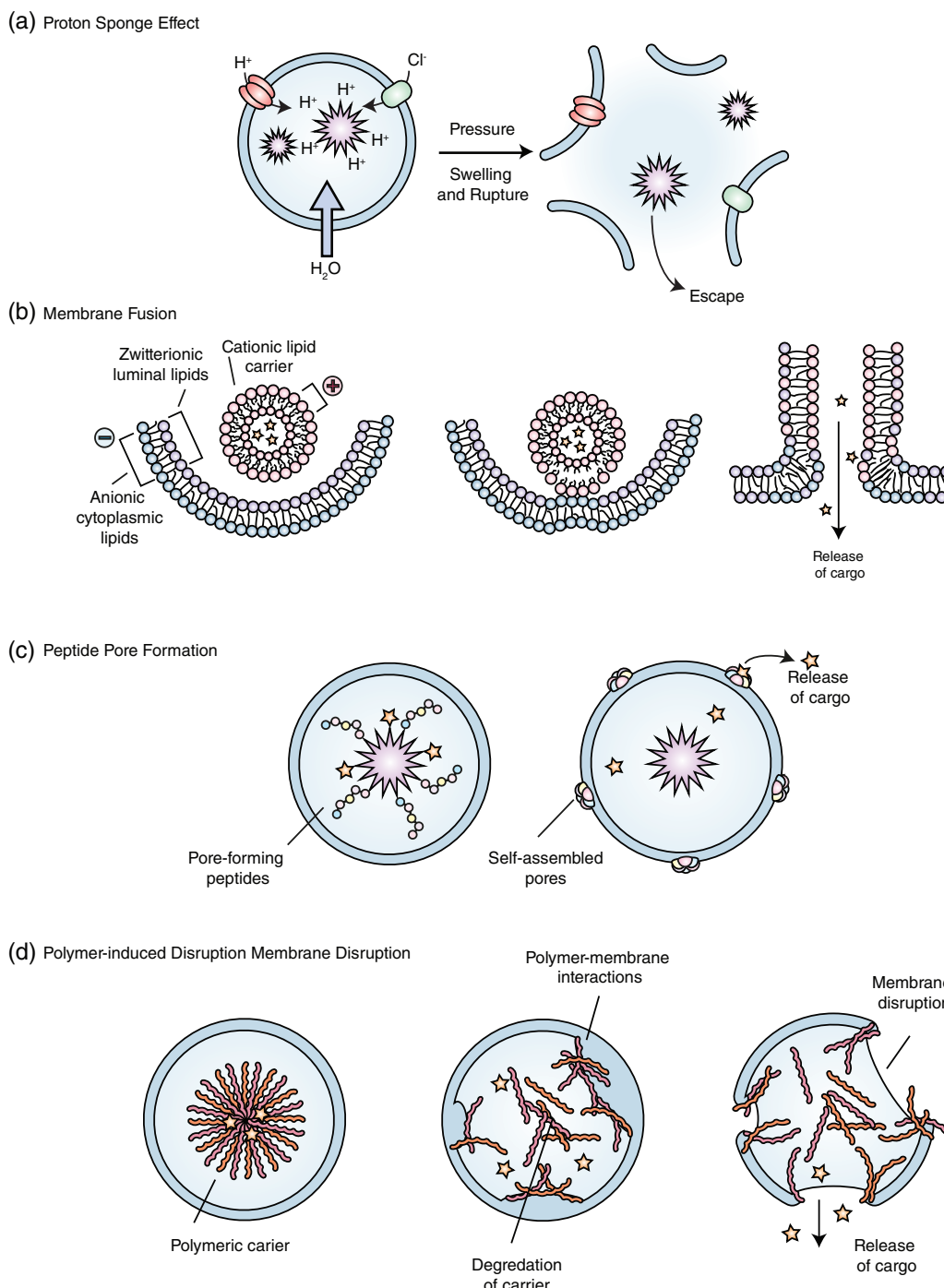


FIGURE 2 | Mechanisms of endosomal escape. (a) Proton sponge effect—Polymers capable of buffering become protonated as protons are pumped into endosomes as part of the regular trafficking process by ATPases. Chloride ions are also transported to maintain the charge balance within the endosome. The increase in ion concentration causes osmotic swelling and ruptures the membrane.⁷⁹ (b) Membrane fusion—Anionic lipids on the cytoplasmic side of the endosomes rearrange to form a neutral ion pair with cationic lipids of the carrier, destabilizing the membrane. The membranes fuse and allow the cargo to move into the cytoplasm.⁸⁰ (c) Pore formation—Certain peptides self-assemble in the lipid membrane to form pores that enable low-molecular therapeutics to escape. (d) Membrane disruption—Polymers or peptides interact directly with the endosomal membrane causing disruption, allowing cargo to escape.

escape capacity.⁸⁵ It has also been shown that when PEI is added to HeLa cells, the pH of the lysosomes remains at pH 4.5 over 24 h.⁸⁴ It is clear that changes in pH play an important role in endosomal escape. However, it is difficult to decouple the role that pH buffering plays from other factors such as membrane interactions and conformational changes that are induced by a drop in the pH.

A related mechanism proposed by Battaglia and coworkers describes the role of osmotic pressure upon the disassembly of nanoparticles in the endosome.⁸⁶ In this mechanism, rather than the buffering capacity of the polymer inducing the osmotic pressure and subsequent lysis, it is proposed that the disassembly of a particle into many polymer subunits causes an osmotic shock that ruptures the endosome.⁸⁷

Membrane Fusion

In nature, enveloped viruses can induce endosomal escape by fusion of the viral envelop with the endosomal membrane, allowing the viral capsid to enter the cytoplasm.⁸⁸ Similarly, for particles assembled from lipids or amphiphilic materials, it is proposed that the phospholipid bilayer of a liposome can fuse with the endosomal membrane (Figure 2(b)), inverting the structure of the liposome and delivering the therapeutic core to the cytoplasm.⁸⁰ Safinya and coworkers used synchrotron small-angle X-ray scattering (SAXS) to relate the structure of dioleoyl trimethylammonium propane (DOTAP)-dioleoyl phosphatidylethanolamine (DOPE) to its transfection efficiency.⁸⁹ DOPE was found to induce the transition from a multilamellar structure to an inverted hexagonal liquid crystalline phase in DNA lipoplexes. The inverted hexagonal structure interacts more favorably with model anionic membranes, resulting in membrane fusion and DNA release.

Membrane Disruption and Pore Formation

Destabilizing the endosomal membrane can allow therapeutic cargo to diffuse out of the endosomal compartment through holes or pores. Endosomal disruption can occur through the direct interaction of polymers⁹⁰ or peptides⁹¹ with the endosomal membrane or via peptides that self-assemble across the membrane to create defined pores^{92,93} (Figure 2(c)). Typically, the dimensions of transmembrane pores are ~1-2 nm,⁹⁴ which generally limits their usefulness to induce efficient release of therapeutic cargo. However, the engineered peptide GALA is capable of inducing release of molecules up to ~5000 Da (see section *Peptide-Induced Endosomal Escape*).⁹²

In addition, a large body of evidence suggests that polymer-based systems induce escape by

interacting with cellular membranes (Figure 2(d)). Coarse-grain molecular simulations with asymmetric lipid membranes demonstrated that dendrimers insert into membranes and interfere with asymmetry.⁹⁵ Supported lipid bilayer studies with atomic force microscopy visually demonstrate that dendrimers and PEI induce thinning or hole formation.^{96,97} It is likely simulations and artificial membranes are not able to fully represent the complexities of cell membranes but *in vitro* experiments have shown similar results. Whole-cell patch-clamp conductance measurements show that polycations cause membrane defects and that these can heal over time.⁹⁸ In addition, electron microscopy shows direct interaction and disruption of lysosomal membranes by PEI.⁹⁹ The escape mechanism for polyanionic polymers is attributed to an increase in hydrophobicity due to protonated carboxylate groups, which results in membrane insertion and subsequent membrane disruption.⁹⁰

It is important to understand the mechanism by which endosomal escape can occur when designing a delivery system. Endosomal lysis and membrane fusion have the potential to deliver cargo to the cytoplasm regardless of the cargo size, while membrane disruption and pore formation will inherently have limits to the molecular weight than can diffuse across the destabilized membrane. Additionally, how the cargo is encapsulated or attached to the delivery vehicle can affect the therapeutic outcome. For example, conjugation of therapeutics to the components of the particle responsible for membrane fusion can be counterproductive and even lead to increased localization in endosomes and lysosomes.¹⁰⁰ It is also important to consider the potentially toxic side effects of endosomal escape. Lysosomes play an important role in regulating apoptosis, and the uncontrolled release of cathepsin as well as calcium ions can significantly affect the viability of cells.¹⁰¹

DETECTION OF ENDOSOMAL ESCAPE

The difficulty in engineering materials for endosomal escape is due in part to a lack of understanding how nanoparticles behave in cells. Thus, more robust and reliable methods to detect escape and probe the mechanisms by which it occurs are needed. The complex nature of cellular trafficking means that a number of techniques must be used in combination to probe the mechanisms. It is also important to understand what information each assay can provide, and what it cannot. This review summarizes some of the most commonly used approaches to detect endosomal

escape. A comprehensive review of the methods has recently been published.¹⁰²

Fluorescent Labeling

Fluorescent labeling is one of the simplest methods to identify endosomal escape. The polymers or lipids used to assemble the nanoparticles,^{55,85} or the therapeutic cargo within the nanoparticle,^{103,104} can be conjugated with small fluorescent dyes. This allows for the intracellular distribution of the fluorescence to be imaged. Labeled material trapped in endocytic vesicles has a punctate appearance (Figure 3(a)), while a diffuse appearance (Figure 3(b)) suggests material has left the vesicles and moved into the cytosol. Difficulties arise when the degree of escape is low, causing the fluorescence from escaped material to be indiscernible from the background of the image.

By labeling organelles involved in cellular trafficking, colocalization studies can be performed to gain a better understanding of where nanoparticles are transported. Trafficking vesicles can be labeled in live cells with acidotropic dyes such as acridine orange^{90,105} and LysoTracker,^{106,107} which accumulate nonspecifically in acidic organelles.^{108,109} While these stains can be useful to gain a basic level of understanding of cellular trafficking, they have a number of limitations. Dyes such as LysoTracker often exhibit high levels of background, which leads to low signal-to-noise ratios. There is also potential for nanoparticles to interfere with the fluorescence of these sensors. Nanoparticles that buffer endosomal pH typically suppress LysoTracker signal, as

LysoTracker relies on a decrease in pH to sense the lysosomal compartments.¹⁰⁹

For precise labeling, specific organelle markers such as lysosomal-associated membrane protein-1 (LAMP-1) can be immunostained¹¹⁰ or expressed fused with a fluorescent protein via transfection.¹¹¹ Immunofluorescence labeling can be performed with nanoparticles in almost any cell type after fixing and permeabilizing the cells.¹¹² Fixation relies on cross-linking amines, amides, and hydroxyl groups into a formaldehyde/glutaraldehyde network to preserve the structure of the cell.¹¹³ If the nanoparticles are not crosslinked to the network of proteins during fixation, they will diffuse out of the cell during permeabilization. This is particularly problematic for nanoparticles that are engineered to have stealth characteristics. Imaging localization in live cells can be achieved by transfection with markers for specific cellular compartments, such as LAMP, EEA1, or Rab 4, 5, 7 or 11, fused to fluorescent proteins. This enables colocalization imaging of particles *in situ*.¹¹⁴ The limitation with this technique is that it can only be performed in cell lines that can be readily transfected, making it difficult to study primary cells. Also, the effect of the transfection process and over-expression of trafficking proteins on the behavior of cells has to be considered.¹¹⁵

While organelle labeling is much more specific than using pH-sensitive or lysosomal accumulating dyes, quantitative assessment of colocalization can be challenging. The endosomal/lysosomal markers are associated with the vesicular membrane and as a result may not overlap with the enclosed particle (Figure 4). This can give rise to low degrees of

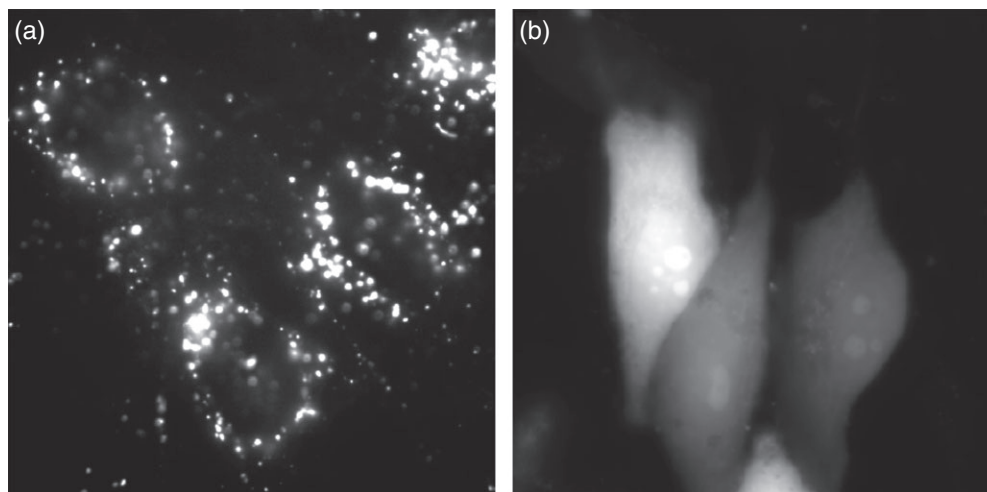


FIGURE 3 | Fluorescence microscopy image contrasting (a) zero to low levels of endosomal escape with (b) high levels of escape. Fluorescently labeled cargo sequestered in endo/lysosomes appears punctate while a cytosolic localization causes a diffuse appearance. (Reprinted with permission from Ref 17. Copyright 2014 Nature Publishing Group)

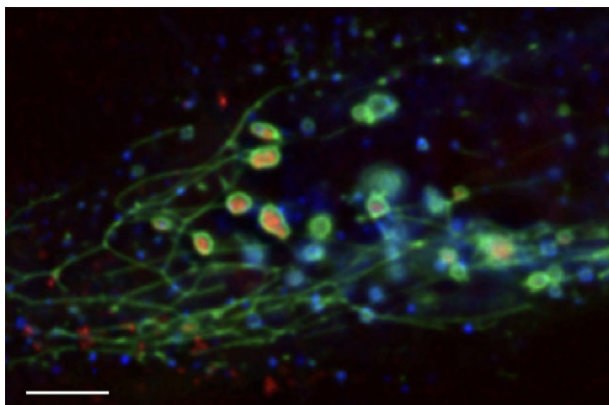


FIGURE 4 | Cargo enclosed in lysosomes appears as a ring of the labeled lysosome marker around the labeled particle and results in low overlap coefficients. Scale bar = 5 μm . (Reprinted with permission from Ref 44. Copyright 2017 American Chemical Society).

colocalization from statistical calculations even though the particle is enclosed in the vesicle. Furthermore, the lack of colocalization of particles with an endosomal/lysosomal marker can be confused with endosomal escape. Punctate fluorescence in the cell is an indicator of nanoparticles or therapeutic cargo encapsulated within vesicular membranes that is not accessible to the cytoplasm.

Fluorescent labeling is a versatile tool for investigating both the trafficking and endosomal escape capacity of nanoparticles. However, imaging gives limited insight into the mechanism of endosomal escape and therefore should be considered as a starting point. Complementary assays to probe the mechanism of escape are required. Furthermore, the use of high-intensity light in fluorescence imaging has been observed to induce the redistribution of fluorescently labeled peptides from the endosome to the cytoplasm. This phenomenon can easily be limited by ensuring low levels of light during imaging with short exposure times, but must be considered as a factor during live-cell imaging assays with extended durations.¹¹⁶

Leakage Assays

These assays examine the ability of a given material to induce leakage in cell and vesicle membranes. The behavior of the material can be examined under either *ex vivo* or *in vitro* conditions.

Ex Vivo Leakage Assays

Preliminary evaluation of the endosome escape capacity of a material can be performed using liposomes as a model membrane. The liposomes are composed of combinations of phospholipids

representative of those found in cells and contain an encapsulated fluorescent dye. The local concentration of the dye is high and this quenches the fluorescence, allowing for a large increase in fluorescence intensity if leakage occurs. An example of this is 6-carboxyfluorescein which increases in fluorescence 30-fold on release.¹¹⁷ This method has been used for a variety of membrane destabilizing materials including cell-penetrating peptides (CPPs)¹¹⁸ and cationic polymers,¹¹⁹ and has been used to show differences in the behavior of liposome nanoparticles functionalized with octaarginine or octalysine.¹²⁰

Red blood cells have also been used as a more biologically relevant model to study membrane disruption. By observing the lysis of red blood cells and release of hemoglobin at varying pH values, the pH-dependent membrane disruption of nanoparticles can be determined. Red blood cells in solutions buffered at pH values mimicking those corresponding to the extracellular, endosomal, and lysosomal environments are co-incubated with the material of interest. pH-induced changes in the material that causes membrane disruption result in hemoglobin release into the surrounding media, which is then measured via spectrophotometry.^{121,122} This information can be used to assess when the material is likely to activate its disruptive properties along the intracellular trafficking pathway. For example, cationic lipid nanoparticles formed from (1-aminoethyl)iminobis [*N*-(oleicysteinyl-1-amino-ethyl)-propionamide] showed ~50% hemolytic activity at the pH of early endosomes and ~90% at the pH of lysosomes but minimal disruption at the pH of the extracellular space.¹²³ The increase in lysis corresponded with an increase in protonation of the lipid head groups as assessed by the zeta potential.

These *ex vivo* assays give insight into the mechanism of escape as they rely on membrane disruption or pore formation to release dye or hemoglobin from within the membrane. Materials that induce escape solely via osmotic lysis are unlikely to induce escape in these assays. It is important to note that in addition to any proton sponge effect that PEI may have, PEI also induces red blood cell lysis,¹²⁴ further indicating the role membrane interactions play in inducing endosomal escape.

In Vitro Leakage Assays

Calcein, 6-carboxyfluorescein, and fluorescently labeled dextran have been used *in vitro* to investigate escape from trafficking vesicles.^{90,120,125,126} Cells macropinocytose the dye and a combination of low pH and self-quenching leads to a weak, punctate fluorescence in the endosomes (Figure 5(d)). If the

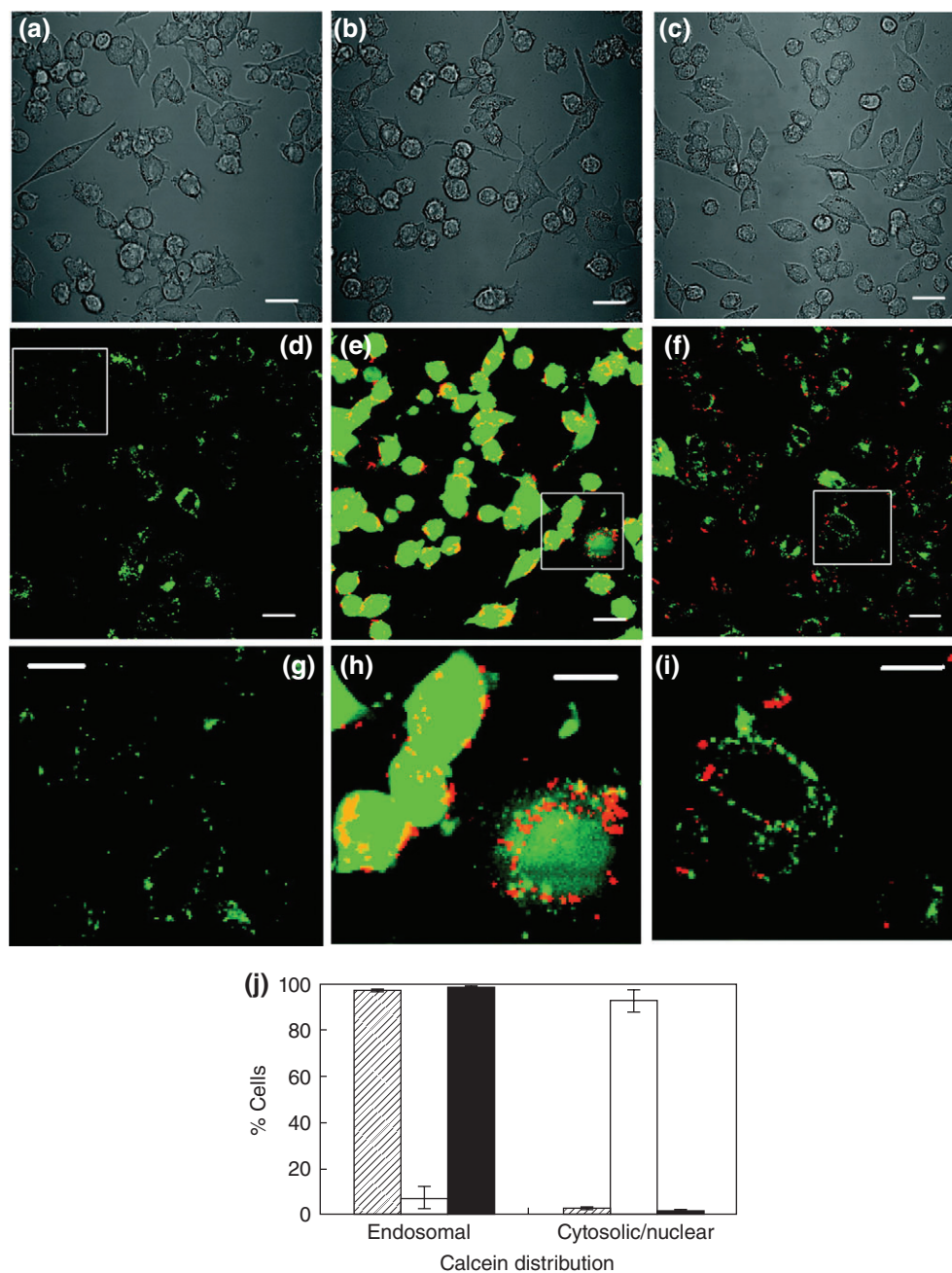


FIGURE 5 | pH-responsive nanoparticles induce endosomal escape of calcein in a dendritic cell line. (a–i) Confocal microscopy images. (a–c) Bright-field images. (d–i) Fluorescence overlays (red, nanoparticles; green, calcein). (a, d, g) Cells were treated with calcein alone. (b, e, h) Cells were co-incubated with calcein and PDEAEMA-core/PAEMA-shell nanoparticles. (c, f, i) Cells were co-incubated with calcein and PMMA-core/PAEMA-shell nanoparticles. Scale bars: (a–f) 20 μm and (g–i) 10 μm . (j) Average percentage of cells observed by confocal microscopy exhibiting endosomal versus cytosolic/nuclear calcein distributions after 1 h from three independent experiments: calcein alone (gray bar), calcein with PDEAEMA core-shell particles (white bar), or calcein with PMMA core-shell particles (black bar). (Reprinted with permission from Ref 126. Copyright 2007 American Chemical Society)

nanoparticles can induce escape, a high-fluorescent signal distributed through the cytoplasm is observed⁹⁰ (Figure 5(e)). This method is limited by low throughput, as cells with diffuse fluorescence are identified and counted manually. Attempts have been

made to improve throughput by incorporating an algorithm to recognize cells with diffuse fluorescence. The escape efficiency of a polyamidoamine–poly(ethylene glycol) (PEG) polyplex system was investigated by acquiring multiple fields of view and using the

intensity of the calcein fluorescence in the nuclear region to count cells with endosomal escape.¹²⁷ Alternatively, the calcein assay can be used with flow cytometry. pH-sensitive poly-(β -amino ester)-core phospholipid-shell particles showed a drastic increase in the percentage of cells positive for a calcein signal, while the signal from samples incubated with pH-insensitive poly-(lactide-*co*-glycolide) particles remained similar to the value for cells incubated with only calcein.¹²⁸ A combination of flow cytometry and microscopy is normally required when assessing escape, as calcein can associate with nanoparticles. This causes an increase in calcein signal due to increased calcein uptake rather than endosomal escape.

Although small-molecule leakage assays have the ability to show that membranes have been compromised, they cannot determine if the disruption is sufficient to allow the escape of particles or cargo unless these are labeled separately. The molecular weight threshold of escape can be investigated using dextran with a range of molecular weights (3000–2,000,000 Da).^{129,130} The release of small, but not large dextran, suggests leakage, while escape of all sizes implies complete disruption. While dextran is a useful model, it should be noted that dextran is a highly flexible molecule, enabling it to diffuse through pores that would inhibit the diffusion of globular proteins of a similar molecular weight. Leakage assays can be complimented by studies that inhibit the acidification of lysosomes through the use of drugs such as bafilomycin A1. Inhibiting lysosomal acidification typically inhibits endosomal escape.¹³¹

Transfection Assays

In addition to small-molecule therapeutics, endosomal escape is important for the delivery of nucleic acids for gene silencing or expression. siRNA must reach the cytosol to access the RNA-induced silencing complex (RISC)¹³² and DNA needs to enter the nucleus before it can be transcribed into RNA for protein expression.^{133,134} These criteria allow transfection assays to indirectly determine if escape has occurred by measuring knockdown or expression of the protein of interest. The most commonly used assays include delivery of genes for the enzymes luciferase^{135,136} and β -galactosidase.^{85,137,138} When successfully delivered and transcribed, an enzyme is produced that converts a specific substrate into a luminescent or colored compound. The luminescence or absorbance of cell lysates in the presence of the substrate can then be compared to nontransfected

cells to give an indirect measure of the relative level of escape. Transfection with plasmids coding for inherently fluorescent molecules such as green fluorescent protein (GFP)^{139,140} have also been used in a similar way using flow cytometry or microscopy. As transportation of DNA to the nucleus can be a significant barrier, RNAi can be used to evaluate cytoplasmic release through delivery of siRNAs to silence reporter genes.^{141,142} RNAi occurs in the cytosol, and hence is a more direct method of assessing endosomal escape.

Transfection assays are able to provide confirmation of escape with a reasonable amount of certainty by detection of or reduction in expression of a reporter gene. Yet, these assays are an indirect indicator of escape and cannot elucidate the mechanism. It is also imperative that the cytotoxicity of the materials is considered to ensure that any signal measured is not simply due to necrotic/apoptotic cells. This is highlighted with PEI, which is widely considered to be one of the most efficient nonviral transfection agents but also highly cytotoxic.⁶⁴ Bieber et al. introduced fluorescently labeled PEI/DNA complexes to human embryonic kidney (HEK) cells and found after an 18-h incubation, the majority of cells displayed fluorescence in a punctate distribution in the perinuclear region.⁹⁹ Although a small proportion of cells had a cytoplasmic distribution of fluorescence, they were also necrotic in appearance. The cells had become nonadherent and the morphology did not reoccur following subsequent media change, which suggested the cells were irreversibly damaged. As these cells were not part of the collective that express the reporter gene, they cannot be used to show escape regardless of the presence of labeled PEI–DNA complexes in the cytoplasm. Godbey et al. also demonstrated an inverse relationship between transfection efficiency and cell viability, using free and complexed PEI on the EA.hy 926 endothelial cell line.¹⁴³ As transfection with toxic materials is futile for the application of gene therapy, this research highlights the need to carefully consider the viability of cells alongside the ability to induce endosomal escape.

There is a significant need for new quantitative assays to assess endosomal escape. End-point assays such as transfection do not quantify the efficiency of escape, but instead give a yes/no answer if escape has occurred in the remaining healthy cells. Endosomal escape efficiency is rarely quoted, partly because it is a difficult parameter to quantify. No individual method is able to provide a conclusive answer on the mechanism and extent of escape. Therefore, it is important for multiple complementary techniques to

be employed before drawing conclusions about the mode and extent of endosomal escape.

STRATEGIES TO ENGINEER ENDOSOMAL ESCAPE

Over the past decade, numerous nanoparticle systems have been developed to enhance the cytoplasmic delivery of therapeutics. These nanoparticles rely on a diverse array of mechanisms to promote escape and in a number of instances, the mechanism by which endosomal escape occurs is not entirely clear. It is important we gain better insight into the parameters that control endosomal escape, to enable nanoparticles to be engineered so their cellular fate can be controlled and thus have improved efficacy.

Lipid-Mediated Membrane Fusion

Liposomal formulations have demonstrated potential for cytoplasmic delivery, particularly through the use of cationic lipids (N-[1-(2,3-dioleoyloxy)propyl]-N,N,N-trimethylammonium chloride (DOTAP), N-[1-(2,3-dioleoyloxy)propyl]-N,N,N-trimethylammonium chloride (DOTMA), dioleoyldimethylammonium chloride (DODAC)) for use in gene therapy.¹⁴⁴ Cationic liposomes are usually prepared with the neutral or helper lipids DOPE or DOPC in the mixture to provide stabilization of the lipid bilayer. Cationic liposomes prepared with DOPE have been shown to facilitate escape due to structural transitions when exposed to the low pH of endocytic vesicles.^{145,146} DOPC is a structural analogue of DOPE and promotes stable lamellar structures, but does not improve endosomal escape and hence transfection. Electron microscopy of DOPE containing cationic liposomes showed an endosomal destabilizing effect, whereas DOPC formulations did not have an effect.¹⁴⁷

Modification of liposomes with PEG is used extensively to improve *in vivo* circulation time, as demonstrated by the clinical liposomal formulation of doxorubicin, Doxil. However, the presence of PEG in liposomes has been observed to reduce endosomal escape. This has also been observed with other polymer-based nanoparticles, including PEI- and β -cyclodextrin-based polyplexes.¹⁰⁴ In contrast to PEGylated polyplexes,¹⁴⁸ PEGylation in this lipid system had minimal effect on cellular uptake¹⁴⁹ and delivery was instead limited by effective escape.^{150,151} The steric barrier provided by PEG is thought to interfere with membrane fusion events that occur between fusogenic lipids and the endosomal membrane.¹⁵⁰ In a study by Song et al., DODAC:DOPE liposomes at a

1:1 mole ratio with 5% PEG-lipid showed inefficient transfection in HepG2 cells.¹⁵⁰ By reducing the molecular weight of the PEG from 3400 to 220 Da and the amide chain length of the lipid anchor, transfection efficiency was improved. This suggests that PEG molecular weight and the size of the hydrophobic anchor are important. With confocal microscopy, they demonstrated a difference in the intracellular fate of PEGylated and naked liposomes. Lipids from liposomes without PEG localized in the perinuclear space while the oligonucleotide cargo escaped from endosomes and accumulated in the nucleus. In PEGylated liposomes, both the cargo and lipid remained perinuclear.

A number of groups have overcome the adverse effect of PEGylation on endosomal escape by designing pH-sensitive PEG analogues¹⁵² or PEG that can be cleaved in reducing conditions.^{153,154} Bio-functionalization with targeting moieties has also been shown to address the effects of PEGylation. Meyer et al. showed that conjugation of anti-HER2 F(ab') fragments on the PEG chains improved uptake, albeit nonspecifically, by a factor of ~ 2.5 compared with PEGylated liposomes alone.¹⁵⁵ Importantly, there was a significant improvement in the release and nuclear localization of encapsulated cargo with targeted PEGylated liposomes. It was suggested that targeted liposomes are trafficked by receptor-mediated endocytosis into early endosomes that are more permissible to cargo release than those in early endosomes from nonspecific pinocytosis; however, the mechanism by which this happens is not clear.¹⁵⁵

Hybrid systems can also be of significant interest as they can combine the advantages of different materials (e.g., proteins with polymers). An interesting example was reported by Rotello and coworkers, where an oil template stabilized by a mixture of protein and gold nanoparticles functionalized with a HKRK peptide motif was prepared.³⁵ The proteins GFP and caspase-3 were incorporated and the resulting particle sizes were 130 ± 40 nm and 140 ± 20 nm, respectively. This study demonstrated that GFP could be delivered effectively into HeLa cells, showing diffuse fluorescence throughout the cell, including the nucleus (Figure 6). The authors postulate that the mechanism for this process is through plasma membrane fusion, delivering the protein directly into the cytoplasm and not through endosomal escape from an acidic compartment.

Polymers Capable of Endosomal Buffering

A number of studies demonstrate that polymers with cationic amino substituents can buffer the

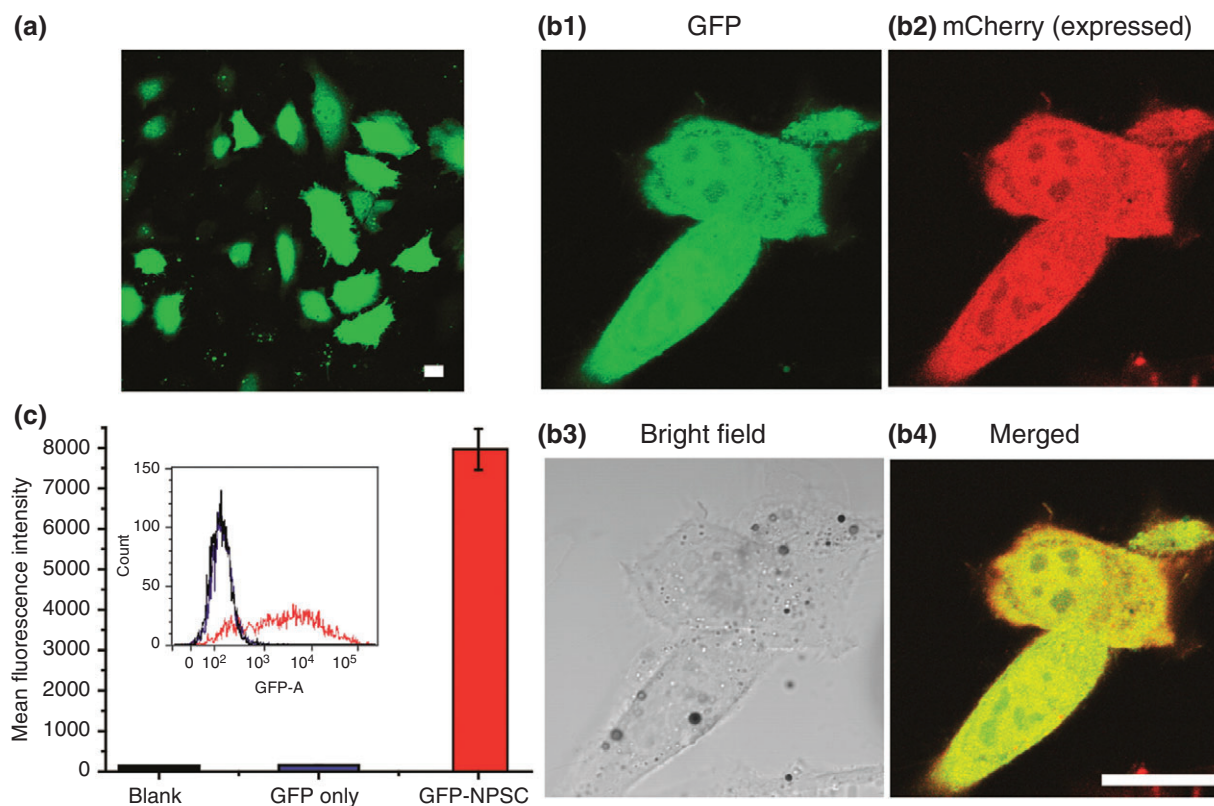


FIGURE 6 | Delivery of GFP into HeLa cells. (a) Confocal image showing GFP delivery into HeLa cells by nanoparticles (NPSCs). (b) Confocal images showing the co-localization of delivered GFP with expressed mCherry in HeLa cell. (c) Flow cytometry results of HeLa cells treated with GFP-NPSCs (red) or GFP alone (blue) for 2 h, using untreated HeLa cells as the control (black). Scale bars: 20 μm . (Reprinted with permission from Ref 35. Copyright 2013 American Chemical Society)

endosomal/lysosomal compartments to induce endosomal escape. PEI is a well-known example of such a polymer and is commonly used to complex DNA and siRNA to form polyion complexes. It has generally been observed that higher molecular weight PEI achieves better transfection than lower molecular weight but is also significantly more toxic. Recent studies have looked at using different PEI hybrids to improve transfection efficiency of low-molecular-weight variants.¹⁵⁶ The polypeptides poly(L-histidine) (PHis)¹⁵⁷ and poly(arginine) (PArg)¹⁵⁸ have also been shown to assist with endosomal buffering and thus have been incorporated into different polymer carriers.¹⁵⁹ While pH plays an important role in the endosomal escape of these materials, it is likely that other escape mechanisms are also involved.

Expandable pH-Responsive Nanoparticles

Mechanical stress has also been used to induce endosomal disruption by designing nanoparticles that change size upon a change in pH. One strategy is the synthesis of crosslinked polymer nanoparticles that

are assembled from pH-responsive polymers. Such materials swell significantly when they become ionized due to repulsion between the polymer chains.¹⁶⁰

Irvine and coworkers have performed a number of elegant studies on emulsion particles with a 2-diethylamino ethyl methacrylate (DEAEMA) core crosslinked with poly(ethylene glycol) dimethacrylate (PEGDMA) and a 2-aminoethyl methacrylate (AEMA) shell.¹²⁶ Changing the pH from an extracellular pH of 7.4 to an endolysosomal pH of 5 caused the particles to undergo a 2.8-fold change in diameter, as determined by dynamic light scattering. A pH-insensitive control particle was also synthesized based on crosslinked methyl methacrylate (MMA). These particles had minimal toxicity at concentrations below 25 $\mu\text{g}/\text{mL}$. The capability of these particles to disrupt the endosome was investigated using calcein in the model dendritic cell line, DC2.4. Microscopy showed cells loaded with control particles (pH insensitive) demonstrated only punctate fluorescence of the calcein, while PDEAEMA particles showed diffuse fluorescence throughout the cell,

indicating release from the endosomal compartments. Approximately 90% of cells incubated with PDEAEMA had diffuse cytosol fluorescence compared with fewer than 5% of cells incubated with calcein or calcein with control particles. Functional escape was also confirmed by loading particles with the model antigen ovalbumin (OVA) and measuring interferon- γ (IFN- γ) secretion by primary T cells in response to antigen presentation by DCs.¹²⁵ The responsive nanoparticles showed a 9- to 10-fold increase in IFN- γ production compared with nonresponsive particles or soluble OVA. In addition, the level of response was related to the concentration of OVA, with higher levels of protein showing an increased response.

The authors hypothesized that the mechanism of endosomal escape for these particles is a combination of increased water uptake into the endosome caused by counterion build-up and mechanical pressure from particle swelling. Interestingly, it was found that particles had to be delivered at the same time as the fluid phase marker (e.g., calcein) for endosomal escape to occur, suggesting the fluid phase marker needed to be colocalized in the same endosome. The nanoparticles were also used to load fluorescently labeled siRNA. While 40% of cells had diffuse siRNA fluorescence when incubated for 1 h, knockdown of this system was lower compared with a commercially available lipid reagent at $23 \pm 14\%$ and $6 \pm 1.2\%$, respectively. This was thought to be due to an electrostatic interaction between the cargo and the carrier when in the cytosol.

A similar nanoparticle was reported by Nagasaki and coworkers based on the emulsion polymerization of DEAEEMA in the presence of heterobifunctional PEG ($\text{CH}_2=\text{CH}-\text{Ph}-\text{PEG}-\text{COOH}$) and using ethylene glycol dimethacrylate (EGDMA) as a crosslinker.¹⁶¹ The nanoparticles were shown to increase in size between 5.1- and 6.8-fold when the PDEAEMA was protonated, depending on the size of the heterofunctional PEG used. A nanoparticle based on this chemistry was then functionalized with a lactose group (*p*-aminophenyl- β -D-lactopyranoside) using the carboxylic acid functional group on the PEG. This particle was added in combination with a PEG-*b*-poly(L-Lysine)/pDNA polyplex to investigate the effect on transfection efficiency of HuH-7 cells. A significant increase was observed when the two nanoparticles were added together, while a control sample with asialofetuin (ASF) showed less binding. This suggested that the particles were being internalized through an asialoglycoprotein receptor (ASGP)-mediated process as ASF acts as a competitive inhibitor of ASGP receptor-mediated endocytosis.

Rapid Disassembly of pH-Responsive Nanoparticles

Another endosomal escape mechanism postulated in the literature involves the disassembly of a cationic polymer particle into component unimers to create an increase in osmotic pressure and rupture of the endosomal membrane. One of the initial studies using this approach involved the synthesis of a responsive polymersome that could disassemble within the endosomal pH range. The polymersomes were synthesized from poly(2-methacryloyloxy)ethyl-phosphorylchlorine-*co*-poly(2-(diisopropylamino)ethyl methacrylate) (PMPC-*b*-PDPAEMA).⁸⁷ Stable vesicles were formed at physiological pH but disassembled below pH 6 due to a change in hydrophobicity of the PDPAEMA component. To test transfection efficiency, the plasmid encoding luciferase was encapsulated within the polymersome and delivered into primary human dermal fibroblast cells. Transfection efficiency was significantly enhanced by plasmid-loaded polymersomes compared with plasmid alone.

Irvine and coworkers have also reported a rapidly degradable, pH-dependent nanoparticle based on 10 kDa molecular weight poly(β -amino ester) (poly-1). Poly-1 is a weak polyelectrolyte that is water insoluble at elevated pH but dissolves in aqueous solutions below pH 7.¹²⁸ This polymer is stabilized by a lipid bilayer and a PEG-lipid and forms particles by nanoprecipitation. The particles formed were ~200 nm in diameter and were found to rapidly degrade *ex vivo* with a decrease in pH (within 5 min). Endosomal escape capacity was investigated by incubating the particles for 1 h with DC2.4 cells in the presence of calcein. Particles with a nonresponsive polylactic-*co*-glycolic acid (PLGA) core were used as a control. Both flow cytometry and microscopy showed an increase in calcein fluorescence when added in the presence of poly-1 particles compared with calcein or PLGA particles added in isolation. In a separate experiment, particles with electrostatically associated mRNA encoding for GFP were incubated with cells and the subsequent expression was assessed by flow cytometry. Approximately 30% of the cells were successfully transfected thus indicating evidence of endosomal escape. The authors proposed two mechanisms for the endosomal escape capacity of their particles: (1) An osmotic pressure gradient across the endosomal membrane caused by solid particles disassembling into individual polymer chains and (2) the proton sponge effect (see section *Proton Sponge Effect and Osmotic Lysis*).

Recently, our group has demonstrated the synthesis of a new pHlexi nanoparticle based on a combination of PDEAEMA homopolymer and a block PEG-*b*-PDEAEMA copolymer using nanoprecipitation.¹⁶² The particles were found to disassemble rapidly *ex vivo* when the pH was decreased below 6.8 and found to induce endosomal escape as determined via the calcein leakage assay. Endosomal escape was observed in ~40% of the cells, and there was strong colocalization of the polymer building blocks with the lysosomal compartments of the cells. This suggests that release was more likely due to a membrane disrupting or pore-forming mechanism than complete vesicle rupture. Later work showed that the endosomal escape of these pHlexi particles could be tuned by the molecular weight of the polymer building blocks.¹⁶³ This indicates that small variations in nanoparticle properties can also play an important role in cellular behavior.

Nanoparticles Capable of Interacting With the Endosomal Membrane

An additional avenue to enhance endosomal escape is engineering the polymer to interact with membranes. Some useful polymers to achieve such interactions are poly(propylacrylic acid) (PPAA) and poly(butyl acrylate) (PBA). Recently, a new micelle carrier was synthesized based on a cationic poly(2-dimethylamino ethyl methacrylate) (PDMAEMA) and a second pH-responsive membrane disruption block containing DMAEMA, propylacrylic acid (PAA) and butyl methacrylate (BMA).¹⁰³ This polymer formed micelles in the size range of 45 nm in physiological conditions. The particles were stable in PBS (pH 7.4) but disassembled readily in the lower pH conditions (pH 5.8) that would be present in an endosomal compartment. Further confirmation of their action within a biologically relevant range was obtained by a red blood cell hemolysis assay, which demonstrated that the particles increased lysis at a pH range of 6.6–5.8. The micelles were also loaded with siRNA targeting mRNA for the housekeeping gene GAPDH by interacting the negatively charged cargo with the PDMAEMA shell. Significant knockdown was observed for all concentrations above the critical micelle concentration. Fluorescence microscopy was also conducted using fluorescein-labeled siRNA in both loaded carriers and Lipofectamine complexes. Lipofectamine transfection resulted in punctate fluorescence while the micelle system showed diffuse siRNA release (Figure 7).

Polymersomes assembled from a triblock copolymer of consisting PEG and poly(glycerol methacrylate)

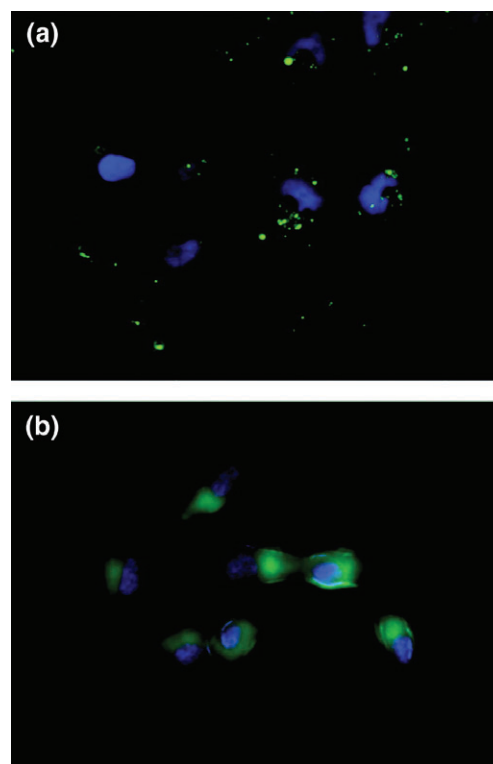


FIGURE 7 | Polymer-enhanced intracellular delivery of FAM-labeled siRNA. Representative images illustrating (a) punctate staining (green) in the samples treated with Lipofectamine/siRNA complexes alone and (b) dispersed fluorescence within the cytosol following delivery of diblock copolymer/siRNA complexes. Samples were treated for 15 min with 25 nM FAM-siRNA and prepared for microscopic examination following DAPI nuclear staining (blue). (Reprinted with permission from Ref 103. Copyright 2010 American Chemical Society)

(poly-GMA) ends, and a central weakly basic block, polyimidazole-hexyl methacrylate (poly-ImHeMA), showed similar siRNA delivery efficiency.¹⁶⁴ A PDAEMA polymer micelle has also been used as a vaccine delivery system by including pyridyl disulfide methacrylate in the PDAEMA block to load OVA.¹²² The polymer was then complexed with an unmethylated cytosine-phosphate-guanine (CpG) sequence acting as an adjuvant. The efficacy of these particles was tested *in vivo* by injecting C57BL/6 mice subcutaneously with polymer–protein conjugate/CpG, polymer–protein conjugate, or free OVA alone. The CD8+ response was determined by *ex vivo* stimulation of isolated splenocytes with the ova epitope SIINFEKL to determine IFN- γ production. Cytokine production was enhanced significantly when CpG and the polymer conjugate were present, inducing a sevenfold increase in production compared with conjugate alone and an 18-fold increase over free antigen.

In another recent study, Zhan et al. used a tri-polymer based on PAA, BMA and DMAEMA in

combination with PLGA to make blend particles.¹²⁹ To investigate endosomal escape, fluorescent molecules with varying molecular weights (calcein and fluorescein isothiocyanate (FITC)-dextran with the molecular weight of 4, 40, 150, and 2000 kDa) were co-delivered with particles into DC2.4 cells. A control of no particles or polystyrene (PS) was used for comparison of the cellular distribution. For both controls, the fluorescence remained punctate indicating little diffusion outside the endosomal membrane. In the case of the blend particles, diffuse fluorescence was seen for the lower molecular weight fluorescent species but remained punctate in the case of 150 and 2000 kDa dextran. This study gave interesting insight into the size of the pores that were formed in the membrane.

Poly(*N*-(2-aminoethyl)-2-aminoethyl-*a,b*-aspartamide) PAsp(DET) has also shown evidence of endosomal escape due to membrane interactions. Kataoka and coworkers used particles with either a disulfide or nondegradable linker between the PEG and AspDET components and compared their transfection efficiency.¹⁶⁵ Knockdown of luciferase expression was enhanced in the carrier containing PEG-SS-PAsp(DET) relative to the control sample that contained no disulfide moieties. Such polymers are thought to also have capability to fuse with membranes due to their hydrophobic components but only below a certain pH range.

Drug-Induced Endosomal Escape

While a number of particle systems undergo endosomal escape as a result of rapid pH-induced disassembly to unimers, other similar systems that undergo rapid particle disassembly do not show clear evidence of escape.^{166,167} A recent example is a micelleplex based on PDMAEMA-*b*-PDPAEMA, which allows for siRNA complexation and pH-induced disassembly below pH 6.3.¹⁶⁶ In this system, pH-responsive cationic components cause an increase in endosomal osmotic pressure due to disassembly of the particles into individual polymers. However, fluorescence from labeled siRNA remained punctate after 12-h incubation *in vitro*. To improve endolysosomal escape, particles were loaded with amphotericin B (AmB), a hydrophobic antifungal drug known to increase membrane permeability by forming transmembrane pores. The cellular distribution of siRNA loaded into the particles and a fluid marker [tetramethylrhodamine (TMR)-dextran] was investigated using confocal microscopy. Diffuse fluorescence was clearly observed with increasing concentration of AmB, especially in the case of the fluid phase marker

(TMR-dextran). This was confirmed by the enhanced knockdown of luciferase in the presence of AmB.

Peptide-Induced Endosomal Escape

Beyond using the intrinsic properties of the polymers or lipids, nanoparticles can be modified with endosomal escape agents to further enhance trafficking to the cytoplasm. A number of polypeptides derived from viral or bacterial proteins have been demonstrated to facilitate endosomal escape. A common motif present in many CPPs that have been observed to escape the endosome is the presence of arginine residues.¹⁶⁸ Arginine has a guanidinium functional group, which readily forms a complex with phosphate groups on phospholipids through a combination of hydrogen bonding and electrostatic interactions.¹⁶⁹ A number of materials that contain the guanidinium group, such as polymers and lipids, also show enhanced membrane permeation.^{35,169} The role of guanidinium has been demonstrated in studies comparing octaarginine-functionalized liposomes to octalysine-functionalized liposomes. Liposomes functionalized with a high density of octaarginine showed significantly increased transfection efficiency compared with liposomes functionalized with octalysine.¹²⁰

One of the most ubiquitous arginine-rich peptide sequences used for inducing endosomal escape is the TAT peptide, which is derived from the Trans-Activator of Transcription protein in HIV. The primary role of TAT protein is in the replication of the viral genome and does not play an active role in HIV infection.¹⁷⁰ However, the high content of arginine residues within the 11-amino acid sequence allows the protein to readily translocate across cell membranes.¹⁷⁰ This protein transduction domain of TAT can be fused to proteins and polymers to induce endosomal escape. TAT-induced escape is generally quite inefficient, requires high concentrations of TAT, and can be highly variable depending on the cargo to escape and the cells being targeted.¹⁷ In particular, direct fusion of TAT to materials to induce trafficking from the endosome has had limited success.¹⁷ This suggests that either free TAT is required for membrane disruption or that TAT remains in the endosomal membrane as part of the destabilization process. In recent work, a disulfide-linked TAT dimer has shown significantly enhanced endosomal escape at concentrations more than an order of magnitude less than that of monomeric TAT.¹⁷ The mechanism by which TAT and dimeric TAT induce endosomal escape is not understood.

TAT is initially trafficked to Rab5+ early endosomes then to Rab7+ late endosomes before it can

escape from endosomal compartments.¹⁶⁸ Schepartz and coworkers have developed peptide sequences with controlled arginine topology, whereby five arginine residues are presented on the same face of an alpha-helical peptide. This peptide (5.3) induces endosomal escape that is more efficient than TAT or Arg8, and interestingly enables endosomal escape from the Rab5+ early endosomes without the need for maturation into Rab7+ late endosomes.¹⁶⁸

The second class of endosomal escape peptides lack arginine residues and are thought to disrupt the endosomal membrane via insertion into the lipid bilayer. A number of useful peptides have been derived from the hemagglutinin HA2 subunit of the influenza virus. The flu virus escapes from the endosomal compartment by pH-induced conformational changes in the HA2 subunit that enables the virus to fuse with the endosomal membrane. The 23 N-terminal amino acid sequence of HA2 fuses and disrupts cell membranes, and has been shown to induce membrane fusion, leakage, and lysis.¹⁷¹ While the HA2 peptide and its variants can effectively induce membrane fusion and leakage, direct attachment of the HA2 peptide to a protein cargo increased association to endosomal compartments. However, when free HA2 was co-delivered with the protein, escape was induced but the HA2 fusion protein remained in the endosome.¹⁰⁰ This is likely due to HA2 remaining inserted in the endosomal membrane, preventing the conjugated protein cargo from escaping. Although HA2 and related peptides have potential, their application must be carefully considered so they cause release of the particle or cargo without remaining attached.

A peptide with a related mechanism of action is GALA, a purely synthetic sequence designed to adopt an alpha-helical conformation at low pH that can span the lipid bilayer of the endosome. GALA is negatively charged at pH 7 and comprises a repeated EALA (glu-ala-leu-ala) motif, which forms an alpha helix when the glutamic acid residues become protonated. The sequence induces pH-dependent fusion of lipid membranes and can also self-assemble to form transmembrane pores capable of transporting molecules up to ~5000 Da.⁹² Cationic variants of GALA have been engineered by substituting the glutamic acid for lysine (KALA). Despite the KALA sequence undergoing the opposite conformational change to GALA (alpha helix to random coil, rather than random coil to alpha helix), KALA is still able to induce endosomal escape. DNA complexed with KALA has shown significantly increased transfection efficiency compared with polylysine-condensed DNA. Modification of liposomes with a shortened GALA (shGALA) has

also been shown to enhance endosomal escape. shGALA-modified and PEGylated lipid-based particles called multifunctional nanodevices (PEG-MEND) demonstrated 82% knockdown of the target gene through RNA silencing.¹⁷² Reduced gene silencing efficiency was seen in cells incubated with NH₄Cl, which suppresses endosome acidification. This pH dependence suggests that the peptide requires an acid environment to exert its fusogenic properties.¹⁷²

Using a screen of antimicrobial peptides from the antimicrobial peptide database, Liu and coworkers have identified the aurein 1.2 peptide sequence to have endosomolytic properties.¹⁷³ This sequence has been demonstrated to induce endosomal escape both *in vitro* and *in vivo*. In another study, Liang et al. demonstrated enhanced cytoplasmic localization of a therapeutic-loaded nanoparticle when it contained a H4R4 peptide consisting of four arginine units and four histidine units.¹⁷⁴

CONCLUSIONS

Significant progress has been made over the last 10 years in developing nanoparticles to address the challenges of cytoplasmic delivery. However, as we rapidly generate new materials, our knowledge of how nanoparticles induce endosomal escape lags behind. Furthermore, significant promise seen *in vitro* is not matched with efficient delivery *in vivo*. A fundamental understanding of how nanoparticles are transported within the cell is key to engineering materials to improve escape and overcome this significant bottleneck.

Our ability to understand the mechanisms of escape is limited by the current techniques used to detect it. We need to move beyond assays that simply report the percent of cells that show escape, and develop techniques that can also quantify efficiency. New assays and sensors will help us address some of the fundamental questions behind endosomal escape. These include: Does the mechanism of nanoparticle internalization affect the subsequent trafficking and escape of the particle? What physical and chemical properties such as size, shape, or charge must a particle possess in order to be successful at escaping the endosome and are they interdependent? What role does targeting play in endosomal escape, and does targeting to a specific pathway dominate trafficking over the native pathways untargeted nanoparticles take?

The answers to these questions will not be straightforward. Mammalian cells are innately complex and highly regulated, coordinating a multitude of biochemical processes. This is compounded by interactions between the nanoparticle and endogenous

biomolecules in the extracellular space. This complexity highlights the need for studies where the properties of nanoparticles are understood and controlled in order to link their attributes to how they behave in cells.

Although the interactions between cell and particle are complicated, it is imperative that we make the nanoparticle solution simple. Nanoparticles must be engineered keeping their eventual application in mind and as such must have characteristics

suitable for a drug delivery system if they are going to have a significant impact in the way we treat diseases. Next-generation treatment of diseases with gene therapy, vaccination, and drugs active in the cytosol all rely on the development of delivery systems that effectively deliver cargo from the endosome into the cytoplasm. We must overcome the barrier of endosomal escape to fulfill the promise these therapies offer. This begins with a greater understanding of how materials interact with cells.

REFERENCES

1. Johnston APR, Such GK, Ng SL, Caruso F. Challenges facing colloidal delivery systems: from synthesis to the clinic. *Curr Opin Colloid* 2011, 16:171–181.
2. Van Dongen SFM, De Hoog HPM, Peters RJRW, Nallani M, Nolte RJM, Van Hest JCM. Biohybrid polymer capsules. *Chem Rev* 2009, 109:6212–6274.
3. Zhang L, Gu F, Chan J, Wang A, Langer R, Farokhzad O. Nanoparticles in medicine: therapeutic applications and developments. *Clin Pharmacol Ther* 2008, 83:761–769.
4. De Geest BG, Willart MA, Hammad H, Lambrecht BN, Pollard C, Bogaert P, De Filette M, Saelens X, Vervaet C, Remon JP, et al. Polymeric multilayer capsule-mediated vaccination induces protective immunity against cancer and viral infection. *ACS Nano* 2012, 6:2136–2149.
5. Davis ME, Zuckerman JE, Choi CHJ, Seligson D, Tolcher A, Alabi CA, Yen Y, Heidel JD, Ribas A. Evidence of RNAi in humans from systemically administered siRNA via targeted nanoparticles. *Nature* 2010, 464:1067–1070.
6. Singh R, Lillard JW Jr. Nanoparticle-based targeted drug delivery. *Exp Mol Pathol* 2009, 86:215–223.
7. Canton I, Battaglia G. Endocytosis at the nanoscale. *Chem Soc Rev* 2012, 41:2718–2739.
8. Kanasty R, Dorkin JR, Vegas A, Anderson D. Delivery materials for siRNA therapeutics. *Nat Mater* 2013, 12:967–977.
9. Pack DW, Hoffman AS, Pun S, Stayton PS. Design and development of polymers for gene delivery. *Nat Rev Drug Discov* 2005, 4:581–593.
10. Zhao L, Seth A, Wibowo N, Zhao C-X, Mitter N, Yu C, Middelberg APJ. Nanoparticle vaccines. *Vaccine* 2014, 32:327–337.
11. Torchilin V. Intracellular delivery of protein and peptide therapeutics. *Drug Discov Today Technol* 2008, 5:e95–e103.
12. Leader B, Baca QJ, Golan DE. Protein therapeutics: a summary and pharmacological classification. *Nat Rev Drug Discov* 2008, 7:21–39.
13. Shete HK, Prabhu RH, Patravale VB. Endosomal escape: a bottleneck in intracellular delivery. *J Nanosci Nanotechnol* 2014, 14:460–474.
14. Varkouhi AK, Scholte M, Storm G, Haisma HJ. Endosomal escape pathways for delivery of biologicals. *J Control Release* 2011, 151:220–228.
15. Heath F, Haria P, Alexander C. Varying polymer architecture to deliver drugs. *AAPS J* 2007, 9: E235–E240.
16. Wagner E, Plank C, Zatloukal K, Cotten M, Birnstiel ML. Influenza virus hemagglutinin HA-2N-terminal fusogenic peptides augment gene transfer by transferrin-polylysine-DNA complexes: toward a synthetic virus-like gene-transfer vehicle. *Proc Natl Acad Sci USA* 1992, 89:7934–7938.
17. Erazo-Oliveras A, Najjar K, Dayani L, Wang T-Y, Johnson G a, Pellois J-P. Protein delivery into live cells by incubation with an endosomolytic agent. *Nat Methods* 2014, 11:861–867.
18. Kakimoto S, Hamada T, Komatsu Y, Takagi M, Tanabe T, Azuma H, Shinkai S, Nagasaki T. The conjugation of diphtheria toxin T domain to poly(ethylenimine) based vectors for enhanced endosomal escape during gene transfection. *Biomaterials* 2009, 30:402–408.
19. Cross KJ, Burleigh LM, Steinhauer DA. Mechanisms of cell entry by influenza virus. *Expert Rev Mol Med* 2001, 3:1–18.
20. Collier RJ. Understanding the mode of action of diphtheria toxin: a perspective on progress during the 20th century. *Toxicon* 2001, 39:1793–1803.
21. Wyman T, Nicol F, Zelphati O, Scaria P. Design, synthesis, and characterization of a cationic peptide that binds to nucleic acids and permeabilizes bilayers. *Biochemistry* 1997, 2960:3008–3017.
22. Subbarao NK, Parente RA, Szoka FC, Nadasdi L, Pongracz K. The pH-dependent bilayer destabilization

- by an amphipathic peptide. *Biochemistry* 1987, 26:2964–2972.
23. Raof M, Mackeyev Y, Cheney MA, Wilson LJ, Curley SA. Internalization of C60 fullerenes into cancer cells with accumulation in the nucleus via the nuclear pore complex. *Biomaterials* 2012, 33:2952–2960.
 24. Cheung W, Pontoriero F, Taratula O, Chen AM, He H. DNA and carbon nanotubes as medicine. *Adv Drug Deliv Rev* 2010, 62:633–649.
 25. Probst CE, Zrazhevskiy P, Bagalkot V, Gao X. Quantum dots as a platform for nanoparticle drug delivery vehicle design. *Adv Drug Deliv Rev* 2013, 65:703–718.
 26. Bogart LK, Pourroy G, Murphy CJ, Puentes V, Pellegrino T, Rosenblum D, Peer D, Lévy R. Nanoparticles for imaging, sensing, and therapeutic intervention. *ACS Nano* 2014, 8:3107–3122.
 27. Jiang Y, Huo S, Hardie J, Liang X, Rotello VM. Progress and perspective of inorganic nanoparticle-based siRNA delivery systems. *Expert Opin Drug Deliv* 2016, 13:547–559.
 28. Cho YW, Kim J-D, Park K. Polycation gene delivery systems: escape from endosomes to cytosol. *J Pharm Pharmacol* 2003, 55:721–734.
 29. Yessine M-A, Leroux J-C. Membrane-destabilizing polyanions: interaction with lipid bilayers and endosomal escape of biomacromolecules. *Adv Drug Deliv Rev* 2004, 56:999–1021.
 30. Nazareno M, Zhang Q, Soliman MG, Del Pino P, Pelaz B, Carregal-Romero S, Rejman J, Rothen-Rutishauser B, Clift MJD, Zellner R, et al. In vitro interaction of colloidal nanoparticles with mammalian cells: what have we learned thus far? *Beilstein J Nanotechnol* 2014, 5:1477–1490.
 31. Sahay G, Alakhova DY, Kabanov AV. Endocytosis of nanomedicines. *J Control Release* 2010, 145:182–195.
 32. Parton RG, Simons K. The multiple faces of caveolae. *Nat Rev Mol Cell Biol* 2007, 8:185–194.
 33. Kinchen JM, Ravichandran KS. Phagosome maturation: going through the acid test. *Nat Rev Mol Cell Biol* 2008, 9:781–795.
 34. Stenmark H. Rab GTPases as coordinators of vesicle traffic. *Nat Rev Mol Cell Biol* 2009, 10:513–525.
 35. Tang R, Kim CS, Solfiell DJ, Rana S, Mout R, Velázquez-Delgado EM, Chompoosor A, Jeong Y, Yan B, Zhu ZJ, et al. Direct delivery of functional proteins and enzymes to the cytosol using nanoparticle-stabilized nanocapsules. *ACS Nano* 2013, 7:6667–6673.
 36. Doherty GJ, McMahon HT. Mechanisms of endocytosis. *Annu Rev Biochem* 2009, 78:857–902.
 37. Kirkham M, Parton RG. Clathrin-independent endocytosis: new insights into caveolae and non-caveolar lipid raft carriers. *Biochim Biophys Acta* 2005, 1746:350–363.
 38. Bhattacharyya S, Singh RD, Pagano R, Robertson JD, Bhattacharya R, Mukherjee P. Switching the targeting pathways of a therapeutic antibody by nanodesign. *Angew Chem Int Ed* 2012, 51:1563–1567.
 39. Mintern JD, Percival C, Kamphuis MMJ, Chin WJ, Caruso F, Johnston APR. Targeting dendritic cells: the role of specific receptors in the internalization of polymer capsules. *Adv Healthc Mater* 2013, 2:940–944.
 40. Lin GG, Scott JG. Transferrin receptor-targeted lipid nanoparticles for delivery of an antisense oligodeoxynucleotide against Bcl-2. *Mol Pharm* 2009, 6:221–230.
 41. Van Steenis JH, Van Maarseveen EM, Verbaan FJ, Verrijck R, Crommelin DJA, Storm G, Hennink WE. Preparation and characterization of folate-targeted pEG-coated pDMAEMA-based polyplexes. *J Control Release* 2003, 87:167–176.
 42. Pereira P, Pedrosa SS, Wymant JM, Sayers E, Correia A, Vilanova M, Jones AT, Gama FM. siRNA inhibition of endocytic pathways to characterize the cellular uptake mechanisms of folate-functionalized glycol chitosan nanogels. *Mol Pharm* 2015, 12:1970–1979.
 43. Zhang LW, Monteiro-Riviere NA. Mechanisms of quantum dot nanoparticle cellular uptake. *Toxicol Sci* 2009, 110:138–155.
 44. Johnston APR. *ACS Sensors* 2017. DOI: 10.1021/acssensors.6b00725.
 45. Iversen T-G, Skotland T, Sandvig K. Endocytosis and intracellular transport of nanoparticles: present knowledge and need for future studies. *Nano Today* 2011, 6:176–185.
 46. Christoforidis S, McBride HM, Burgoyne RD, Zerial M. The Rab5 effector EEA1 is a core component of endosome docking. *Nature* 1999, 397:621–625.
 47. Beyenbach KW, Wiczorek H. The V-type H⁺ ATPase: molecular structure and function, physiological roles and regulation. *J Exp Biol* 2006, 209:577–589.
 48. Casey JR, Grinstein S, Orlowski J. Sensors and regulators of intracellular pH. *Nat Rev Mol Cell Biol* 2010, 11:50–61.
 49. Sheff DR, Daro EA, Hull M, Mellman I. The receptor recycling pathway contains two distinct populations of early endosomes with different sorting functions. *J Cell Biol* 2013, 145:123–139.
 50. Lübke T, Lobel P, Sleat DE. Proteomics of the lysosome. *Biochim Biophys Acta* 2009, 1793:625–635.
 51. Pinto-González Howell D, Krieser RJ, Eastman A, Barry MA. Deoxyribonuclease II is a lysosomal barrier to transfection. *Mol Ther* 2003, 8:957–963.

52. Laurent N, Coninck SW, Mihaylova E, Leontieva E, Wattiaux R, Jadot M. Uptake by rat liver and intracellular fate of plasmid DNA complexed with poly-L-lysine or poly-D-lysine. *FEBS Lett* 1999, 443:61–65.
53. Johnston APR, Lee L, Wang Y, Caruso F. Controlled degradation of DNA capsules with engineered restriction-enzyme cut sites. *Small* 2009, 5:1418–1421.
54. Roberg K, Kågedal K, Ollinger K. Microinjection of cathepsin d induces caspase-dependent apoptosis in fibroblasts. *Am J Pathol* 2002, 161:89–96.
55. Thomas TP, Majoros I, Kotlyar A, Mullen D, Holl MMB, Baker JR. Cationic poly(amidoamine) dendrimer induces lysosomal apoptotic pathway at therapeutically relevant concentrations. *Biomacromolecules* 2009, 10:3207–3214.
56. Schmaljohann D. Thermo- and pH-responsive polymers in drug delivery. *Adv Drug Deliv Rev* 2006, 58:1655–1670.
57. Gao W, Chan J, Farokhzad O. pH-responsive nanoparticles for drug delivery. *Mol Pharm* 2010, 7:1913–1920.
58. Dutta D, Donaldson JG. Search for inhibitors of endocytosis. *Cell Logist* 2012, 2:203–208.
59. Parton RG, Howes MT. Revisiting caveolin trafficking: the end of the caveosome. *J Cell Biol* 2010, 191:439–441.
60. Hayer A, Stoeber M, Ritz D, Engel S, Meyer HH, Helenius A. Caveolin-1 is ubiquitinated and targeted to intraluminal vesicles in endolysosomes for degradation. *J Cell Biol* 2010, 191:615–629.
61. Albanese A, Tang PS, Chan WCW. The effect of nanoparticle size, shape, and surface chemistry on biological systems. *Annu Rev Biomed Eng* 2012, 14:1–16.
62. Zhao F, Zhao Y, Liu Y, Chang X, Chen C, Zhao Y. Cellular uptake, intracellular trafficking, and cytotoxicity of nanomaterials. *Small* 2011, 7:1322–1337.
63. Parhamifar L, Larsen AK, Hunter AC, Andresen TL, Moghimi SM. Polycation cytotoxicity: a delicate matter for nucleic acid therapy—focus on polyethylenimine. *Soft Matter* 2010, 6:4001.
64. Sohaebuddin SK, Thevenot PT, Baker D, Eaton JW, Tang L. Nanomaterial cytotoxicity is composition, size, and cell type dependent. *Part Fibre Toxicol* 2010, 7:1–17.
65. Nel AE, Mädler L, Velegol D, Xia T, Hoek EM V, Somasundaran P, Klaessig F, Castranova V, Thompson M. Understanding biophysicochemical interactions at the nano-bio interface. *Nat Mater* 2009, 8:543–557.
66. Lundqvist M, Stigler J, Elia G, Lynch I, Cedervall T, Dawson KA. Nanoparticle size and surface properties determine the protein corona with possible implications for biological impacts. *Proc Natl Acad Sci USA* 2008, 105:14265–14270.
67. Fleischer CC, Payne CK. Nanoparticle-cell interactions: molecular structure of the protein corona and cellular outcomes. *Acc Chem Res* 2014, 47:2651–2659.
68. Salvati A, Pitek AS, Monopoli MP, Prapainop K, Bombelli FB, Hristov DR, Kelly PM, Åberg C, Mahon E, Dawson KA. Transferrin-functionalized nanoparticles lose their targeting capabilities when a biomolecule corona adsorbs on the surface. *Nat Nanotechnol* 2013, 8:137–143.
69. Maiorano G, Sabella S, Sorce B, Brunetti V, Malvindi MA, Cingolani R, Pompa PP. Effects of cell culture media on the dynamic formation of protein-nanoparticle complexes and influence on the cellular response. *ACS Nano* 2010, 4:7481–7491.
70. Gabrielson NP, Pack DW. Efficient polyethylenimine-mediated gene delivery proceeds via a caveolar pathway in HeLa cells. *J Control Release* 2009, 136:54–61.
71. Rejman J, Bragonzi A, Conese M. Role of clathrin- and caveolae-mediated endocytosis in gene transfer mediated by lipo- and polyplexes. *Mol Ther* 2005, 12:468–474.
72. Gottstein C, Wu G, Wong BJ, Zasadzinski JA. Precise quantification of nanoparticle internalization. *ACS Nano* 2013, 7:4933–4945.
73. Fraser L, Hamm-alvarez SF. Intracellular uptake and trafficking of difluoroboron dibenzoylmethane-poly(lactic acid) nanoparticles in HeLa cells. *ACS Nano* 2011, 4:2735–2747.
74. Braun GB, Friman T, Pang H-B, Pallaoro A, de Mendoza TH, Willmore A-MA, Kotamraju VR, Mann AP, She Z-G, Sugahara KN, et al. Etchable plasmonic nanoparticle probes to image and quantify cellular internalization. *Nat Mater* 2014, 13:1–19.
75. Rosenholm JM, Meinander A, Peuhu E, Niemi R, Eriksson JE, Sahlgren C, Lindén M. Targeting of porous hybrid silica nanoparticles to cancer cells. *ACS Nano* 2009, 3:197–206.
76. Liu H, Johnston APR. A programmable sensor to probe the internalization of proteins and nanoparticles in live cells. *Angew Chemie Int Ed* 2013, 52:5744–5748.
77. Mann SK, Czuba E, Selby LI, Such GK, Angus P, Johnston R. Quantifying nanoparticle internalization using a high throughput internalization assay. *Pharm Res* 2016, 33:2421–2432.
78. Selby LI, Kongkatigumjorn N, Such GK, Johnston APR. HD flow cytometry: an improved way to quantify cellular interactions with nanoparticles. *Advanced Healthcare Materials* 2016, 5:2333–2338. doi:10.1002/adhm.201600445.
79. Behr J. The proton sponge: a trick to enter cells the viruses did not exploit. *Chim Int J Chem* 1997, 2:34–36.

80. Zelphati O, Szoka F. Mechanism of oligonucleotide release from cationic liposomes. *Proc Natl Acad Sci USA* 1996, 93:11493–11498.
81. Patil ML, Zhang M, Taratula O, Garbuzenko OB, He H, Minko T. Internally cationic polyamidoamine PAMAM-OH dendrimers for siRNA delivery: effect of the degree of quaternization and cancer targeting. *Biomacromolecules* 2009, 10:258–266.
82. Boussif O, Lezoualc'h F, Zanta MA, Mergny MD, Scherman D, Demeneix B, Behr JP. A versatile vector for gene and oligonucleotide transfer into cells in culture and in vivo: polyethylenimine. *Proc Natl Acad Sci USA* 1995, 92:7297–7301.
83. Won Y-Y, Sharma R, Konieczny SF. Missing pieces in understanding the intracellular trafficking of polycation/DNA complexes. *J Control Release* 2009, 139:88–93.
84. Benjaminsen RV, Matthebjerg MA, Henriksen JR, Moghimi SM, Andresen TL. The possible 'proton sponge' effect of polyethylenimine (PEI) does not include change in lysosomal pH. *Mol Ther* 2013, 21:149–157.
85. Funhoff AM, van Nostrum CF, Koning GA, Schuurmans-Nieuwenbroek NME, Crommelin DJA, Hennink WE. Endosomal escape of polymeric gene delivery complexes is not always enhanced by polymers buffering at low pH. *Biomacromolecules* 2004, 5:32–39.
86. Massignani M, Lopresti C, Blanazs A, Madsen J, Armes SP, Lewis AL, Battaglia G. Controlling cellular uptake by surface chemistry, size, and surface topology at the nanoscale. *Small* 2009, 5:2424–2432.
87. Lomas H, Massignani M, Abdullah KA, Canton I, Presti L, Macneil S, Du J, Blanazs A, Madsen J, Armes SP, et al. Non-cytotoxic polymer vesicles for rapid and efficient intracellular delivery. *Faraday Discuss* 2008, 139:143–159.
88. White JM, Whittaker GR. Fusion of enveloped viruses in endosomes. *Traffic* 2016, 17:593–614.
89. Koltover I, Salditt T, Rädler JO, Safinya CR. An inverted hexagonal phase of cationic liposome-DNA complexes related to DNA release and delivery. *Science* 1998, 281:78–81.
90. Jones RA, Cheung CY, Black FE, Zia JK, Stayton PS, Hoffman AS, Wilson MR. Poly(2-alkylacrylic acid) polymers deliver molecules to the cytosol by pH-sensitive disruption of endosomal vesicles. *Biochem J* 2003, 372:65–75.
91. Nakase I, Kobayashi S, Futaki S. Endosome-disruptive peptides for improving cytosolic delivery of bioactive macromolecules. *Biopolymers* 2010, 94:763–770.
92. Li W, Nicol F, Szoka FC. GALA: a designed synthetic pH-responsive amphipathic peptide with applications in drug and gene delivery. *Adv Drug Deliv Rev* 2004, 56:967–985.
93. Danial M, Perrier S, Jolliffe KA. Effect of the amino acid composition of cyclic peptides on their self-assembly in lipid bilayers. *Org Biomol Chem* 2015, 13:2464–2473.
94. Qian S, Wang W, Yang L, Huang HW. Structure of the alamethicin pore reconstructed by x-ray diffraction analysis. *Biophysical journal* 2008, 94:3512–3522.
95. Tian W, Ma Y. Insights into the endosomal escape mechanism via investigation of dendrimer-membrane interactions. *Soft Matter* 2012, 8:6378.
96. Leroueil PR, Berry SA, Duthie K, Han G, Rotello VM, McNerny DQ, Baker JR, Orr BG, Banaszak Holl MM. Wide varieties of cationic nanoparticles induce defects in supported lipid bilayers. *Nano Lett* 2008, 8:420–424.
97. Hong S, Leroueil PR, Janus EK, Peters JL, Kober M-M, Islam MT, Orr BG, Baker JR, Banaszak Holl MM. Interaction of polycationic polymers with supported lipid bilayers and cells: nanoscale hole formation and enhanced membrane permeability. *Bioconjug Chem* 2006, 17:728–734.
98. Chen J, Hessler JA, Putschakayala K, Panama BK, Khan DP, Tew GN, Lopatin AN, Baker JRJ, Banaszak Holl MM, Orr BG. Cationic nanoparticles induce nanoscale disruption in living cell plasma membranes. *J Phys Chem B* 2009, 113:11179–11185.
99. Bieber T, Meissner W, Kostin S, Niemann A, Elsasser H-P. Intracellular route and transcriptional competence of polyethylenimine-DNA complexes. *J Control Release* 2002, 82:441–454.
100. Lee Y, Johnson G, Peltier GC, Pellois J. A HA2-fusion tag limits the endosomal release of its protein cargo despite causing endosomal lysis. *Biochim Biophys Acta* 2011, 1810:752–758.
101. Turk B, Turk V. Lysosomes as 'suicide bags' in cell death: myth or reality? *J Biol Chem* 2009, 284:21783–21787.
102. Martens TF, Remaut K, Demeester J, De Smedt SC, Braeckmans K. Intracellular delivery of nanomaterials: how to catch endosomal escape in the act. *Nano Today* 2014, 9:344–364. doi:10.1016/j.nantod.2014.04.011.
103. Convertine AJ, Diab C, Prieve M, Paschal A, Hoffman AS, Johnson PH, Stayton PS. pH-responsive polymeric micelle carriers for siRNA drugs. *Biomacromolecules* 2010, 11:2904–2911.
104. Mishra S, Webster P, Davis ME. PEGylation significantly affects cellular uptake and intracellular trafficking of non-viral gene delivery particles. *Eur J Cell Biol* 2004, 83:97–111.
105. Lu J, Liang M, Zink JJ, Tamanoi F. Mesoporous silica nanoparticles as a delivery system for hydrophobic anticancer drugs. *Small* 2007, 3:1341–1346.
106. Panyam J, Zhou W-Z, Prabha S, Sahoo SK, Labhasetwar V. Rapid endo-lysosomal escape of poly(DL-lactide-co-glycolide) nanoparticles: implications

- for drug and gene delivery. *FASEB J* 2002, 16:1217–1226.
107. Liu P, Sun Y, Wang Q, Sun Y, Li H, Duan Y. Intracellular trafficking and cellular uptake mechanism of mPEG-PLGA-PLL and mPEG-PLGA-PLL-Gal nanoparticles for targeted delivery to hepatomas. *Biomaterials* 2014, 35:760–770.
 108. Via LE, Fratti RA, McFalone M, Pagan-Ramos E, Deretic D, Deretic V. Effects of cytokines on mycobacterial phagosome maturation. *J Cell Sci* 1998, 905:897–905.
 109. Chikte S, Panchal N, Warnes G. Use of LysoTracker dyes: a flow cytometric study of autophagy. *Cytom Part A* 2014, 85:169–178.
 110. Chen JW, Pan W, D'Souza MP, August JT. Lyso-some-associated membrane proteins: characterization of LAMP-1 of macrophage P388 and mouse embryo 3T3 cultured cells. *Arch Biochem Biophys* 1985, 239:574–586.
 111. Ames RS, Kost TA, Condreay JP. BacMam technology and its application to drug discovery. *Expert Opin Drug Discov* 2007, 2:1669–1681.
 112. Bivas-Benita M, Romeijn S, Junginger HE, Borchard G. PLGA-PEI nanoparticles for gene delivery to pulmonary epithelium. *Eur J Pharm Biopharm* 2004, 58:1–6.
 113. Thavarajah R, Mudimbaimannar VK, Elisabeth J, Rao UK, Ranganathan K. Chemical and physical basics of routine formaldehyde fixation. *J Oral Maxillofac Pathol* 2012, 16:400–405.
 114. Wiedenmann J, Oswald F, Nienhaus GU. Fluorescent proteins for live cell imaging: opportunities, limitations, and challenges. *IUBMB Life* 2009, 61:1029–1042.
 115. Lisenbee CS, Karnik SK, Trelease RN. Overexpression and mislocalization of a tail-anchored GFP redefines the identity of peroxisomal ER. *Traffic* 2003, 4:491–501.
 116. Maiolo JR III, Ottinger EA, Ferrer M. Specific redistribution of cell-penetrating peptides from endosomes to the cytoplasm and nucleus upon laser illumination. *J Am Chem Soc* 2004, 126:15376–15377.
 117. Weinstein JN, Yoshikami S, Henkart P, Blumenthal R, Hagins WA. Liposome-cell interaction: transfer and intracellular release of a trapped fluorescent marker. *Science* 1977, 195:489–492.
 118. Madani F, Perálvarez-Marín A, Gräslund A. Liposome model systems to study the endosomal escape of cell-penetrating peptides: transport across phospholipid membranes induced by a proton gradient. *J Drug Deliv* 2011, 2011:897592.
 119. Funhoff AM, van Nostrum CF, Lok MC, Kruijtz JAW, Crommelin DJA, Hennink WE. Cationic poly-methacrylates with covalently linked membrane destabilizing peptides as gene delivery vectors. *J Control Release* 2005, 101:233–246.
 120. El-Sayed A, Khalil IA, Kogure K, Futaki S, Harashima H. Octaarginine- and octalysine-modified nanoparticles have different modes of endosomal escape. *J Biol Chem* 2008, 283:23450–23461.
 121. Evans BC, Nelson CE, Yu SS, Beavers KR, Kim AJ, Li H, Nelson HM, Giorgio TD, Duvall CL. Ex vivo red blood cell hemolysis assay for the evaluation of pH-responsive endosomolytic agents for cytosolic delivery of biomacromolecular drugs. *J Vis Exp* 2013:e50166. doi:10.3791/50166.
 122. Wilson JT, Keller S, Manganiello MJ, Cheng C, Lee C-C, Opara C, Convertine A, Stayton PS. pH-responsive nanoparticle vaccines for dual-delivery of antigens and immunostimulatory oligonucleotides. *ACS Nano* 2013, 7:3912–3925.
 123. Gujrati M, Malamas A, Shin T, Jin E, Sun Y, Lu ZR. Multifunctional cationic lipid-based nanoparticles facilitate endosomal escape and reduction-triggered cytosolic siRNA release. *Mol Pharm* 2014, 11:2734–2744.
 124. Tomlinson R, Klee M, Garrett S, Heller J, Duncan R, Brocchini S. Pendant chain functionalized polyacetals that display pH-dependent degradation: a platform for the development of novel polymer therapeutics. *Macromolecules* 2002, 35:473–480.
 125. Hu Y, Atukorale PU, Lu JJ, Moon JJ, Um SH, Cho EC, Wang Y, Chen J, Irvine DJ. Cytosolic delivery mediated via electrostatic surface binding of protein, virus, or siRNA cargos to pH-responsive core-shell gel particles. *Biomacromolecules* 2009, 10:756–765.
 126. Hu Y, Litwin T, Nagaraja R, Kwong B, Katz J, Watson N, Irvine DJ. Cytosolic delivery of membrane impermeable molecules in dendritic cells using pH responsive core-shell nanoparticles. *Nano Lett* 2007, 7:3056–3064.
 127. Bonner D, Leung C, Chen-Liang J, Chinghoza L, Langer R, Hammond PT. Intracellular trafficking of polyamidoamine - polyethylene glycol block copolymers in DNA delivery. *Bioconjugate* 2011, 22:1519–1525.
 128. Su X, Fricke J, Kavanagh D, Irvine DJ, Chase C. In vitro and in vivo mRNA delivery using lipid-enveloped pH-responsive polymer nanoparticles. *Mol Pharm* 2011, 8:774–787.
 129. Zhan X, Tran KK, Wang L, Shen H. Controlled endolysosomal release of agents by pH-responsive polymer blend particles. *Pharm Res* 2016, 32:2280–2291.
 130. Su X, Yang N, Wittrup KD, Irvine DJ. Synergistic antitumor activity from two-stage delivery of targeted toxins and endosome-disrupting nanoparticles. *Biomacromolecules* 2013, 14:1093–1102.
 131. Wang K, Hu Q, Zhu W, Zhao M, Ping Y, Tang G. Structure-invertible nanoparticles for triggered

- co-delivery of nucleic acids and hydrophobic drugs for combination cancer therapy. *Adv Funct Mater* 2015, 25:3380–3392.
132. Zeng Y, Cullen BR. RNA interference in human cells is restricted to the cytoplasm. *RNA* 2002, 8:855–860.
133. Zelphati O, Liang X, Hobart P, Felgner PL. Gene chemistry: functionally and conformationally intact fluorescent plasmid DNA. *Hum Gene Ther* 1999, 10:15–24.
134. Glover DJ, Leyton DL, Moseley GW, Jans DA. The efficiency of nuclear plasmid DNA delivery is a critical determinant of transgene expression at the single cell level. *J Gene Med* 2010, 12:77–85.
135. Abdallah B, Hassan A, Benoist C, Goula D, Behr JP, Demeneix B. A powerful nonviral vector for in vivo gene transfer into the adult mammalian brain: polyethylenimine. *Hum Gene Ther* 1996, 7:1947–1954.
136. Hatakeyama H, Ito E, Akita H, Oishi M, Nagasaki Y, Futaki S, Harashima H. A pH-sensitive fusogenic peptide facilitates endosomal escape and greatly enhances the gene silencing of siRNA-containing nanoparticles in vitro and in vivo. *J Control Release* 2009, 139:127–132.
137. Pollard H, Remy H-S, Loussouran G, Demolombe S, Behr J-P, Escande D. Polyethylenimine but Not Cationic Lipids Promotes Transgene Delivery to the Nucleus in Mammalian Cells. *J Biol Chem* 1998, 273:7507–7511.
138. Haensler J, Szoka FC Jr. Polyamidoamine cascade polymers mediate efficient transfection of cells in culture. *Bioconjug Chem* 1993, 4:372–379. doi:10.1021/bc00023a012.
139. Song YK, Liu F, Chu S, Liu D. Characterization of cationic liposome-mediated transfer in vivo by intravenous gene administration. *Hum Gene Ther* 1997, 8:1585–1594.
140. Wang Y, Gao S, Ye W-H, Yoon HS, Yang Y-Y. Co-delivery of drugs and DNA from cationic core-shell nanoparticles self-assembled from a biodegradable copolymer. *Nat Mater* 2006, 5:791–796.
141. Spagnou S, Miller AD, Keller M. Lipidic carriers of siRNA: differences in the formulation, cellular uptake, and delivery with plasmid DNA. *Biochemistry* 2004, 43:13348–13356.
142. Lee H, Lytton-Jean AKR, Chen Y, Love KT, Park AI, Karagiannis ED, Sehgal A, Querbes W, Zurenko CS, Jayaraman M, et al. Molecularly self-assembled nucleic acid nanoparticles for targeted in vivo siRNA delivery. *Nat Nanotechnol* 2012, 7:389–393.
143. Godbey WT, Wu KK, Mikos AG. Poly(ethylenimine)-mediated gene delivery affects endothelial cell function and viability. *Biomaterials* 2001, 22:471–480.
144. Balazs DA, Godbey W, Balazs DA, Godbey W. Liposomes for use in gene delivery. *J Drug Deliv* 2011, 2011:1–12.
145. Cullis PR, Hope MJ, Tilcock CPS. Lipid polymorphism and the roles of lipids in membranes. *Chem Phys Lipids* 1986, 40:127–144.
146. Farhood H, Serbina N, Huang L. The role of dioleoyl phosphatidylethanolamine in cationic liposome mediated gene transfer. *Biochim Biophys Acta* 1995, 1235:289–295.
147. Zhou X, Huang L. DNA transfection mediated by cationic liposomes containing lipopolylysine: characterization and mechanism of action. *Biochim Biophys Acta* 1994, 1189:195–203.
148. Deshpande MC, Davies MC, Garnett MC, Williams PM, Armitage D, Bailey L, Vamvakaki M, Armes SP, Stolnik S. The effect of poly(ethylene glycol) molecular architecture on cellular interaction and uptake of DNA complexes. *J Control Release* 2004, 97:143–156.
149. Harvie P, Wong FMP, Bally MB. Use of poly (ethylene glycol)-lipid conjugates to regulate the surface attributes and transfection activity of lipid-DNA particles. *J Pharm Sci* 2000, 89:652–663.
150. Song LY, Ahkong QF, Rong Q, Wang Z, Ansell S, Hope MJ, Mui B. Characterization of the inhibitory effect of PEG-lipid conjugates on the intracellular delivery of plasmid and antisense DNA mediated by cationic lipid liposomes. *Biochim Biophys Acta* 2002, 1558:1–13.
151. Remaut K, Lucas B, Braeckmans K, Demeester J, De Smedt SC. Pegylation of liposomes favours the endosomal degradation of the delivered phosphodiester oligonucleotides. *J Control Release* 2007, 117:256–266.
152. Choi JS, Mackay JA, Szoka FC. Low-pH-sensitive PEG-stabilized plasmid-lipid nanoparticles: preparation and characterization. *Bioconjug Chem* 2003, 14:420–429.
153. Kirpotin D, Hong K, Mullah N, Papahadjopoulos D, Zalipsky S. Liposomes with detachable polymer coating: destabilization and fusion of dioleoylphosphatidylethanolamine vesicles triggered by cleavage of surface-grafted poly (ethylene glycol). *FEBS Lett* 1996, 388:115–118.
154. Kuai R, Yuan W, Qin Y, Chen H, Tang J, Yuan M, Zhang Z, He Q. Efficient delivery of payload into tumor cells in a controlled manner by TAT and thiolytic cleavable PEG. *Mol Pharm* 2010, 7:1816–1826.
155. Meyer O, Kirpotin D, Hong K, Sternberg B, Park JW, Woodle MC, Papahadjopoulos D. Cationic liposomes coated with polyethylene glycol as carriers for oligonucleotides. *J Biol Chem* 1998, 273:15621–15627.
156. Zhong Z, Zheng M, Zhong Z, Zhou L, Meng F, Peng R. Poly(ethylene oxide) grafted with short polyethylenimine gives DNA polyplexes with superior colloidal stability, low cytotoxicity, and potent in vitro gene transfection under serum conditions. *Biomacromolecules* 2012, 13:881–888.

157. Wu H, Zhu L, Torchilin VP. pH-sensitive poly(histidine)-PEG/DSPE-PEG co-polymer micelles for cytosolic drug delivery. *Biomaterials* 2013, 34:1213–1222.
158. Zhao ZX, Gao SY, Wang JC, Chen CJ, Zhao EY, Hou WJ, Feng Q, Gao LY, Liu XY, Zhang LR, et al. Self-assembly nanomicelles based on cationic mPEG-PLA-b-polyarginine(R15) triblock copolymer for siRNA delivery. *Biomaterials* 2012, 33:6793–6807.
159. Kodama Y, Yatsugi Y, Kitahara T, Kurosaki T, Ega-shira K, Nakashima M, Muro T, Nakagawa H, Higuchi N, Nakamura T, et al. Quaternary complexes modified from pDNA and poly-L-lysine complexes to enhance pH-buffering effect and suppress cytotoxicity. *J Pharm Sci* 2015, 104:1470–1477.
160. Mura S, Nicolas J, Couvreur P. Stimuli-responsive nanocarriers for drug delivery. *Nat Mater* 2013, 12:991–1003.
161. Oishi M, Nagasaki Y. Synthesis, characterization, and biomedical applications of core-shell-type stimuli-responsive nanogels—nanogel composed of poly[2-(N,N-diethylamino)ethyl methacrylate] core and PEG tethered chains. *React Funct Polym* 2007, 67:1311–1329.
162. Wong ASM, Mann SK, Czuba E, Sahut A, Liu H, Suekama TC, Bickerton T, Johnston AP, Such GK. Self-assembling dual component nanoparticles with endosomal escape capability. *Soft Matter* 2015, 11:2993–3002. doi:10.1039/c5sm00082c.
163. Kongkatigumjorn N, Cortez-Jugo C, Czuba E, Wong ASM, Hodgetts RY, Johnston APR, Such GK. Probing endosomal escape using pHlexi nanoparticles. *Macromol Biosci*. Submitted for publication. doi:10.1002/mabi.201600248.
164. Gallon E, Matini T, Sasso L, Mantovani G, Armiñan de Benito A, Sanchis J, Caliceti P, Alexander C, Vicent MJ, Salmaso S. Triblock copolymer nanovesicles for pH-responsive targeted delivery and controlled release of siRNA to cancer cells. *Biomacromolecules* 2015, 16:1924–1937.
165. Suma T, Miyata K, Anraku Y, Watanabe S, Christie RJ, Takemoto H, Shioyama M, Gouda N, Ishii T, Nishiyama N, et al. Smart multilayered assembly for biocompatible siRNA delivery featuring dissolvable silica, endosome-disrupting polycation, and detachable PEG. *ACS Nano* 2012, 6:6693–6705.
166. Dual AB, Zou Y, Wang Y, Huang X, Huang G, Sumer BD, Boothman D, Gao J. Overcoming endosomal barrier by amphotericin B-loaded dual pH-responsive PDMA-b-PDPA micelleplexes for siRNA delivery. *ACS Nano* 2011, 5:9246–9255.
167. Zhou K, Wang Y, Huang X, Luby-Phelps K, Sumer BD. Tunable ultrasensitive pH-responsive nanoparticles targeting specific endocytic organelles in living cells. *Angew Chemie Int Ed* 2011, 50:6109–6114.
168. Appelbaum JS, Larochelle JR, Smith BA, Balkin DM, Holub JM, Schepartz A. Arginine topology controls escape of minimally cationic proteins from early endosomes to the cytoplasm. *Chem Biol* 2012, 19:819–830.
169. Pantos A, Tsogas I, Paleos CM. Guanidinium group: a versatile moiety inducing transport and multicompartmentalization in complementary membranes. *Biochim Biophys Acta* 2008, 1778:811–823.
170. Romani B, Engelbrecht S, Glashoff RH. Functions of Tat: the versatile protein of human immunodeficiency virus type 1. *J Gen Virol* 2010, 91:1–12.
171. Erazo-Oliveras A, Muthukrishnan N, Baker R, Wang T-Y, Pellois J-P. Improving the endosomal escape of cell-penetrating peptides and their cargos: strategies and challenges. *Pharmaceuticals* 2012, 5:1177–1209.
172. Sakurai Y, Hatakeyama H, Sato Y, Akita H, Takayama K, Kobayashi S, Futaki S, Harashima H. Endosomal escape and the knockdown efficiency of liposomal-siRNA by the fusogenic peptide shGALA. *Biomaterials* 2011, 32:5733–5742.
173. Li M, Tao Y, Shu Y, LaRochelle JR, Steinauer A, Thompson D, Schepartz A, Chen Z-Y, Liu DR. Discovery and characterization of a peptide that enhances endosomal escape of delivered proteins in vitro and in vivo. *J Am Chem Soc* 2015, 137:14084–14093.
174. Liang K, Richardson JJ, Ejima H, Such GK, Cui J. Peptide-tunable drug cytotoxicity via one-step assembled polymer nanoparticles. *Adv Mater* 2014, 26:2398–2402.

1.4 Purpose of the Research

Gaining insight into how materials interact with biological systems is difficult with currently available techniques. The aim of this thesis was to design a set of tools to examine the processing of nanomaterials and proteins by cells. The collection of methods was developed to be applicable to nanomaterial scientists, as well as to be useful in answering fundamental questions in the biological sciences. The aims and objectives of the individual experimental projects included:

Chapter 2. HD Flow Cytometry: An Improved Way to Quantify Cellular Interactions with Nanoparticles

- To enhance analysis of flow cytometry data generated through fluorescence-based assays by using a deconvolution algorithm that identifies negative cells within fluorescence histograms

Chapter 3. Quantifying Cellular Internalisation with a Fluorescent Click Sensor

- To develop a sensor for quantifying internalisation in cells by using a click chemistry pair to quench extracellular fluorescence.

Chapter 4. SNAP_{Switch}: A Molecular Sensor to Quantify Cytosolic Delivery and Cellular Localisation

- To produce a sensor that enables localisation to be quantified in live cells by synthesising a quenched and attachable substrate that becomes fluorescent when in proximity to the SNAP-tag enzyme.

Chapter 5. Oligonucleotide Switches for Quantifying Endosomal Escape Efficiency

- To improve detection of endosomal escape by using a DNA sequence that becomes fluorescent in response to an endogenous mRNA present in the cytosol.

Chapter 2. HD Flow Cytometry: An Improved Way to Quantify Cellular Interactions with Nanoparticles

2.1 Summary

Flow cytometry is used extensively to study the association of fluorescently labelled nanoparticles and proteins with cells. The results are most often presented as two numerical values: percent of positive cells and the mean fluorescence intensity. Positive cells are generally identified as those with a fluorescence intensity above the top 1-2% of the control cells. However, weak fluorescence of nanoparticles and low binding causes the fluorescence histogram of the treated cells to significantly overlap with that of the control cells, leading to an underestimation of the percentage of positive cells. In addition, the binding of material to a sub-population of cells results in an underestimation of the true response when the mean is presented. Like blurring in microscopy, the mathematical operation of convolution changes the true signal from the cells due to cellular autofluorescence and noise from the flow cytometer. This chapter describes the development and demonstration of a script based on the Richardson-Lucy deconvolution algorithm to improve flow cytometry data analysis. By deconvolving histograms, the positive cells can be identified with more precision. This improves percent positive estimations and allows the mean fluorescence intensity of positive cells to be evaluated while displaying the underlying distribution of the cells.

HD Flow Cytometry: An Improved Way to Quantify Cellular Interactions with Nanoparticles

Laura I. Selby, Nachnicha Kongkatigumjorn, Georgina K. Such,
and Angus P. R. Johnston*

Quantifying the interactions of nanoparticles with cells is critical to engineering better drug delivery systems. Flow cytometry is a valuable tool for analyzing these interactions,^[1–6] however it can be hindered by the binding of a low number of nanoparticles or by weak nanoparticle fluorescence, resulting in only a small shift in the intensity of the cells. Here, we present a new technique (histogram deconvolution – HD Flow) to improve the analysis of flow cytometry data that allows the detection of interactions that would typically be lost in the background noise.

Flow cytometry offers the ability to rapidly quantify the fluorescence intensity and scatter properties of thousands of individual cells in a high throughput fashion.^[7,8] The association of nanoparticles or proteins with cells is commonly analyzed with a histogram overlay of treated and untreated samples. Quantification of the change in cell fluorescence is typically based on the mean fluorescence intensity (MFI) and/or the percent of cells that have a fluorescence signal above the background of untreated cells.^[9,10] The simplest approach to obtain the percent of positive cells is to subjectively or automatically apply a threshold whereby all cells higher than the threshold are counted as positive.^[11] Typically this threshold is set at a value where less than 1% of the untreated cells are identified as positive. However, when the fluorescence signal is weak, the treated and untreated histograms can overlap. This makes it difficult to differentiate positive from negative cells, which causes a significant underestimate of the true value (Figure 1a).^[12] When the separation between the treated and untreated samples is low, MFI is often used to determine the extent of the interaction. A limitation of this approach is that it assumes that 100% of the cells have interacted with the nanoparticles or protein, whereas in reality the interaction may only occur for a subset of the cells. The use of MFI on histograms containing multiple populations is not strictly correct and lowers the MFI due to the presence of the negative cells.

Several methods have been proposed to improve the analysis of flow cytometry data. These include mathematical modeling^[13]

or Overton subtraction^[14] and super-enhanced maximum absolute difference (SEDymax),^[15] which are included in commercially available flow cytometry packages such as FlowJo. While these techniques can aid the interpretation of flow cytometry data, they are only rarely used for nanoparticle analysis. They also have some inherent limitations such as subtraction underestimating the number of positive cells when overlapping data is analyzed^[16] and mathematical modeling methods being difficult to implement.^[17]

Here we report the use of a histogram deconvolution (HD Flow) algorithm to analyze heterogeneous cell samples with overlapping fluorescence distributions. Using this technique, we have demonstrated the ability to accurately quantify the number of positive cells while also determining the MFI and displaying a fluorescence histogram of the underlying positive population. By applying HD Flow to data generated from a nanoparticle association assay, we can obtain information about nanoparticle/cell association that would otherwise be missed. We anticipate HD Flow will be broadly applicable to both materials scientists and cell biologists and allow for significantly improved analysis of bio-interactions by flow cytometry.

The overlapping of cell populations in flow cytometry data sets is analogous to the blurring of a fluorescence microscopy image.^[18,19] In mathematical terms, the distribution of fluorescence signal measured by the flow cytometer (g) can be considered as the actual signal (f) convolved by a point spread function (h) (Equation (1)).^[20] The point spread function in this case is a combination of the heterogeneous distribution of autofluorescence of the cells combined with the noise of the flow cytometer, and can be easily determined by measuring the fluorescence of untreated cells on the flow cytometer. Of the numerous methods for deconvolution that exist, the Richardson–Lucy^[21,22] algorithm is recognized for its uses across many scientific disciplines.^[23]

$$g = f \otimes h \quad (1)$$

$$f^{n+1} = f^n \left(\hat{h} \otimes \frac{g}{f^n \otimes h} \right) \quad (2)$$

The iterative deconvolution approach (Equation (2))^[24] requires the raw flow cytometry data to be divided into equal bins and uses this as the initial estimate for input to HD flow. This is then convolved with distribution of untreated cells and compared to the original test data as a ratio. The estimate is updated by convolution of the ratio with the complex conjugate of the original data. All negative values and the last ten bins of

L. I. Selby, Dr. A. P. R. Johnston
Drug Delivery, Disposition and Dynamics
Monash Institute of Pharmaceutical Sciences
Monash University
Parkville, Victoria 3052, Australia
E-mail: angus.johnston@monash.edu
N. Kongkatigumjorn, Dr. G. K. Such
Department of Chemistry
The University of Melbourne
Parkville, Victoria 3010, Australia



DOI: 10.1002/adhm.201600445

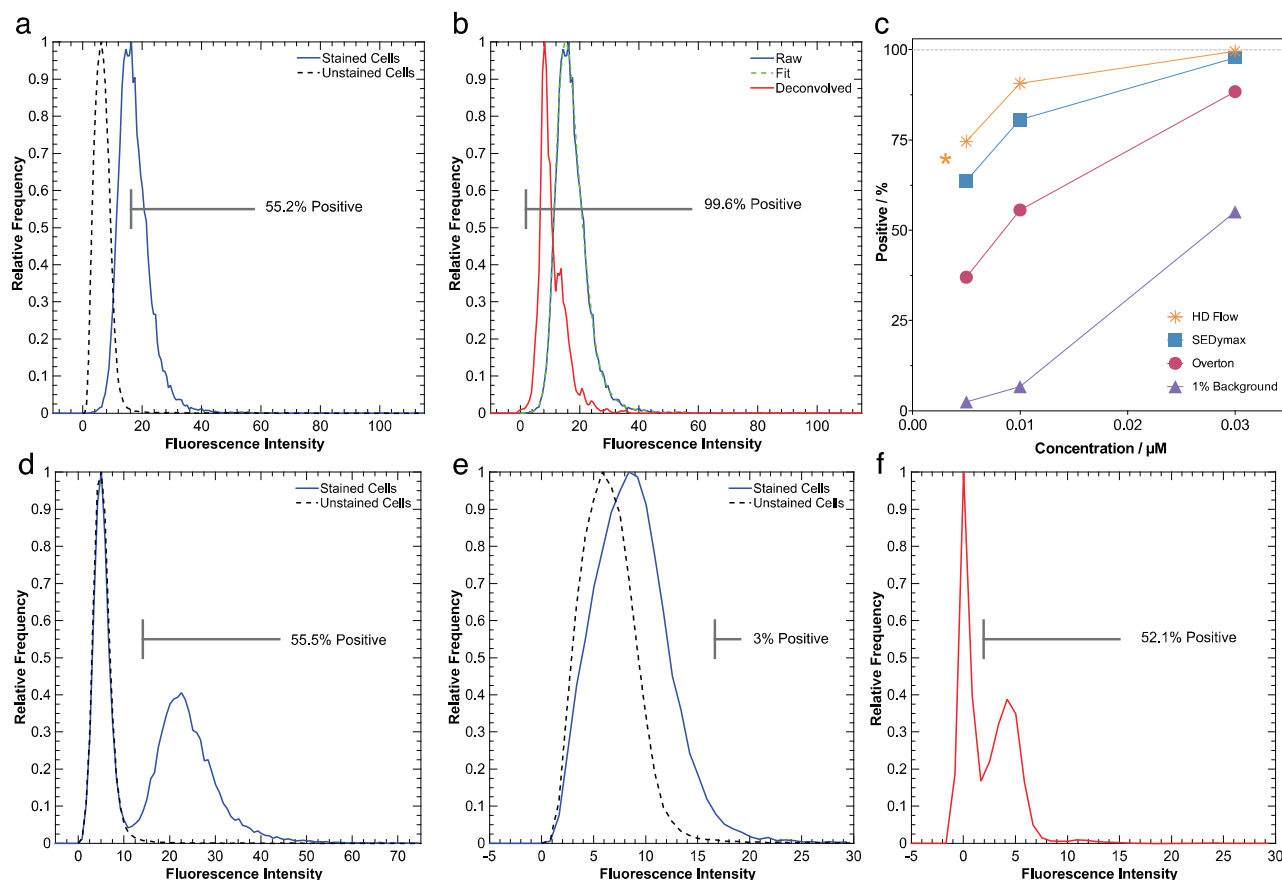


Figure 1. Comparison of analysis techniques and demonstration of histogram deconvolution. a) Spillover fluorescence of C1R cells incubated with 3×10^{-8} M CTO and b) deconvolution of the same data shows HD-flow corrects for autofluorescence showing over 99% of cells are positive. c) Analysis of increasing CellTracker Orange (CTO) concentrations demonstrates HD flow (*) out performs conventional 1% thresholding (\blacktriangle), Overton subtraction (\bullet) and SEDymax (\blacksquare) in the percent of positive cells for the spillover channel. C1R cells incubated with 1×10^{-8} M CellTracker manually mixed with unstained cells in a 1:1 ratio generates a bimodal distribution in (d,e) the maximum fluorescence channel that is concealed in (e) the spillover channel. f) Deconvolving the spillover fluorescence data restores exposes both populations. Gates show the percent positive calculated by 1% of background thresholding (a, d, and e) and HD Flow (b,f). Deconvolution parameters: Range = 0–250, bins = 300, iterations = 250, negative shift = 10 (a–c) and 5 (d–e), smoothing = false. *Indicates shift too small to accurately determine the positive population.

the histogram are set to zero to avoid high frequency noise due to the circular nature of fast Fourier transforms. The process is then repeated with the updated estimate for the set number of iterations (n).

To calculate the percent of positive cells, a cut-off threshold must be set that designates cells below that value as negative. We have defined the threshold value by deconvolving three untreated control samples against each other and determining the point where 99% of the control cells are below the threshold value.

To ensure HD Flow is robust and to determine its sensitivity, one of the untreated control samples was shifted until the algorithm was able to identify that 99% of the shifted sample was positive compared to the unshifted controls. This value was considered to be the minimum shift detectable by HD Flow. Data from the untreated control cells are combined and deconvolution is repeated with each sample against the combined control. The MFI of the positive cells in each deconvolved data set are compared to this minimum shift. If the MFI was less than the minimum shift, HD Flow cannot confidently determine the

percent of positive cells and the reported value is likely to be an underestimate of the true value. This prevents calculations for when the degree of overlap between the test and control histograms is too high for accurate quantification (Figure S1a,b, Supporting Information). Once corrected for autofluorescence, the percent positive and mean fluorescence intensity are written to a file and a histogram of the test data is displayed.

To evaluate the validity of HD Flow for calculating the percent of positive cells, we compared it to the commonly used manual thresholding approach, as well as SEDymax and Overton subtraction available in the commercially available FlowJo software package. In order to compare methods, data sets where the actual percent positive value is known are required. Avoiding artificially generated data sets is desirable, as performance on simulations may not translate to real data sets.^[25] Test data with $\approx 100\%$ positive cells and peaks well-separated from the untreated control data sets were generated using the fluorescent stain CellTracker Orange (CTO) and analyzed by the fluorescence intensity in the 565–595 nm channel. The shift from the control was adjusted by altering the concentration of

Table 1. Comparison of methods for percent of positive cells and MFI calculated with different methods. Actual percent positive value and the true MFI of the positive cells were determined by gating cells using linear side-scatter area versus log 565–595 nm channel where the positive and negative populations are well-separated. Analysis of the spillover fluorescence channel (661–690 nm) allows for comparison of HD Flow to Overton subtraction, SEDymax and 1% thresholding for overlapped stained and unstained histograms.

Concentration [μM]	Gated positive [%]	HD flow ^{a)} [%]	SEDymax [%]	Overton subtraction [%]	1% of background thresholding [%]	True MFI	MFI of ungated	HD flow MFI
0.03	99.9	99.7	97.7	88.4	51.0	10.5	10.5	10.8
	55.6	56.0	54.3	47.8	24.8	9.71	4.31	9.81
	13.2	13.9	13.5	11.5	5.44	8.71	0.80	8.63
0.01	99.7	92.1	80.6	55.6	5.60	4.31	4.21	4.64
	56.6	51.9	45.1	20.0	2.96	4.31	1.99	4.25
	12.1	8.85	9.31	6.14	1.08	3.81	0.34	4.06

^{a)}Deconvolution parameters: range = 0–250, bins = 300, iterations = 250, negative shift = 10, smoothing = false.

the stain in the incubation media (Figure S2a–c, Supporting Information). To investigate the ability of HD Flow to distinguish overlapped populations, we used the spillover fluorescence measured from the 661–690 nm channel (Figure 1a), which has a significantly reduced signal. This results in the histogram of the treated cells overlapping with untreated cells (Figure S2d–f, Supporting Information). The maximum and spillover fluorescence data sets are generated from the same cells so consequently have the same percentage of positive cells. As calculation of the true percent positive from separated histograms is straightforward through applying a gate to positive cells, this value can be used to compare with the results calculated by HD Flow.

HD Flow requires two key input parameters that are dependent on the nature of the data set before initiating calculations; number of iterations and bin size. We manipulated these parameters using data generated from the highest concentration of CTO to observe the effect on the calculated percent positive value and graphical output (see Supporting Information). If the bin size is too large, the resolution of the deconvolved data set will not be sufficient to distinguish between small shifts in the population. However, if the bin size is too small, there will be significant noise in the deconvolved histograms. Similarly, performing too many iterations also increases the noise in the deconvolved histograms. Typically 250 iterations are sufficient to deconvolve the data set without introducing excessive noise. The algorithm takes less than a second to process a standard flow cytometry data file. The noise introduced does not typically affect the percent of positive cells or the mean fluorescence intensity, and can be suppressed by introducing a Gaussian smoothing factor if required.

Having identified the necessary parameters for HD Flow, we moved to demonstrating the advantage of HD Flow over conventional analysis methods. Agreement between results generated using HD Flow and the true percent of positive cells determined through gating confirms the ability of the algorithm to accurately calculate the percent of positive cells for monomodal stained distributions when well-separated (Figure S8, Supporting Information) and overlapped (Figure 1a–c). When the treated and untreated histograms are overlapped, HD Flow performs better than the three alternative methods by determining a percent of positive cells over 92% for the two highest CTO concentrations (Figure 1c). Thresholding has the lowest

accuracy and provides a value of only 52.4% at the highest stain concentration in spillover analysis. HD Flow also indicates that the degree of overlap is too high for accurate calculations at 5×10^{-9} M, information which is not provided by the other methods and suggests that fluorescence spillover generated from this lowest concentration (Figure S2d, Supporting Information) is below the detection limit of all the techniques.

HD Flow is able to restore the ability to visualize multiple populations that would otherwise be concealed within one peak. By mixing 1×10^{-8} M stained cells with unstained cells in a 1:1 ratio, a distribution with two populations was generated with 56.6% of positive cells (Figure 1d). Viewing spillover fluorescence data shows the collapse of the two populations into one broad peak (Figure 1e) and 1% of background thresholding underestimates the percent positive as 3%, as does Overton (20%) and SEDymax (45.1%). HD Flow is able to reveal the two underlying populations (Figure 1f) and significantly improves the estimation of the percent of positive cells (52.1%). HD Flow is also capable of analyzing samples with three populations, however the population with highest fluorescence appeared as a shoulder rather than a distinct peak (Figure S9c, Supporting Information). The ability of the algorithm to identify multiple populations is governed by the full width half maximum of the deconvolved populations, the shift between the different populations, and the relative number of cells in each population. There is no theoretical limit to the number of populations that could be identified. HD Flow's ability to uncover concealed populations demonstrates how fluorescent histograms can conceal the composition of the sample and that conventional methods are not satisfactory for determining the percent positive value when the fluorescence of the positive population is low.

Table 1 summarizes the performance of the four analysis techniques on samples with manually mixed ratios of stained and unstained cells to generate multiple populations (Figure 1e; Figure S10c,d, Supporting Information). Comparing results from the spillover data shows HD Flow performs better than SEDymax, Overton subtraction and 1% of background thresholding. Spillover based calculations for the 1×10^{-8} M CTO stain are within 8% of the true value for HD Flow while SEDymax and Overton subtraction values were underestimated by up to 19% and 44%, respectively. All methods vastly exceed conventional 1% of background threshold method that underestimated the correct value by 94%.

HD Flow also allows the calculation of the MFI of the positive cells within the distribution, a statistic that is useful to determine the amount of association rather than just if association occurred. This provides additional information about the interactions of the material with cells, such as concentration- or time-dependent biological effects as assessed through an increase or decrease in the MFI. However, the MFI data are only useful if applied to the population of cells with material

bound, and give inaccurate results when the positive and negative distributions are overlapped. Since HD Flow is able to identify the positive cells within the sample, it is also able to provide a MFI of these cells. To demonstrate this, we used the maximum fluorescence channel to apply a gate to the positive cells of the manually mixed samples and calculated the MFI in the spillover channel to obtain the true MFI of the positive cells when overlapped with unstained cells. This was compared

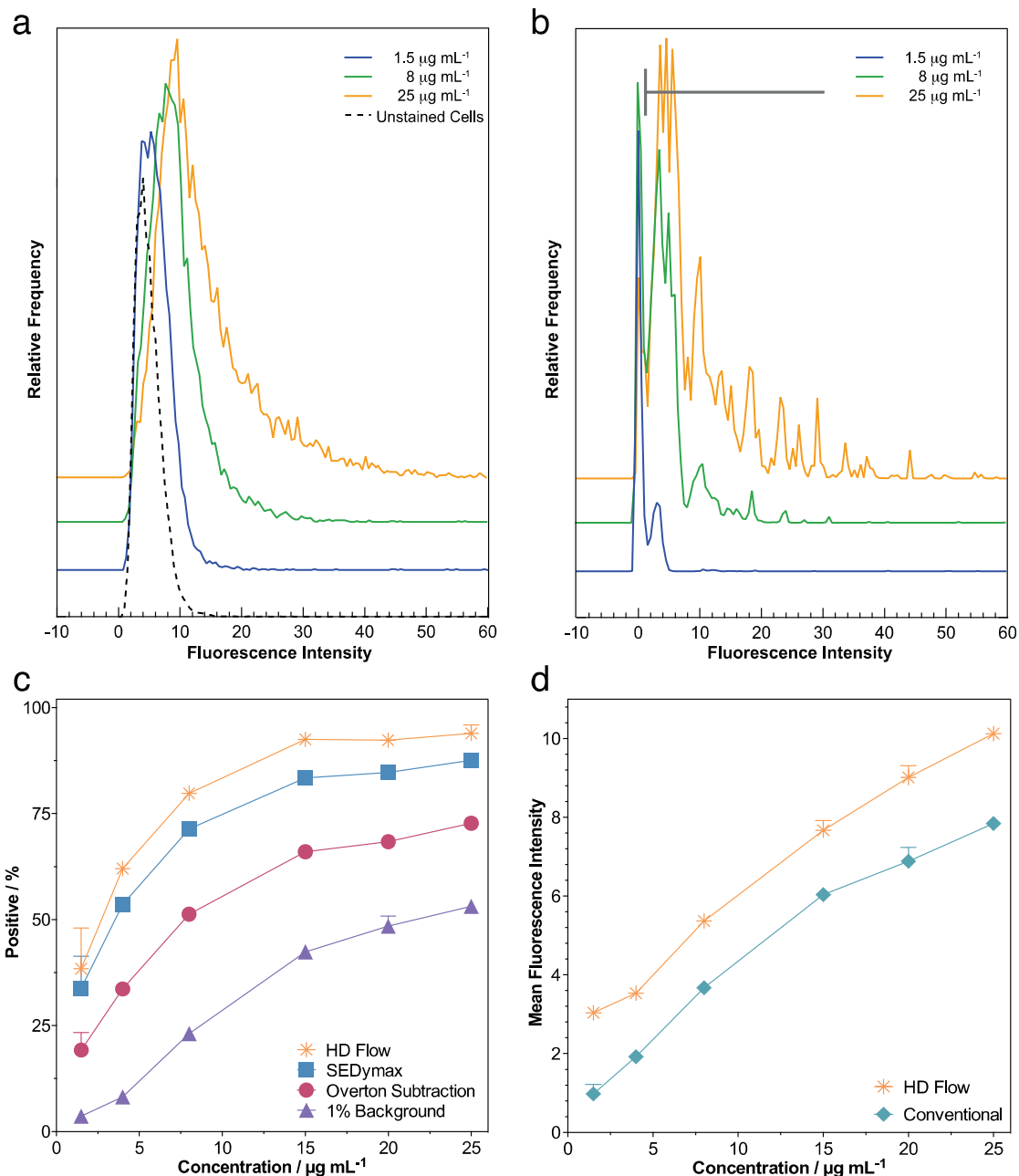


Figure 2. Association dependence on nanoparticle concentration. 150 nm nanoparticles labeled with Cy5 were incubated with 3T3 cells in concentrations ranging from 0 to 25 $\mu\text{g mL}^{-1}$. Fluorescence histogram of the a) raw and b) deconvoluted data for cells incubated with 1.5 (blue), 8 (green), and 25 $\mu\text{g mL}^{-1}$ (yellow) particles. c) Comparison of percent positive calculation by HD Flow (*), SEDymax (■), Overton subtraction (●), and 1% threshold (▲) performed in duplicate. d) Mean fluorescence intensity calculated by HD Flow (*) and using conventional flow analysis with the MFI (◆) of the unstained cells subtracted from the calculated MFI. Deconvolution parameters: Range = 0–200, bins = 400, iterations = 250, negative shift = 10, smoothing = false.

with the MFI calculated with no gate and using HD Flow (Table 1). As the cells within the positive population of the manually mixed samples originate from the pure samples, the MFI of the positive population is expected to be similar regardless of the ratio the stained cells were mixed with unstained cells. HD Flow accurately recovered the MFI of the positive cells in heavily overlapped distributions within 10% of the value calculated using the gated cells. The importance of this is exemplified by comparison to the MFI calculation applied to the entire distribution. The true MFI for the 3×10^{-8} M sample with 90% unstained cells is 8.71 and HD Flow calculates it as 8.63, the ungated calculation returns a significantly lower value of 0.80. As such, HD Flow can be used to compute the MFI in overlapped distributions containing high levels of negative cells.

As HD Flow is better than the existing techniques for recovering the percent of positive cells and is able to give a robust MFI for the positive population in mixed populations of cells, we moved to analyzing data generated through a nanoparticle association with cells. Fluorescently labeled nanoparticles were added to wild-type mouse fibroblasts (3T3-WT) at concentrations ranging from 1.5 to 25 $\mu\text{g mL}^{-1}$ to increase the amount of association. The subsequent fluorescent histograms significantly overlapped with the untreated cells at these concentrations with the highest amount of overlap seen at the lowest concentration of nanoparticles (Figure 2a). In accordance with the CTO results, calculated percent positive values for the nanoparticle association experiment via HD Flow were higher than 1% of background thresholding, Overton subtraction and SEDymax analysis (Figure 2c). HD Flow also provides a histogram of the corrected distribution (Figure 2b), enabling the population distribution to be visualized. The percent of cells with nanoparticles associated across the concentration range was shown by HD Flow to increase from an average of 38% at the lowest concentration through to a maximum of 94% at the highest concentration. Visualizing the histograms, along with HD Flow's built in test for determining the minimum shifts that can be accurately determined, gives confidence to infer that at the lowest concentrations of particles only a subset of the cells have interacted. Overton and SEDymax, underestimate the association of nanoparticles by 19% and 5%, respectively, and do not indicate if the low levels of association are real, or an artifact of the small population shift. If a 1% of background threshold was used, a change of only 3.5% to 52% association was observed, greatly underestimating the true level of association. Furthermore, since these samples are not artificially overlapped and the fluorescence is already measured in the maximum fluorescence channel, the MFI cannot be determined by gating positive cells. The MFI of the positive population can be obtained through HD Flow (Figure 2d). Using standard methods, the MFI of the 1.5 $\mu\text{g mL}^{-1}$ sample is only 0.98 while the MFI of the positive population as calculated by HD Flow is 3.04. As there is usually a concentration-dependence on cell viability,^[26] knowledge of the minimum amount of material required to illicit a biological response is desirable. Using HD Flow allows for a better understanding of the interactions of nanoparticles with cells by exposing changes otherwise hidden due to low fluorescence.

Objective and accurate methods for calculating the percent of positive cells from overlapped populations of cells is critical to

understand the interactions of nanoparticles with cells. Simple thresholding analysis significantly underestimates the extent of the nanoparticle interactions with cells, and while commercially available flow cytometry software packages offer improved methods, they still underestimate the extent of interaction. We have developed a simple algorithm that accurately calculates the percent of positive cells and the MFI of the positive population. We have demonstrated the application of this algorithm to data from real nanoparticle association experiments, and shown nanoparticle association is higher than determined by existing methods. A standalone application along with the matlab source code is available for download from www.nanomb.org. We believe HD Flow will be of significant use for the nanoparticle delivery field and will also find use in a wide range of applications beyond nanoparticle/cell interactions, including identifying rare populations of cells and measuring small changes in gene expression.

Supporting Information

Supporting Information is available from the Wiley Online Library or from the author.

Received: April 20, 2016

Revised: June 2, 2016

Published online: July 5, 2016

- [1] B. G. De Geest, M. A. Willart, H. Hammad, B. N. Lambrecht, C. Pollard, P. Bogaert, M. De Filette, X. Saelens, C. Vervaet, J. P. Remon, J. Grooten, S. De Koker, *ACS Nano* **2012**, *6*, 2136.
- [2] S. R. Abulateefeh, S. G. Spain, K. J. Thurecht, J. W. Aylott, W. C. Chan, M. C. Garnett, C. Alexander, *Biomater. Sci.* **2013**, *1*, 434.
- [3] S. K. Hamilton, A. L. Sims, J. Donovan, E. Harth, *Polym. Chem.* **2011**, *2*, 441.
- [4] A. Elbakry, E. C. Wurster, A. Zaky, R. Liebl, E. Schindler, P. Bauer-Kreisel, T. Blunk, R. Rachel, A. Goepferich, M. Breunig, *Small* **2012**, *8*, 3847.
- [5] J. D. Mintern, C. Percival, M. M. J. Kamphuis, W. J. Chin, F. Caruso, A. P. R. Johnston, *Adv. Healthcare Mater.* **2013**, *2*, 940.
- [6] R. C. Luo, B. Neu, S. S. Venkatraman, *Small* **2012**, *8*, 2585.
- [7] M. Rieseberg, C. Kasper, K. F. Reardon, T. Scheper, *Appl. Microbiol. Biotechnol.* **2001**, *56*, 350.
- [8] N. Aghaepour, G. Finak, H. Hoos, T. R. Mosmann, R. Brinkman, R. Gottardo, R. H. Scheuermann, *Nat. Methods* **2013**, *10*, 228.
- [9] M. Ahmed, P. Wattanaarsakit, R. Narain, *Polym. Chem.* **2013**, *4*, 3829.
- [10] V. Gajbhiye, L. Escalante, G. Chen, A. Laperle, Q. Zheng, B. Steyer, S. Gong, K. Saha, *Nanoscale* **2014**, *6*, 521.
- [11] E. Lugli, M. Roederer, A. Cossarizza, *Cytom. Part A* **2010**, *77*, 705.
- [12] L. T. Nguyen, D. Wong, M. Ramanathan, *J. Immunol. Methods* **2000**, *238*, 151.
- [13] F. Lampariello, A. Aiello, *Cytometry* **1998**, *32*, 241.
- [14] W. R. Overton, *Cytometry* **1988**, *9*, 619.
- [15] C. Bagwell, *Clin. Immunol. Newsletter* **1996**, *16*, 1.
- [16] T. L. Sladek, J. W. Jacobberger, *Cytometry* **1993**, *14*, 23.
- [17] F. Lampariello, *Cytometry Part A* **2009**, *75*, 665.

- [18] J. P. Corsetti, S. V. Sotirchos, C. Cox, J. W. Cowles, J. F. Leary, N. Blumberg, *Cytometry* **1988**, 9, 539.
- [19] J. G. McNally, T. Karpova, J. Cooper, J. A. Conchello, *Methods* **1999**, 19, 373.
- [20] D. S. C. Biggs, *Curr. Protoc. Cytom.* **2010**, 12.19, 12.19.1.
- [21] W. H. Richardson, *J. Opt. Soc. Am.* **1972**, 62, 55.
- [22] L. B. Lucy, *Astron. J.* **1974**, 79, 745.
- [23] M. Prato, R. Cavicchioli, L. Zanni, P. Boccacci, M. Bertero, *Astron. Astrophys.* **2012**, 539, A133.
- [24] H. L. Yang, P. H. Huang, S. H. Lai, *Signal Process.* **2014**, 103, 399.
- [25] W. Wallace, L. H. Schaefer, J. R. Swedlow, *Biotechniques* **2001**, 31, 1076.
- [26] A. S. M. Wong, S. K. Mann, E. Czuba, A. Sahut, H. Liu, T. C. Suekama, T. Bickerton, A. P. R. Johnston, G. K. Such, *Soft Matter* **2015**, 11, 2993.
-

**ADVANCED
HEALTHCARE
MATERIALS**

Supporting Information

for *Adv. Healthcare Mater.*, DOI: 10.1002/adhm.201600445

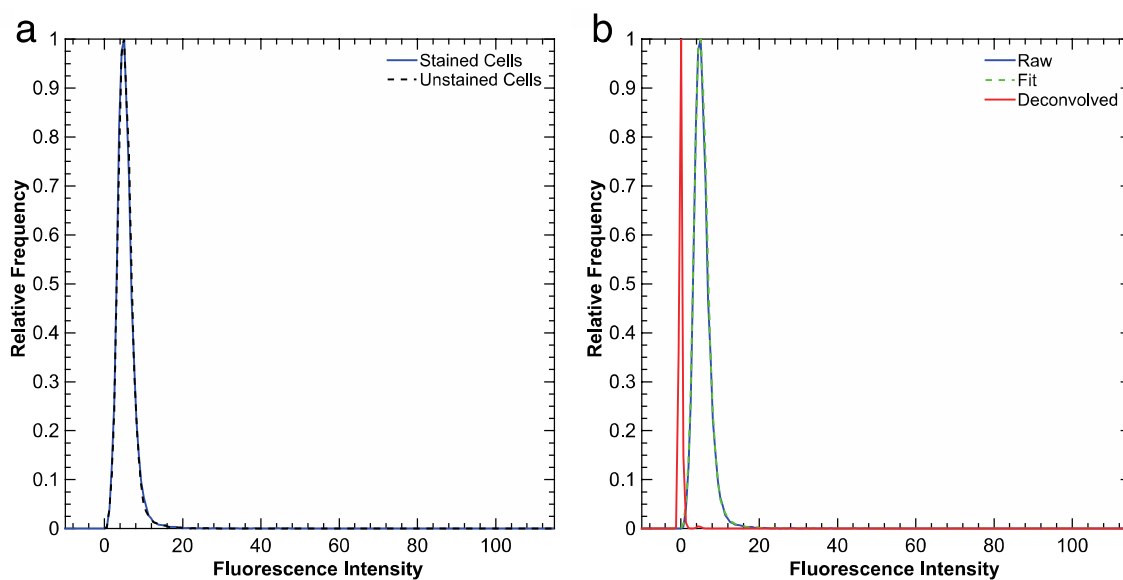
HD Flow Cytometry: An Improved Way to Quantify Cellular Interactions with Nanoparticles

*Laura I. Selby, Nachnicha Kongkatigumjorn, Georgina K. Such, and Angus P. R. Johnston**

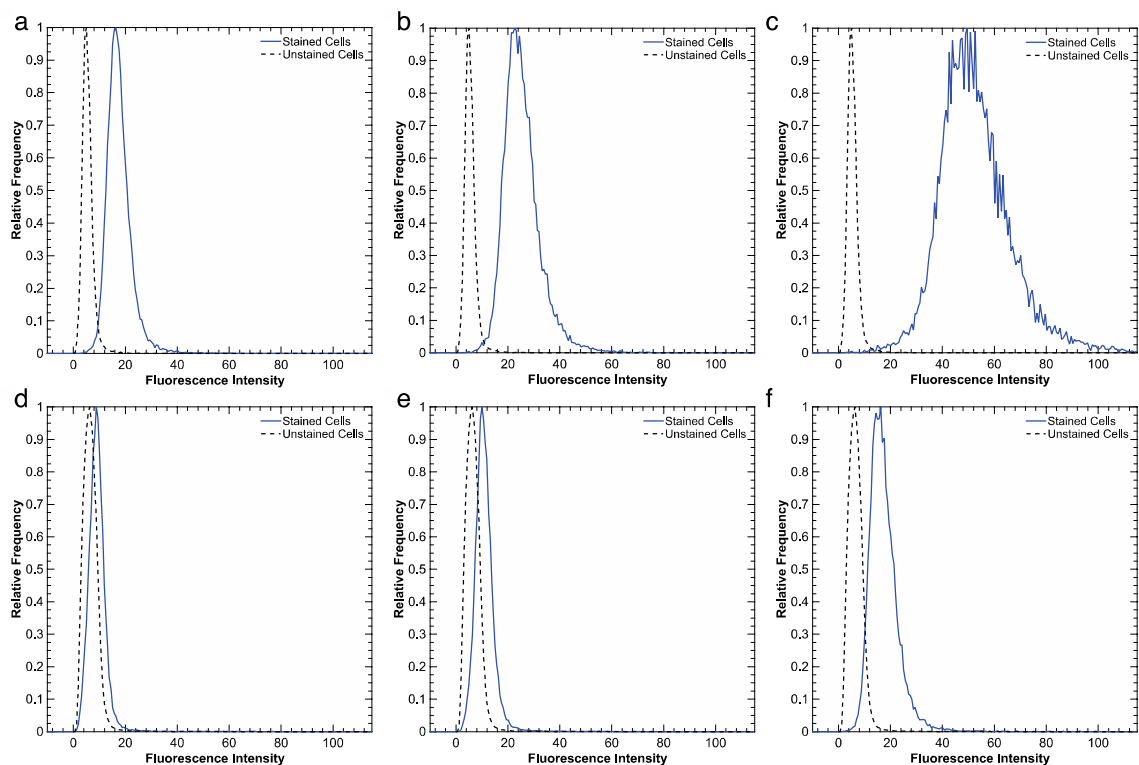
Supporting Information

HD Flow Cytometry: An Improved Way to Quantify Cellular Interactions with Nanoparticles

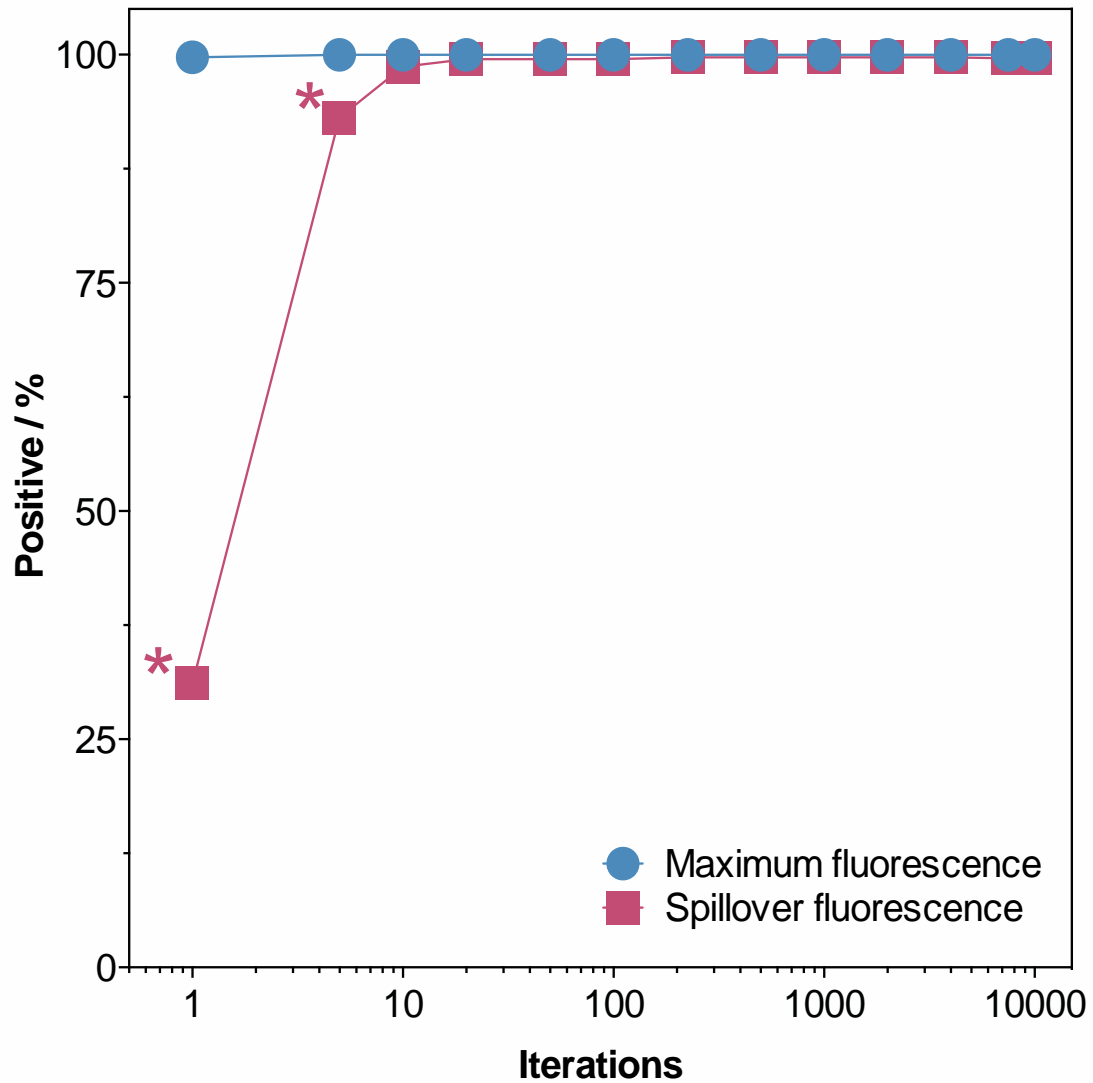
Laura I. Selby, Nachnicha Kongkatigumjorn, Georgina K. Such and Angus P.R. Johnston*



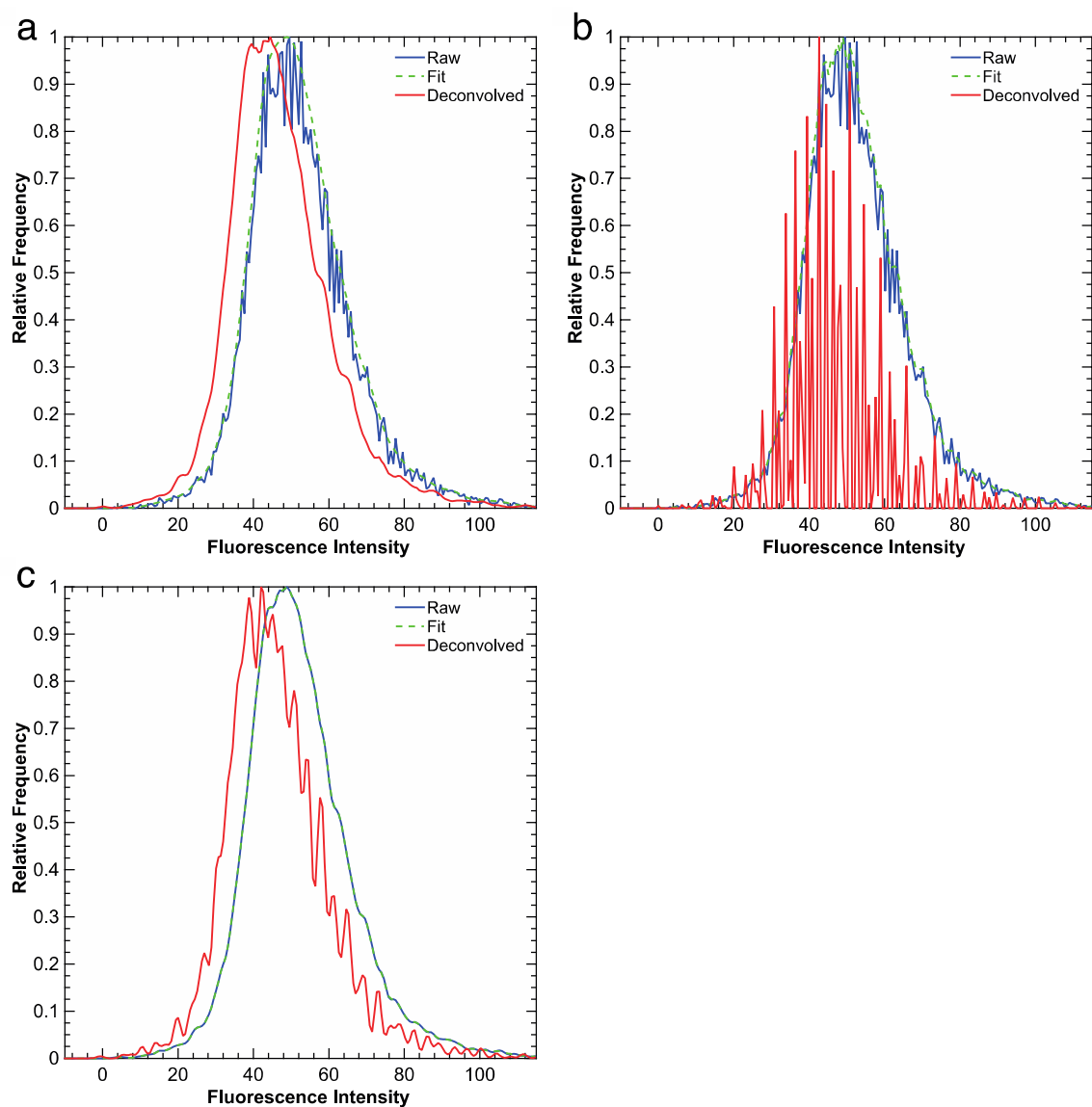
Supplementary Figure 1. Fluorescence histograms for control C1R cells. (a) An additional control sample is compared against three combined control data sets and deconvolved to produce the (b) underlying distribution (red). As the cells are negative, the HD Flow output is centered about zero. Deconvolution parameters: range = 0 - 250, bins = 300, iterations = 250, negative shift = 10, smoothing = false.



Supplementary Figure 2. Fluorescence histograms for fluorescently stained C1R cells. Cells were incubated with 0.005 μM (a and d), 0.01 μM (b and e) and 0.03 μM (c and f) CTO for 30 minutes. Data was collected by flow cytometry in the 565 – 595 nm channel with maximum fluorescence (a - c) and 661 – 690 nm channel with spillover to overlap test distributions with the control (d - f). Histogram parameters: range = 0 - 250, bins = 300, smoothing = false.



Supplementary Figure 3. Effect of number of algorithm iterations on calculated percent positive value. The number of iterations was manipulated when analyzing the brightest cellular stain (0.03 μM) in both the maximum and spillover fluorescence channels while keeping the range and number of bins constant (range = 0 - 250, bins = 300). Convergence on a solution occurs within 1 iteration for well-separated data but takes up to 10 iterations for overlapped data. *Indicates shift too small to accurately determine the positive population



Supplementary Figure 4. Effect of iterations and smoothing on HD Flow histograms for the

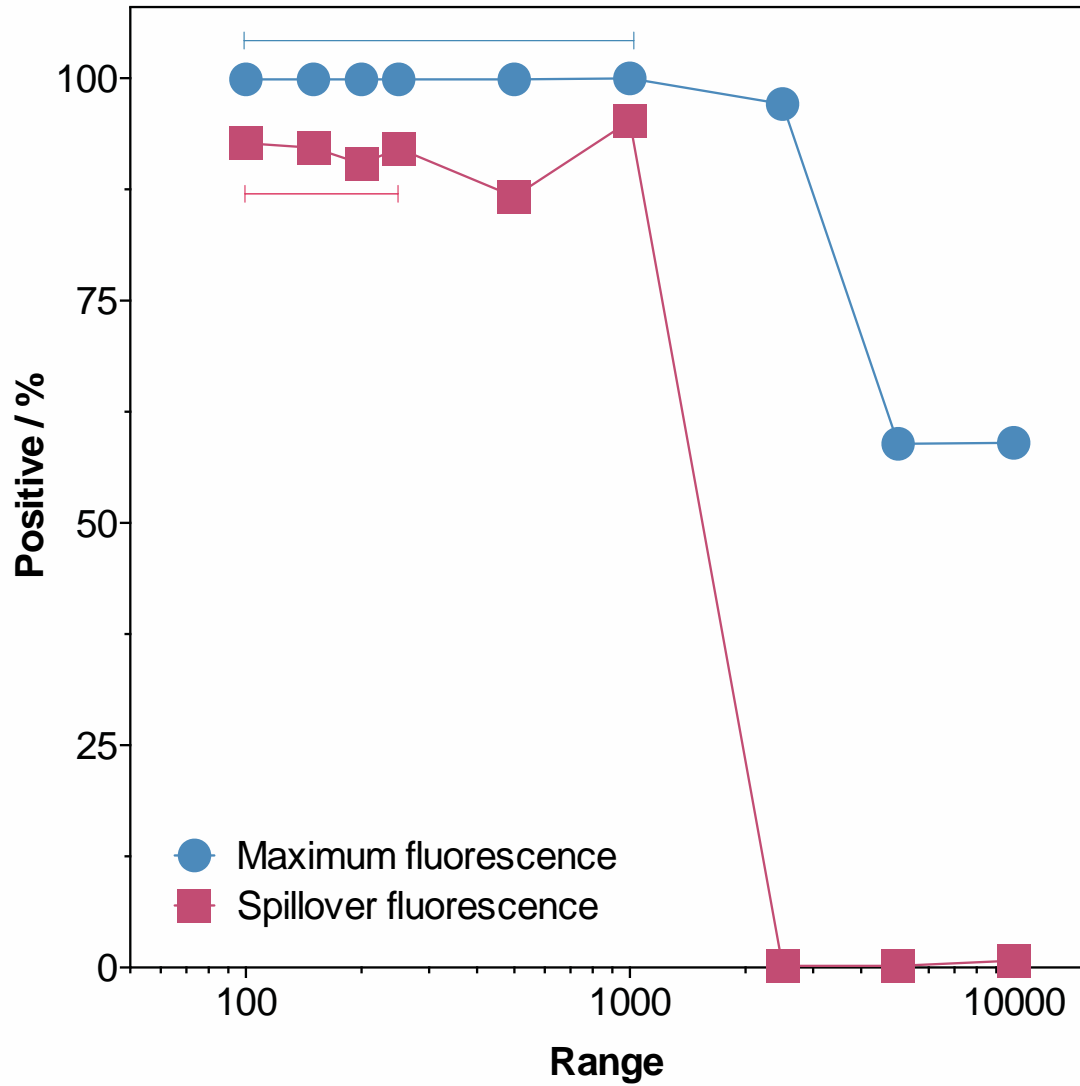
highest CTO concentration ($0.03 \mu\text{M}$), reading the maximum fluorescence channel data.

Increasing the number of iterations from 5 (a) to 10,000 (b) introduces oscillatory behavior in the HD Flow output. By implementing a Gaussian filter, the deterioration effect from 10,000 iterations is reduced (c). Deconvolution parameters: range = 0 - 250, bins = 300, iterations = 250, negative shift = 10.

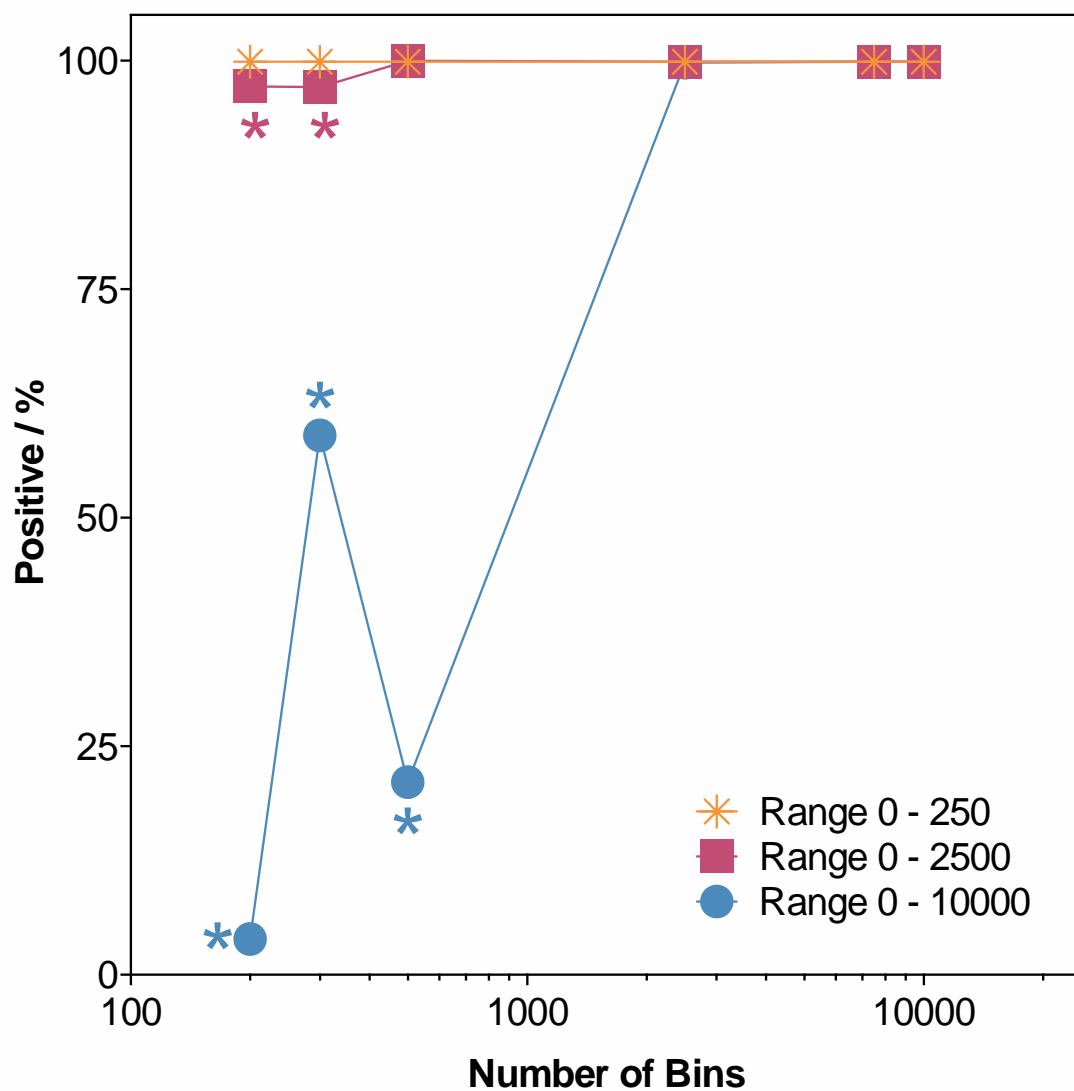
Supplementary Table 1. Effect of number of iterations and smoothing on calculated percent positive for the highest concentration of cellular stain (0.03 μM) with range = 250, bins = 300, iterations = 250, negative shift = 10.

Iterations	Maximum Fluorescence Positive [%]	Smoothed Maximum Fluorescence Positive [%]	Spillover Fluorescence Positive [%]	Smoothed Spillover Fluorescence Positive [%]
20	100	100	99.3	98.6
100	100	100	99.7	99.4
500	100	100	99.7	99.5
1000	100	100	99.7	99.5
10000	100	100	99.7	99.5

*Indicates shift too small to accurately determine the positive population



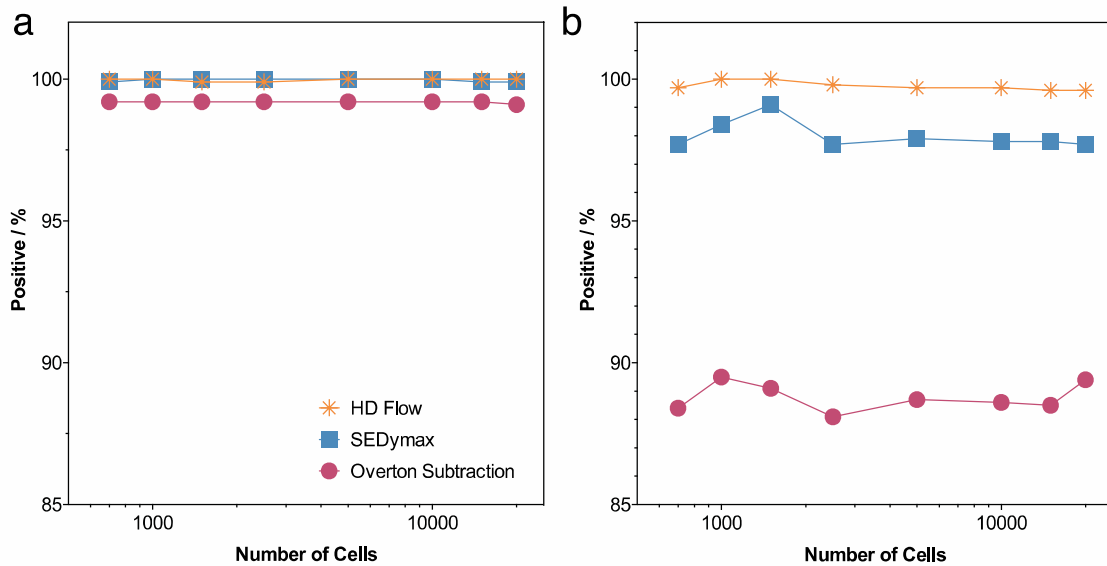
Supplementary Figure 5. Effect of range on calculated percent positive. The intermediate CTO stain (0.01 μM) was used to investigate the limits of the range parameter. Setting the range too high with constant bins causes underestimation of the percent positive. The bars represent the data points for which the shift is high enough for the percent positive to be accurately determined. Deconvolution parameters: bins = 300, iterations = 250, negative shift = 10, smooth = false.



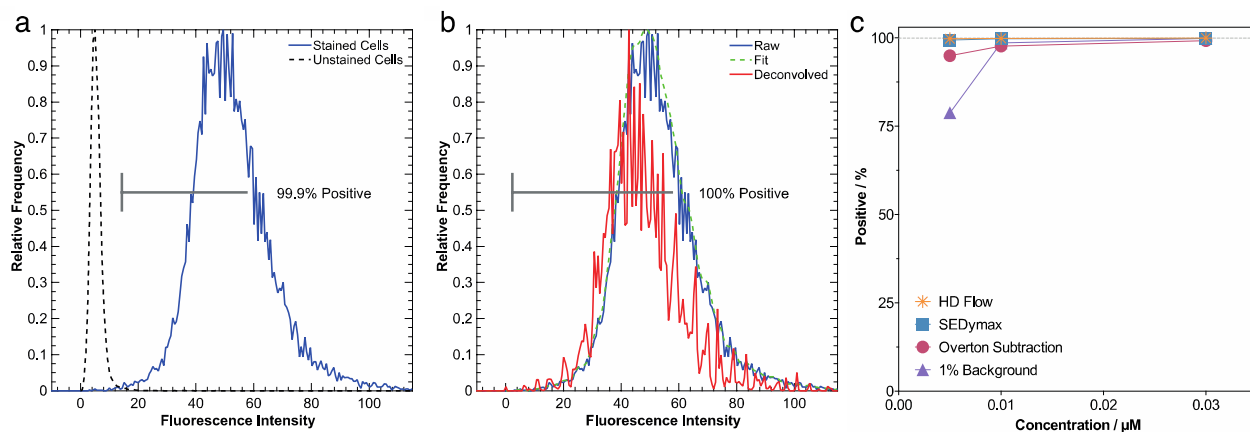
Supplementary Figure 6 Linked effect of bins and iterations. The number of bins required is dependent on the range set for the data. Percent positive calculated on the maximum fluorescence intensity channel for the 0.01 μM CTO stain with iterations = 250, negative shift = 10, smooth = false. *Indicates shift too small to accurately determine the positive population

Supplementary Table 2. Effect of number of bins on calculated percent positive for the 0.01 μM concentration stain with range = 0 - 100, iterations = 250, negative shift = 10, smooth = false.

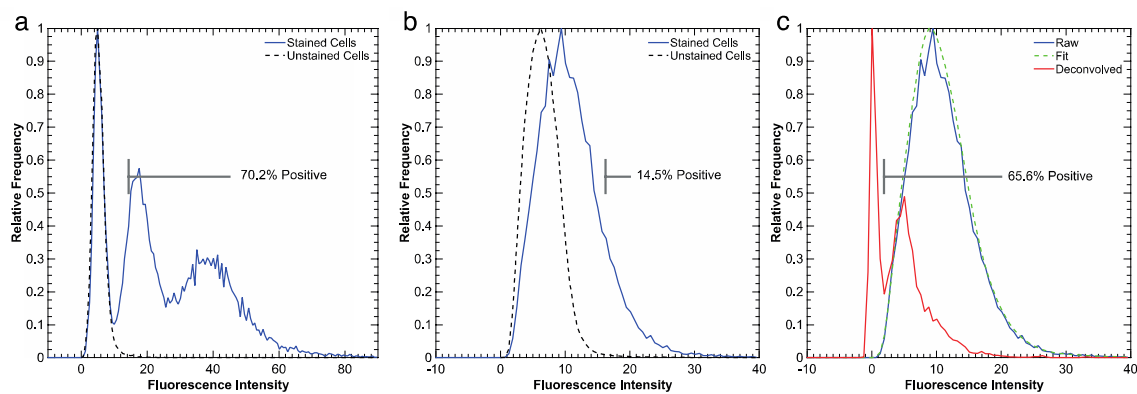
Number of Bins	Maximum Fluorescence Positive [%]	Spillover Fluorescence Positive [%]
250	99.9	92.1
300	99.9	92.7
500	99.9	92.0
800	99.9	92.6
1000	100	92.7



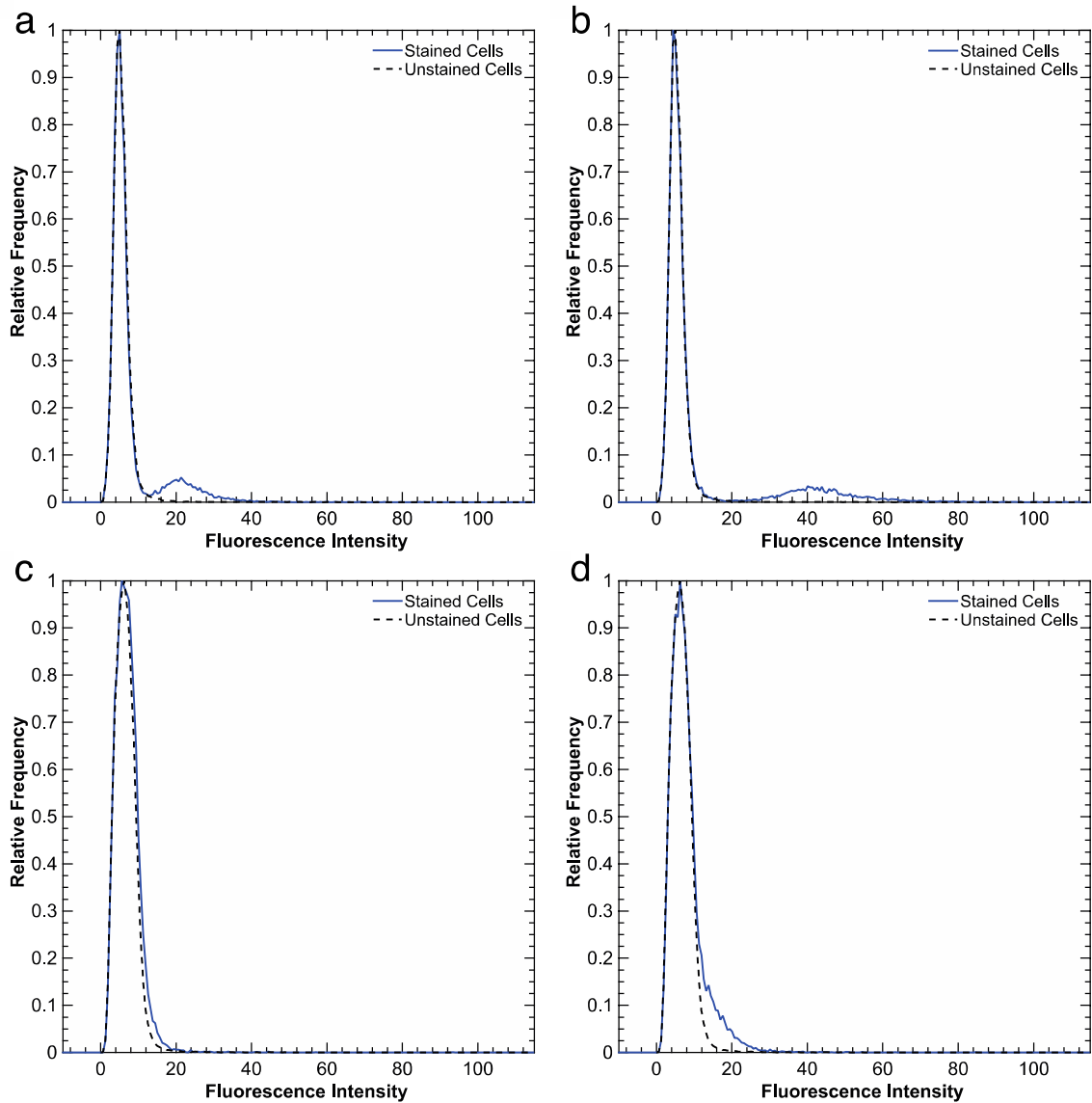
Supplementary Figure 7. Effect of cell count on calculated percent positive. Data from the highest CTO concentration (0.03 μM) were exported with FlowJo constrained to varying numbers of exported cells. HD Flow is compared to SEDymax and Overton subtraction for the maximum fluorescence intensity channel data (a) and spillover (b). Deconvolution parameters: range = 0 - 250, bins = 300, iterations = 250, negative shift = 10, smooth = false.



Supplementary Figure 8. Comparison of analysis techniques and demonstration of deconvolution in the maximum fluorescence channel. Deconvolution of (a) the maximum fluorescence of C1R cells incubated with 0.03 μM CTO fits to the raw data and corrects for autofluorescence showing over 99% of cells are positive (b). (c) Analysis of increasing CTO concentrations demonstrates HD Flow is equivalent to SEDymax out performs conventional 1% thresholding and Overton subtraction. Gates show the percent positive calculated by 1% of background thresholding (a) and HD Flow (b). Deconvolution parameters: Range = 0 - 250, bins = 300, iterations = 250, negative shift = 10, smoothing = false. *Indicates shift too small to accurately determine the positive population.



Supplementary Figure 9. Fluorescence histograms for manually mixed CTO stained and unstained C1R cells. Unstained cells were combined with cells from the 0.03 μM stained samples in a 1:1:1 ratio to produce multiple populations with an approximate percent positive 66%. Data was collected by flow cytometry in the (a) 565 – 595 nm channel with maximum fluorescence and (b) 661 – 690 nm channel with spillover to overlap test distributions with the control. Gates show the percent positive calculated by 1% of background subtraction (a) and HD Flow (b). Deconvolution parameters: range = 0 - 250, bins = 300, negative shift = 10, smoothing = false.



Supplementary Figure 10. Fluorescence histograms for manually mixed 10% positive and 90% negative C1R cells. Unstained cells were combined with (a) 0.01 μM and (b) 0.03 μM CTO stained samples to produce a heterogeneous sample with an estimated 10% positive value. Data was collected by flow cytometry in the 565 – 595 nm channel with maximum fluorescence (a and b) and 661 – 690 nm channel with spillover to overlap test distributions with the control (c and d). Histogram parameters: range = 0 - 250, bins = 300, smoothing = false.

Supplementary Table 3. Comparison of HD Flow to 1% of background thresholding, Overton subtraction and SEDymax percent positive values for samples manually mixed with control cells to generate overlapped histograms. Cells gated in the 565 – 595 nm channel where the positive population is highly separated from the control reveal the true percent positive value.

Fluorescence Channel	Gated Positive [%]	HD Flow ^{a)} [%]	SEDymax [%]	Overton Subtraction [%]	1% of Background Thresholding [%]
565 – 595 nm	74.8	74.8	75.8	72.8	70.9
661 – 690 nm	74.8	68.2	59.9	45.0	15.2

^{a)} Deconvolution parameters: Range = 0 - 100, bins = 300, iterations = 250, negative shift = 10, smoothing = false

Experimental Section

Materials: CellTracker™Orange CMTMR, Alexa Fluor® 647 succinimidyl ester, dimethyl sulfoxide (DMSO), Dulbecco's Modified Eagle Medium (DMEM) with high glucose, Dulbecco's phosphate-buffered saline (DPBS), heat inactivated fetal bovine serum (FBS), penicillin-streptomycin (10,000 U mL⁻¹), 2 mL 7kDa molecular weight cut-off (MWCO) Zeba™ desalting columns and 3.5 kDa MWCO SnakeSkin™ dialysis tubing were obtained from Thermo Fisher Scientific. Phosphate buffered saline tablets, sodium bicarbonate, bovine serum albumin (BSA), ovalbumin and 100 kDa MWCO Spectra-Por® Float-A-Lyzer® dialysis tubes were purchased from Sigma-Aldrich. Non-sterile, Millex®Syringe Filter Units with 0.45 µm pore diameter were obtained from Merck Millipore.

Cell Maintenance: Two cell lines were used to generate data to test the deconvolution algorithm. The human lymphoblast cell line C1R (ATCC CRL-1993) and the wild type mouse embryonic fibroblast cell line 3T3-WT (ATCC CRL-2752) were maintained at 37 °C

and 5% CO₂ in DMEM with high glucose supplemented with 10% FBS, 1% 10,000 U mL⁻¹ penicillin-streptomycin.

CellTracker Cell Staining: Generation of data with known percent positive values was performed using the retainable fluorescent dye CellTracker Orange. C1R cells were pelleted for 5 minutes at 300 relative centrifugal force (rcf) and resuspended in DMEM at a concentration of 2×10^6 cells per mL. Stock CellTracker at 10 mM in DMSO was diluted to 5 μ M in DMEM and incubated with 1×10^6 cells per mL for 30 minutes at final concentrations of 0, 0.005, 0.01 and 0.03 μ M. After washing four times in DMEM, cells were transferred to a 96-well V-bottom plate and manually mixed in set ratios with control cells to give varying approximate percent positive values before analysis by flow cytometry.

Nanoparticle Synthesis and Protein Loading: Self-assembling nanoparticles loaded with fluorescently labeled ovalbumin were prepared to test HD Flow on nanoparticle-cellular association data. The polymers poly(ethylene glycol)-b-poly[2-(diethylamino) ethyl methacrylate] (PEG-b-PDEAEMA) and poly[2-(diethylamino) ethyl methacrylate] (PDEAEMA) were synthesized and purified as previously described.^[29] Ovalbumin (3 mg) was labeled in PBS (100 mL), pH 8 with four molar equivalents of Alexa Flour 647 succinimidyl ester in DMSO. The reaction volume was made up to 1 mL with 0.1 M sodium bicarbonate, pH 8 and left at room temperature for 3 hours followed by an overnight incubation at 4 °C. Unreacted dye was removed using a 7 kDa MWCO Zeba desalting column with PBS at pH 8 as per the manufacture's instructions. PEG-b-PDEAEMA and PDEAEMA at a 1:2 w/w ratio (3 mg) were mixed with labeled-ovalbumin solution (15.3 μ g, 2 mg mL⁻¹) in PBS (3 mL) at pH 6. The mixture was dialyzed for 7 hours using 3.5 kDa MWCO SnakeSkin dialysis tubing in PBS. The solution was then transferred to 100 kDa MWCO dialysis tubing, and dialyzed for 24 hours in PBS at pH 8 with five buffer changes.

The particles were rested for 48 hours at room temperature then filtered through a 0.45 μm syringe filter prior to use. Particle concentration was estimated from a standard curve of polymer concentration (PEG-b-PDEAEMA and PDEAEMA at 1:2 w/w ratio) versus absorbance at 310 nm as measured by UV-Vis spectroscopy (Cary 60 UV-Vis, Agilent Technologies). Filtered particles in PBS at pH 8 were freeze-dried and made up to the original volume in PBS at pH 6 prior to absorbance measurements.

Nanoparticle-Cell Association Assay: 3T3-WT cells were seeded at a density of 6×10^4 cells per well in a 24-well plate, one day prior to the experiment. Particles were added to wells in duplicate at concentrations of 1.5, 4, 8, 15, 20 and 25 $\mu\text{g mL}^{-1}$ in DMEM, and incubated for 2 hours at 37 °C with 5% CO_2 . After incubation, the media was removed and the cells were washed with PBS (200 μL) 4 times. Cells were detached by trypsinization with 0.25 % trypsin (150 μL) for 3 minutes. Trypsin was inhibited with 1 % bovine serum albumin in PBS (PBS-BSA) (150 μL). The cells were transferred to a 96-well V-bottom plate and spun at 200 rcf for 5 minutes. The supernatant was discarded and cells were washed once with PBS-BSA (300 μL). The cells were pelleted again, resuspended in PBS (150 μL) and analyzed by flow cytometry.

Data Acquisition by Flow Cytometry: To produce test histograms with both separate and overlapped peaks, data was recorded from the maximum fluorescence intensity channel for CellTracker (565 – 595 nm) and from spillover into a channel where fluorescence was lower (661 – 690 nm) was collected. 5×10^4 cells were analyzed per sample with a Stratadigm S1000EXI flow cytometer (Stratadigm, California, USA) with 488 nm excitation with emission collected in the 565 – 595 nm and 661 – 690 nm channels and 552 nm excitation with emission collected in the 565 – 595 nm channel. FCS3.0 files were exported using CellCapTure Analysis Software (Stratadigm, California, USA), gated by forward and

side scatter in FlowJo (version 10, Tree Star, Oregon, USA) then exported again as FCS3.0 format. For the nanoparticle association assay, 1×10^4 cells were analyzed per sample with a BD FACS Canto II flow cytometer (BD Biosciences, USA) with 640nm excitation and emission collected in the 650 – 670 nm channels. FCS2.0 files were exported using BD FACSDIVA (version 6.0, BD Biosciences, USA), gated by forward and side scatter in FlowJo (version 10, Tree Star, Oregon, USA) then exported again as FCS3.0 format.

Data Analysis: Deconvolution was performed in MATLAB (release R2014b, version 8.4, MathWorks, Massachusetts, USA) using a custom script. HD Flow reads FCS files using a modified version of a freely available FCS data reader function (fca_readfcs.m, L. Balkay, 2014) and presents histograms using a figure generation script (plotPub.m, K. M. Masum Habib, 2015).

HD Flow Parameter Optimization

The number of iterations the algorithm passes through must be specified as Richard-Lucy deconvolution does not reach a final answer independently. We observed that as the number of iterations increases, the percent positive value increases until it converges to a solution that does not change with further iterations. The number of iterations to reach this solution depends on the separation between the treated and untreated samples, with overlapped distributions requiring a much larger number of iterations before the value stabilizes (Figure S3). However, this must be limited as high numbers of iterations causes noise to be amplified in the graphical output (Figure S4a and b). Implementing a constraint through a regularization term has the potential to alleviate this issue.^[1] Alternatively, a Gaussian filter can be applied by convolution with both the treated and untreated control data prior to deconvolution.^[2] This has negligible effect on the calculated percent positive (Table S1) but negates the oscillatory behavior in the autofluorescence corrected histogram (Figure S4c). Smoothing had a negligible effect on well-separated data and a decrease of only 0.2 –

0.7% in the percent of positive cells for data obtained from significantly overlapped data suggesting it is acceptable to use the filter to aid in visualization.

Data imported from flow cytometry standard (FCS) files is formatted as the fluorescence intensity of each individual cell, and must be converted to a histogram before deconvolution. This requires defining the 'resolution' of the histogram by setting the size of data bin. The bin size is dependent on the number of bins the data is compiled into and the range of fluorescence intensities the bins are to cover. The two parameters are related and changing one requires modifying the other. Setting a large range with a low number of bins reduces the resolution of the data set and results in a reduced ability to detect small shifts in the population (Figure S5). This can be rectified by increasing the number bins to increase the spread of the data across those bins (Figure S6). Once a critical point is reached that is dependent on the range of the data set, the output from the algorithm stabilizes and increasing the number of bins past this point has negligible effect on the calculated percent positive (Table S2).

The data collected from flow cytometry should theoretically be positive but negative values are possible from particular cytometers with noisy analog to digital converters, or can occur due to errors in fluorescence compensation.^[3] Furthermore, allowing negative values for the deconvolved histogram allows the cells with no signal to follow a Gaussian distribution, rather than being truncated at zero. To permit these negative values, a linear shift can be applied to the data set. Addition of the constant to each individual data point of the test samples does not interfere with the calculated percent positive, as long as the shift value is added to the threshold and subtracted from the MFI.

HD Flow optimization was performed on data files containing tens of thousands of cells but this may not always be possible due to experimental conditions. As the number of cells decreases, the shape of the histogram is maintained but appears noisier due to

fluctuations between bins, as each contains less cells. We observed the effect of lowering the number of cells on performance of HD Flow by exporting files ranging from 2×10^4 down to 700 cells. The calculated percent positive for well-separated test and control histograms was unaffected by cell number within this range for HD Flow or for SEDymax and Overton subtraction (Figure S7). All three methods had difficulty calculating the correct value for cell counts under 1×10^3 when histograms were overlapped which emphasizes the need for a sufficient cell count when quantifying positive cells with low fluorescence.

- [1] N. Dey, L. Blanc-Feraud, C. Zimmer, P. Roux, Z. Kam, J.-C. Olivo-Marin, J. Zerubia, *Microsc. Res. Tech.* **2006**, *69*, 260.
- [2] G. M. P. Van Kempen, L. J. Van Vliet, P. J. Verveer, H. T. M. Van Der Voort, *J. Microsc.* **1997**, *185*, 354.
- [3] D. R. Parks, M. Roederer, W. A. Moore, *Cytom. Part A* **2006**, *69*, 541.

Chapter 3. Quantifying Cellular Internalisation with a Fluorescent Click Sensor

3.1 Summary

The internalisation of material into the cell is critical for both the delivery of drugs using nanotechnology and in the understanding of fundamental cell biology. To quantify uptake using fluorescence, the extracellular signal from material bound to the cell surface must be separated from that emanating from internalised cargo. The current methods to achieve this are either non-specific or require the conjugation of large oligonucleotides that confer a significant negative charge to the material. This may interfere with the way the material associates with, and is taken up by cells. The first section of this chapter details the design, synthesis and demonstration of a click chemistry-based internalisation sensor used to evaluate the uptake of proteins of different sizes. The second section examines the feasibility of modifications to the sensor to increase the ease of conjugation to materials or to study the uptake of much smaller cargo (peptides).

Quantifying Cellular Internalisation with a Fluorescent Click Sensor

Laura I. Selby^{†‡}, Luigi Aurelio[†], Daniel Yuen[†], Bim Graham[†] and Angus P. R. Johnston^{*†‡}

[†]Monash Institute of Pharmaceutical Sciences, Monash University, Parkville, Victoria, Australia, [‡]ARC Centre of Excellence in Convergent Bio-Nano Science and Technology, Monash University, Parkville, Australia

ABSTRACT: The ability to determine the quantity of material endocytosed is important for our understanding of cell biology and in the design of effective carriers for drug delivery. To quantify the amount of material internalised by fluorescence, the signal remaining on the cell surface must be differentiated from that of the endocytosed cargo. Sensors for internalisation are advantageous over traditional methods for achieving this as they exhibit improved signal-to-noise ratios, and allow for multiple fluorescent markers to be used simultaneously, due to their specificity. We have developed a small fluorescent internalisation sensor, similar in size to a standard fluorescent dye that can be conjugated to proteins and uses click chemistry to switch off the surface signal. The quenching was demonstrated to be highly specific and rapid in its action. The sensor can be attached to a variety of materials using simple chemistry and is compatible with flow cytometry and fluorescent microscopy, making it a useful tool within the biological sciences to study the uptake of material into cells.

Endocytosis is a critical cellular process that governs the entry of a multitude of materials into the cell. It plays a role in numerous cell activities, including the uptake of nutrients,¹ signal transduction² and in immune responses.³ In addition, endocytosis is the main route of entry for many nanomaterials,⁴ highlighting its importance in the development of drug delivery systems. Quantifying the amount of material internalised requires the ability to distinguish between material inside the cell from that remaining bound to the surface. The majority of current techniques for determining internalisation employ fluorescent dyes and rely either on confocal microscopy to identify material inside the cell membrane,⁵ or by non-specifically removing surface fluorescence using trypan blue quenching^{6,7} or acid-washing.^{8,9} Microscopy limits the number of cells that can be analysed while the other methods remove all surface fluorescence, making them incompatible with immunophenotyping and other fluorescent cell surface markers.

To improve the specificity of quenching, anti-dye antibodies that bind to a specific fluorophore and quench their fluorescence have been developed.^{8,10} While effective, they are expensive and only available for a limited number of dyes. In addition, dyes that change their fluorescence in response to pH have also been used to quantify internalisation by exploiting the acidification of endosomes that occurs during endocytosis as a trigger to signify the material is inside the cell. However, these dyes

can fluoresce significantly at the neutral pH of the extracellular environment, resulting in high background levels and a low signal-to-noise ratio.

A recent advance is the advent of a DNA sensor (Specific Hybridization Internalisation Probe - SHIP) that can be specifically quenched through hybridization.¹¹⁻¹³ A fluorescent internalisation probe (FIP) is conjugated to the material of interest and surface bound material is quenched using a complementary strand with an attached quencher. This method has previously been demonstrated to be superior to both trypan blue and acid wash methods for removing cell surface fluorescence without interfering with other fluorescent signals.

However, labeling of proteins and particles via conjugation of large tags has been shown perturb intracellular trafficking pathways.^{14,15} Although it was demonstrated FIP did not interfere with the trafficking of the protein studied, oligonucleotides are innately large and carry a significant negative charge that may interfere with the internalisation of smaller materials. The need to quantify the internalisation of materials of all sizes prompted us to design an equivalent sensor but with a reduced molecular weight and with a net charge closer to zero.

To be equivalent to the DNA sensor in terms of speed and specificity requires a robust biorthogonal reaction pair.^{16,17} Copper-free click chemistry has become prevalent for both *in vitro*¹⁸ and *in vivo*¹⁹ labelling applications and meets these requirements. Furthermore, click groups have been incorporated into proteins within live cells

though the use of non-canonical amino acids, which demonstrates their ability to retain reactivity under biological conditions.^{20,21}

Here, we present a fluorescent sensor, similar in size to a conventional fluorophore and based on click chemistry for quantifying the internalisation of material into cells. We demonstrate its ability to visualise the internalisation of protein through fluorescence microscopy and quantify the amount of material internalised via flow cytometry.

EXPERIMENTAL

Materials. All materials were purchased from Sigma-Aldrich or Merck Millipore unless otherwise stated. The PEG linkers Fmoc-N-amido-dPEG3 and Fmoc-N-amido-dPEG4 were purchased from Quanta BioDesign. The quencher Black Hole Quencher® 2 – Amine (BHQ2-amine) was purchased from Biosearch Technologies. SulfoQSY21 carboxylic acid (sQSY21-COOH)²² and sulfoCyanine5 carboxylic acid (sCy5-COOH)^{23,24} were synthesised in house from published procedures. Peptide synthesis reagents including N^α-Fmoc-N^ε-Boc-L-Lysine, N-(3-Dimethylaminopropyl)-N'-ethylcarbodiimide hydrochloride (EDC) and (Benzotriazol-1-yloxy)tripyrrolidinophosphonium hexafluorophosphate (PyBOP) were purchased from Chem-Impex International, Inc.

The click chemistry reagent tetrazine-PEG5-NHS (TET-PEG4-NHS) was purchased from Conju-Probe, methyltetrazine-PEG4-NHS ester (mTET-PEG4-NHS) ester and *trans*-cyclooctene NHS ester (TCO-NHS) from Click Chemistry Tools and Click-IT® Succinimidyl Ester Dibenzocycloctyne (DIBO – NHS) from Thermo Fisher Scientific.

Cell culture reagents including Dulbecco's Modified Eagle's Medium with GlutaMAX (DMEM), McCoy's 5a modified medium, fetal bovine serum (FBS), penicillin/streptomycin, TrypLE express enzyme and the additional materials, Alexa Fluor 488-NHS ester, wheat germ agglutinin-Alexa Fluor 488 conjugate (WGA-AF488), pHrodo Red succinimidyl ester (pHrodo Red-SE) and 0.5 mL Zeba Spin desalting columns with 7 kDa MWCO were obtained from Thermo Fisher Scientific.

Trastuzumab (Herceptin®) was purchased from Roche, reconstituted to 20 mg mL⁻¹ in Milli-Q water and passed through a 7 kDa Zeba Spin desalting column before use to remove excipients.

Oligonucleotide Sensor. The previously published oligonucleotide internalisation sensor¹¹ was purchased as the following custom sequences: 5' - Cy5 - TCA GTT CAG GAC CCT CGG CT – azide – 3' and 5' - AGC CGA GGG TCC TGA ACT GA – BHQ2 – 3' from Integrated DNA Technologies (IDT). Oligonucleotides were reconstituted in Milli-Q water to prepare 150 μM or 600 μM stock solutions and stored in at -20°C.

Fluorescent Click Sensor Component Synthesis – sCy5-TCO. The backbone of the sensor was synthesised via Fmoc-solid-phase synthesis on 2-chlorotriethyl chloride resin. Fmoc-N-amido-dPEG3 (3.4 equiv, 0.30 g, 0.68 mmol) was combined with 2-chlorotriethyl chloride resin (0.20 g) in dichloromethane (DCM) and bubbled with nitrogen gas for 1 hour. After washing in DCM, an additional equivalent was added with 100 μL triethylamine (TEA) and left for 30 minutes. The resin was capped with methanol (MeOH) and TEA (67 μL) for 15 minutes. The Fmoc protecting group was removed using two cycles of 2 mL 20% piperidine in dimethylformamide (DMF) for 2 minutes and one cycle with

2 mL for five minutes. N^α-Fmoc-N^ε-Boc-L-Lysine (2 equiv, 0.187 g, 0.398 mmol) was conjugated with PyBOP (2 equiv, 0.204 g, 0.392 mmol) and TEA (4 equiv, 11 μL, 0.80 mmol) for 25 minutes then rinsed, and deprotected. Fmoc-N-amido-dPEG4 (3.3 equiv, 0.21 g, 0.420 mmol) was added with (2.1 equiv, 0.215 g, 0.413 mmol) and TEA (4 equiv, 11 μL, 0.80 mmol) for 50 minutes, rinsed and then deprotected.

To attach the fluorescent group, an excess of resin was combined with sCy5-COOH (4.0 mg, 6.4 μmol), PyBOP (3 equiv, 9.8 mg, 18.9 μmol) and N,N-diisopropylethylamine (DIPEA) (10 equiv, 10.6 μL, 0.61 mmol) in DMF. The reaction was bubbled for two minutes with nitrogen then left overnight, protected from light. After washing unreacted components with DMF, the conjugate was cleaved from the resin with 30/65/5% trifluoroacetic acid (TFA)/DCM/triisopropylsilane (TIPS) (2 mL) for 1 hour. Excess solvent was evaporated under nitrogen and the mass was confirmed via peptide liquid chromatography-mass spectrometry (LCMS). The sample was dissolved in DMF (400 μL) and combined with an excess of TCO-NHS to the total amount of sCy5 added in the previous step (6 equiv, 10.1 mg, 37.6 μmol) and DIPEA (8 equiv, 8.48 μL, 48.7 μmol) and left overnight. The presence of the product mass was confirmed by LCMS (**SI Figure 1**) and the product was purified by preparative high-performance liquid chromatography (HPLC) with a 20 – 100% acetonitrile (MeCN)/water with 0.1% TFA gradient over 50 minutes with a flow rate of 7 mL min⁻¹. The product was lyophilised and the mass confirmed by high resolution mass spectrometry (HRMS) (**SI Figure 2**). HRMS (ESI) m/z: calculated for C₆₈H₁₀₂N₆O₂₀S₂ [M+Na]⁺ 1409.6483, found 1409.646, calculated for [M+2H]⁺² 694.3368, found 694.3374. The purity of the conjugate was estimated to be over 95% by analytical HPLC (**SI Figure 3**). The fluorescent component of the click sensor was reconstituted in dimethyl sulfoxide (DMSO) and stored at -20 °C. The concentration was estimated using the absorbance at 646 nm with an extinction coefficient of 271,000 M⁻¹cm⁻¹.

BHQ2-mTet Synthesis. BHQ2-amine (1.0 equiv, 2.22 mg, 4.6 μmol) was combined with mTet-PEG4-NHS (1.0 equiv, 3.13 mg, 4.2 μmol) in DMF (400 μL) and left at room temperature overnight. The presence of product was confirmed via LCMS and purified using preparative HPLC with a 30 – 100% MeCN/water with 0.1% TFA gradient over 42 minutes. The presence of the product mass in the dark purple fraction was confirmed by LCMS, the product was lyophilised, confirmed by HRMS (**SI Figure 4**) and an estimated purity of 81% estimated by analytical HPLC (**SI Figure 5**). HRMS (ESI) m/z: calculated for C₄₄H₅₃N₁₁O₁₀ [M+H]⁺ 896.405, found 896.405, calculated for [M+2H]⁺² 448.7061, found 448.7064, calculated for [M+Na]⁺ 918.3869, found 918.3871. BHQ2-mTet was reconstituted in DMSO and the concentration determined by using the absorbance at 579 nm with an extinction coefficient of 38,000 M⁻¹cm⁻¹.

BHQ2-Tet Synthesis. BHQ2-amine (1.0 equiv, 2.39 mg, 4.2 μmol) was combined with TET-PEG4-NHS (3.13 mg, 4.2 μmol) in DMF (400 μL) and left at room temperature overnight. The presence of product was confirmed via LCMS and purified using preparative HPLC with a 30 – 100% MeCN/water with 0.1% TFA gradient over 42 minutes. The presence of the product mass in the dark purple fraction was confirmed by LCMS, the product was lyophilised, confirmed by HRMS (**SI Figure 6**) and the purity of 91% estimated by analytical HPLC (**SI Figure 7**). HRMS (ESI) m/z: calculated for C₄₇H₅₈N₁₂O₁₁ [M+H]⁺ 967.4421, found

967.4436, calculated for $[M+2H]^+$ 484.2247, found 484.2259, calculated for $[M+Na]^+$ 989.424, found 989.4262. BHQ2-Tet was reconstituted in DMSO and the concentration determined by using the absorbance at 579 nm with an extinction coefficient of $38,000 \text{ M}^{-1}\text{cm}^{-1}$.

sQSY-Tet Synthesis. The sQSY-Tet quencher was synthesized on the same backbone as the TCO sensor, on resin. sQSY21-COOH (1 equiv, 4.2 mg, $5.0 \mu\text{mol}$) was combined with an excess of resin (11.8 mg), PyBOP (4.0 equiv, 10.3 mg, $19.8 \mu\text{mol}$) and DIPEA (10 equiv, $50 \mu\text{mol}$, $8.7 \mu\text{L}$) in 80/20% DMF/DMSO and left overnight at room temperature. The resin was washed with DMSO, followed by DCM and then drained. The conjugate was cleaved from the resin with 30/65/5% TFA/DCM/TIPS (2 mL) for 1 hour and then rinsed into a round-bottom flask with hexafluoroisopropanol (HFIP). The bulk of the solvent was removed under nitrogen gas and the remaining solution was transferred to a 1.5 mL Eppendorf tube before removing the remaining HFIP.

The crude sQSY conjugate (1 equiv, $4.75 \mu\text{mol}$, 4 mg) was combined with Tet-PEG4-NHS (3.13 mg, $4.2 \mu\text{mol}$) and DIPEA (24 equiv, $20 \mu\text{mol}$) in 43/57 % DMF/DMSO (0.76 mL) and allowed to react overnight at room temperature. The presence of product was confirmed via LCMS and purified using preparative HPLC with a 5 – 100% MeCN/water with 0.1% TFA gradient over 50 minutes. The presence of the product mass in the dark fraction was confirmed by LCMS, the product was freeze dried, confirmed by HRMS (SI Figure 8) and the purity of 84% estimated by analytical HPLC (SI Figure 9). HRMS (ESI) m/z : calculated for $\text{C}_{90}\text{H}_{116}\text{N}_{12}\text{O}_{28}\text{S}_3$ $[M+2H]^+$ 955.868, found 955.869, calculated for $[M+3H]^+$ 637.5811, found 637.5827. sQSY-Tet was reconstituted in DMSO and the concentration determined by using the absorbance at 660 nm with an extinction coefficient of $89,000 \text{ M}^{-1}\text{cm}^{-1}$.

Fluorescence Measurements. Fluorescence spectra were obtained using a Shimadzu RF-5301PC spectrofluorophotometer in a 500 μL quartz SUPRASIL cuvette. Fluorescent samples at a concentration of $0.6 \mu\text{M}$ were excited at 646 nm and the emission collected between 656 – 700 nm before addition of 5 equivalents of quencher. The spectrum of PBS alone was obtained before the addition of the sensor and subtracted from all fluorescent spectra. For the pHorodo measurements, the pH of 10 mM PBS was adjusted to pH 8 with 1 M sodium hydroxide and the pH of 5 mM citrate solutions was adjusted to pH 4 with 1 M hydrochloric acid. These were then mixed to produce solutions at pH 4.5 and pH 7.5.

Nanobody Expression. Histidine-tagged anti-human epidermal growth factor receptor 2 (anti-HER2) nanobody clone 2D3²⁵ was expressed in *E. coli* BL21(DE3) and purified using immobilised metal affinity chromatography followed by size exclusion chromatography. Nanobody protein concentration was determined via the UV/Vis absorbance at 280 nm using an extinction coefficient of $35,075 \text{ M}^{-1}\text{cm}^{-1}$, calculated using ProtParam.²⁶

DNA Sensor Bioconjugation. Labeling reactions used 50 μL of 5.0 mg mL^{-1} transferrin in PBS. An excess of 1 mg mL^{-1} DIBO-NHS was added (20 equivs) and allowed to react for 2 hours at 4°C . Unreacted DIBO-NHS was removed using a Zeba Spin Desalting column, 7 kDa MWCO. The column was first equilibrated with PBS by washing with 300 μL and spinning at 1500 g for 1 minute, repeating 3 times. After adding the sample and spinning at 1500 g, an excess of azide was added (1.5 equivs) and allowed

to react overnight at 4°C . Excess azide was then removed using an Amicon Ultra – 0.5 mL 30 kDa MWCO centrifugal filter. The filter was rinsed with 500 μL PBS by spinning at 13,000 g for 0.5 minutes. After adding the sample, the unit was topped up to reach a total volume of 0.5 mL and spun at 13,000 g for 3 minutes and repeated until the filtrate was clear. After washing, the unit was placed upside and spun at 1000 g for 2 minutes to collect the product. Concentration of protein and label were calculated using the extinction coefficients of $87,000 \text{ cm}^{-1} \text{ M}^{-1}$ for transferrin and $250,000 \text{ cm}^{-1} \text{ M}^{-1}$ for Cy5 and the absorbance obtained via a NanoDrop Spectrophotometer ND-1000 as described previously.²⁷

pHrodo Red Bioconjugation. pHrodo red NHS ester (1.5 equivs, 3.3 μg , 5 nmol) at 1 mg mL^{-1} was added to 5 mg mL^{-1} human holo transferrin (0.25 mg, 3.1 nmol) and incubated at 4°C overnight before purifying using a Zeba Spin Desalting column, 7 kDa MWCO. The concentration and degree of labeling were obtained via a NanoDrop Spectrophotometer ND-1000 ND by measuring the absorbance at 560 nm and using an extinction coefficient of $65,000 \text{ M}^{-1}\text{cm}^{-1}$.

Click Sensor Bioconjugation. Labeling reactions used 50 μL of 5.0 mg mL^{-1} transferrin (0.25 mg), 38 μL of 0.9 mg mL^{-1} 2D3 (0.035 mg) or 14 μL of 14 mg mL^{-1} trastuzumab (0.2 mg) in PBS. An excess of the sensor (2 – 4 equivs to the amount of protein) was added to the solution followed by EDC and N-hydroxysuccinimide (NHS) dissolved in PBS to bring the final concentration of those reagents to 0.1 M and 5 mM respectively. In the case of trastuzumab, the sensor was pre-incubated with 10, 50 or 100 mM EDC/5mM NHS for 15 minutes before adding this volume to the antibody in addition to Alexa Fluor 488-NHS dissolved in DMSO (2.5 equivs). sCy5 alone was also conjugated to trastuzumab to assess cross linking via EDC/NHS using sCy5-NHS (2.5 equivs). All reactions were incubated over night at 4°C . Unreacted sensor was removed using Zeba Spin Desalting column, 7 kDa MWCO. The concentration and degree of labeling were obtained via a NanoDrop Spectrophotometer ND-1000 ND using an extinction coefficient of $271,000 \text{ cm}^{-1} \text{ M}^{-1}$ for sCy5 at 646 nm, $73,000 \text{ M}^{-1} \text{ cm}^{-1}$ for Alexa Fluor 488 at 495 nm and $210,000 \text{ M}^{-1} \text{ cm}^{-1}$ for trastuzumab at 280 nm.

SDS-PAGE. Samples were prepared by adding approximately 500 ng protein to 6 μL 0.2% 2-mercaptoethanol in SDS-page loading dye.²⁸ The samples were then heat treated for 2 minutes at 94°C and added to the wells of a precast, 12% polyacrylamide gel (Bio-Rad). The gel was run for 50 minutes at 120 V in running buffer (25 mM Tris, 250 mM glycine, 0.1% SDS at pH 8.3). Fluorescence images of the gel were obtained on a Amersham Typhoon 5 Biomolecular Imager (GE Healthcare Life Sciences).

Cell Culture. The non-adherent human lymphoblast cell line C1R (ATCC CRL-1993) was maintained at 37°C and 5% CO_2 in DMEM with GlutaMAX supplemented with 10% FBS, 1% penicillin/streptomycin. The adherent human ovarian epithelial cell line SKOV-3 (ATCC HTB-77) was maintained at 37°C and 5% CO_2 in McCoy's 5a modified medium with 10% FBS, 1% penicillin/streptomycin.

Cell Surface Quenching and Internalisation. C1R cells at a concentration of $2 \times 10^6 \text{ cells mL}^{-1}$ were split into tubes with 4×10^5 cells per sample and cooled on ice for 10 minutes. Transferrin labeled with sensor was added at a final concentration of $15 \mu\text{g mL}^{-1}$ and left on ice for 15 minutes to allow binding to the cell surface.

Cells were washed twice in cold PBS before incubating the cells at either 4°C or 37°C for 15 mins. In experiments involving wheat germ agglutinin, the lectin was added at 1 µg mL⁻¹ for the final 5 minutes of binding time. The cells were split into a 96-well V-bottom plate and spun at 300 g for 5 minutes. The cells were re-suspended in 200 µL of PBS with or without quencher (4 equiv for the click sensor, 5 equiv for the DNA sensor) to the total amount of sensor added, as calculated using the degree of labeling. The samples were mixed and then left on ice for approximately 15 minutes before analysis by flow cytometry.

Trastuzumab and 2D3 Binding and Internalisation. SKOV-3 cells were seeded at 1×10⁵ cells per well in 400 µL McCoy's 5a modified medium with 10% FBS, 1% penicillin/streptomycin in 24-well plates one day prior to the experiment. One plate of cells was cooled to 4°C on ice for 15 minutes while the other was maintained at 37°C. 4 nM antibody or 8 nM nanobody labelled with click sensor was added per well at 0.5, 1, 2 and 4 hours. The cells were washed twice in cold PBS and detached with 200 µL TrypLE for 10 minutes. 100 µL 1% bovine serum albumin in PBS was added to each sample and the entire contents transferred to a 96-well, V-bottom plate. The cells were spun at 350 g for 5 minutes and resuspended in 200 µL PBS with or without 0.5 µM sQSY-Tet before analysis by flow cytometry.

Flow Cytometry. Flow cytometry was performed using a Stratadigm S1000EXI flow cytometer (Stratadigm, California, USA) with a 488 nm excitation and emission collected between 515 – 545 nm and a 642 nm excitation with emission collected between 661 – 691 nm. FCS3.0 files were exported using CellCapture Analysis Software (Stratadigm, California, USA) and gated by forward and side scatter in FlowJo (version 10, Tree Star, Oregon, USA) before subsequent analysis.

Fluorescence Microscopy. Fluorescence microscopy was performed using a 60X 1.3 NA silicone or 40X 0.9 NA air objective with a standard "PINKEL" DAPI/FITC/Cy3/Cy5 Filter set (Semrock). Emission was separated and captured using a 414/497/565/653 nm dichroic mirror and a quad-band bandpass emission filter between 503 – 515 nm and 614 – 804 nm. All image analysis was performed in Slidebook 6.0 (Intelligent Imaging Innovations, Denver, USA) except for images requiring deconvolution. For deconvolution, 10 slices were captured with a 0.33 µm step size, exported from Slidebook and deconvolved using the Richard-Lucy algorithm^{29,30} via the CUDA deconvolution plugin in ImageJ.³¹

Quenching Efficiency and Internalisation. Quenching efficiency and was calculated as a percentage from the following equation using the geometric mean fluorescence intensity (MFI) from flow cytometry:

$$\eta_Q = \left[1 - \left(\frac{Q_0}{N_0} \right) \right] \times 100 \quad (1)$$

Where, η_Q = quenching efficiency, N_0 = MFI of the unquenched sample at 4°C, Q_0 = MFI of the unquenched sample at 4°C.

The percentage of material internalised, compensating for incomplete surface quenching was calculated from the following equation:³²

$$I_f = \left[1 - \frac{N_1 - Q_1}{N_1 - \frac{N_1 Q_0}{N_0}} \right] \times 100 \quad (2)$$

Where, I_f = fraction internalised, N_1 = MFI of the unquenched sample at 37°C, Q_1 = MFI of the quenched sample 37°C

For the antibody experiment, the average quenching efficiency determined at 30 minutes and 4 hours was used to compensate for incomplete surface quenching.

RESULTS AND DISCUSSION

Internalisation Sensor Design.

When designing the internalisation sensor, two main attributes of the DNA sensor were considered: the kinetics and selectivity of DNA hybridisation. The hybridisation of complementary DNA sequences is extremely rapid. The second-order rate constant is approximately 10⁴ – 10⁵ M⁻¹ s⁻¹ for oligonucleotides containing 15 – 20 base pairs.^{33,34} The process is also highly selective and can identify a specific target amongst many sequences, as demonstrated by its application in molecular beacons^{35,36} and fluorescence in situ hybridization (FISH).^{37,38} mRNA detection probes based on DNA-RNA hybridization have been shown to be non-responsive with as little as 1 – 2 mismatched base pairs.³⁹ To achieve these properties while maintaining a low molecular weight, we looked to bio-orthogonal copper-free click chemistry which is renowned for its specificity and rapid reaction rate.¹⁷

For flow cytometry and microscopy applications using live cells, the quenching of surface fluorescence must proceed to completion over a time scale of seconds to several minutes. Reaction rates for click chemistry pairs is highly variable and depends on the particular groups used. Strain-promoted azide-alkyne cycloadditions (SPAAC), such as the reaction between an azide and dibenzocyclooctyne (DIBO) have a reaction rate in the order of 0.2 – 0.5 M⁻¹ s⁻¹ and were considered too slow to be practical for this purpose, especially as the concentration of the sensor expected to be present on the cell surface is very low. To carry out reactions quickly at low concentrations requires a reaction pair with a high rate constant. The reaction of tetrazine with *trans*-cyclooctene (TCO) is rapid, with reaction rates up to 2×10⁶-fold higher than azide-cyclooctyne reactions. TCO has been used in numerous *in vitro* labeling applications, demonstrating its suitability for bio-orthogonal labelling.^{20,40,41} Based on these attributes, we chose the TCO-Tet click chemistry reaction pair as the basis for the sensor.

The internalisation sensor is composed of two components (**Figure 1a**). The first component contains a fluorescent dye (sCy5), a click group (TCO) and anchor point for conjugation to a molecule or particle of interest (**SI Figure 10**). The distance between each of these functional groups

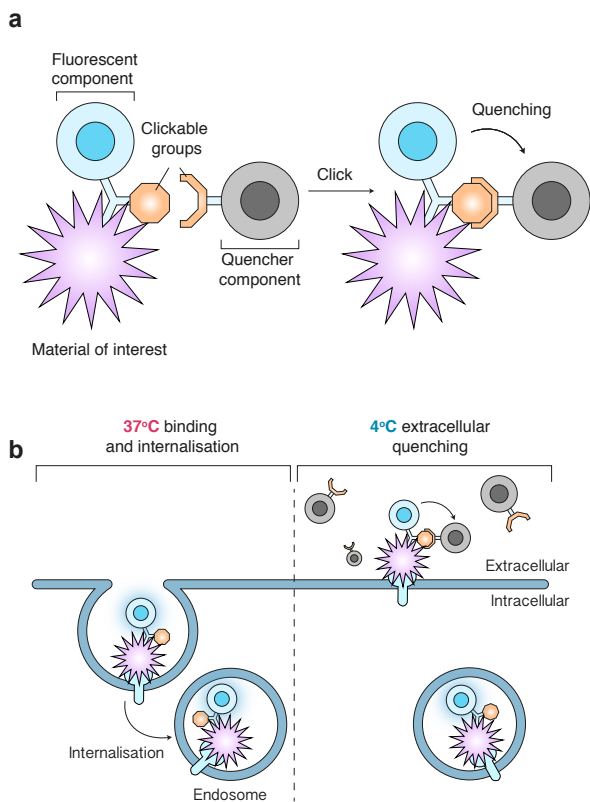


Figure 1. Click internalisation sensor scheme. (a) The fluorescent component of the sensor is attached to a material of interest and contains a click group compatible with that on the quencher unit. (b) Following binding and internalisation of the protein or material into cells at 37°C, uptake is halted by bringing the temperature down to 4°C. The fluorescence of any material on the surface is removed selectively by adding the quencher component of the sensor, leaving the intracellular signal unaffected.

was extended with short polyethylene glycol (PEG) linkers to minimize steric hindrance so reactivity was maintained once conjugated to the material of interest.⁴² The second component contains a quencher dye with absorbance matched to the emission of sCy5 (BHQ2 or sQSY21) and a compatible click group. The reaction rates of 1,2,4,5-tetrazines are tunable by modification of the attached functional groups at the 3- and 6- positions on the ring, but stability is compromised in exchange for speed.⁴³ Substitution of a methyl group at the 6- position (mTet) exhibits higher stability under biological conditions, but is over 30-fold less reactive than the non-methylated counterpart (Tet).⁴⁴ We synthesised both mTet and Tet versions of the quencher component to determine the compromise between optimal stability and reaction kinetics. It is anticipated that degradation over the timescale needed for the quencher to react to the fluorescent component is likely to be insignificant.

To then quantify internalisation, the fluorescent component is first attached to the material of interest and incubated with cells for a desired length of time. Cooling

the cells to 4°C arrests endocytosis, allowing the quencher component to interact with remaining surface-accessible sensor, but not internalised material (**Figure 1b**). For this reason, it is critical that the quencher component is not membrane permeable and remains restricted to the extracellular surroundings.

Quenching Efficiency in Solution.

The quenching capacity of BHQ2 functionalised with either mTet (**SI Figure 11a**) or Tet (**SI Figure 11b**) were compared to the DNA internalisation sensor. Addition of BHQ2-Tet to the fluorescent click component in solution caused an immediate reduction in the intensity (**SI Figure 12**). Both the DNA sensor quenched with its complementary oligonucleotide and click sensor quenched with BHQ2-Tet, reached their maximum signal reduction rapidly (<5 min), with no further quenching seen after 6 minutes (**Figure 2a**). The quenched product of both these sensors was stable, with no change seen over an hour. The reaction of the fluorescent click component with BHQ2-mTet was much slower and took approximately one hour to reach completion (**Figure 2a**). The reaction rate of BHQ2-mTet quencher with the click sensor was deemed too slow to be practical in live cell experiments, so we instead focused on the Tet quencher.

The equilibrium quenching efficiency was similar for both tetrazine quenchers (~75%) and was lower than for the DNA sensor (~99%) (**SI Figure 13**). However, this difference can be compensated for when calculating internalisation (**Equation 1**) by using a 4°C control to determine the quenching efficiency. Furthermore, the signal-to-noise is similar to anti-dye antibodies³² and vastly superior to pH-responsive dyes such as pHrodo. A change in intensity of only ~50% is observed when changing from pH 7.5 to 4.5 (**SI Figure 14**), similar to the transition in pH experienced during internalisation and trafficking through the endo/lysosomal pathway.

In Vitro Quenching.

After establishing the quencher component could switch off the signal from the fluorescent component in solution, we tested the ability to quench signal when attached to a protein bound to the cell surface. The click sensor was conjugated using carbodiimide and N-hydroxysuccinimide (EDC/NHS) chemistry^{45,46} to transferrin (Tf), an 80 kDa protein involved in the transport of iron into cells.⁴⁷ Reaction conditions were optimised to minimise protein cross linking (as assessed via SDS-PAGE (**SI Figure 15a**)). While a small band was present above the 75 kDa ladder marker, indicating partial crosslinking, the majority of the labelled protein corresponded to monomeric transferrin.

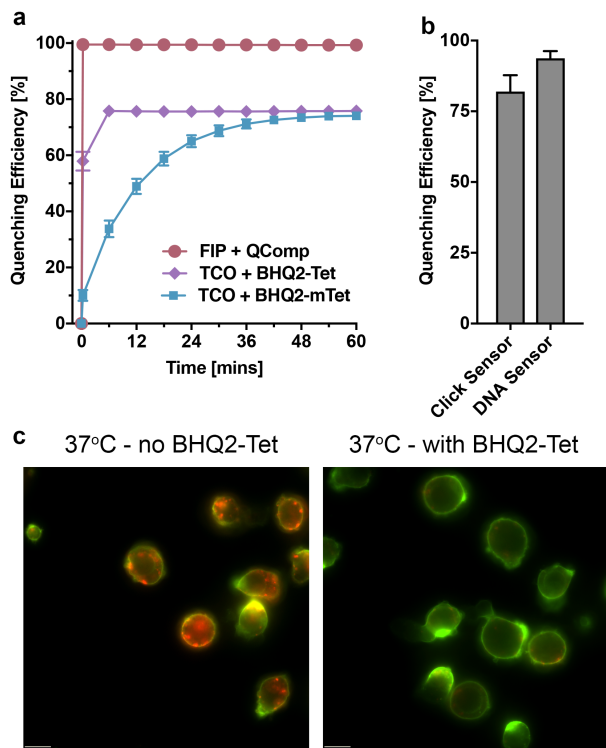


Figure 2. Sensor response to BHQ2 quencher tetrazine in solution and *in vitro*. (a) Kinetics of quenching 0.6 μM TCO click with 5 equivalents of tetrazine or methyl-tetrazine quencher and DNA sensor with complementary DNA quencher strand (QComp) in solution. The mean of $n = 3$ data points is plotted with error bars representing the standard deviation. (b) Comparison of transferrin labeled with sCy5-TCO or the DNA sensor quenched with BHQ2-Tet or QComp on transferrin. Transferrin at $15 \mu\text{g mL}^{-1}$ was bound to C1R cells at 4°C for 15 minutes before washing twice and incubation at either 4°C or 37°C for 20 minutes before quenching with $0.25 \mu\text{M}$ BHQ2-Tet or $0.60 \mu\text{M}$ QComp before analysis by flow cytometry. Quenching efficiency calculated from duplicate binding samples, quenched in triplicate from $n = 4$ (click sensor) and $n = 2$ (DNA sensor) separate experiments. Results were combined to give an overall average with error bars representing the standard deviation. (c) Fluorescence microscopy images of C1R cells incubated with $15 \mu\text{g mL}^{-1}$ Tf labelled with the click sensor for 25 minutes and WGA-AF488 for 5 minutes at 37°C , with or without $1.7 \mu\text{M}$ BHQ2-Tet. Scale bar = $10 \mu\text{m}$.

Sensor attached to Tf and bound to the cell surface of C1R cells at 4°C was quenched by BHQ2-Tet. The fluorescence was reduced by approximately 82% compared to 94% when using the DNA sensor (Figure 2b). While BHQ2-Tet was effective at quenching the surface signal, it

was also found to be membrane permeable, and quenched internalised Tf. At 37°C , Tf was observed both as a ring around the cell that localises with the cell membrane stain (WGA-AF488), and as punctate structures within the cell (Figure 2c, panel 1). When BHQ2-Tet was added at 37°C , the punctate structures within the cell also disappeared (Figure 2c, panel 2). The small size and lack

of charge of the BHQ2-Tet conjugate suggests that it can pass freely through the plasma membrane.

To overcome this, we engineered the quencher to possess increased hydrophilicity and size. The quencher component was modified to include two PEG linkers between the quencher and Tet group, as well as an additional PEG linker terminated with a carboxylic acid. In addition, the BHQ2 was replaced with sulfonated QSY21 (sQSY) as the quenching dye (SI Figure 16). These modifications resulted in a 2-fold increase in the molecular weight of the quencher component, as well as introducing several charged groups, which together assists in preventing diffusion across the cell membrane. As the

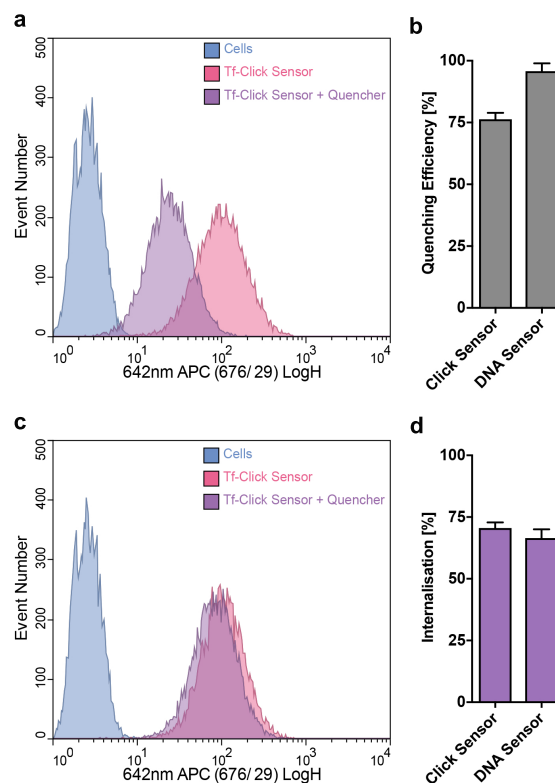


Figure 3. Flow cytometry analysis of transferrin quenching and internalisation with sQSY-Tet in C1R cells. (a) Representative histogram of cells incubated with Tf-sCy5-TCO at $15 \mu\text{g mL}^{-1}$ at 4°C for 15 minutes, washed twice and then incubated for a further 15 minutes at 4°C before quenching with sQSY-Tet. (b) Quenching efficiency of the click sensor (sCy5-TCO) or DNA sensor conjugated to transferrin and bound to the cell surface at 4°C (c) Representative histogram of cells incubated with Tf-sCy5-TCO at $15 \mu\text{g mL}^{-1}$ at 4°C for 15 minutes, washed twice and then incubated for a further 15 minutes at 37°C before quenching with sQSY-Tet. (d) Internalisation efficiency calculated from duplicate binding samples, quenched in triplicate from $n = 4$ (click sensor) and $n = 2$ (DNA sensor) separate experiments.

quencher component is not attached to the material of interest, the increased molecular weight and charge does not affect its innate intracellular trafficking.

The quenching efficiency of the hydrophilic quencher sQSY-Tet was similar to that of BHQ2-Tet, both in solution and on the cell surface. Within approximately 30 seconds of the addition of sQSY-Tet to the sensor in solution, the fluorescence dropped by ~84% (SI Figure 17). Addition of sQSY-Tet to sensor conjugated to transferrin and bound to the cell surface at 4°C caused a shift in the fluorescence histogram (Figure 3a) which corresponded to a quenching efficiency of 76% (Figure 3b). At 37°C, the

sQSY-Tet was not able to diffuse through the cell membrane, and only the surface fluorescence was quenched (Figure 3c). The amount of Tf uptake calculated via Equation 1 and when using the click sensor quenched with sQSY-Tet ($71 \pm 2\%$) agreed well with the internalisation determined using the DNA sensor ($67 \pm 4\%$) (Figure 3d), with no statistical significant difference between the two values (two-tailed P-value = 0.1503, unpaired t-test). The consistency between the two methods demonstrates the click sensor functions as intended and can be used to accurately quantify the internalisation of proteins. In addition, the sensor is highly specific, as the presence of the

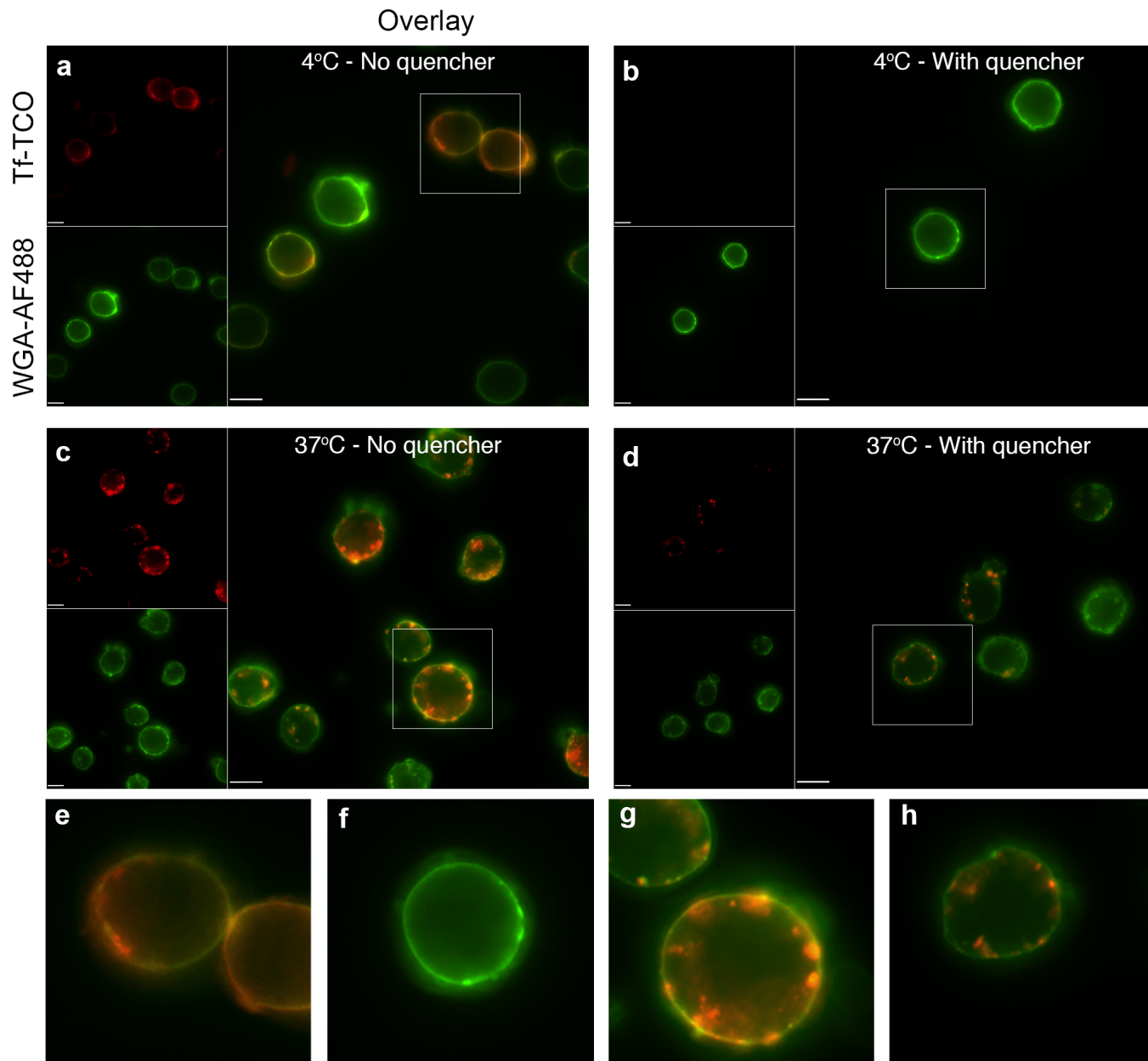


Figure 4. Extracellular, but not intracellular transferrin labeled with the click sensor is quenched by sQSY-Tet. C1R cells incubated with $15 \mu\text{g mL}^{-1}$ transferrin labeled with the sCy5-TCO click sensor at 4°C for 10 minutes, washed twice, then incubated for a further 25 minutes at (a) 4°C without or (b) with addition of $1.8 \mu\text{M}$ sQSY-Tet. Cells incubated for a further 25 minutes at 37°C (c) without and (d) with quencher. (e-h) Zoomed views of the boxed areas in (a-d) respectively. Scale bar = 10 μm .

quencher had minimal effect on the fluorescence of a separate cell surface marker. Incubation at either 4°C or 37°C with sQSY-Tet quencher caused negligible change in the WGA-AF488 signal (SI Figure 18a, b).

The sensor also allows internalisation to be visualised by fluorescence microscopy. Transferrin bound to the cell surface at 4°C (Figure 4a) was observed as a ring around the cell membrane that localises with WGA-AF488, and disappears when quenched with sQSY-Tet (Figure 4b). At 37°C with both internalised and extracellular transferrin present (Figure 4c), sQSY-Tet quenched the external fluorescence but did not affect the endocytosed fraction (Figure 4d). This further demonstrates the effectiveness of the fluorescent component and sQSY-Tet in determining internalisation.

Nanobody and Antibody Internalisation.

After establishing the sensor functioned correctly with Tf, we moved to demonstrating its use on both smaller and larger proteins. Nanobodies are composed of a single antigen binding domain and consequently have a 10-fold smaller molecular weight (15 kDa) relative to regular immunoglobulin G antibodies (150 kDa).⁴⁸ Unlike IgG antibodies, nanobodies can be expressed in *Escherichia coli*⁴⁹ making them easier to produce. They also have similar binding affinities and have been engineered to possess improved stability.⁵⁰ The internalisation of nanobodies is difficult to study using the DNA sensor as the sensor and nanobody have a similar molecular weight (7 kDa and 15 kDa respectively). This makes removal of unconjugated oligonucleotide from the nanobody difficult, and has the potential to significantly interfere with its binding and trafficking, as a third of the nanobody/sensor conjugate weight is due to the sensor.

As a proof-of-principal, we chose to conjugate the click sensor to the nanobody (2D3)²⁵ and the monoclonal antibody (trastuzumab), both of which bind to the human epidermal growth factor receptor 2 (HER2). HER2 is a tyrosine kinase involved in a range of cellular processes and is found overexpressed in some breast and ovarian cancers.^{51,52} It has been reported that the receptor remains localised to the cell surface and is not internalised into endosomes.⁵³ However this, along with the question if trastuzumab can trigger internalisation of HER2, is debated.^{54,55}

To investigate the role of protein binding to HER2 and the induction of internalisation, we conjugated the click sensor to both the antibody and nanobody for this receptor. Labelling 2D3 using the same conditions as for Tf resulted in a single fluorescent band in the correct position for the expected size via SDS-PAGE (SI Figure 15b), however these conditions caused cross linking of trastuzumab

(SI Figure 19). Reducing the concentration of EDC significantly decreased the amount of cross linking while maintaining a satisfactory degree of labelling (SI Figure 19).

The labelled proteins were incubated with SKOV-3 cells, an ovarian cancer cell line that overexpresses HER2.⁵⁶ 2D3 was added at double the molar concentration of trastuzumab to account for the differences in the number of binding sites between the two proteins. When the proteins were bound to the cell surface at 4°C, a quenching efficiency of ~80% was observed (Figure 5a). In addition, there was no significant difference in the quenching efficiency obtained at either the 30 minute or 4 hour time point (SI Figure 20). This demonstrates the stability of the sensor under extracellular conditions and that only one

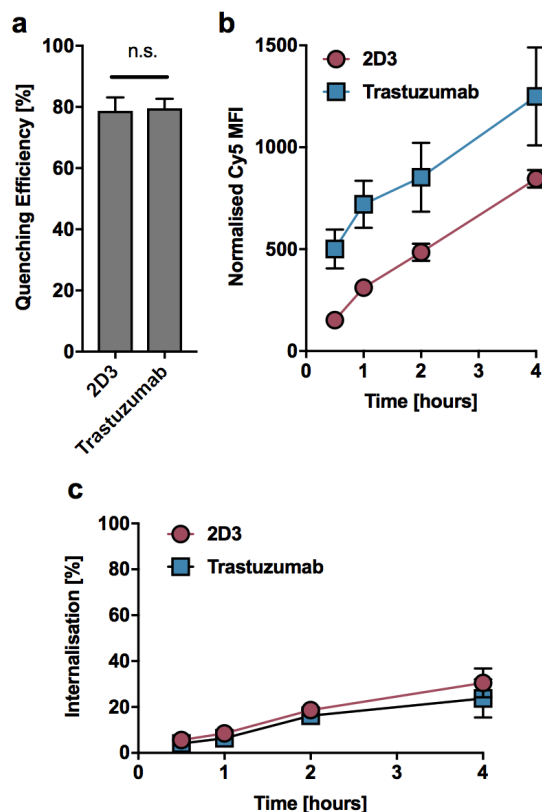


Figure 5. Quenching and internalisation of nanobody (2D3) and anti-HER2 (trastuzumab) antibody labelled with the click sensor by flow cytometry in SKOV-3 cells. Cells at 4°C were incubated with 2D3 (8 nM) or trastuzumab (4 nM) at 37°C or at 4°C over a 4 hour time period before adding sQSY-Tet at a concentration of 0.5 μM or PBS. (a) Average quenching efficiency of 2D3 and trastuzumab labelled with the click sensor. (b) Association of 2D3 and trastuzumab with SKOV-3 cells at 37°C. Mean fluorescence intensity values were divided by the degree of labelling. (c) Internalisation over time. All graphs show the mean from two experiments in triplicate, with any error bars representing the standard deviation. (n.s. = non-significant, P = 0.7660 unpaired t-test)

4°C binding control time point is sufficient to experimentally determine a correction factor to compensate for incomplete surface quenching.

At 37°C, 2D3 and trastuzumab increasingly associated with cells over time with both proteins following a similar trend (**Figure 5b**). However, only a small fraction of bound protein entered cells while most of the protein remained on the cell surface. After 30 minutes, only ~6% of the protein had internalised (**Figure 5c**). This slowly increased over time and no statistical difference ($P = 0.4565$, unpaired t-test) in the final amount of uptake was seen between 2D3 (~30%) or trastuzumab (~24%).

These results demonstrate that both the nanobody and antibody are internalised into SKOV-3 cells to some degree. However, it is not clear by which mechanism the proteins are being taken up in to cell. This could be explored using a panel of inhibitors in conjunction with the click internalisation sensor, in a similar manner to the DNA sensor in probing the internalisation of nanoparticles.⁵⁷ Furthermore, it been reported that trastuzumab bound to HER2 can passively recycle following endocytosis of the receptor in SKBr3 cells.⁵⁸ The recycling of trastuzumab and 2D3 could also be investigated using the click internalisation system, as has been demonstrated using the DNA sensor.²⁷

CONCLUSIONS

Quantifying the internalisation of materials is important for gaining further insight into endocytic cellular processes and in improving the delivery of therapeutics. There is a need for simple methods to achieve this, which are ideally compatible with conventional fluorescence based techniques, such as flow cytometry and microscopy. To address this, we have developed a click-based sensor for quantifying the uptake of materials into cells. The sensor rapidly and specifically quenches the fluorescence of tagged material on the cell surface. It has a similar size and net charge compared to a typical fluorescent dye used in the labeling of proteins and nanoparticles, which is an advantage over the existing DNA internalisation sensor, particularly for labelling small proteins. We anticipate this probe will be a useful tool across multiple disciplines in the study of cellular uptake.

ASSOCIATED CONTENT

Supporting Information

The Supporting Information is available free of charge on the ACS Publications website.

The document includes chemical structures, SDS-PAGE images, supplementary fluorescence data and detailed information on the conditions for LCMS, HPLC and HRMS (PDF)

AUTHOR INFORMATION

Corresponding Author

* Dr. Angus Johnston

Drug Delivery, Disposition and Dynamics Monash Institute of Pharmaceutical Sciences, Monash University
Parkville, Victoria 3052, Australia

E-mail: angus.johnston@monash.edu

Author Contributions

The manuscript was written through contributions of all authors. All authors have given approval to the final version of the manuscript.

Funding Sources

Any funds used to support the research of the manuscript should be placed here (per journal style).

ACKNOWLEDGMENT

The authors wish acknowledge Josh Conner (Monash University, Melbourne) for the synthesis of SulfoCyanine5 and description of HPLC/LCMS conditions as well as Dr. Jason Dang (Monash University) for performing HRMS.

ABBREVIATIONS

AF488, Alexa Fluor 488, BHQ2, BlackHole Quencher2; sCy5, Sulfo-Cyanine 5, DIBO, Dibenzocyclooctyne; mTet, methyltetrazine; TCO, *trans*-Cyclooctene; Tet, Tetrazine; Tf, Transferrin; WGA, Wheat germ agglutinin; EDC, 1-Ethyl-3-(3-dimethylaminopropyl)carbodiimidecarbodiimide; NHS, N-hydroxysuccinimide

REFERENCES

- (1) Mayle, K. M.; Le, A. M.; Kamei, D. T. The Intracellular Trafficking Pathway of Transferrin. *Biochim. Biophys. Acta* **2012**, *1820* (3), 264–281.
- (2) Sorkin, A.; von Zastrow, M. Endocytosis and Signalling: Intertwining Molecular Networks. *Nat. Rev. Mol. Cell Biol.* **2009**, *10* (9), 609–622.
- (3) Lim, J. P.; Gleeson, P. A. Macropinocytosis: An Endocytic Pathway for Internalising Large Gulps. *Immunol. Cell Biol.* **2011**, *89* (8), 836–843.
- (4) Canton, I.; Battaglia, G. Endocytosis at the Nanoscale. *Chem. Soc. Rev.* **2012**, *41*, 2718–2739.
- (5) Gottstein, C.; Wu, G.; Wong, B. J.; Zasadzinski, J. A. Precise Quantification of Nanoparticle Internalization. *ACS Nano* **2013**, *7* (6), 4933–4945.
- (6) Nuutila, J.; Lilius, E.-M. Flow Cytometric Quantitative Determination of Ingestion by Phagocytes Needs the Distinguishing of Overlapping Populations of Binding and Ingesting Cells. *Cytometry. A* **2005**, *65* (2), 93–102.
- (7) Van Amersfoort, E. S.; Van Strijp, J. A. G. Evaluation of a Flow Cytometric Fluorescence Quenching Assay of Phagocytosis of Sensitized Sheep Erythrocytes by Polymorphonuclear Leukocytes. *Cytometry* **1994**, *17*, 294–301.
- (8) Göstring, L.; Chew, M. T. C.; Orlova, A.; Höidén-Guthenberg, I.; Wennborg, A.; Carlsson, J.; Frejd, F. Y.

- Quantification of Internalization of EGFR-Binding Affibody Molecules: Methodological Aspects. *Int. J. Oncol.* **2010**, *36*, 757–763.
- (9) Kondapalli, K. C.; Hack, A.; Schushan, M.; Landau, M.; Ben-Tal, N.; Rao, R. Functional Evaluation of Autism-Associated Mutations in NHE9. *Nat. Commun.* **2013**, *4* (May), 2510.
- (10) Adie, E. J.; Kalinka, S.; Smith, L.; Francis, M. J.; Marengi, A.; Cooper, M. E.; Briggs, M.; Michael, N. P.; Milligan, G.; Game, S. A pH-Sensitive Fluor, CypHer5, Used to Monitor Agonist-Induced G Protein-Coupled Receptor Internalization in Live Cells. *Biotechniques* **2002**, *33* (5), 1152–1157.
- (11) Liu, H.; Johnston, A. P. R. A Programmable Sensor to Probe the Internalization of Proteins and Nanoparticles in Live Cells. *Angew. Chemie - Int. Ed.* **2013**, *52* (22), 5744–5748.
- (12) Reuter, a.; Panozza, S. E.; Macri, C.; Dumont, C.; Li, J.; Liu, H.; Segura, E.; Vega-Ramos, J.; Gupta, N.; Caminschi, I.; et al. Criteria for Dendritic Cell Receptor Selection for Efficient Antibody-Targeted Vaccination. *J. Immunol.* **2015**, *194* (6), 2696–2705.
- (13) Ana-Sosa-Batiz, F.; Johnston, A. P. R.; Liu, H.; Center, R. J.; Rerks-Ngarm, S.; Pitisuttithum, P.; Nitayaphan, S.; Kaewkungwal, J.; Kim, J. H.; Michael, N. L.; et al. HIV-Specific Antibody-Dependent Phagocytosis Matures during HIV Infection. *Immunol. Cell Biol.* **2014**, *92* (April), 1–9.
- (14) Marks, K.; Nolan, G. Chemical Labeling Strategies for Cell Biology. *Nat. Methods* **2006**, *3* (8), 591–596.
- (15) Hinner, M. J.; Johnsson, K. How to Obtain Labeled Proteins and What to Do with Them. *Curr. Opin. Biotechnol.* **2010**, *21* (6), 766–776.
- (16) Sletten, E. M.; Bertozzi, C. R. Bioorthogonal Chemistry: Fishing for Selectivity in a Sea of Functionality. *Angew. Chemie - Int. Ed.* **2009**, *48* (38), 6974–6998.
- (17) Sletten, E. M.; Bertozzi, C. R. Bioorthogonal Reactions. *Acc. Chem. Res.* **2011**, *44* (9), 666–676.
- (18) Jewett, J. C.; Bertozzi, C. R. Cu-Free Click Cycloaddition Reactions in Chemical Biology. *Chem. Soc. Rev.* **2010**, *39* (4), 1272–1279.
- (19) Baskin, J. M.; Prescher, J. a.; Laughlin, S. T.; Agard, N. J.; Chang, P. V.; Miller, I. a.; Lo, A.; Codelli, J. a.; Bertozzi, C. R. Copper-Free Click Chemistry for Dynamic in Vivo Imaging. *Proc. Natl. Acad. Sci. U. S. A.* **2007**, *104* (43), 16793–16797.
- (20) Borrmann, A.; Milles, S.; Plass, T.; Dommerholt, J.; Verkade, J. M. M.; Wießler, M.; Schultz, C.; van Hest, J. C. M.; van Delft, F. L.; Lemke, E. A. Genetic Encoding of a Bicyclo[6.1.0]nonyne-Charged Amino Acid Enables Fast Cellular Protein Imaging by Metal-Free Ligation. *ChemBioChem* **2012**, *13* (14), 2094–2099.
- (21) Blizzard, R. J.; Backus, D. R.; Brown, W.; Bazewicz, C. G.; Li, Y.; Mehl, R. A. Ideal Bioorthogonal Reactions Using a Site-Specifically Encoded Tetrazine Amino Acid. *J. Am. Chem. Soc.* **2015**, *137* (32), 10044–10047.
- (22) Foley, J. W.; Locatell, L. J.; Zepp, C. M. Novel Xanthene Compounds and Photographic Products and Processes Employing the Same. Patent US4258118, 1981.
- (23) Mujumdar, R. B.; Ernst, L. A.; Mujumdar, S. R.; Lewis, C. J. Cyanine Dye Labeling Reagents: Sulfoindocyanine Succinimidyl Esters. *Bioconjug. Chem.* **1993**, *4* (2), 105–111.
- (24) Pisoni, D. S.; Todeschini, L.; Borges, A. C. A.; Petzhold, C. L.; Rodembusch, F. S.; Campo, L. F. Symmetrical and Asymmetrical Cyanine Dyes. Synthesis, Spectral Properties, and Bsa Association Study. *J. Org. Chem.* **2014**, *79* (12), 5511–5520.
- (25) Revets, H.; Hoogenboom, H. R. J. M. Method for Obtaining Polypeptide Constructs Comprising Two or More Single Domain Antibodies. Patent App. EP20080853257, 2010.
- (26) Gasteiger, E.; Hoogland, C.; Gattiker, A.; Duvaud, S.; Wilkins, M. R.; Appel, R. D.; Bairoch, A. Protein Identification and Analysis Tools on the ExPASy Server. In *The Proteomics Protocols Handbook*; Walker, J. M., Ed.; Humana Press, 2005; pp 571–607.
- (27) Dumont, C.; Chen, E. C. M.; Villadangos, J. A.; Johnston, A. P. R.; Mintern, J. D. DNA-Based Probes for Flow Cytometry Analysis of Endocytosis and Recycling. *Traffic* **2016**, *18*, 242–249.
- (28) Sambrook, J.; Russell, D. W. . *Molecular Cloning: A Laboratory Manual*; Cold Spring Harbor Laboratory: New York, 2001.
- (29) Richardson, W. H. Bayesian-Based Iterative Method of Image Restoration. *J. Opt. Soc. Am.* **1972**, *62* (1), 55–59.
- (30) Lucy, L. B. An Iterative Technique for the Rectification of Observed Distributions. *Astron. J.* **1974**, *79* (6), 745–749.
- (31) Bruce, M. a; Butte, M. J. Real-Time GPU-Based 3D Deconvolution. *Opt. Express* **2013**, *21* (4), 4766–4773.
- (32) Liao-Chan, S.; Daine-Matsuoka, B.; Heald, N.; Wong, T.; Lin, T.; Cai, A. G.; Lai, M.; D’Alessio, J. A.; Theunissen, J.-W. Quantitative Assessment of Antibody Internalization with Novel Monoclonal Antibodies against Alexa Fluorophores. *PLoS One* **2015**, *10* (6), 1–15.
- (33) Wetmur, J. G. DNA Probes: Applications of the Principles of Nucleic Acid Hybridization. *Crit. Rev. Biochem. Mol. Biol.* **1991**, *26* (3–4), 227–259.
- (34) Hariadi, R. F.; Yurke, B.; Winfree, E. Thermodynamics and Kinetics of DNA Nanotube Polymerization from Single-Filament Measurements. *Chem. Sci.* **2015**, *6*, 2252–2267.
- (35) Tyagi, S.; Kramer, F. R. Molecular Beacons: Probes That Fluoresce upon Hybridization. *Nat. Biotechnol.* **1996**, *14*, 303–308.
- (36) Tan, W.; Wang, K.; Drake, T. J. Molecular Beacons. *Curr. Opin. Chem. Biol.* **2004**, *8* (5), 547–553.
- (37) Levsky, J. M.; Singer, R. H. Fluorescence in Situ Hybridization: Past, Present and Future. *J. Cell Sci.* **2003**, *116* (14), 2833–2838.
- (38) Buxbaum, A. R.; Haimovich, G.; Singer, R. H. In the Right Place at the Right Time: Visualizing and Understanding mRNA Localization. *Nat. Rev. Mol. Cell Biol.* **2014**, *16* (2), 95–109.
- (39) Prigodich, A. E.; Seferos, D. S.; Massich, M. D.; Giljohann, D. a; Lane, B. C.; Mirkin, C. a. Nano-Flares for mRNA Regulation and Detection. *ACS Nano* **2009**, *3* (8), 2147–2152.
- (40) Machida, T.; Lang, K.; Xue, L.; Chin, J. W.; Winssinger, N. Site-Specific Glycoconjugation of Protein via Bioorthogonal Tetrazine Cycloaddition with a Genetically Encoded Trans-Cyclooctene. *Bioconjug. Chem.* **2015**, *26*, 802–806.
- (41) Rutkowska, A.; Thomson, D. W.; Vappiani, J.; Werner, T.; Mueller, K. M.; Dittus, L.; Krause, J.; Muelbaier, M.; Bergamini, G.; Bantscheff, M. A Modular Probe Strategy for Drug Localization, Target Identification and Target Occupancy Measurement on Single Cell Level. *ACS Chem. Biol.* **2016**, *11*, 2541–2550.
- (42) Rahim, M. K.; Kota, R.; Haun, J. B. Enhancing Reactivity for Bioorthogonal Pretargeting by Unmasking Antibody-Conjugated Trans -Cyclooctenes. *Bioconjug. Chem.* **2015**, *26* (2), 352–360.
- (43) Chen, W.; Wang, D.; Dai, C.; Hamelberg, D.; Wang, B.

- Clicking 1,2,4,5-Tetrazine and Cyclooctynes with Tunable Reaction Rates. *Chem. Commun.* **2012**, 48 (12), 1736.
- (44) Karver, M.; Weissleder, R.; Hilderbrand, S. A. Synthesis and Evaluation of a Series of 1,2,4,5-Tetrazines for Bioorthogonal Conjugation. *Bioconjug. Chem.* **2011**, 22, 2263–2270.
- (45) Staros, J. V.; Wright, R. W.; Swingle, D. M. Enhancement by N-Hydroxysulfosuccinimide of Water-Soluble Carbodiimide-Mediated Coupling Reactions. *Anal. Biochem.* **1986**, 156 (1), 220–222.
- (46) Sehgal, D.; Vijay, I. K. A Method for the High Efficiency of Water-Soluble Carbodiimide-Mediated Amidation. *Analytical biochemistry*. 1994, pp 87–91.
- (47) Huebers, H. A.; Finch, C. A. The Physiology of Transferrin and Transferrin Receptors. *Physiol. Rev.* **1987**, 67 (2), 520–582.
- (48) Muyldermans, S. Nanobodies: Natural Single-Domain Antibodies. *Annu. Rev. Biochem.* **2013**, 82 (1), 775–797.
- (49) Desmyter, A.; Spinelli, S.; Roussel, A.; Cambillau, C. Camelid Nanobodies: Killing Two Birds with One Stone. *Curr. Opin. Struct. Biol.* **2015**, 32, 1–8.
- (50) Steeland, S.; Vandenbroucke, R. E.; Libert, C. Nanobodies as Therapeutics: Big Opportunities for Small Antibodies. *Drug Discov. Today* **2016**, 21 (7), 1076–1113.
- (51) Arteaga, C. L.; Sliwkowski, M. X.; Osborne, C. K.; Perez, E. A.; Puglisi, F.; Gianni, L. Treatment of HER2-Positive Breast Cancer: Current Status and Future Perspectives. *Nat. Rev. Clin. Oncol.* **2011**, 9 (1), 16–32.
- (52) Pils, D.; Pinter, A.; Reibenwein, J.; Alfan, A.; Horak, P.; Schmid, B. C.; Hefler, L.; Horvat, R.; Reinthaller, A.; Zeillinger, R.; et al. In Ovarian Cancer the Prognostic Influence of HER2/neu Is Not Dependent on the CXCR4/SDF-1 Signalling Pathway. *Br. J. Cancer* **2007**, 96 (3), 485–491.
- (53) Hommelgaard, A. M.; Lerdrup, M.; van Deurs, B. Association with Membrane Protrusions Makes ErbB2 an Internalization-Resistant Receptor. *Mol. Biol. Cell* **2004**, 15 (April), 1557–1567.
- (54) Bertelsen, V.; Stang, E. The Mysterious Ways of ErbB2/HER2 Trafficking. *Membranes (Basel)*. **2014**, 4 (3), 424–446.
- (55) Ram, S.; Kim, D.; Ober, R. J.; Ward, E. S. The Level of HER2 Expression Is a Predictor of Antibody-HER2 Trafficking Behavior in Cancer Cells. *MAbs* **2014**, 6 (5), 1211–1219.
- (56) Luistro, L. L.; Rosinski, J. A.; Bian, H.; Bishayee, S.; Rameshwar, P.; Ponzio, N. M.; Ritland, S. R. Development and Characterization of a Preclinical Ovarian Carcinoma Model to Investigate the Mechanism of Acquired Resistance to Trastuzumab. *Int. J. Oncol.* **2012**, 41 (2), 639–651.
- (57) Mann, S. K.; Czuba, E.; Selby, L. I.; Such, G. K.; Angus, P.; Johnston, R. Quantifying Nanoparticle Internalization Using a High Throughput Internalization Assay. *Pharm. Res.* **2016**, 33, 2421–2432.
- (58) Austin, C. D.; De Mazière, A. M.; Pisacane, P. I.; van Dijk, S. M.; Eigenbrot, C.; Sliwkowski, M. X.; Klumperman, J.; Cheller, R. H. Endocytosis and Sorting of ErbB2 and the Site of Action of Cancer Therapeutics Trastuzumab and Geldanamycin. *Mol. Biol. Cell* **2004**, 15, 5268–5282.
-

Supporting Information

Quantifying Cellular Internalisation with a Fluorescent Click Sensor

Laura I. Selby^{†,‡}, Luigi Aurelio[†], Daniel Yuen^{†,‡}, Bim Graham[†] and Angus P. R. Johnston^{*†,‡}

[†]Monash Institute of Pharmaceutical Sciences, Monash University, Parkville, Victoria, Australia, [‡]ARC Centre of Excellence in Convergent Bio-Nano Science and Technology, Monash University, Parkville, Australia

E-mail: angus.johnston@monash.edu

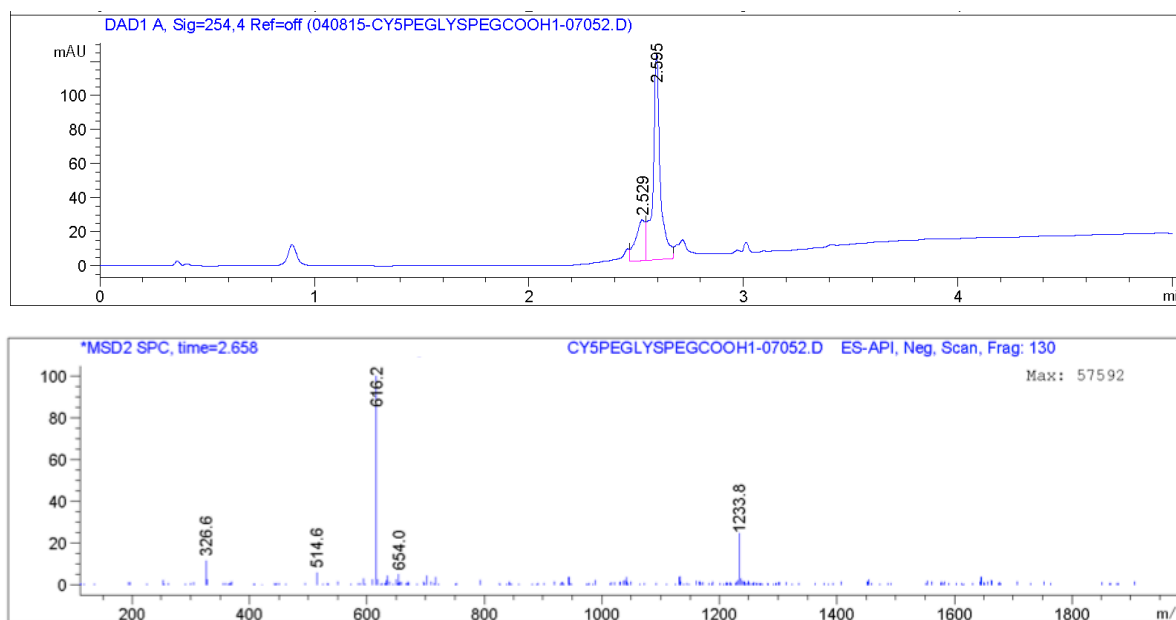
Liquid Chromatography and Mass Spectrometry Detailed Information

Liquid chromatography – mass spectrometry (LCMS) was performed on an Agilent 6100 Series Single Quad LCMS with a photodiode array detector (214/254 nm) coupled to an Agilent 1200 Series HPLC with a G1311A quaternary pump, G1329A thermostated auto sampler and 1200 Series G1314B variable wavelength detector with a scan range between 100–1000 m/z and a 5-minute acquisition time.

High-performance liquid chromatography (HPLC) was performed on an Agilent 1260 series modular HPLC fitted with a G1312B binary pump, G1316A compartment equipped with an Agilent Eclipse Plus C18 3.5 μm , 4.6 x 100 mm column and a G1312B diode array detector using an elution protocol of 0 – 10 min, gradient from 5% MeCN/0.1% TFA/95% H₂O/0.1% TFA to 100% MeCN/0.1% TFA with a flow rate of 1 mL min⁻¹. Preparative high-performance liquid chromatography (HPLC) used a Grace Alltima C8 5 μ particle size, 22 x 250 mm column.

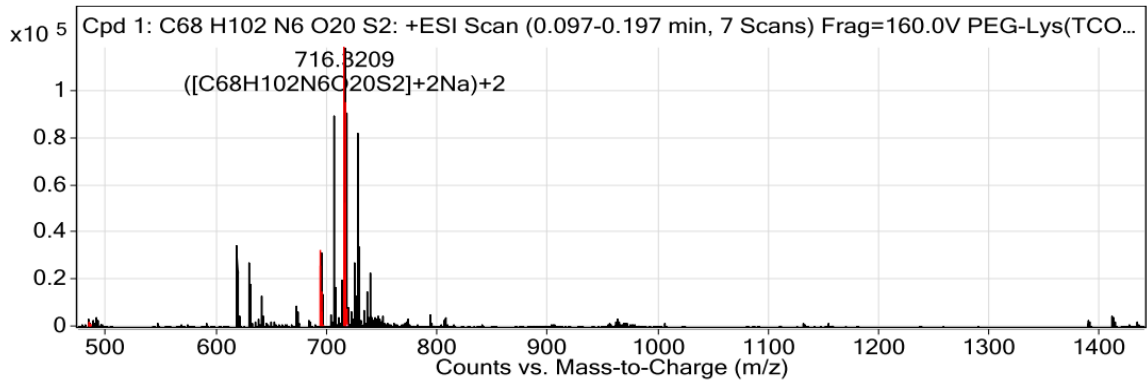
High resolution – mass spectrometry (HRMS) was performed on a Waters LCT TOF LCMS Mass Spectrometer coupled to a 2795 Alliance Separations module. All data was acquired and mass corrected via a dual-spray Leucine Enkephaline reference sample. Mass spectra were created by averaging the scans across each peak and background subtracted of the TIC. Acquisition and analysis were performed using the Masslynx software version 4.1.

Liquid Chromatography Traces and Mass Spectra

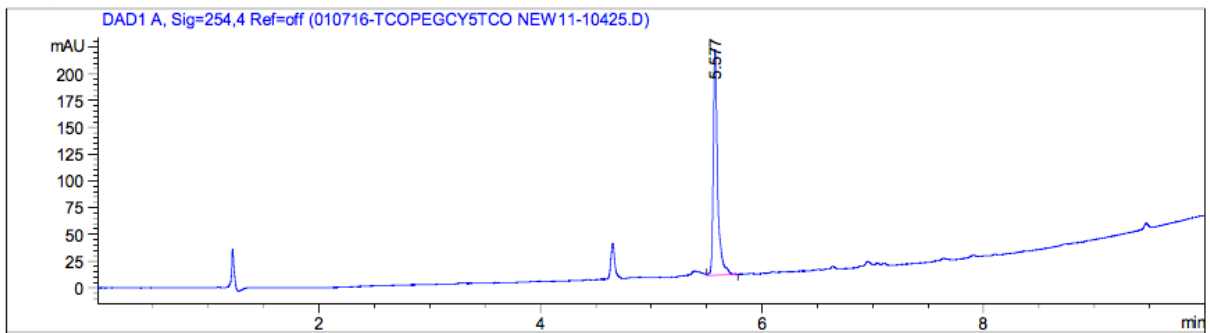


SI Figure 1. LCMS absorbance trace and mass spectrum of sCy5-PEG-Lys-PEG-COOH.

MS Zoomed Spectrum

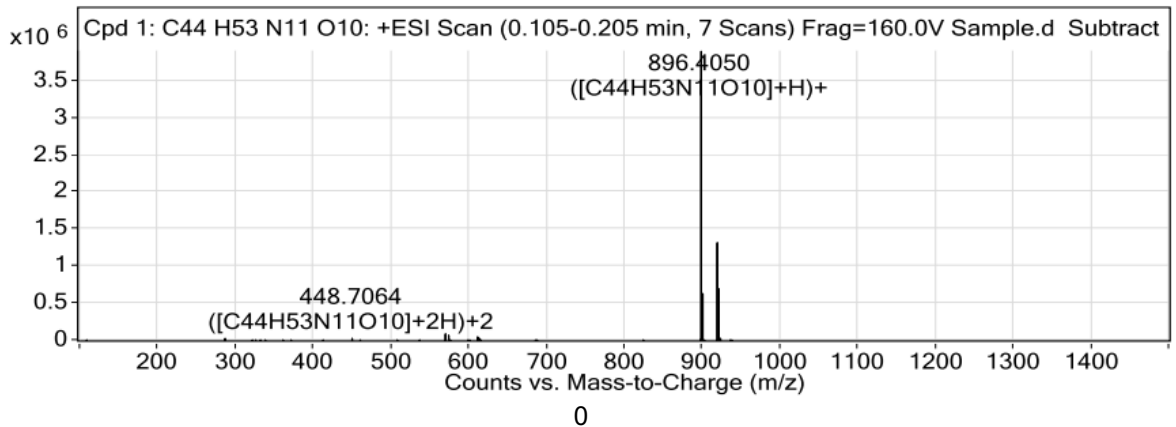


SI Figure 2. HRMS spectra of Cy5-PEG-Lys(TCO)-PEG-COOH.

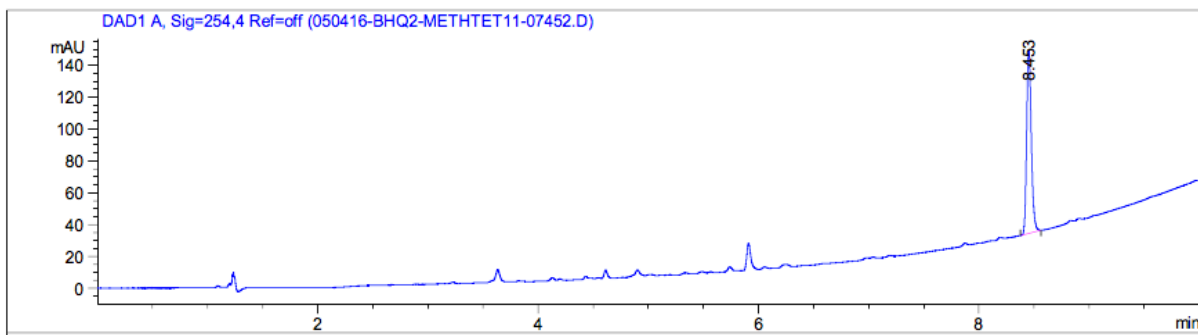


SI Figure 3. Analytical HPLC absorbance trace of Cy5-PEG-Lys(TCO)-PEG-COOH.

MS Spectrum

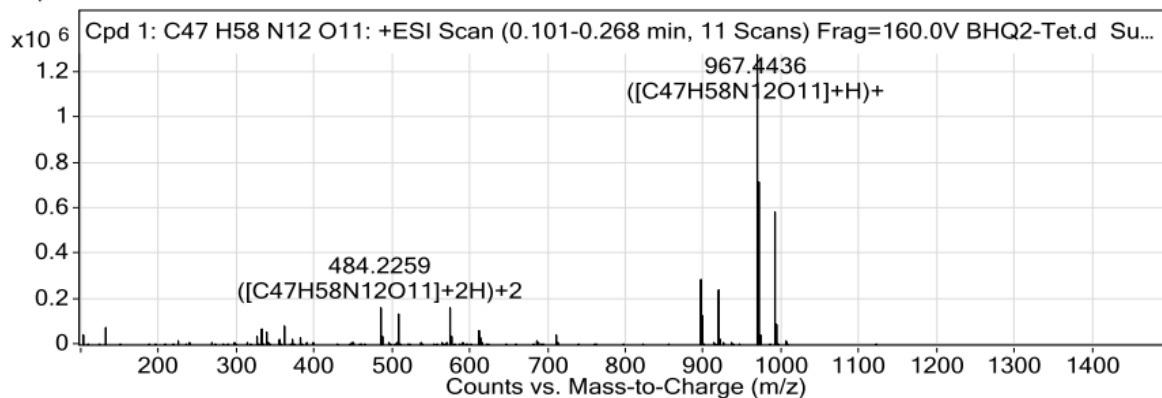


SI Figure 4. HRMS spectra of BHQ2-mTet.

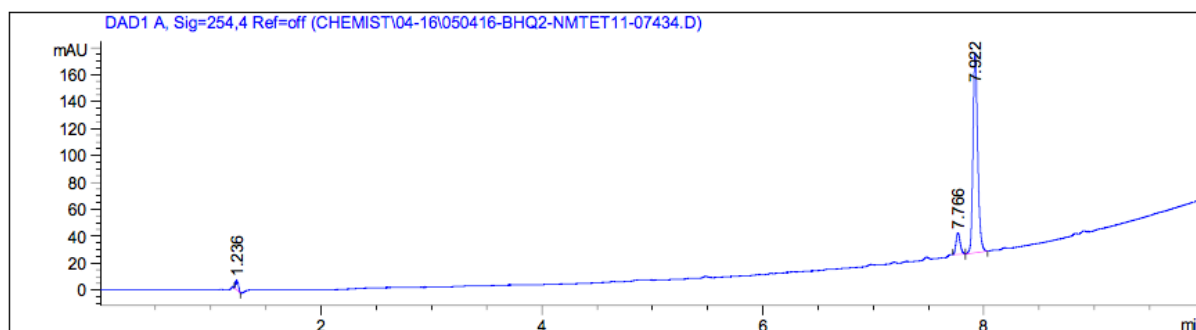


SI Figure 5. Analytical HPLC absorbance trace of BHQ2-mTet.

MS Spectrum

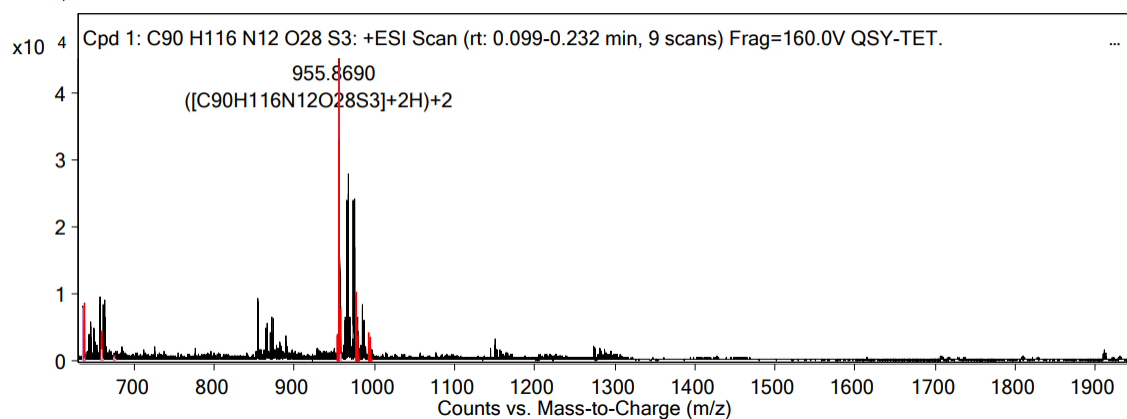


SI Figure 6. HRMS spectra of BHQ2-Tet.

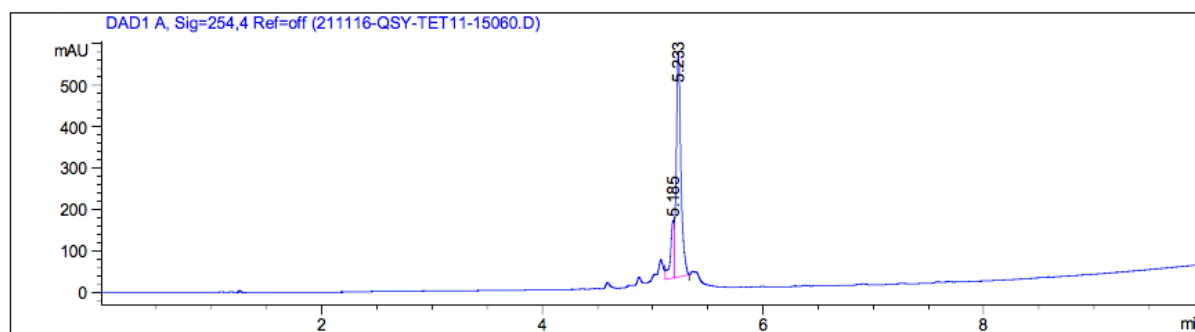


SI Figure 7. Analytical HPLC absorbance trace of BHQ2-Tet.

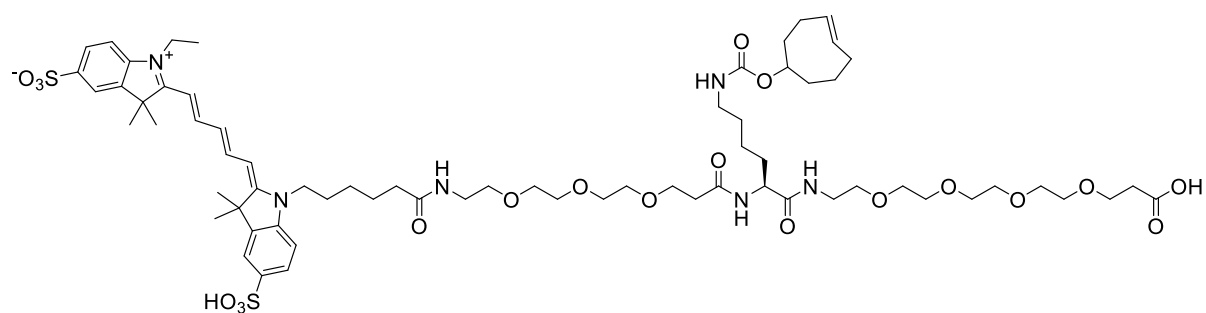
MS Zoomed Spectrum



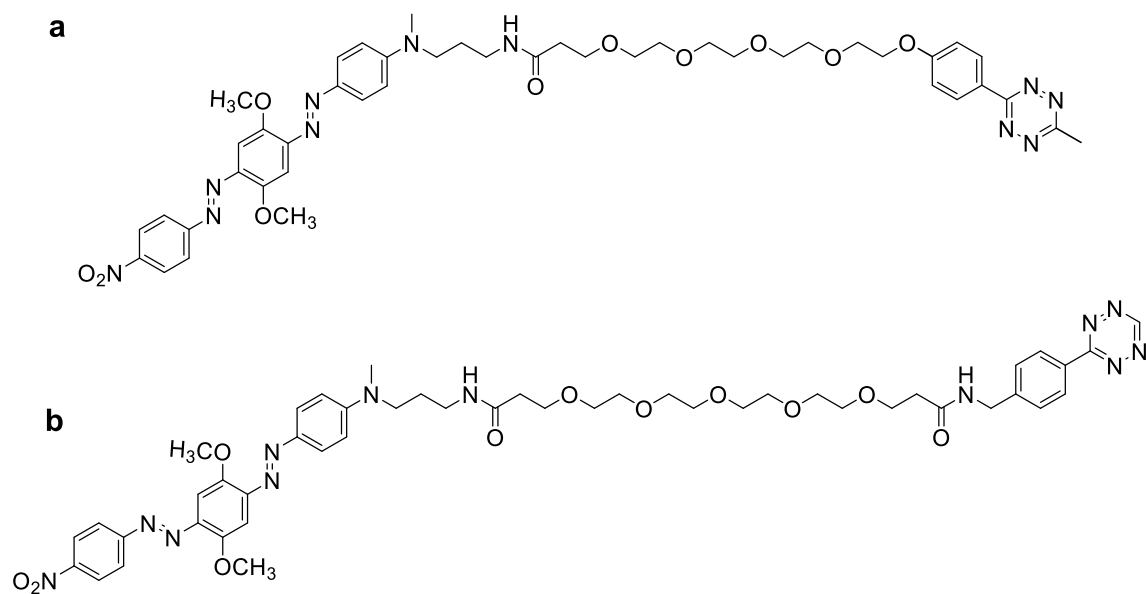
SI Figure 8. HRMS spectra of sQSY-Tet.



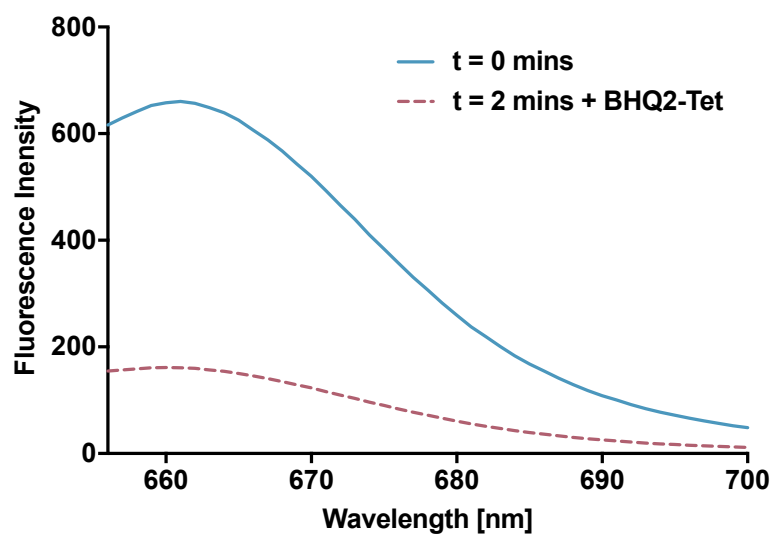
SI Figure 9. Analytical HPLC absorbance trace of sQSY-Tet.



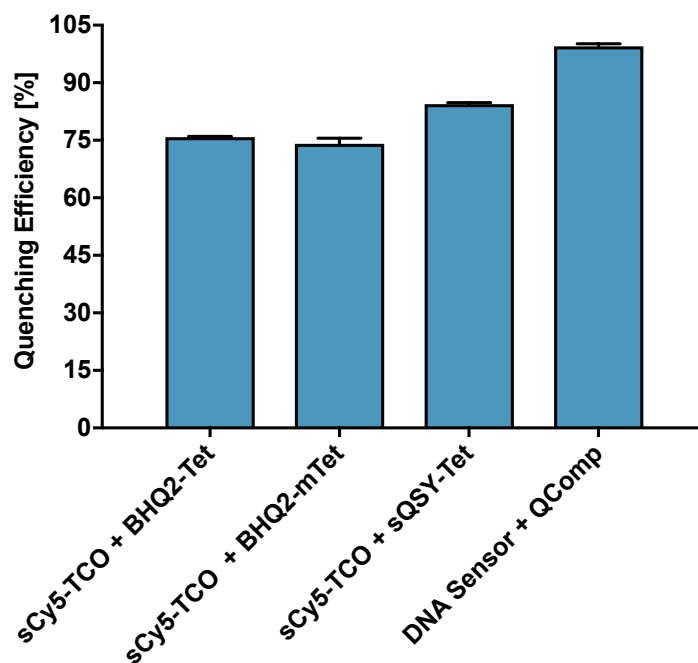
SI Figure 10. Chemical structure of the click sensor, sCy5-TCO.



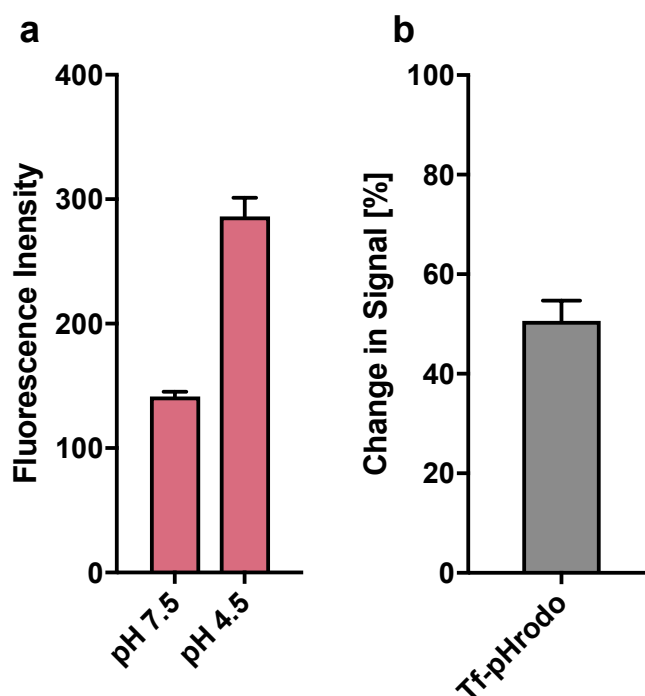
SI Figure 11. Chemical structure of the click-quenchers with BlackHole Quencher 2. (a) BHQ2-mTet. (b) BHQ2-Tet.



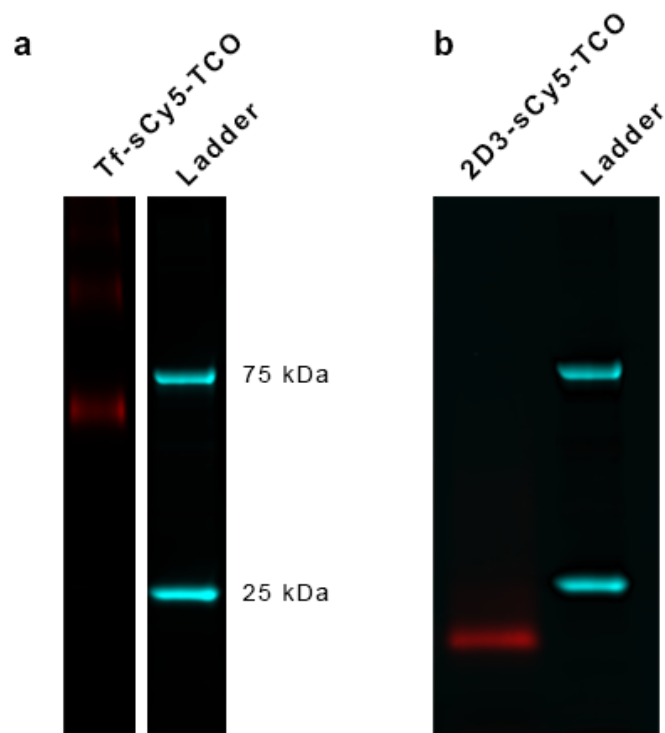
SI Figure 12. Quenching in solution of 0.6 μM TCO click sensor with 5 equivalents of BHQ2-Tet.



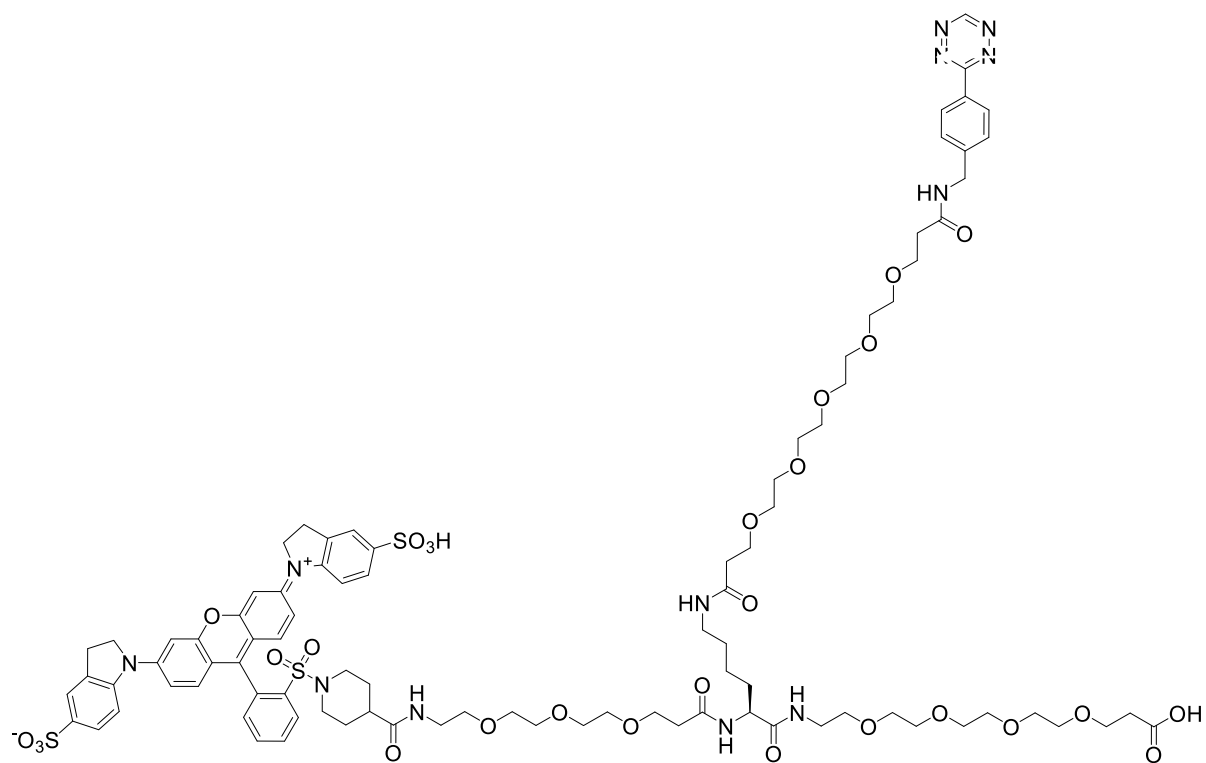
SI Figure 13. Maximum quenching efficiency in solution. 0.6 μM TCO or DNA sensor quenched with 5 equivalents of the corresponding quencher until the signal stabilised ($t = 0.5$ mins for DNA + Qcomp and TCO + sQSYtet, $t = 6$ minutes for TCO + sQSY-Tet and $t = 60$ mins for TCO + BHQ2-mTet). Mean of $n = 3$ or $n = 2$ samples (TCO + sQSY-Tet) is plotted with error bars representing the standard deviation.



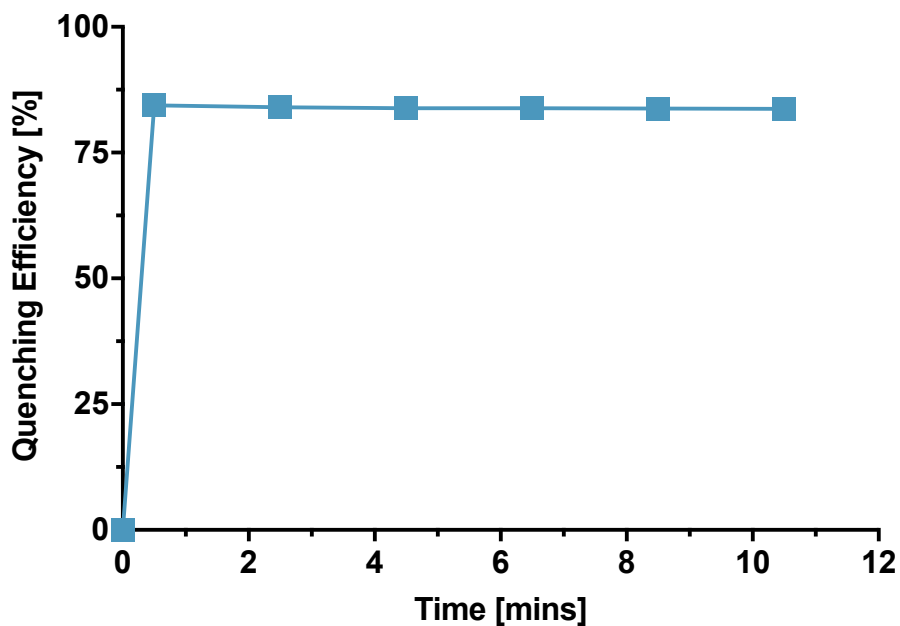
SI Figure 14. Fluorescence of pHrodo red, a pH responsive dye conjugated to transferrin. (a) Effect of pH on the fluorescence of 20 μg transferrin labelled with pHrodo red, equivalent to a final concentration of dye at 0.25 nM in sodium citrate/PBS buffer. Samples were excited at 570 nm with emission measured between 575 – 700 nm using a slit with 5 nm. (b) Percentage increase in fluorescence intensity between pH 7.5 and pH 4.5. Mean of the fluorescence intensity or change in fluorescence at 585 nm is plotted in triplicate with error bars representing the standard deviation.



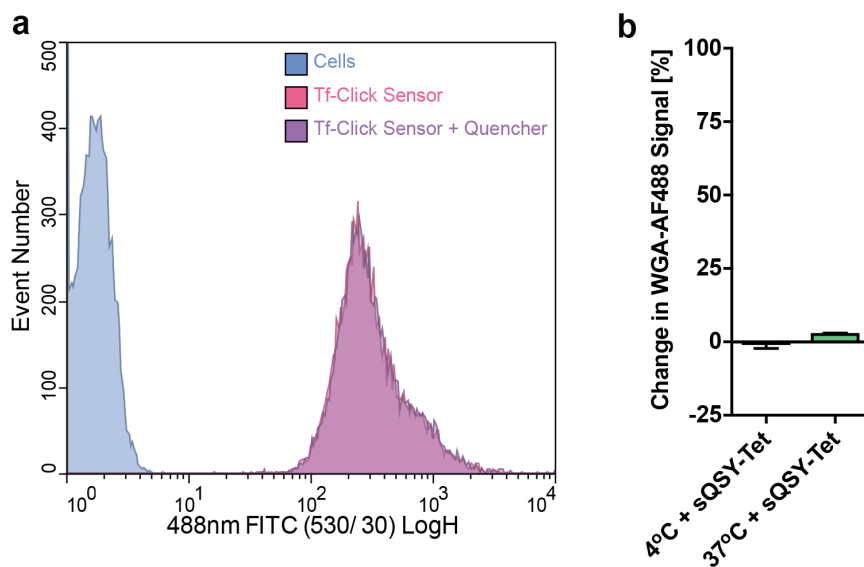
SI Figure 15. In-gel fluorescence image of a SDS-PAGE with (a) transferrin and (b) 2D3 labelled with the sCy5-TCO click (red) sensor using EDC/NHS, in reference to a protein ladder (blue).



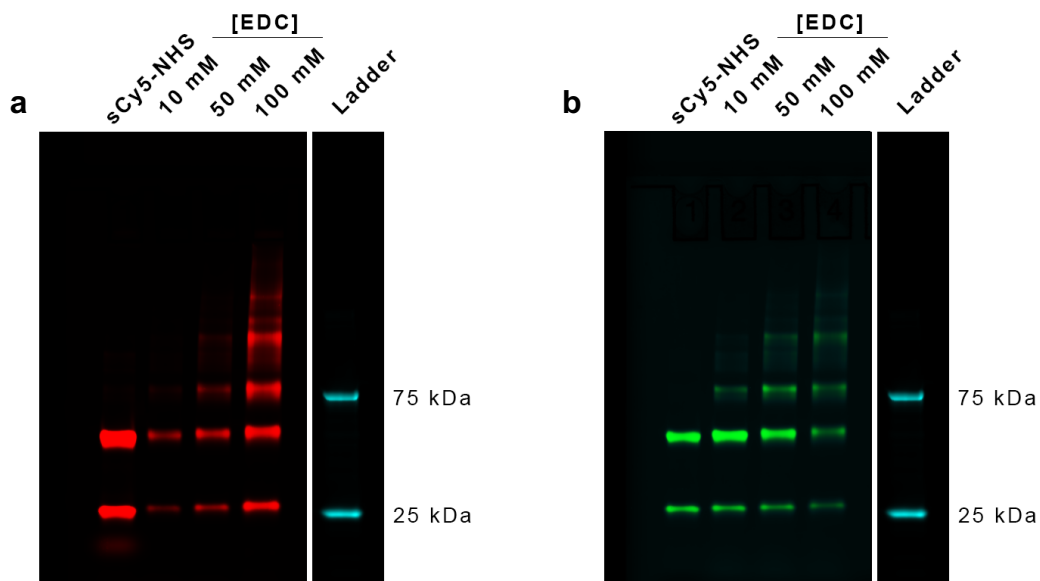
SI Figure 16. Chemical structure of the click-quencher with sulfoQSY-21 (sQSY-Tet).



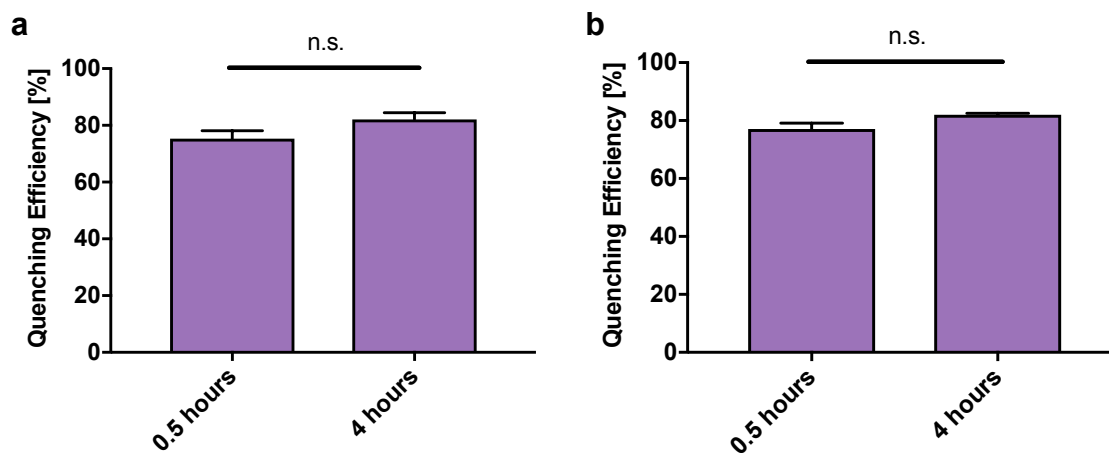
SI Figure 17. sQSY-Tet kinetics and efficiency. Quenching of 0.6 μM TCO click sensor with 5 equivalents of sQSY-Tet. Mean of $n = 2$ data points plotted with error bars representing the standard deviation.



SI Figure 18. Effect of quencher on WGA-AF488 fluorescence. (a) Representative histograms of cells labelled with Tf-sCy5-TCO and WGA-AF488 in the presence of 0.6 μM sQSY-Tet (purple) or without quencher (red), compared to control cells (blue). (b) Percentage change in FITC signal of cells labelled with WGA-AF488 in the presence of sQSY-Tet.



SI Figure 19. In-gel fluorescence image of a SDS-PAGE with trastuzumab labelled with the (a) sCy5 or sCy5-TCO click sensor (red) and (b) Alexa Fluor 488 (green) using increasing amounts of EDC with 5 mM NHS in reference to a protein ladder (blue).



SI Figure 20. Quenching efficiency of the click sensor on (a) 2D3 or (b) trastuzumab at 30 minutes and 4 hours. The proteins were incubated with SKOV-3 cells over a 4-hour time period at 4°C before adding PBS or sQSY-Tet at a concentration of 0.5 μ M and analysing by flow cytometry. The average quenching efficiency from two experiments in triplicate is plotted with error bars representing the standard deviation. n.s. = non-significant, ((a) $P = 0.1211$, (b) $P = 0.0822$, unpaired t-test)

3.3 Introduction

In addition to the work contained within the above manuscript, further options for the internalisation sensor were also investigated. This is covered in two sections:

1. Modification of the sensor to include an azide instead of a carboxylic acid for attachment to the material of interest
2. Construction of the sensor on a peptide, to explore if the internalisation of small cargo could be quantified

3.3.1 *Modifying the Internalisation Sensor Attachment Group*

There are numerous strategies for covalently conjugating fluorophores to proteins or nanoparticles. These methods have been developed to react with functional groups that are innately present on the amino acids of the protein or that have been engineered into the nanoparticle such as amines and carboxylic acids. In proteins, amines are found on lysine amino acids while carboxylic acids are present on aspartic and glutamic acid residues in addition to the N/C-terminus. To facilitate this reaction, a coupling reagent such as 1-ethyl-3-(3-dimethylaminopropyl)carbodiimide hydrochloride (EDC) is required to activate the carboxylic acid.¹ As the intermediate formed is unstable under aqueous conditions, N-hydroxysuccinimide (NHS) is often used to form an activated ester which prolongs the duration of reactivity.²⁻⁵

Unless protocols are optimised, coupling agents can cause crosslinking between proteins due to the multiple reactive groups present on their surfaces.³ To avoid this issue, we investigated the potential of modifying the carboxylic acid on the fluorescent component of the sensor with an additional click chemistry group. This modification would also allow the use of the sensor for site specific labelling on proteins expressing click groups generated through non-canonical amino acids.⁶ The reaction between an azide and a strained alkyne was deemed too slow for investigating internalisation into live cells (see section 3.2). To be practical for use with flow cytometry or fluorescence microscopy, the quencher should be able to switch off the surface signal within minutes of addition. However, the required reaction rate for conjugation to a protein or particle is far less stringent as it is common practice when labelling these materials to incubate the components overnight. Therefore, an azide is adequate as a second click group for conjugating the sensor to the protein or particle.

Although different sets of click reactive groups are orthogonal to each other, cross reactivity is a possibility. The *trans*-cyclooctene (TCO)/tetrazine reaction has been used in the presence of azide/dibenzocyclooctynes (DBCO) to label antibodies bound to a cell surface with minimal cross reactivity.⁷ However, azides and TCOs have been reported to react with similar kinetics to that between an azide and a strained alkyne with both exhibiting a second order rate constant of around $0.1 \text{ M}^{-1} \text{ s}^{-1}$.⁸ To determine if the degree of cross reactivity is low enough for conjugation to occur without destruction of the TCO group, the sensor was synthesised with an azide to allow attachment to a material modified with a strained alkyne via copper-free click chemistry (**Figure 3.1**). Once conjugated to a material, cross reactivity is not an issue as the azide can no longer react with any TCO groups. This leaves the TCO available for reaction with the tetrazine quencher as intended.

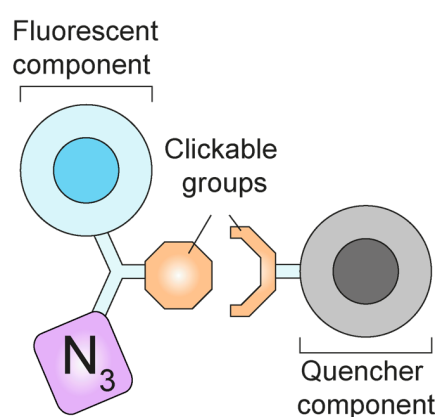


Figure 3.1 – Modification of the attachment group on the fluorescent component of the click internalisation sensor. The carboxylic acid is replaced with an azide for attachment to alkynes present on the material of interest.

3.3.2 Quantifying the Internalisation of Peptides

The previous section of this chapter (see section 3.2) details the use of the internalisation sensor on proteins ranging from 15 – 150 kDa. To investigate if this scheme could be applied to smaller cargo, the sensor was constructed on a peptide (~1.3 kDa). Labelling a peptide with the oligonucleotide used in the specific hybridization internalisation probe (SHIP) assay has a much higher likelihood of affecting its interaction with cells than it does for a regular protein due to the similarity in size of the two molecules. Routine labelling with certain common small organic fluorophores has been shown to alter biological behaviour of peptides,⁹ suggesting the effect would be even more pronounced for a bulky and negatively charged oligonucleotide. Therefore, the click sensor is a more suitable option for quantifying

the internalisation of peptides. Instead of attaching the sensor as one component, the fluorophore and click group are attached to separate, but nearby amino acids (**Figure 3.2**).

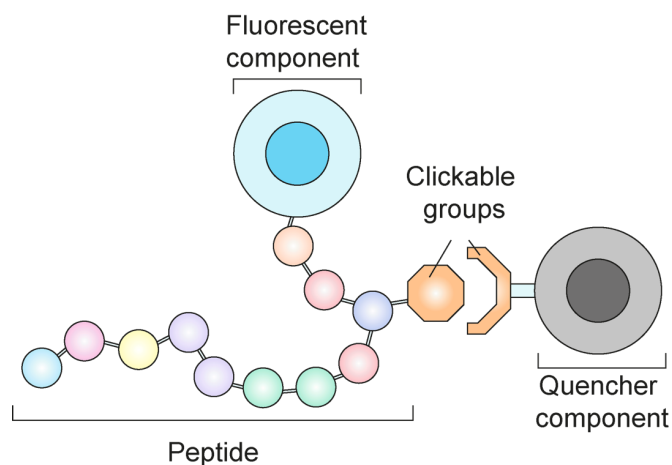


Figure 3.2 – Peptide internalisation sensor scheme. The click internalisation sensor is assembled across two amino acids. One amino acid is labelled with a fluorophore while a nearby residue is labelled with a click group that reacts with tetrazine, allowing quenching if the peptide remains at the cell surface.

To investigate the viability of this system, the peptides Substance P and Spantide I were chosen. Substance P is a neuropeptide in the tachykinins family involved in pain signalling that binds to the neurokinin 1 receptor (NK1R).¹⁰ Following binding, substance P is internalised by clathrin-mediated endocytosis into early endosomes where the acidic environment causes dissociation. This allows NK1R to recycle back to the surface while substance P is trafficked onwards for degradation (**Figure 3.3**).^{11,12} Spantide I is an antagonist for the NK1R,¹³ however, its mechanism of action has not yet been established. It is unclear if this peptide is taken up into the cell or remains bound to the receptor at the cell surface (**Figure 3.3**).

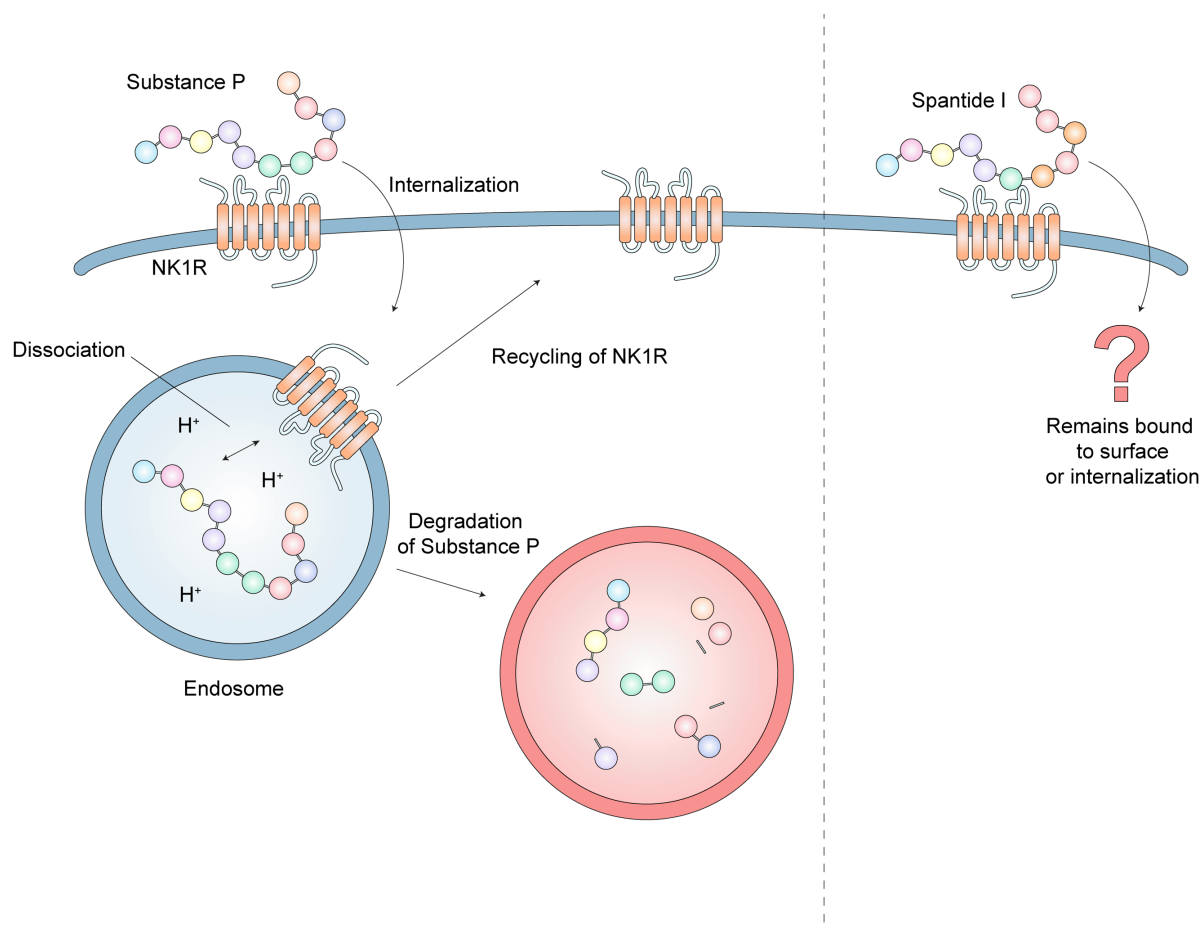


Figure 3.3 – Endocytic pathways of Substance P and Spantide I. Following binding to the NK1R, the endogenous agonist substance P is internalised into endosomes. Acidification of the endosome dissociates substance P from the receptor. Substance P is then trafficked onwards where it is degraded while the receptor recycles back to the cell surface. Spantide I, an antagonist for the NK1R binds and inhibits signalling through an unknown mechanism.

3.4 Results and Discussion

3.4.1 Click-Attachable Internalisation Sensor

When conjugating the internalisation sensor to a protein, cross-linking can occur due to the multiple amine and carboxylic acid groups present. To address this, the sensor was modified to include a second click chemistry group (azide) as the point of attachment instead of conjugation through a carboxylic acid (**Figure 3.4**). The sensor was constructed by first conjugating sCy5 to an azide-modified lysine residue (sCy5-Lys(N₃)). This was purified and the product mass confirmed (**Figure 3.6**) before attaching the TCO group to the carboxylic acid on the lysine residue (sCy5-Lys(N₃)-TCO).

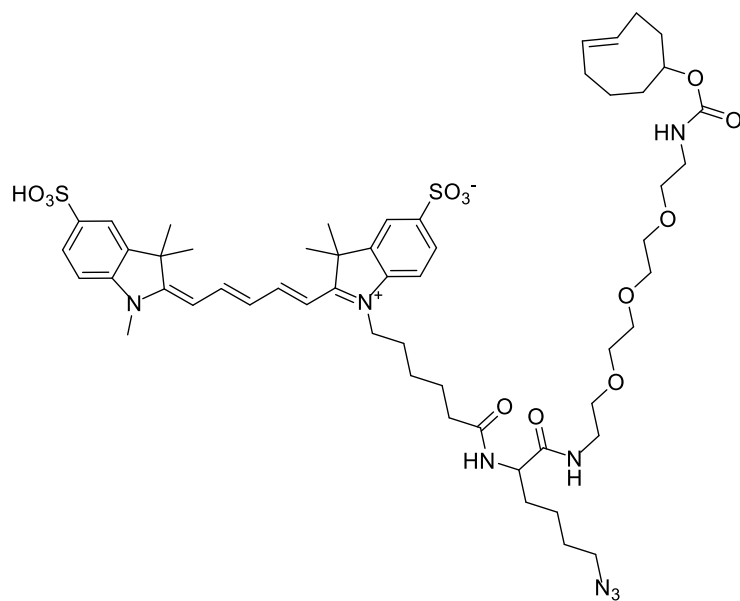


Figure 3.4 – Structure of sCy5-Lys(N₃)-TCO.

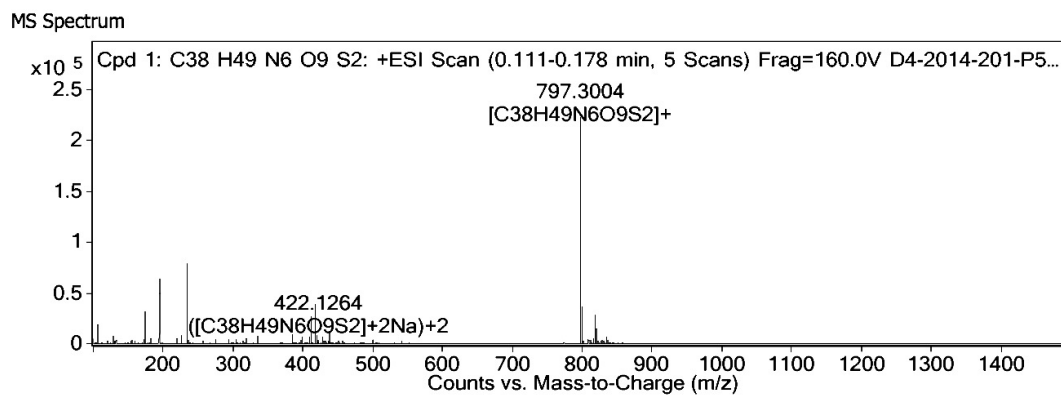


Figure 3.6 – High resolution mass spectrometry spectrum of sCy5-Lys(N₃)-COOH.

TCO-tetrazine ligations are claimed to be predominately orthogonal to azide-cyclooctyne cycloadditions. However, formation of product due to a cross reaction has been observed over a 45-hour time period.⁷ TCO-azide reactions occur via a 1,3-dipolar cycloaddition to form an unstable 1,2,3-triazoline which breaks down to form an imine bond before producing the final product (**Figure 3.5**).¹⁴ The sCy5-Lys(N₃)-TCO conjugate was initially uncontaminated by the products of this side reaction following synthesis and purification. An absorbance trace from the LCMS of the product fraction obtained directly following preparative HPLC showed one major peak (**Figure 3.7A**) with the mass (**Figure 3.7C**) corresponding to the desired structure (**Figure 3.7E**). However, this disappeared and was replaced with a new peak with a shorter retention time after lyophilisation and reconstitution in water (**Figure 3.7B**). The mass of the new peak in the LCMS spectrum (**Figure 3.7D**) agrees with that of the predicted structure from the azide-TCO pathway (**Figure 3.7F**). These results show that an azide cannot be used to attach the sensor to the material of interest. The rate of cross reactivity between the two groups is too high to allow conjugation to occur before the TCO is broken down.

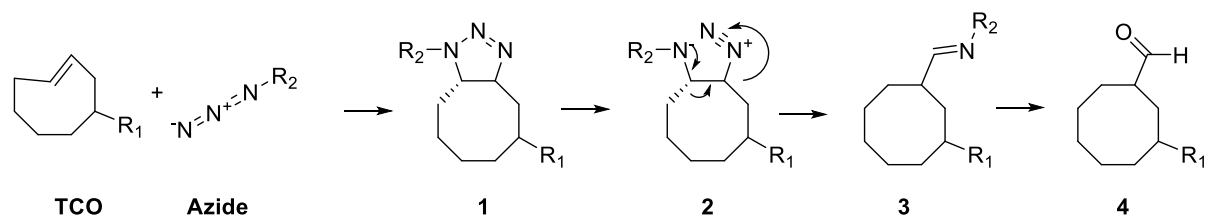


Figure 3.5 – Azide *trans*-cyclooctene reaction scheme. Modified from Matikonda et al. 2015.¹⁴

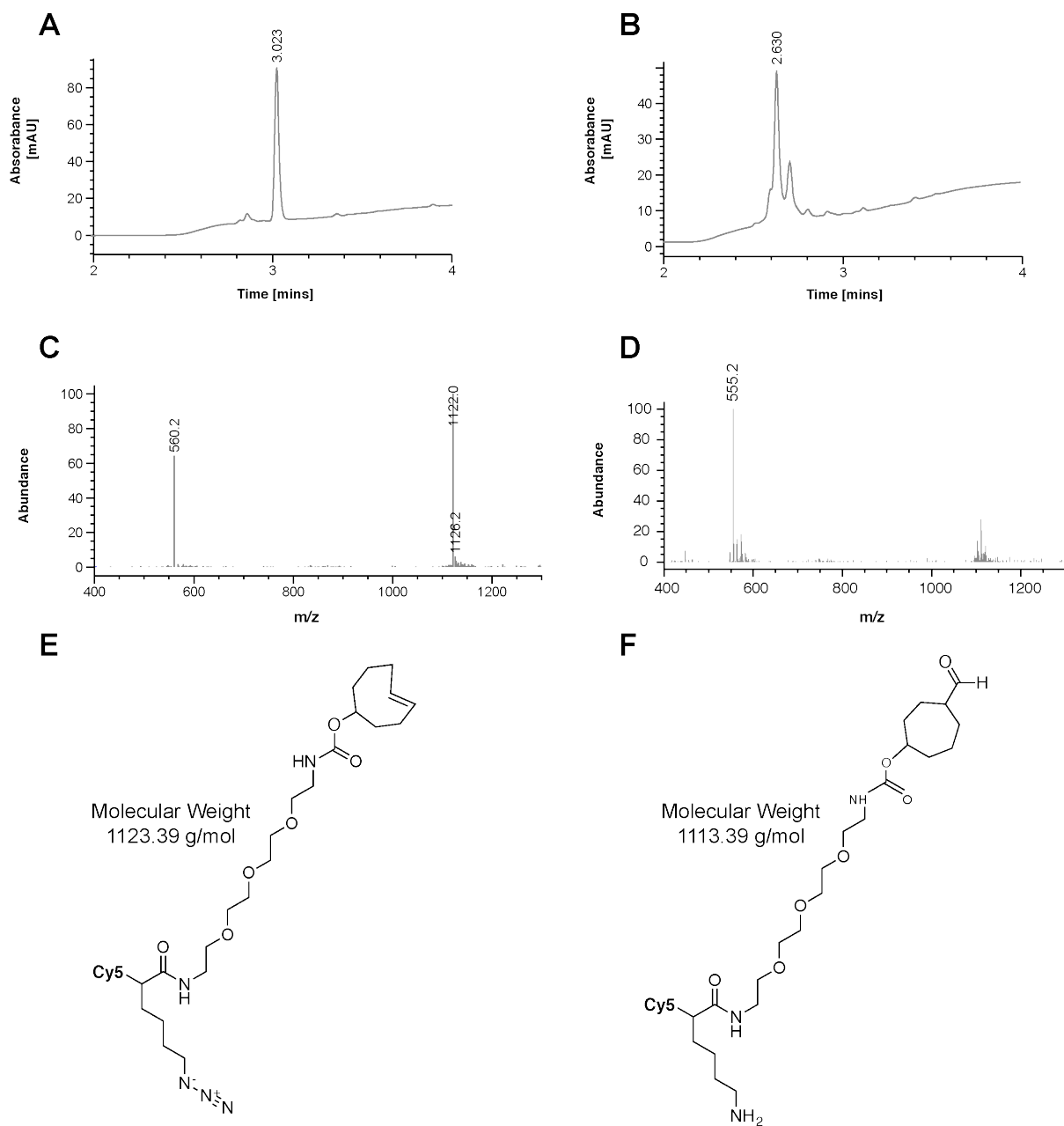


Figure 3.7 – Self-reactivity of the sCy5-Lys(N3)-TCO internalisation sensor. LCMS of freshly purified (**A**, **C**, **E**) or lyophilised and reconstituted (**B**, **D**, **F**) internalisation sensor. (**A**, **B**) UV-diode array detection chromatogram at 254 nm. Negative ion atmospheric pressure ionization (ES-API) chromatogram with time (**C**, **D**) and mass to charge ratio (m/z). Structures of the (**E**) target and (**F**) self-reaction products.

3.4.2 Peptide Internalisation Sensor Synthesis

The ability of the click sensor to probe the uptake of fluorescently labelled peptides was also investigated to test the size limits of the system. This was done by assembling the key components of the sensor on to the peptides Substance P (**Figure 3.8A**) and Spantide I (**Figure 3.8B**) across two separate but nearby residues. Attachment of sCy5 to the peptides was performed via Fmoc solid-phase peptide synthesis while the click group was attached in solution after cleavage of the peptides from the resin. Similar to TCO, bicyclo[6.1.0]nonyne (BCN) is alternative copper-free click group that reacts rapidly with tetrazine.¹⁵ BCN was included on the peptide sensor as it may be more stable than TCO which has been demonstrated to degrade in the presence of proteins containing copper.¹⁶

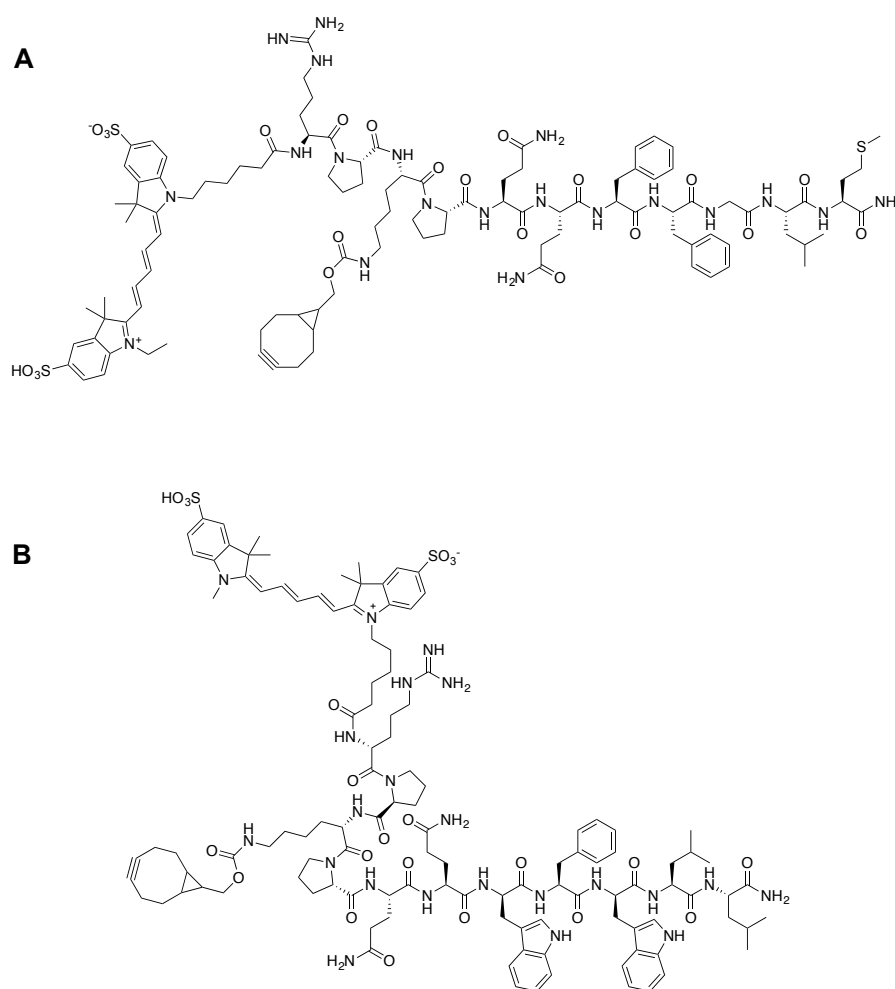


Figure 3.8 – Structures of (A) Substance P and (B) Spantide I modified with sCy5 and BCN.

It is critical that the conjugation of the sensor components do not interfere with the biological activity of the peptide. Modification of Substance P with a fluorophore at the lysine residue present at position three on the peptide sequence has been shown to retain agonist activity.^{9,17,18} Therefore, this position was chosen for attachment of the click group while the fluorescent group (sCy5) was attached to the N-terminus. Following purification by HPLC, one major peak containing the target mass was obtained for both peptides (sCy5-Substance P-BCN and sCy5-Spantide-BCN) (**Figure 3.9 & 3.10**).

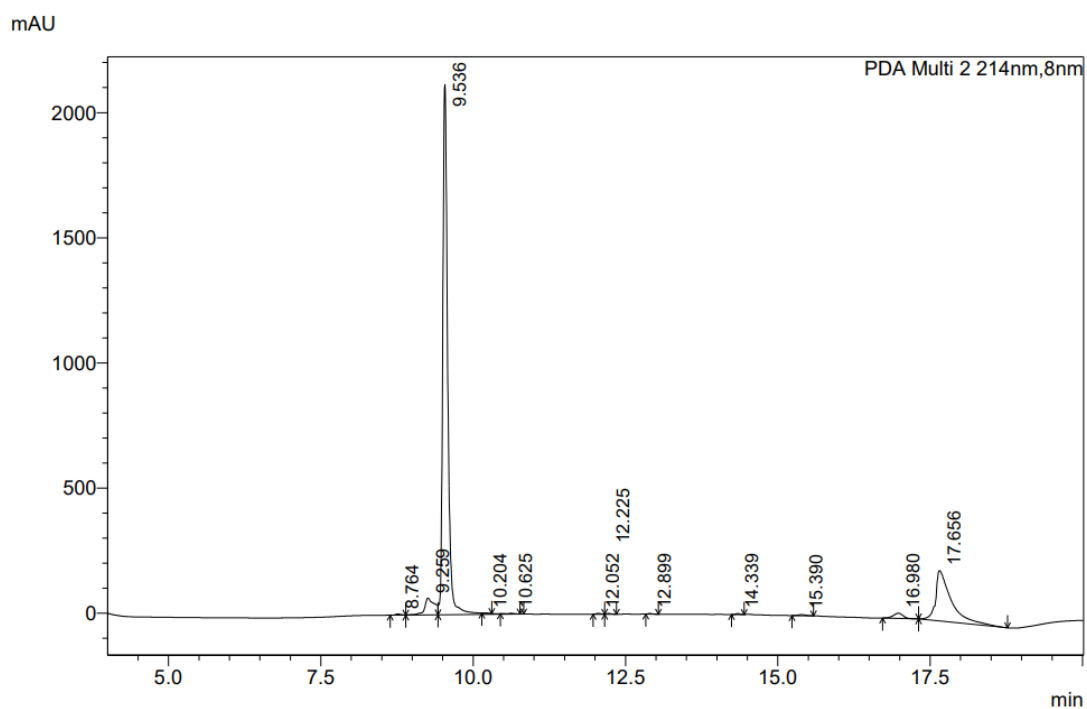


Figure 3.9 – LCMS Chromatogram of sCy5-Substance P-BCN.

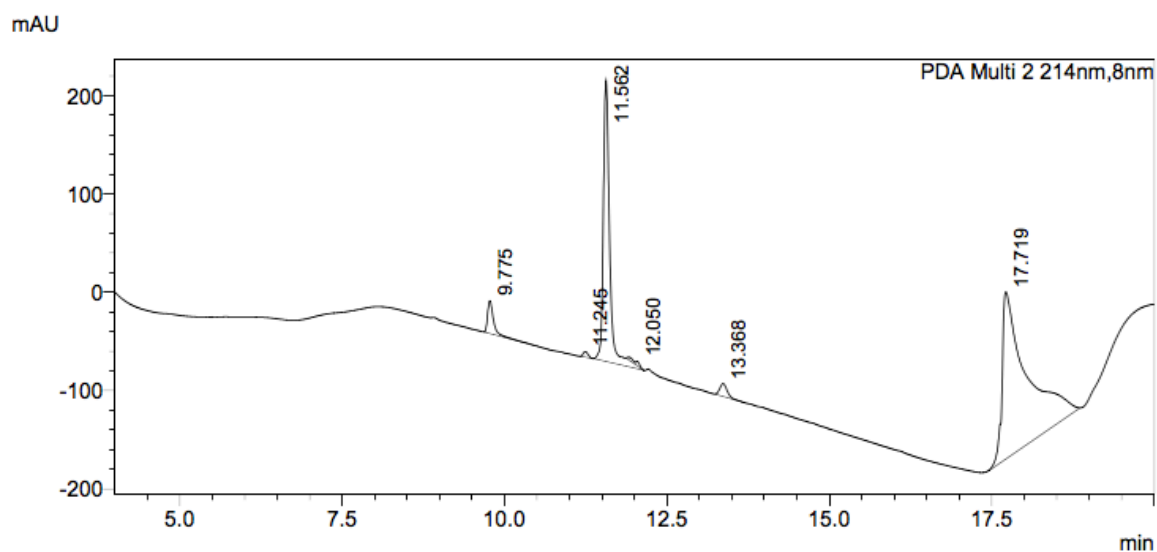


Figure 3.10 – LCMS Chromatogram of sCy5-Spantide-BCN.

3.4.3 Fluorescence and Quenching of Substance P and Spantide I in Solution

The fluorescence intensity of the labelled peptides was investigated using fluorescence spectrophotometry. The fluorescence of Cy5-Substance P-BCN was over 20 times more intense than Cy5-Spantide-BCN at the same concentration (**Figure 3.11**). No evidence of Spantide I aggregation was observed by scattering in the absorbance spectra of sCy5 (data not shown). Fluorescently labelled peptides have been shown to self-quench if the sequence contains tryptophan residues through the formation of non-fluorescent ground state complexes.¹⁹ Although this effect was shown to be minimal on sCy5, it is possible that the additional BCN group on Spantide I is contributing and rendering the sCy5-Spantide-BCN significantly less fluorescent.

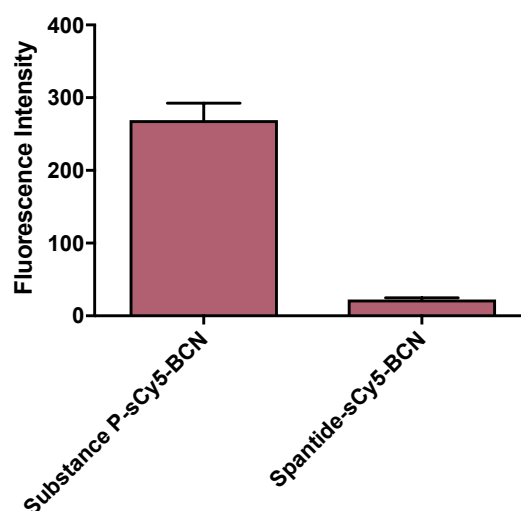


Figure 3.11 – Fluorescence intensity at 663 nm of 0.6 μ M Substance P-sCy5-BCN or Spantide-sCy5-BCN excited at 656 nm in PBS. The mean of triplicate results is plotted with error bars representing the standard deviation.

To test if these hydrophobic interactions were interfering with the fluorescence intensity, a surfactant was added. Addition of sodium dodecyl sulphate (SDS) at 2% w/v, resulted in an 11-fold increase in fluorescence compared to dilution in PBS only (**Figure 3.12A**). The effect was more pronounced than the addition of dimethyl sulfoxide (DMSO) at 5% w/v, which had minimal effect on the intensity. However, addition of surfactant to the peptide may not be feasible *in vitro* as it effects cell viability. Studies have demonstrated that SDS is toxic to dog kidney epithelial cells (MDCK) at concentrations above ~0.01% w/v.²⁰ The fluorescence of Spantide I in 0.01% w/v SDS was similar to the peptide in PBS alone (**Figure 3.12B**). Due to the low fluorescence of the antagonist, focus was shifted to the agonist sCy5-Substance P-BCN. In solution, Cy5-Substance P-BCN fluorescence was rapidly

quenched by BHQ2-Tet causing an ~80% reduction in intensity within approximately 30 seconds (Figure 3.13A). The quenching in the presence of a 10-molar excess of BHQ2-Tet was stable over the observation period of 30 minutes (Figure 3.13B).

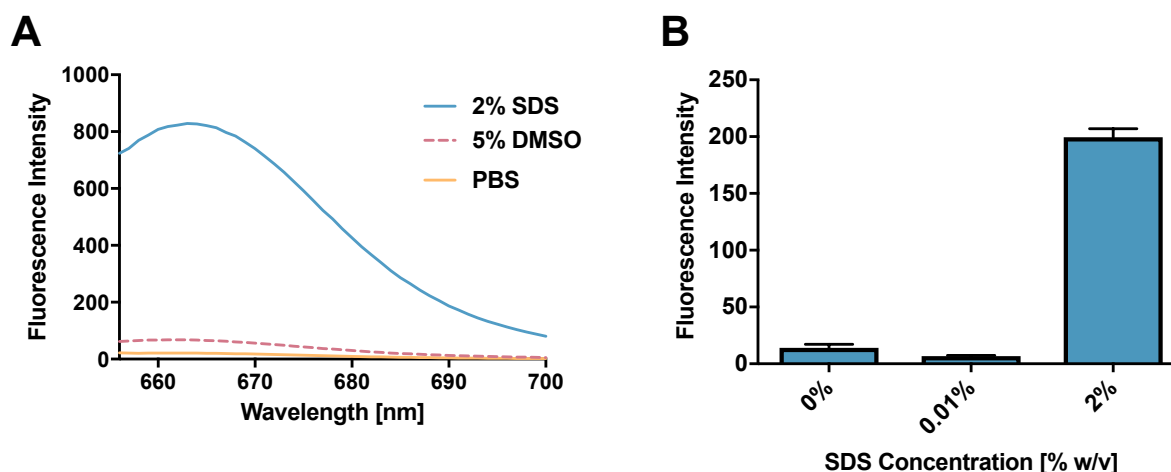


Figure 3.12 – Effect of additives on Spantide I fluorescence. (A) Fluorescence emission spectrum between 656 – 700 nm of 0.2 μM Spantide I-sCy5-BCN excited at 656 nm in PBS with SDS, DMSO or alone. (B) Fluorescence intensity of 0.03 μM Spantide I-sCy5-BCN at 663 nm in PBS with 0, 0.1 or 2 w/v % SDS. The mean of triplicate results is plotted with error bars representing the standard deviation.

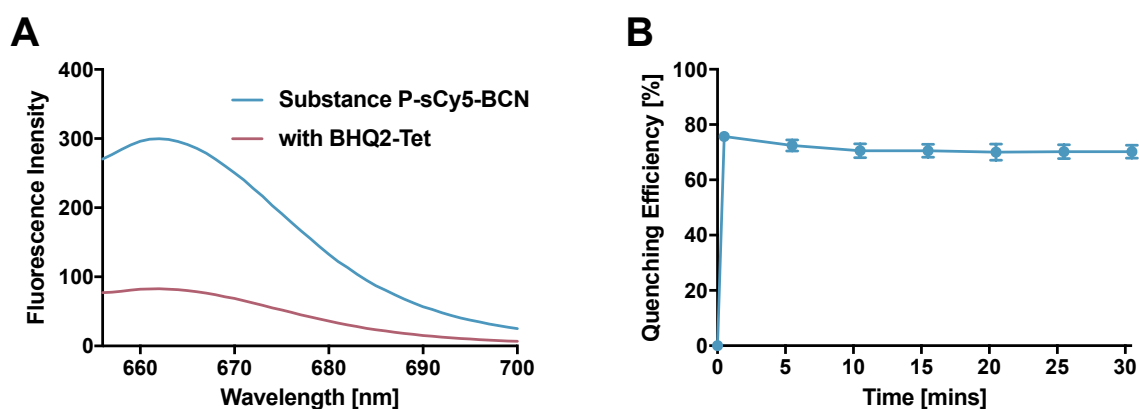


Figure 3.13 – Fluorescence of Substance P-sCy5-BCN. (A) Fluorescence emission spectrum between 656 – 700 nm of 0.6 μM Substance P-sCy5-BCN excited at 656 nm and quenched with 10 equivalents BHQ2-Tet for 5 minutes in PBS (B) Quenching efficiency calculated from fluorescence intensity at 663 nm over a 30-minute time-period. Average of triplicate quenching experiments plotted with error bars representing the standard deviation.

3.4.4 In Vitro Quenching of Peptides Bound to the Neurokinin 1 Receptor

The peptide Substance P could also be quenched when bound to a receptor on the cell surface. Human embryonic kidney (HEK-293) cells stably expressing the NK1R (HEK-NK1R) were incubated with sCy5-Substance P-BCN at 4°C to assess the ability of BHQ2-Tet to reduce the fluorescent signal. Substance P was found to associate strongly with the cells, causing a large shift in the fluorescence histogram from the control cells (**Figure 3.14A**). Addition of quencher reduced the fluorescence, shifting the histogram back towards the control cells (**Figure 3.13A**).

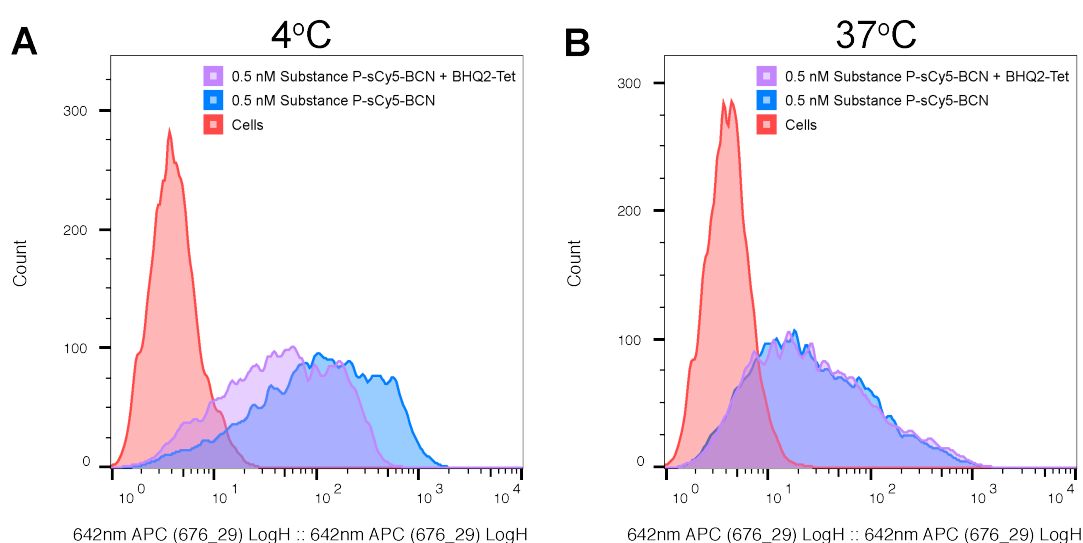


Figure 3.14 – Representative histograms from flow cytometric analysis of Substance P incubated with HEK-NK1R cells at 4 and 37°C. **(A)** Cell surface quenching of Cy5-Substance P-BCN in HEK-NK1R cells. Cells incubated with 1 nM substance P for 25 minutes at 4°C were analysed by flow cytometry. **(B)** A 100-molar excess of BHQ2-Tet to the total Cy5-Substance P-BCN was added for 25 minutes before analysis.

Quenching of the peptide at the cell surface was less efficient than in solution. At 4°C, BHQ2-Tet quenching reduced the fluorescence intensity by only 46 – 53% (**Figure 3.15**), compared to the 80% efficiency observed in solution. However, no quenching was observed under internalising conditions. There was minimal difference between the fluorescence histograms of cells incubated with sCy5-Substance P-BCN at 37°C with and without BHQ2-Tet (**Figure 3.14B**). As BHQ2-Tet was demonstrated to possess the ability to permeate through cell membranes (see section 3.2), this lack of quenching cannot correspond to complete internalisation of the peptide.

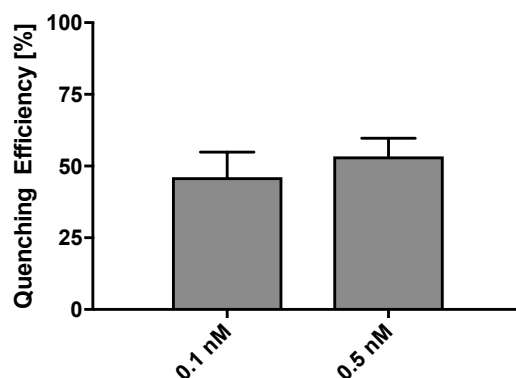


Figure 3.15 – Quenching efficiency of sCy5-Substance P-BCN by BHQ2-Tet at 4°C in HEK-NK1R cells. Cells incubated with 1 nM substance P for 25 minutes at 4°C were analysed by flow cytometry after quenching with 100-molar excess of BHQ2-Tet to the total sCy5-Substance P-BCN added.

The inability of membrane permeable BHQ2-Tet to quench intracellular sCy5-Substance P-BCN was attributed to degradation of the peptide following internalisation. Although this is insignificant for quantifying internalisation, the mechanism behind this occurrence was examined. Endothelin-converting enzyme 1 (ECE-1) has been demonstrated to degrade substance P in endosomes but not at the cell surface. Substance P was degraded at the pH of late endosomes (pH 5.5) but not at an extracellular pH of 7.4 in the presence of ECE-1.²¹ In addition, intracellular degradation was prevented by incubation with Bafilomycin A,²¹ an inhibitor of vacuolar-type H⁺ ATPases which are responsible for endosomal acidification.^{22,23} Rapid degradation of Substance P after internalisation may separate the fluorophore from the BCN click group soon after it is trafficked into endosomes. This would explain why BHQ2-Tet cannot quench the intracellular fluorescence from Substance P even though it has access to it.

To test if sCy5-Substance P-BCN was being rapidly degraded, cells were pre-incubated with Bafilomycin A. As seen previously, no significant quenching of sCy5-Substance P by BHQ2-Tet was observed at 37°C without bafilomycin A (**Figure 3.16**). However, when cells were pre-treated with the inhibitor, the mean fluorescence intensity decreased from ~116 to ~68 (**Figure 3.16**). As the fluorescence intensity of samples treated with bafilomycin A does not drop to background levels, it suggests some peptide is still degraded and cannot be quenched. However, this does provide evidence that the inhibitor is able to avert degradation of a proportion of peptide. This prevents separation of the

fluorophore from the click group and allows BHQ2-Tet to quench within the endosome, in line with the observations for transferrin labelled with the internalisation sensor.

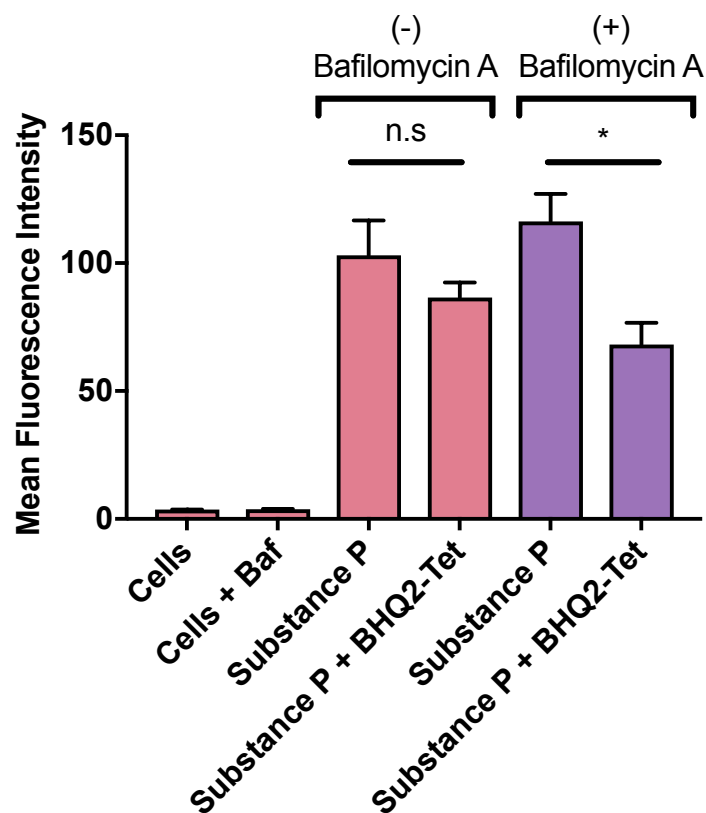


Figure 3.16 – Treatment of HEK-NK1R cells with inhibitor bafilomycin A. Cells were pre-treated with the inhibitor before incubation with the sCy5-SubstanceP-BCN at 37°C for 30 minutes followed by quenching with or without 100 equivalents of BHQ2-Tet. The average of results in triplicate is plotted with the error bars representing the standard deviation (*P < 0.05, unpaired t-test).

To quantify internalisation, the membrane impermeable quencher sQSY-Tet must be used so that only the fluorescence of extracellular peptide is switched off. The quenching of sCy5-Substance P-BCN by sQSY-Tet in solution was similar to that observed for BHQ2-Tet (**Figure 3.17A**). Quenching was almost instantaneous with an efficiency of approximately 80% obtained. Although quenching in solution occurred as expected, the signal from the peptide could not be removed when bound to receptors on the cell surface at 4°C. While there was a small difference in the mean fluorescence intensity of membrane bound peptide in the presence sQSY-Tet (**Figure 3.17B**), this corresponded to quenching efficiency of only ~25% (**Figure 3.17C**). Increasing the equivalents of sQSY-Tet from 4 to a 100, 250 and 500 molar excess did increase the extracellular quenching efficiency (**Figure 3.17D**). However, at the maximum concentration, the signal was reduced by only ~38%. By extrapolating, an

estimated 1200 molar excess of quencher would be required to match the reduction in fluorescence observed in section 3.2.

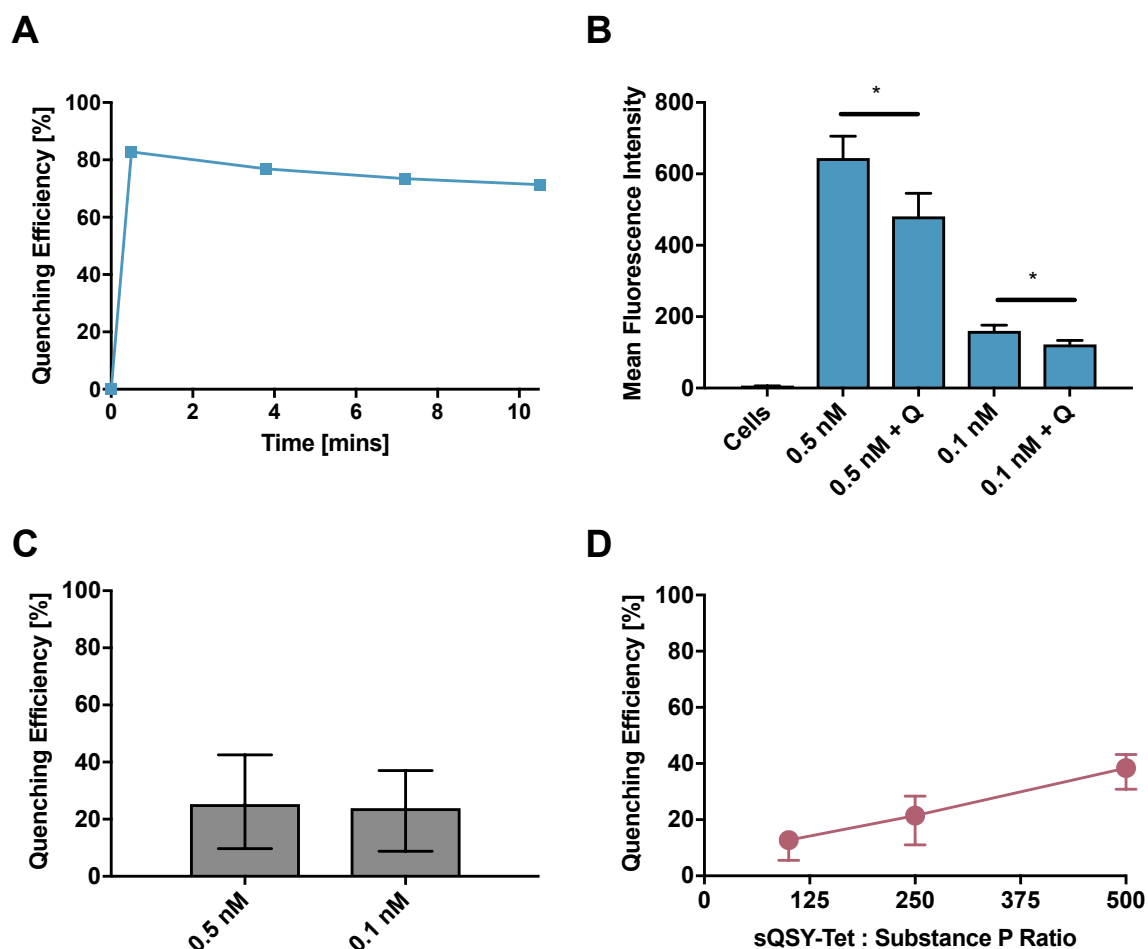


Figure 3.17 – Quenching of sCy5-Substance P-BCN with sQSY-Tet. (A) 80 nM sCy5-Substance P-BCN quenched with 10 equivalents sQSY-Tet in solution. The sample was excited at 636 nm with emission collected between 656 – 700 nm every 3.3 minutes over a 10 minute time period. (B) Flow cytometric analysis of HEK-NK1R cells incubated with 0.1 or 0.5 nM Substance P-sCy5-BCN with and without sQSY-Tet at 4°C. The average of results in triplicate is plotted with the error bars representing the standard deviation (*P < 0.05, unpaired t-test). (C) Average fluorescence quenching, with error bars representing the upper and lower limits of quenching calculable from triplicate results. (D) Average quenching efficiency with increasing equivalents of sQSY-Tet, with error bars representing the upper and lower limits calculable from the results in triplicate.

The inability of sQSY-Tet to quench Substance P bound to NK1R but not transferrin bound to its receptor can be explained by comparison of these structures. Inspection of the transferrin-receptor complex shows large regions of the protein are exposed to the surrounding environment and away from the binding region (**Figure 3.18**) As the amino acid sequence of transferrin contains over 50 lysine residues,²⁴ several of these are expected to be exposed in this area. This grants access of the

hydrophilic sQSY-Tet to any click group conjugated in these regions. The inefficient quenching of sCy5-Substance P-BCN fluorescence in solution suggests the click group is obstructed when the peptide is bound to the NK1R.

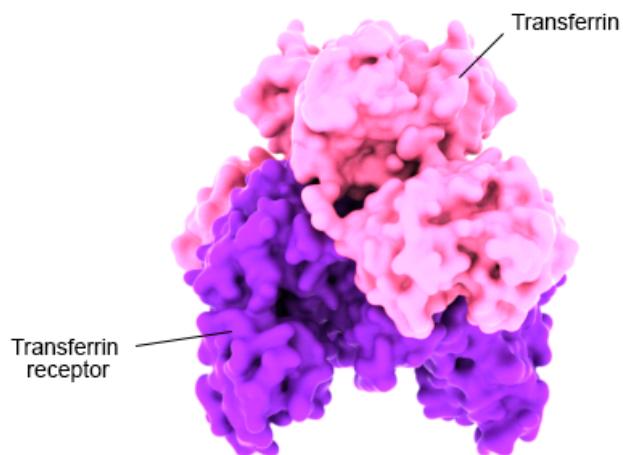


Figure 3.18 – Illustration of receptor bound transferrin. (A) Transferrin receptor with two bound holo-transferrin molecules rendered from protein data bank entry 1SUV.²⁴

In contrast to transferrin, there is only a single point on Substance P where the click group is present. The BCN is positioned on the lysine residue which in its native form, points into the receptor surface (**Figure 3.19**). Although conjugation of BCN may alter the adopted orientation of this residue, the structure of the peptide-receptor complex does suggest the poor quenching efficiency is due to steric hindrance. The quencher sQSY-Tet may have reduced access to this location. In addition, the hydrophilic properties of sQSY-Tet augment this issue as the quenching efficiency of the hydrophobic quencher BHQ2-Tet was less affected. An alternative possibility is that the modifications to Substance P increase the non-specific interactions of the peptide with the cell surface which may also hinder access of the quencher to the TCO group. This was not investigated here, but could be probed by determining binding in both non-transformed HEK cells which lack the NK1R and in the presence of unlabelled Substance P.

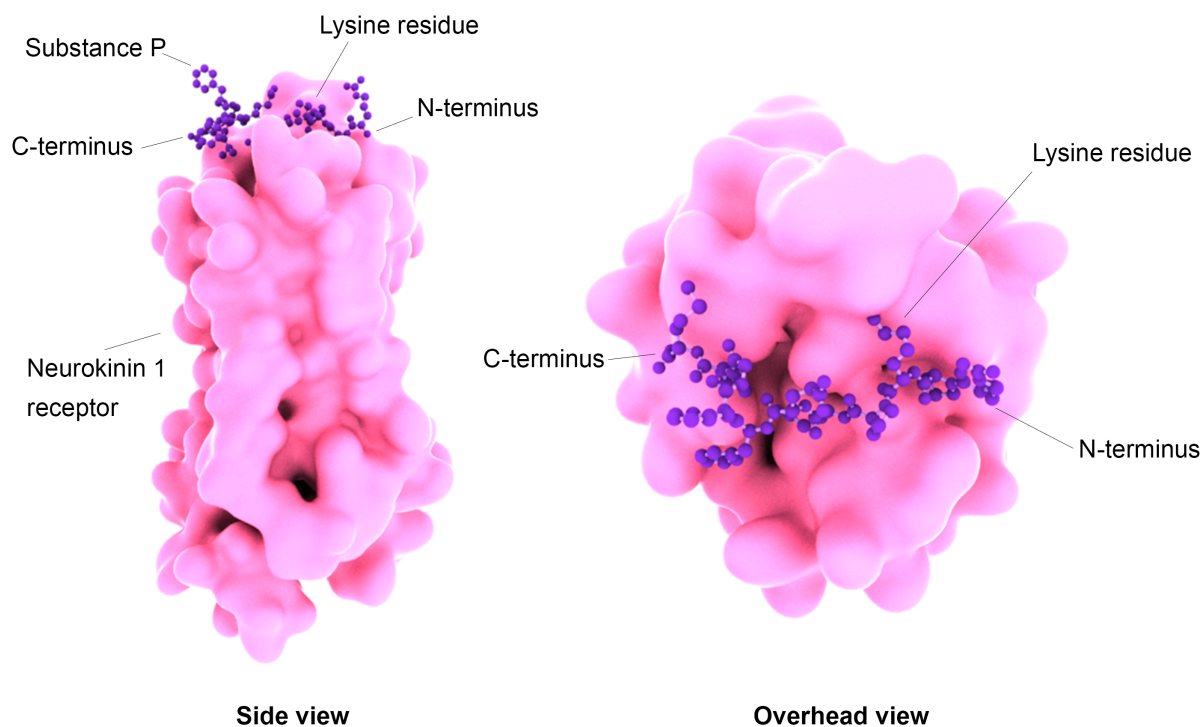


Figure 3.19 – Side and overhead illustrations of Substance P bound to the neurokinin I receptor in solution rendered from protein data bank entry 2KS9.²⁵ Major atoms of the peptide (C, N, O, S) are represented.

3.5 Conclusions

The fundamental importance of endocytosis in biology and medicine necessitates the generation of better tools to understand this process. In addition to the development of the fluorescent internalisation covered in the first section of this chapter, two modifications to the system were also investigated. Alterations to the sensor structure to improve the method of conjugation to the material of interest was pursued by adding an azide group. The sensor components were also assembled on to two peptide sequences in an attempt to probe their internalisation behaviour.

Conversion of the sensor attachment group to an azide from a carboxylic acid was not feasible. While this rate of reaction between TCO and azide groups is slow enough that TCO-Tetrazine is considered orthogonal to the azide-strained alkyne reaction pair, this is only over a short time scale such as when labelling proteins on a cell surface. The reaction rate was significant enough to cause the conjugate to react with itself following synthesis and purification. However, other options are available for the attachment group that could be pursued in the future. This includes changing the carboxylic acid to a

maleimide for attachment to thiol residues or exchanging the click groups on the sensor components so that fluorescent component is composed of an azide for attachment and a tetrazine for a click reaction with a TCO-modified quencher.

In addition, the sensor could not be assembled functionally on the specific peptide sequences for Substance P and Spantide I. The fluorescence of modified Spantide I self-quenched due to the highly hydrophobic sequence of the peptide. While the fluorescence could be restored by addition of a surfactant, the concentration required was too high to be used under *in vitro* assay conditions. Substance P behaved as intended in solution but could not be quenched efficiently when bound to its receptor on the cell surface by the membrane impermeable quencher. Although not possible for the two sequences described here, the construction of the internalisation sensor system on a peptide may be possible when access to lysine residues is not hindered. This work emphasises how hydrophobicity and orientation effect quencher access which is critical for the action of the sensor.

3.6 Materials and Methods

3.6.1 Materials

Peptide coupling reagents including

1-[Bis(dimethylamino)methylene]-1H-1,2,3-triazolo[4,5-b]pyridinium 3-oxid hexafluorophosphate 1-[Bis(dimethylamino)methylene]-1H-1,2,3-triazolo[4,5-b]pyridinium 3-oxid hexafluorophosphate (HATU) and Bromotripyrrolidinophosphonium hexafluorophosphate (PyBroP) were purchased from ChemImpex. Bicyclononyne-succinimidyl ester (BCN-NHS) was obtained from Synaffix and sCy5-NHS ester was attained from Lumiprobe.

Substance P (Amino acid sequence: Arg - Pro - Lys - Pro - Gln - Gln - Phe - Phe - Gly - Leu - Met) and Spantide I ([D-Arg¹, D-Trp^{7,9}, Leu¹¹] Substance P) was obtained from Josh Conner (Monash University, Melbourne). Spantide was synthesised on rink amide resin and substance P on NovaSyn TGR resin via standard Fmoc solid-phase peptide coupling conditions on a PS3 benchtop peptide synthesiser (Gyros Protein Technologies). All side groups were BOC protected except the N-terminal arginine which was protected with a pentamethyldihydrobenzofuran-5-sulfonyl (PBF) group.

3.6.2 Azide Modified TCO Sensor Synthesis

BOC-lysine(N₃)-COOH (8.9 mg) was deprotected in 50/50 % DCM/TFA for 3 hours at room temperature. The solvent was evaporated under nitrogen and dissolved in 1.1 mL sodium bicarbonate solution (4 equivs, 11 mg, 0.13 mmol). To the theoretical yield of deprotected amino acid (5.63 mg), sCy5-NHS (1 equiv, 2.5 mg, 3.28 μ mol) was added in water (1 mL) to EDC, also dissolved in water (200 μ L, 1.2 equiv, 0.75 mg, 3.94 μ mol). The reaction was stirred overnight at room temperature and lyophilised. The product mass was confirmed via LCMS and HRMS.

The crude product (2.6 mg) was combined with TCO-amine (2 equiv, 1.72 mg, 6.56 μ mol) and HATU (1.5 equiv, 1.87 mg, 4.92 μ mol) with DIPEA (6 equiv, 2.54 mg, 19.7 μ mol) in DMF (300 μ L) and reacted for 1 hour at room temperature before purification via preparative HPLC with a 0 – 80% MeCN/H₂O gradient containing 0.1% TFA at a flow rate of 7 ml min⁻¹ over 38 minutes. The product fraction was lyophilised and the mass confirmed via LCMS and HRMS. The purity was estimated by HPLC to be approximately 85%.

3.6.3 Peptide Liquid Chromatography – Mass Spectrometry

Peptide liquid chromatography – mass spectrometry (peptide LCMS) was performed on a Shimadzu LC-MS system with a LC-20AD liquid chromatograph system, SPD-M20A diode array detector, CTO-20A column oven with a Luna 3 micron C8(2) 3 μ m, 100 Å, 100 x 2.0 mm column and a LC-MS-2020 system, functioning in positive mode.

3.6.4 sCy5-Substance P-BCN Synthesis

Substance P was fluorescently labelled on resin, cleaved and then modified with the click group, BCN. Substance P (20 mg resin with 0.18 mmol g⁻¹ binding) on rink amide resin was swelled in DCM and washed in DMF in a solid-phase peptide synthesis column. The resin was combined with sCy5 carboxylic acid (2 equivalents, 2.6 mg), PyBroP (2.2 equivalents, 2.05 mg) and an excess of DIEPA (40 μ L). the solution was bubbled in DMF for 2 hours, disconnected and then left overnight.

The resin was washed 3 times in DMF and the conjugate cleaved with 95/5% TFA/TIPS for 1 hour at room temperature. The solution was filtered through cotton wool and the solvent was evaporated under

nitrogen gas. The conjugate was precipitated in ether, centrifuged and the supernatant discarded before drying under nitrogen again. The conjugate was then dissolved in 1 mL 25/75% MeCN/H₂O and purified using preparative HPLC with a 0 – 60% MeCN/H₂O gradient over 40 minutes with 0.1% TFA and a flow rate of 7 mL min⁻¹.

The conjugate was combined with BCN-NHS (2.2 equivs to the total sCy5 added in the previous conjugation, 2.31 mg) with an excess of DIPEA (40 µL) in DMF (200 µL) and left overnight at room temperature. The presence of the target mass was confirmed via peptide LCMS and the conjugate was purified using preparative HPLC with a 20 – 100% MeCN/H₂O gradient with 0.1% TFA over 45 minutes and a flow rate of 7 mL min⁻¹. The product fraction was lyophilised and the mass confirmed via peptide LCMS. The purity was estimated to be 82% based on the absorbance spectrum via analytical HPLC.

3.6.5 sCy5-Spantide-BCN Synthesis

Synthesis assisted by PhD student, Josh Conner (Monash University, Melbourne).

Excess Spantide I (16 mg resin with 0.59 mmol g⁻¹ binding) on rink amide resin was combined with sCy5-NHS (2.3 mg equivalents, 2.6 mg), PyBroP (1.2 equivalents to sCy5, 3.72 mg) and DIEPA (10 equivalents to Spantide, 16 µL) in a 1.6 mL Eppendorf tube in DMSO (200 µL) overnight at room temperature. Additional PyBroP (2.1 equivalents, 6.5 mg) was added and the reaction left overnight at room temperature.

The resin was transferred to a peptide synthesis column and washed with DMSO until the flow through was clear. It was then washed with MeOH before a final rinse in DCM. The resin was then cleaved with 93.6/4.7/1.7% TFA/H₂O/TIPS (3 mL) for 2 hours at room temperature. The solution was transferred into a round bottom flask and the resin was rinsed with HFIP. The solvent was evaporated under nitrogen gas. The conjugate was then dissolved in 1 mL 75/25% MeCN/H₂O and purified using preparative HPLC with a 20 – 100% MeCN/H₂O gradient over 45 minutes with 0.1% TFA and a flow rate of 7 mL min⁻¹.

The conjugate was combined with BCN-NHS (2.2 equivalents to the total sCy5 added in the previous conjugation, 2.31 mg) with DIPEA (10 equivalents, 7 µL) in DMF (200 µL) and left overnight at room temperature. The presence of the target mass was confirmed via peptide LCMS and the conjugate was

purified using preparative HPLC with a 20 – 100% MeCN/H₂O gradient with 0.1% TFA over 45 minutes and a flow rate of 7 mL min⁻¹. The product fraction was lyophilised and the mass confirmed via peptide LCMS. The purity was estimated to be approximately 92% based on the absorbance spectrum via analytical HPLC.

3.6.6 Peptide Conjugate Reconstitution

Both peptide conjugates were reconstituted in 50/50% MeCN/H₂O and stored at -20°C. The concentration of the dissolved peptide was estimated by measuring the absorbance at 646 nm on a NanoDrop ND-1000 spectrophotometer and an extinction coefficient of $\epsilon_{sCy5} = 271,000 \text{ M}^{-1} \text{ cm}^{-1}$. The concentrations of sCy5-Substance P-BCN and sCy5-Spantide-BCN stock was 18.1 μM and 22.5 μM respectively.

3.6.7 Peptide Fluorescence in Solution

The fluorescence emission spectra of sCy5-Substance P-BCN and sCy5-Spantide-BCN in solution was obtained with a Shimadzu RF-5310PC fluorescence spectrophotometer. The background fluorescence of PBS, SDS (0.01 or 2 w/v % in PBS) or DMSO (5 w/v % in PBS) was collected before adding the fluorescent peptides. Peptides were diluted to a final concentration of 0.6 μM and the spectra was obtained by excitation at 646 nm with emission measured between 655 – 700 nm with a 5 nm slit width and fast scanning speed.

To assess the ability of BHQ2-Tet to quench sCy5-Substance P-BCN, the fluorescence spectrum of 0.16 μM peptide was obtained before adding 10 equivalents quencher. The emission was collected every 5 minutes over a 30 minute time period. The quenching efficiency using sQSY-Tet was also assessed on 80 nM peptide with 10 equivalents quencher with emission collected every 3.3 minutes over a 10 minute time period.

3.6.8 sCy5-Substance P-BCN Internalisation by Flow Cytometry

HEK293 cells stably expressing the NK1R were kindly donated by Dr. Nicholas Veldhuis, Monash University. HEK-NK1R cells were seeded in two 24-well plates at 100,000 cells per well in in 400 μL

DMEM supplemented with 10% FBS one day prior to the experiment. After both plates were cooled on ice for 30 minutes to stop internalisation, 50 μ L of diluted sCy5-Substance P-BCN was added at a final concentration of 0.1 (stock diluted to 0.95 nM) and 0.5 nM (stock diluted to 4.5 nM) and allowed to bind for 30 minutes. The cells were washed twice in DMEM with 10% FBS and incubated at 4°C or 37°C for 30 minutes. The cells were then detached with 200 μ L citric saline buffer (135 mM potassium chloride, 15 mM sodium citrate)²⁶ for 5 minutes, transferred to a 96 well V-bottom plate and spun at 250 g for 5 minutes before resuspension in PBS with or without 100 equivalents of BHQ2-Tet to the amount of peptide added and analysed by flow cytometry.

In experiments quenched with sQSY-Tet, cells were cooled on ice for 15 minutes to stop internalisation before sCy5-Substance P-BCN was added at a final concentration of 0.1 and 0.5 nM and allowed to bind for 15 minutes. The cells were washed twice in DMEM with 10% FBS and incubated at 4°C or 37°C for 30 minutes. The cells were then detached with 200 μ L citric saline buffer for 5 minutes, transferred to a 96 well V-bottom plate and spun at 250 g for 5 minutes before resuspension in PBS with or without 4, 100, 250 or 500 equivalents of sQSY-Tet to the amount of peptide added and analysed by flow cytometry.

3.6.9 *Inhibiting Endosomal Acidification with Bafilomycin A*

HEK-NK1R cells were seeded in two 24-well plates at 120,000 cells per well in 400 μ L DMEM supplemented with 10% FBS one day prior to the experiment. Bafilomycin A was added to half of the wells at a final concentration of 1 μ M for one hour²⁷ and bafilomycin A was included in all media, detachment solution, PBS and quenching solutions at the same concentration for all subsequent washes for samples with endosomal acidification inhibition.

The cells were cooled on ice for 15 minutes to stop internalisation before adding sCy5-Substance P-BCN (25 μ L of stock diluted to 9 nM) for a final concentration of 0.5 nM and allowed to bind to the cells for 30 minutes. The cells were washed twice in DMEM with 10% FBS and incubated at 4°C or 37°C for 30 minutes. The cells were then detached with 200 μ L citric saline buffer for 5 minutes, transferred to a 96 well V-bottom plate and spun at 250 g for 5 minutes before resuspension in PBS with or without 100 equivalents of BHQ2-Tet and analysis by flow cytometry.

3.7 References

1. Valeur, E. & Bradley, M. Amide bond formation: beyond the myth of coupling reagents. *Chem. Soc. Rev.* **38**, 606–31 (2009).
2. Staros, J. V., Wright, R. W. & Swingle, D. M. Enhancement by N-hydroxysulfosuccinimide of water-soluble carbodiimide-mediated coupling reactions. *Anal. Biochem.* **156**, 220–222 (1986).
3. Grabarek, Z. & Gergely, J. Zero-length crosslinking procedure with the use of active esters. *Anal. Biochem.* **185**, 131–135 (1990).
4. Lomant, A. J. & Fairbanks, G. Chemical probes of extended biological structures: Synthesis and properties of the cleavable protein cross-linking reagent [35S]dithiobis(succinimidyl propionate). *J. Mol. Biol.* **104**, 243–261 (1976).
5. Stephanopoulos, N. & Francis, M. B. Choosing an effective protein bioconjugation strategy. *Nat. Chem. Biol.* **7**, 876–884 (2011).
6. Zimmerman, E. S. *et al.* Production of site-specific antibody-drug conjugates using optimized non-natural amino acids in a cell-free expression system. *Bioconjug. Chem.* **25**, 351–361 (2014).
7. Karver, M. R., Weissleder, R. & Hilderbrand, S. A. Bioorthogonal reaction pairs enable simultaneous, selective, multi-target imaging. *Angew. Chem., Int. Ed.* **51**, 920–922 (2012).
8. Patterson, D. M., Nazarova, L. A. & Prescher, J. A. Finding the Right (Bioorthogonal) Chemistry. *ACS Chem. Biol.* **9**, 592–605 (2014).
9. Bennett, V. J. & Simmons, M. A. Analysis of fluorescently labeled substance P analogs: binding, imaging and receptor activation. *BMC Chem. Biol.* **1**, 1 (2001).
10. Steinhoff, M. S., von Mentzer, B., Geppetti, P., Pothoulakis, C. & Bunnett, N. W. Tachykinins and their receptors: contributions to physiological control and the mechanisms of disease. *Physiol. Rev.* **94**, 265–301 (2014).
11. Grady, E. F. *et al.* Delineation of the endocytic pathway of substance P and its seven-transmembrane domain NK1 receptor. *Mol. Biol. Cell* **6**, 509–524 (1995).
12. Garland, A. M., Grady, E. F., Payan, D. G., Vigna, S. R. & Bunnett, N. W. Agonist-induced internalization of the substance P (NK1) receptor expressed in epithelial cells. *Biochem. J.* **303**,

- 177–186 (1994).
13. Maggi, C. A., Patacchini, R., Rovero, P. & Giachetti, A. Tachykinin receptor antagonists and potential clinical applications at peripheral level. *Biochem. Soc. Trans.* **19**, 909–912 (1991).
 14. Matikonda, S. S. *et al.* Bioorthogonal prodrug activation driven by a strain-promoted 1,3-dipolar cycloaddition. *Chem. Sci.* **6**, 1212–1218 (2015).
 15. Chen, W., Wang, D., Dai, C., Hamelberg, D. & Wang, B. Clicking 1,2,4,5-tetrazine and cyclooctynes with tunable reaction rates. *Chem. Commun.* **48**, 1736 (2012).
 16. Rossin, R. *et al.* Highly Reactive trans-Cyclooctene Tags with Improved Stability for Diels-Alder Chemistry in Living Systems. *Bioconjug. Chem.* **24**, 1210–1217 (2013).
 17. Tota, M. R. *et al.* Characterization of a fluorescent substance P analog. *Biochemistry* **33**, 13079–13086 (1994).
 18. Southwell, B. R., Woodman, H. L., Murphy, R., Royal, S. J. & Furness, J. B. Characterisation of substance P-induced endocytosis of NK1 receptors on enteric neurons. *Histochem. Cell Biol.* **106**, 563–571 (1996).
 19. Marm, N., Knemeyer, J., Sauer, M., Wolfrum, J. & Marme, N. Inter- and Intramolecular Fluorescence Quenching of Organic Dyes by Tryptophan I. *Bioconjug. Chem.* **14**, 1133–1139 (2003).
 20. Inácio, Â. S. *et al.* In vitro surfactant structure-toxicity relationships: Implications for surfactant use in sexually transmitted infection prophylaxis and contraception. *PLoS One* **6**, (2011).
 21. Roosterman, D. *et al.* Endothelin-converting enzyme 1 degrades neuropeptides in endosomes to control receptor recycling. *Proc. Natl. Acad. Sci. U. S. A.* **104**, 11838–11843 (2007).
 22. Yoshimori, T., Yamamoto, A., Moriyama, Y., Futai, M. & Tashiro, Y. Bafilomycin-A1, a Specific Inhibitor of Vacuolar-Type H⁺-Atpase, Inhibits Acidification and Protein-Degradation in Lysosomes of Cultured-Cells. *J. Biol. Chem.* **266**, 17707–17712 (1991).
 23. Beyenbach, K. W. & Wieczorek, H. The V-type H⁺ ATPase: molecular structure and function, physiological roles and regulation. *J. Exp. Biol.* **209**, 577–89 (2006).
 24. Cheng, Y. *et al.* Structure of the Human Transferrin Receptor-Transferrin Complex. *Cell* **116**, 565–576 (2004).
 25. Gayen, A., Goswami, S. K. & Mukhopadhyay, C. NMR evidence of GM1-induced conformational change of Substance P using isotropic bicelles. *Biochim. Biophys. Acta - Biomembr.* **1808**, 127–

- 139 (2011).
26. Zhang, B. *et al.* Different methods of detaching adherent cells significantly affect the detection of TRAIL receptors. *Tumori* **98**, 800–803 (2012).
 27. Cottrell, G. S. *et al.* Endosomal endothelin-converting enzyme-1. A regulator of β -arrestin-dependent ERK signaling. *J. Biol. Chem.* **284**, 22411–22425 (2009).

Chapter 4. SNAP_{Switch}: A Molecular Sensor to Quantify Endosomal Escape and Cellular Localisation

4.1 Summary

The ability to determine where internalised cargo is trafficked to following endocytosis is critical when engineering nanomaterials for intracellular delivery. This includes determining if inbound cargo remains trapped in endocytic vesicles or if it is able to reach the cytosol and nucleus. However, there are currently limited tools available to establish how much material is transported to a given location in real-time. To overcome this, a sensor that can signal when material arrives at a location of interest is required. This chapter describes the synthesis and evaluation of a quenched SNAP-tag substrate (SNAP_{Switch}) that can be conjugated to a material. The trafficking of the material can then be followed by expressing the SNAP-tag at locations of interest in the cell as the sensor will begin to fluoresce if it reaches this area. It was demonstrated that SNAP_{Switch} is responsive to the SNAP-tag and that the fluorescence of SNAP_{Switch} was efficiently quenched unless in the presence of the enzyme. In addition, SNAP_{Switch} attached to a protein was only activated by SNAP-tag fused to the receptor for that protein, demonstrating the specificity of activation. Finally, SNAP_{Switch} was able to detect delivery of a DNA oligonucleotide to the cytosol and translocation to the nucleus induced by a commonly used transfection reagent.

SNAP_{Switch}: A Molecular Sensor to Quantify Cytosolic Delivery and Cellular Localisation

Laura I Selby^{1,2}, Luigi Aurelio¹, Moore Chen¹, Daniel Yuen¹, Bim Graham¹ & Angus P R Johnston^{1,2*}

¹Monash Institute of Pharmaceutical Sciences, Monash University, Parkville, Victoria, Australia.

²ARC Centre of Excellence in Convergent Bio-Nano Science and Technology, Monash University, Parkville, Australia.

Correspondence

Email: Angus.Johnston@monash.edu

Background

The trafficking of proteins and nanoparticles following endocytosis is critical across many areas of the biological sciences including cell signalling, pathogenesis, immunological responses and in the cellular fate of nanomedicines. Ascertaining movement of cargo to a specific place within the cell is commonly performed through colocalisation analysis, where the overlap of fluorescent markers observed via microscopy signifies presence in a subcellular organelle. The implication of the results can be difficult to interpret, and the method is inherently low throughput. Based on the enzymatic SNAP-tag system, we have developed a quenched substrate (SNAP_{Switch}) that can be attached to a nanoparticle or protein and allows for the detection of material trafficked to specific locations. The fluorescence of SNAP_{Switch} is initially quenched. However, when the sensor is in close proximity to the SNAP-tag, the quencher is transferred to the enzyme, and the fluorescence is switched on. We show SNAP_{Switch} can be used to detect cytosolic and nuclear delivery of cargo, demonstrating its power as a tool to probe the subcellular localisation of materials.

Main Text

Understanding where material is trafficked to once it is endocytosed is essential for improving the therapeutic delivery of proteins and nanoparticles. Following internalisation, many therapeutics become trapped in endo/lysosomes, preventing access to their site of action.^{1,2} For example, delivery of nucleic acids for silencing and gene delivery applications requires transfer to the cytosol and nucleus.³ In order to design efficient drug carriers, we need to understand how the properties of the material dictate biological fate. Intracellular trafficking is routinely probed by performing colocalisation analysis. The overlap between fluorescently labeled nanomaterial or proteins with markers for intracellular compartments is assessed via microscopy.⁴ Rigorous statistical analysis such as calculation of the Pearson correlation coefficient is required to quantify the degree of colocalisation, the results of which can be unclear when intermediate values are obtained.⁵ A potential avenue to overcome this is to develop a sensor that signals only when a particle or protein has reached a location of interest within the cell.⁶

Although fluorescent protein fusions have traditionally been used to specifically label a location within the cell,⁷ enzyme tagging systems have recently attracted attention as an alternative. These systems were developed to allow fluorescent labelling with small organic dyes which can be superior in terms of brightness and photostability.^{8,9} One of the most established schemes is the SNAP-tag, which is an engineered variant of the 19 kDa O⁶-alkylguanine-DNA alkyltransferase repair enzyme that reacts with benzylguanine, covalently linking a fluorescent label to the tag.^{7,9,10}

To address the issues with conventional colocalisation analysis, we have developed a clickable¹¹ and quenched substrate (SNAP_{Switch}). SNAP_{Switch} contains a fluorophore and quencher pair conjugated through the benzylguanine moiety that also includes an azido lysine residue for attachment to a material of interest (**Figure 1a**). Current quenched substrates are engineered to be membrane permeable and are not designed for attachment, which prevents their use in studying the localisation of inbound material.^{12,13}

SNAP_{Switch} is structured so that the material begins to fluoresce after interaction with the SNAP-tag (**SI Figure 1**). After activation, the fluorescence is permanently switched on, which means signal strengthens over time, enabling accumulation and fleeting interactions to be detected. The fluorescent component also dissociates from the SNAP-tag allowing for observation of the subsequent material trafficking. Following synthesis, we evaluated the quenching and activation of SNAP_{Switch} by in-gel fluorescence. The SNAP_{Switch} had low a background signal in its quenched state and in the presence of the SNAP-tag, became intensely fluorescent (**Figure 1b**). The fluorescent band corresponds to the free dye, and not the molecular weight of the SNAP-tag, as the quencher is transferred to the enzyme and the fluorophore is released. Labeling of free SNAP-tag enzyme with SNAP Cell SiR 647 resulted in a fluorescent band under 25 kDa while unreacted fluorescent substrate appeared at a similar position to the cleaved SNAP_{Switch} (**Figure 1b**).

The SNAP_{Switch} conjugate was stable in the quenched state, showing no increase in fluorescence intensity over a 90 minute incubation period in solution. However, the fluorescent signal was rapidly activated in the presence of SNAP-tag. Incubation of SNAP_{Switch} with 20 molar equivalents of SNAP-tag resulted in a 9.5-fold increase in Cy5 fluorescence intensity after 90 minutes (**Figure 1c**). A distinct difference in SNAP_{Switch} signal compared to the control was observed within 10 minutes.

Having established that SNAP_{Switch} was quenched efficiently and was responsive to the SNAP-tag enzyme in solution, we moved to demonstrating activation *in vitro*. Activation of SNAP_{Switch} by SNAP-tag expressed on the cell surface was tested by fusing the enzyme to the transferrin receptor (SNAP-TfR). SNAP-TfR was transiently expressed in HEK293 cells and SNAP_{Switch} was conjugated to transferrin. An additional fluorophore, Alexa Fluor 488 (AF488) was also attached to transferrin to track the location of the protein while the sensor was switched off.

As anticipated, SNAP_{Switch} attached to transferrin was activated by SNAP-TfR in transfected HEK293 cells (**Figure 2a**). Transferrin was taken up into SNAP-TfR transfected cells, as shown by the punctate SNAP_{Switch} fluorescence (**Figure 2a, SI Figure 4**). SNAP_{Switch} signal colocalised with the signal from SNAP-tag labelled with SNAP Surface 549 (**SI Figure 5**), indicating that the activation is specific to the presence of the SNAP-tag. The SNAP_{Switch} signal also colocalised with AF488 transferrin signal (**Figure 2a, SI Figure 4**), demonstrating that the Cy5 from the SNAP_{Switch} remains attached to the transferrin. Cells without SNAP-tag expression showed transferrin uptake, but minimal Cy5 signal. This demonstrates that SNAP_{Switch} is stable under intracellular conditions and the sensor only becomes fluorescent in the presence of the SNAP-tag.

Material labelled with SNAP_{Switch} must be in close proximity to the SNAP-tag for the sensor to be switched on. Cells expressing TfR-SNAP incubated with an anti-CD44 antibody labeled with SNAP_{Switch} and AF488 show significant binding to the cell surface through the AF488 signal, but no activation of SNAP_{Switch} (**Figure 2b**). CD44 is a membrane glycoprotein involved in cell adhesion, signaling and is predominately located on the plasma membrane.¹⁴ A small proportion of CD44 internalises in 3T3-NIH cells, but by clathrin-independent carrier (CLIC) endocytosis, rather than the clathrin-dependent pathway followed by transferrin.¹⁵ The lack of SNAP_{Switch} signal suggests CD44 bound to the cell surface does not come into the vicinity of SNAP-tagged TfR. The TfR has rapid membrane turnover, so to further demonstrate the specificity of the system we incubated SNAP_{Switch} labeled anti-CD44 with cells expressing SNAP-tag fused to the beta-2-adrenergic receptor (ADR β 2). ADR β 2 is a G-protein-coupled receptor more strictly confined to the extracellular surface.¹⁶ The cells displayed significant binding of anti-CD44 to the cell surface and high SNAP-tag expression on the cell membrane, but no observable SNAP_{Switch} activation (**SI Figure 6**). This further demonstrates that SNAP_{Switch} activation is

specific, and that labelled proteins must come into close proximity to the SNAP-tag for fluorescence to occur. Therefore, SNAP_{Switch} can be used with fluorescence microscopy to investigate localisation qualitatively.

Activation of SNAP_{Switch} can also be quantified by flow cytometry. Cells transfected with SNAP-TfR showed slight increases in the background fluorescence intensity in both the AF488 (**SI Figure 7a**) and Cy5 (**SI Figure 7b**) channels. The cells were then incubated with Tf dual-labelled with AF488 and SNAP_{Switch}. After subtracting the background fluorescence, there was no significant difference in the AF488 signal, which shows the level of association was the same between non-transfected and transfected cells (**Figure 2c**). However, the Cy5 signal was significantly higher in transfected cells than in cells with no SNAP-tag (**Figure 2d**). This demonstrates the ability of SNAP_{Switch} to determine co-localisation of sensor and tag in a high throughput manner. To account for any differences in the association across non-transfected and TfR-SNAP cells, the ratio between the mean Cy5 fluorescence and AF488 was calculated. This confirms activation of SNAP_{Switch} in TfR-SNAP transfected cells as the ratio is ~1.4, significantly higher than the background ratio of ~0.91 in cells without SNAP-tag (**Figure 2e**).

To test if SNAP_{Switch} could be used to detect localisation in the nucleus and cytosol, and thus measure delivery and transport, we expressed the SNAP-tag in both the cytosol (CytoSNAP) and nucleus (NuclearSNAP). To express SNAP-tag in the cytosol, the commercially available pSNAPf plasmid from New England Biolabs was used. SNAPf is a variant of the SNAP-tag that has been mutated to improve the labeling kinetics.¹² As the sequence is not targeted any specific subcellular organelle, the protein is expressed diffusely throughout the cytoplasm and nucleus. Transfection with this plasmid resulted in high SNAP-tag expression throughout the cell, observable from a diffuse fluorescent signal when labelled with SNAP Cell SiR 647 (**SI Figure 8**). To restrict expression to the nucleus, the SNAP-tag sequence was inserted prior to an mTurquoise-histone 2A (H2A) fusion.¹⁷ H2A is a histone protein involved in the formation of nucleosomes in the nucleus.¹⁸ The presence of the fluorescent protein mTurquoise allowed us to confirm the SNAP-tag was correctly confined to the nucleus as the SNAP Cell SiR 647 signal colocalised with mTurquoise fluorescence in nuclear regions (**SI Figure 9**).

We then tested the ability of SNAP_{Switch} to track cytosolic delivery of an oligonucleotide complexed with Lipofectamine 3000 to the cytosol and subsequent transport to the nucleus. Dual-labelled complexes were formed using a 20-mer oligonucleotide sequence labelled with AF488 and either Cy5 or SNAP_{Switch}. The complexes were then incubated with HEK293 cells transfected with either an empty plasmid, CytoSNAP or NuclearSNAP. Cells incubated with Cy5/AF488 complexes showed a linear increase in Cy5 fluorescence intensity over the 16 hour time period (**SI Figure 10a**) while the AF488 signal increased until 4 hours before decreasing (**SI Figure 10b**). Importantly, SNAP-tag expression in these cells did not cause any significant differences in the association of the complexes with cells when compared to cells without the enzyme.

Lipofectamine 3000 induced cytosolic delivery of the oligonucleotides which were then transported to the nucleus. In cells incubated with SNAP_{Switch} complexes, the Cy5 fluorescence of both CytoSNAP and NuclearSNAP was significantly higher than the SNAP-free cells, signifying activation of SNAP_{Switch} and thus detecting cytosolic delivery (**Figure 3a**). Presence of the SNAP-tag was confirmed by flow and incubating the cells with SNAP Cell SiR 647. (**SI Figure 10c**). The AF488 signal behaved similarly to the Cy5/AF488 complexes, with no significant difference at any of the time points between the various transfections and followed a comparable trend (**SI Figure 10d**). The increase in mean fluorescence intensity for both CytoSNAP (~44) and NuclearSNAP (~23) at the 16 hour time point confirms SNAP_{Switch} can be used to detect cytosolic delivery and transfer of the oligonucleotides into the nucleus.

The increase in Cy5 signal is useful as an indicator for cytosolic delivery and transport to the nucleus. However, the numerical value is an underrepresentation of the degree at which it has occurred as the experiment is conducted using transiently transfected cells, not all of which express SNAP-tag. Oligonucleotides in the cytosol of cells without SNAP-tag expression remain quenched, lowering the overall mean fluorescence intensity (MFI) from the potential maximum signal. This could be overcome by generation of a cell line stably expressing the SNAP-tag or alternatively, by using the mTurquoise signal from NuclearSNAP transfected cells to identify SNAP-tag expression.

The delivery to the nucleus was reevaluated by examining the SNAP_{Switch} signal in cells positive for mTurquoise expression. By gating on mTurquoise fluorescence, two populations were identified (**SI**

Figure 10e), one with high fluorescence (MFI ~ 100) and one with no expression (MFI ~ 3). The expression of SNAP-tag in the mTurquoise positive population was confirmed by the high SNAP Cell SiR 647 signal within these cells (**SI Figure 10f**). The Cy5 signal from SNAP_{Switch} of the negative cells slowly increases over the 16 hour time period from ~ 2 to 45 while the signal from the cells positive for mTurquoise rapidly increases from ~1.3 to 157 (**Figure 3b**). The SNAP_{Switch} signal from negative cells can then be treated as background fluorescence and subtracted from the MFI of the cells positive for mTurquoise. By removing non-expressing cells, the true delivery and accumulation in the nucleus over time can then be determined (**Figure 3c**).

SNAP_{Switch} was also used to visualise cytosolic delivery and nuclear translocation by fluorescence microscopy. Cells transfected with CytoSNAP or NucleaSNAP and incubated with SNAP_{Switch} oligonucleotide complexes showed activation of fluorescence in different regions of the cell. In cells transfected with CytoSNAP, SNAP_{Switch} signal was observed dispersed throughout the cell in addition to multiple bright punctate structures (**Figure 3d**). This suggests that a proportion of the oligonucleotides may still be complexed with Lipofectamine in the cytosol or potentially associated with the membrane remnants of ruptured endo/lysosomes. The fluorescent signal from within cells transfected with NuclearSNAP was generally confined to the nucleus (**Figure 3e**). The lack of punctate structures here implies that oligonucleotides completely dissociate from Lipofectamine 3000 either before, or after reaching the nucleus. The localisation of the signal for both CytoSNAP and NuclearSNAP was consistent with labelling with a membrane permeable fluorescent substrate (**SI figure 8 & 9**). No signal was observed in cells incubated with SNAP_{Switch} complexes and transfected with an empty plasmid when all images were normalised to the same pixel intensity range (**Figure 3f**).

SNAP_{Switch} provides a method to follow the journey of material in cells and its delivery to sub-cellular locations following endocytosis. The low background fluorescence of the sensor when switched off and the large increase when the SNAP-tag is encountered, provides the basis for a system to definitively identify when internalised cargo has reached a specific location in the cell. The requirement of the labeled material to be in close proximity to the SNAP-tag to trigger fluorescence represents a potential method to further probe intracellular trafficking pathways. Additionally, the ability to detect delivery to

the cytosol and nucleus provides a useful tool in the biological sciences to study the intracellular trafficking, cytosolic delivery and subcellular transport of nanoparticles and proteins.

Acknowledgments

The authors thank Dr. Jason Dang (Monash University, Melbourne) for his assistance with HPLC, LCMS and HRMS.

Author Contributions

L.I.S., A.P.R.J. and B.G. designed the study. L.I.S., L.A and B.G. performed the chemical synthesis. M.C. and D.Y. performed the cloning. L.I.S. and A.P.R.J. analysed the data and wrote the manuscript.

Competing Financial Interests

The authors declare no competing financial interests.

References

1. Martens, T. F., Remaut, K., Demeester, J., De Smedt, S. C. & Braeckmans, K. Intracellular delivery of nanomaterials: How to catch endosomal escape in the act. *Nano Today* **9**, 344–364 (2014).
2. Selby, L. I., Cortez-Jugo, C. M., Such, G. K. & Johnston, A. P. R. Nanoescapology: progress toward understanding the endosomal escape of polymeric nanoparticles. *Wiley Interdiscip. Rev. Nanomedicine Nanobiotechnology* e1452 (2017). doi:10.1002/wnan.1452
3. Rajendran, L., Knölker, H.-J. & Simons, K. Subcellular targeting strategies for drug design and delivery. *Nat. Rev. Drug Discov.* **9**, 29–42 (2010).
4. Bolte, S. & Cordelières, F. P. A guided tour into subcellular colocalization analysis in light microscopy. *J. Microsc.* **224**, 213–32 (2006).
5. Dunn, K. W., Kamocka, M. M. & McDonald, J. H. A practical guide to evaluating colocalization in biological microscopy. *Am. J. Physiol. Cell Physiol.* **300**, C723–C742 (2011).
6. Nadler, A. & Schultz, C. The power of fluorogenic probes. *Angew. Chem. Int. Ed. Engl.* **52**,

- 2408–10 (2013).
7. Giepmans, B. N. G., Adams, S. R., Ellisman, M. H. & Tsien, R. Y. The fluorescent toolbox for assessing protein location and function. *Science* **312**, 217–24 (2006).
 8. Marks, K. & Nolan, G. Chemical labeling strategies for cell biology. *Nat. Methods* **3**, 591–596 (2006).
 9. Jing, C. & Cornish, V. W. Chemical Tags for Labeling Proteins Inside Living Cells. *Acc. Chem. Res.* **44**, 784–792 (2011).
 10. Hussain, A. F., Amoury, M. & Barth, S. SNAP-tag technology: a powerful tool for site specific conjugation of therapeutic and imaging agents. *Curr. Pharm. Des.* **19**, 5437–42 (2013).
 11. Patterson, D. M., Nazarova, L. A. & Prescher, J. A. Finding the Right (Bioorthogonal) Chemistry. *ACS Chem. Biol.* **9**, 592–605 (2014).
 12. Sun, X. *et al.* Development of SNAP-tag fluorogenic probes for wash-free fluorescence imaging. *Chembiochem* **12**, 2217–26 (2011).
 13. Hori, Y. *et al.* Development of fluorogenic probes for quick no-wash live-cell imaging of intracellular proteins. *J. Am. Chem. Soc.* **135**, 12360–5 (2013).
 14. Ponta, H., Sherman, L. & Herrlich, P. A. CD44: From adhesion molecules to signalling regulators. *Nat. Rev. Mol. Cell Biol.* **4**, 33–45 (2003).
 15. Howes, M. T. *et al.* Clathrin-independent carriers form a high capacity endocytic sorting system at the leading edge of migrating cells. *J. Cell Biol.* **190**, 675–691 (2010).
 16. Taylor, M. R. G. Pharmacogenetics of the human beta-adrenergic receptors. *Pharmacogenomics J.* **7**, 29–37 (2007).
 17. Goedhart, J. *et al.* Structure-guided evolution of cyan fluorescent proteins towards a quantum yield of 93%. *Nat. Commun.* **3**, 1–9 (2012).
 18. Mosammaparast, N. *et al.* Nuclear import of histone H2A and H2B is mediated by a network of karyopherins. *J. Cell Biol.* **153**, 251–262 (2001).
 19. Foley, J. W., Locatelli, L. J. & Zepp, C. M. Novel Xanthene Compounds and Photographic Products and Processes Employing the Same. (1981).
 20. Komatsu, T. *et al.* Real-time measurements of protein dynamics using fluorescence activation-coupled protein labeling method. *J. Am. Chem. Soc.* **133**, 6745–51 (2011).
 21. Richardson, W. H. Bayesian-based iterative method of image restoration. *J. Opt. Soc. Am.* **62**,

- 55–59 (1972).
22. Lucy, L. B. An iterative technique for the rectification of observed distributions. *Astron. J.* **79**, 745–749 (1974).
 23. Bruce, M. a & Butte, M. J. Real-time GPU-based 3D Deconvolution. *Opt. Express* **21**, 4766–4773 (2013).
 24. Sambrook, J. & Russell, D. W. . *Molecular Cloning: A Laboratory Manual*. (Cold Spring Harbor Laboratory, 2001).
 25. Tang, H., Zhu, Z., Wan, X., Chen, X. & Zhou, Q. Tailoring Thermotropic Liquid Crystalline Properties of Random Copolymers Based on Vinyl Monomers with Laterally Attached Mesogenic and Nonmesogenic Substituents via No Spacer. *Macromolecules* **39**, 6887–6897 (2006).

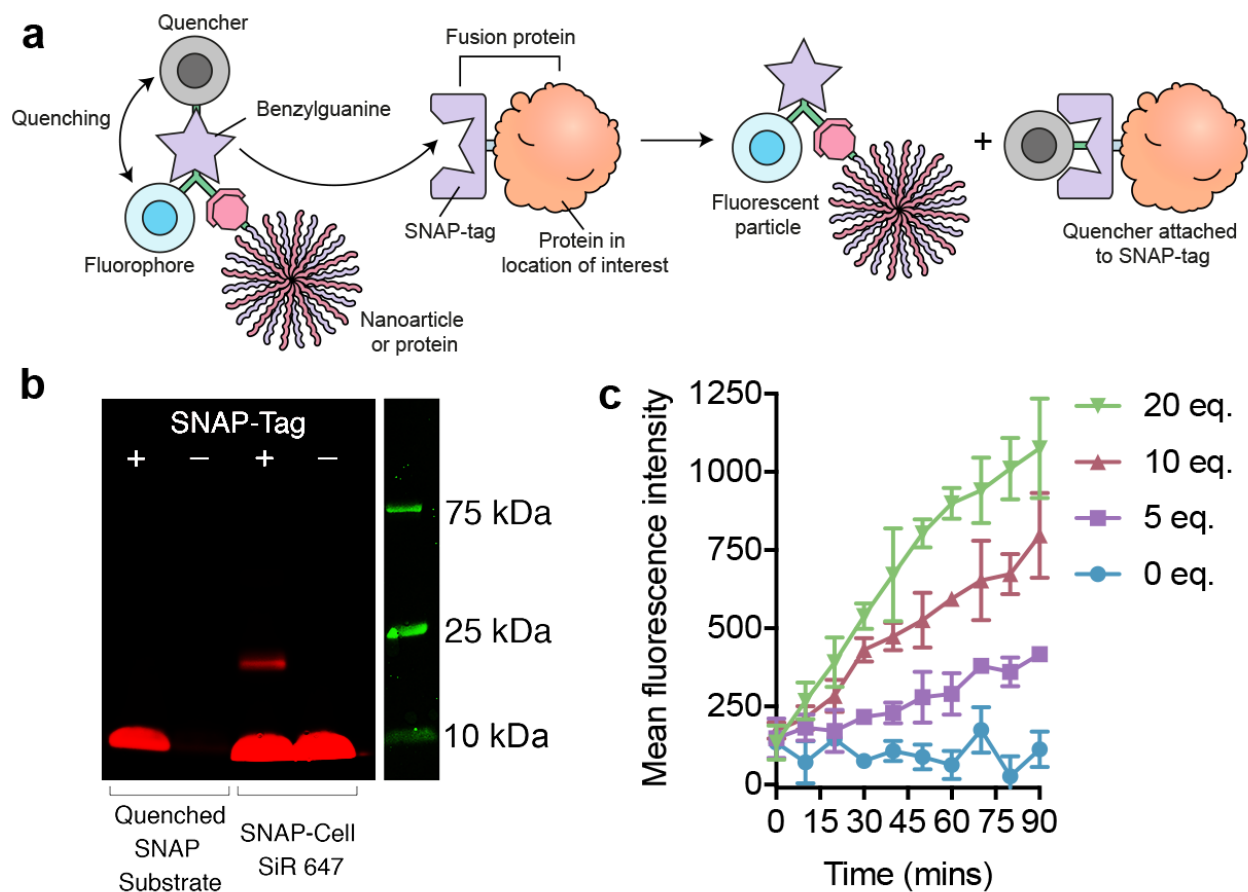


Figure 1 – Attachable and quenched SNAP-tag substrate ($\text{SNAP}_{\text{Switch}}$) scheme and activation. (a) $\text{SNAP}_{\text{Switch}}$ consists of a quencher and fluorophore conjugated to either side of a benzylguanine group. An azide is also included for attachment of the sensor to a nanoparticle or protein through click chemistry. If the material reaches SNAP-tag fused to a protein in a location of interest, the quencher is transferred to the enzyme, breaking the interaction and allowing the sensor to fluoresce. (b) In-gel detection of the quenched SNAP-tag substrate. 600 μM quenched $\text{SNAP}_{\text{Switch}}$ or fluorescent SNAP-Cell 647-SiR with or without 5 μM SNAP-tag protein incubated at 37°C for 30 minutes before adding to wells. (c) Fluorescence activation of 0.10 μM quenched SNAP-tag substrate in the presence of SNAP-tag protein at 27°C over a 1.5-hour time period.

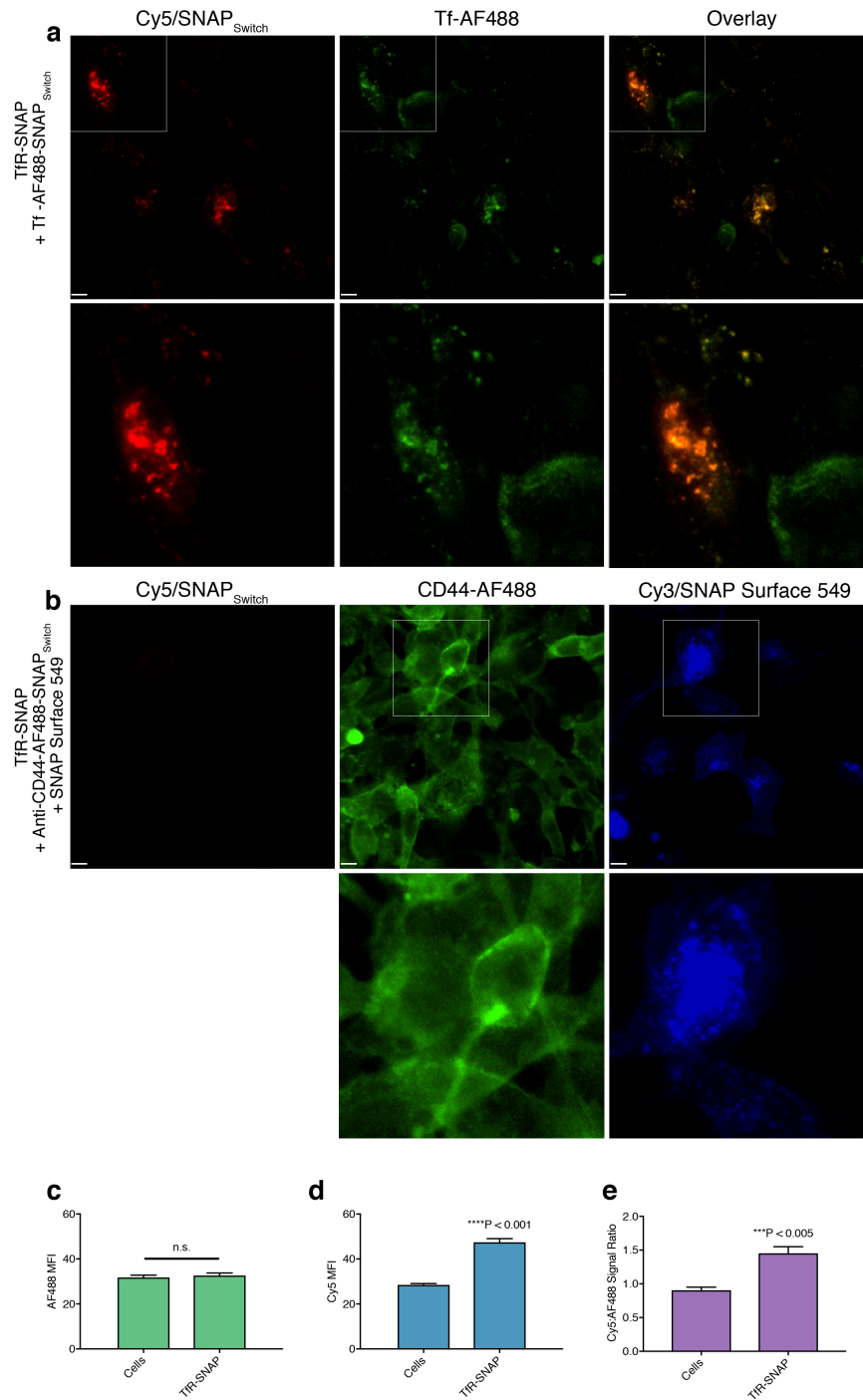


Figure 2 – Surface localised and internalised SNAP-tag. Fluorescence microscopy images of transferrin dual-labelled with SNAP_{Switch} and AF488 incubated for 30 minutes with 3T3-NIH cells transfected to express the SNAP-tag fused to the transferrin receptor (Tfr-SNAP). **(a)** Dual-labelled Tf (2 μ g) in Tfr-SNAP transfected cells. **(b)** Dual-labelled Anti-CD44 (0.5 μ g) binds to the cell surface (AF488) but does not activate SNAP_{Switch} (Cy5) in the presence of the SNAP-tag on the Tfr (Cy3). Bottom panels of **(a and b)** shows zoomed views of the boxed areas. **(c-e)** Flow cytometry analysis of dual-labelled transferrin in HEK293 cells with and without transfection to express Tfr-SNAP. The mean fluorescence intensity of the **(c)** AF488 and **(d)** Cy5 signal is plotted with error bars representing the standard deviation (n = 3). **(e)** The average ratio of the Cy5 and AF488 for cells with and without Tfr is plotted with the error bars representing the maximum and minimum ratios from the available data (P = 0.0009 unpaired t-test, n = 3). Scale bar = 10 μ m.

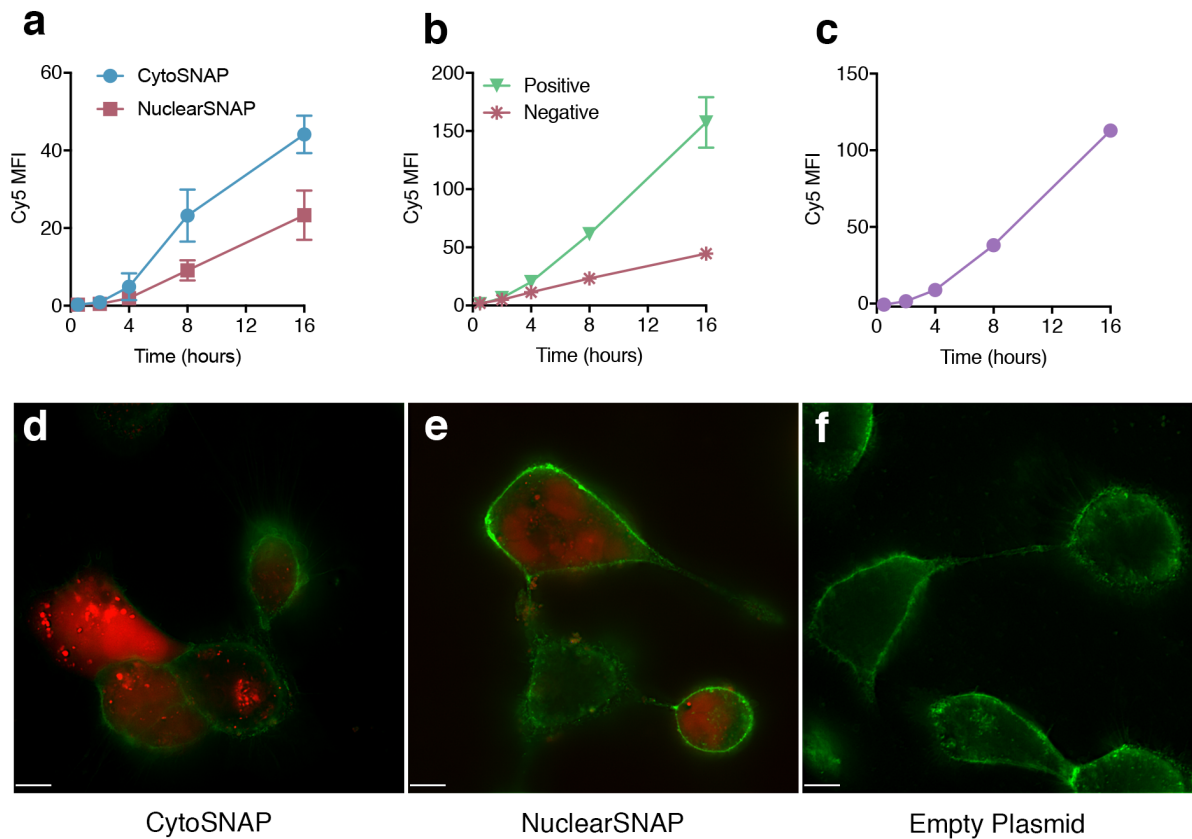


Figure 3 – Time-dependent detection of oligonucleotides in the cytosol and nucleus by SNAP_{Switch} in HEK293 cells transiently expressing Cyto- and NuclearSNAP, delivered by Lipofectamine 3000. (a) Mean fluorescence intensity of Lipofectamine 3000 complexes formed with SNAP_{Switch}-oligonucleotide over time by flow cytometry. The average background signal in cells without SNAP-tag expression but transfected with SNAP_{Switch} labelled oligonucleotide had been subtracted from each time point. (b) SNAP_{Switch} mean fluorescence intensity from flow cytometry in cells expressing mTurquoise versus those without expression. (c) Nuclear accumulation of SNAP_{Switch} labelled oligonucleotide in HEK293 cells transfected with Lipofectamine 3000, the average positive signal from (b) is plotted with the negative signal subtracted at each time point. The mean is plotted with error bars representing the standard deviation over two biological replicates, in duplicate (n = 4). Deconvolved fluorescence microscopy images of oligonucleotide labeled with SNAP-switch delivered into cells transfected with (d) CytoSNAP, (e) NuclearSNAP and (f) an empty plasmid. Scale bar = 10 μ m.

Online Methods

Materials. Peptide synthesis reagents including 2-chlorotrityl chloride resin, N(α)-Fmoc-N(ϵ)-azide-L-lysine and (Benzotriazol-1-yloxy)tripyrrolidinophosphonium hexafluorophosphate (PyBOP) were purchased from ChemImpex. Fmoc-N-amido-dPEG₄-acid was purchased from Quanta Biosciences. Sulfonated Cyanine 5 Succinimidyl Ester (sCy5-NHS) was purchased from Lumiprobe. Solvents and other organic synthesis reagents including acetonitrile (MeCN), ethylenediamine, dichloromethane (DCM), dimethylformamide (DMF), methanol (MeOH), N,N-diisopropylethylamine (DIPEA), anhydrous dimethyl sulfoxide (DMSO), hexafluoroisopropanol (HFIP), triisopropylsilane (TIPS), Dithiothreitol (DTT), piperidine and phosphate buffered saline tablets (PBS) were purchased from Sigma-Aldrich. Sulfonated QSY-21 carboxylic acid (sQSY-21-COOH)¹⁹ and Fmoc-benzylguanine carboxylic acid (Fmoc-BG-COOH)²⁰ were synthesized and purified in house by from published procedures.

Fluorescent SNAP-tag labelling reagents were purchased from New England Biolabs. Additional labels and reagents including Alexa Fluor 488 Succinimidyl Ester (AF488-NHS), Alexa Fluor 488 Azide, Wheat Germ Agglutinin Alexa Fluor 488 conjugate, Click-IT Succinimidyl Ester DIBO Alkyne (DIBO-NHS) Zeba Spin Columns 7k Molecular Weight Cut-Off, Lipofectamine 3000 Transfection Reagent and general tissue culture supplies were obtained from Thermo Fisher Scientific. The monoclonal antibody against mouse CD44 (5035-41.1D) was purchased from Novus Biologicals.

Instrumentation. Liquid Chromatography – Mass Spectrometry (LCMS) was performed on an Agilent 6100 Series Single Quad LCMS with a photodiode array detector (214/254 nm) coupled to an Agilent 1200 Series HPLC with a G1311A quaternary pump, G1329A thermostated auto sampler and 1200 Series G1314B variable wavelength detector with a scan range between 100–1000 m/z and a 5 minute acquisition time.

High-performance Liquid Chromatography (HPLC) was performed on an Agilent 1260 series modular HPLC fitted with a G1312B binary pump, G1316A compartment equipped with an Agilent Eclipse Plus C18 3.5 μ m, 4.6 x 100 mm column and a G1312B diode array detector using an elution protocol of 0 – 10 min, gradient from 5% MeCN/0.1% TFA/95% H₂O/0.1% TFA to 100% MeCN/0.1% TFA with a flow

rate of 1 mL min⁻¹. Preparative high-performance liquid chromatography (HPLC) used a Grace Alltima C8 5 μ particle size, 22 x 250 mm column.

High Resolution – Mass Spectrometry (HRMS) was performed on a Waters LCT TOF LCMS Mass Spectrometer coupled to a 2795 Alliance Separations module. All data was acquired and mass corrected via a dual-spray Leucine Enkephaline reference sample. Mass spectra were created by averaging the scans across each peak and background subtracted of the TIC. Acquisition and analysis were performed using the Masslynx software version 4.1.

Gel fluorescence images were obtained on a Amersham Typhoon 5 Biomolecular Imager (GE Healthcare Life Sciences). Fluorescence intensity measurements in solution were performed with a PerkinElmer EnSpire Multilabel plate reader operating at 27°C. All absorbance measurements were conducted on a NanoDrop ND-1000.

Cell Culture. 3T3-NIH (ATCC: CRL-1658) were maintained in Dulbecco's Modified Eagle Medium (DMEM), high glucose (GlutaMAX) with phenol red, 20% fetal bovine serum (FBS) and 1% penicillin/streptomycin at 37°C with 5%. HEK293A (ThermoFisher Scientific R70507) were maintained under the same conditions except 10% FBS was used.

Flow Cytometry. 10,000 events per sample were analysed with a Stratadigm S1000EXI flow cytometer (Stratadigm, California, USA) using 405 and 552 nm excitation with emission collected between 415 and 475 nm (for mTurquoise), 488 nm excitation with emission collected between 515 – 545 nm (for Alexa Fluor 488) and 642 nm excitation with emission collected between and 661 – 690 nm (for sCy5). FCS3.0 files were exported using CellCapTure Analysis Software (Stratadigm, California, USA) and imported into FlowJo (version 8, Tree Star, Oregon, USA) for further analysis.

Fluorescence Microscopy. Imaging by fluorescence microscopy was performed using a 60X 1.3 NA silicone or 40X 0.9 NA air objective with a standard “Pinkel” DAPI/FITC/Cy3/Cy5 Filter set (Semrock). Emission was separated and captured using a 414/497/565/653 nm dichroic mirror and a quad-band bandpass emission filter. Images were analyzed with Slidebook 6 (Intelligent Imaging Innovations,

Denver, USA). For deconvolution, 10 slices were captured with a 0.33 μm step size, exported and deconvolved using the Richard-Lucy algorithm^{21,22} with the CUDA deconvolution plugin in ImageJ.²³

SNAP_{Switch} Chemical Synthesis. The quenched and attachable benzylguanine substrate (SNAP_{Switch}) was constructed via Fmoc solid-phase peptide synthesis on 2-chlorotrityl chloride resin (200 mg). Fmoc groups were removed using two treatments for 2 minutes and one treatment for 5 minutes with 20% piperidine in DMF. The resin was bubbled for 1 hour in DCM with ethylenediamine (4 equiv, 50 mg, 0.83 mmol). N(α)-Fmoc-N(ϵ)-azide-L-lysine (1.5 equiv, 0.11 g, 0.3 mmol) was attached with PyBOP (1.5 equiv, 0.16 g, 0.3 mmol) and DIPEA (2 equiv to amino acid, 76 mg, 0.6 mmol) in DMF for 1 hour. A PEG linker was then attached by adding Fmoc-N-amido-dPEG₄-acid (1.5 equiv, 0.15 g, 0.3 mmol) with PyBOP (1.5 equiv, 0.16 g, 0.3 mmol) and DIPEA (2 equiv, 76 mg, 0.6 mmol) for 30 minutes in DMF. After deprotection, Fmoc-BG-COOH (1.5 equiv, 0.17 g, 0.3 mmol) was attached with PyBOP (1.5 equiv, 0.16 g, 0.3 mmol) and DIPEA (2 equiv, 76 mg, 0.6 mmol) in DMF overnight before washing with DMF, DCM and then followed by deprotection.

15 mg resin was combined in a 1.5 mL Eppendorf tube with the quencher sQSY-21-COOH (0.4 equiv, 5 mg, 5.94 μmol), PyBOP (1.5 equiv) and an excess of DIPEA (10 μL) in anhydrous DMSO for 23 hours, rotating. The resin was transferred back to a solid-phase peptide synthesis column and washed once with DMSO, followed by washes with MeOH until the flow through was clear and then three times with DCM. The resin was dried under N₂ and the compound cleaved with 4 mL of 50% DCM and 50% HFIP with 10 μL TIPS for 2 hours at room temperature. The mixture was drained into a round bottom flask using HFIP and the solvent evaporated under N₂. The compound was purified via HPLC with a water/MeCN 0.1% TFA 5 - 100% gradient at a flow rate of 7 mL min⁻¹ over 45 minutes. The product mass was confirmed via LCMS.

To the entire fraction from HPLC (4.97 mg), sCy5-NHS (1 equiv) was added with excess DIPEA (10 μL) in 200 μL DMSO and left overnight. The presence of the product mass was confirmed via LCMS and purified using 5 – 100% gradient over 45 minutes at a flow rate of 7 mL min⁻¹. The product mass was identified by LCMS, confirmed by HRMS and lyophilised. HRMS (ESI) m/z: calculated for C₁₀₈H₁₂₄N₁₈O₂₅S₅ [M + 3H]⁺³ 745.2602, found 745.2635, calculated for [M + 2H]⁺² 1117.8882, found

1117.8887, calculated for $[M + 2Na]^{+2}$ 1139.8701, found 1139.8704 (**SI Figure 2**). Purity was estimated by analytical HPLC as ~ 82% (**SI Figure 3**). SNAP_{Switch} was reconstituted in DMSO to a concentration of 4 mM and stored at -20°C.

Fluorescence Activation by the SNAP-tag in Solution. The effect of SNAP-tag protein excess on the SNAP_{Switch} was investigated using a fluorescence plate reader. SNAP_{Switch} was initially diluted in PBS to 0.10 μ M. 45 μ L of this solution was then combined with 0 to 20 molar equivalents of SNAP-tag and PBS to bring the final volume to 65 μ L in a 96-well clear bottom black polystyrene microplate. The fluorescence emission at 661 nm was obtained using a 646 nm excitation and was recorded every 10 minutes over a 90 minute time period.

Fluorescence In-Gel Detection. Samples were prepared by combining 5 μ M SNAP-tag protein or PBS with 10 μ M of SNAP_{Switch} and 1 mM DTT in a final volume of 40 μ L. The reaction was incubated at 37°C for 30 minutes then left to cool for 10 minutes before adding 6 μ L of 0.2% 2-mercaptoethanol in SDS-page loading dye.²⁴ Samples were then heated to 94°C for 2 minutes and added to the wells of a precast 12% polyacrylamide gel (Bio-Rad). The gel was run for 45 minutes at 120 V in running buffer (25 mM Tris, 250 mM glycine, 0.1% SDS at pH 8.3).

Plasmid Construction. The empty transfection control plasmid pcDNA3.1(-) was purchased from Life Technologies. The TfR-SNAP fusion construct was modified from mEmerald-TFR-20 (a gift from Michael Davidson, Addgene plasmid #54278). Briefly, the sequence encoding SNAP-tag was PCR amplified from pSNAPf (New England BioLabs) with primers to append flanking BamHI and NotI restriction sites (Forward: 5' – GGA TCC ACC GGT CGC CAC CAT GGA CAA AGA CTG CG – 3', Reverse 5' – CGC GGC CGC TTA ACC CAG CCC AGG CTT GCC – 3'). This PCR product was subsequently ligated into mEmerald-TFR-20 at the same sites, replacing the mEmerald coding sequence.

Plasmids were constructed from pCDH-EF1-MCS-IRES-Puro (System Bioscience). Briefly, the SNAP-tag coding sequence from pSNAPf was subcloned into pCDH-EF1-MCS-IRES-Puro via NheI and BamHI to generate pCDH-EF1-SNAP-IRES-Puro (Cytosnap). The mTurquoise2-H2A sequence (a gift

from Dorus Gadella, Addgene plasmid #36207)¹⁷ was PCR amplified to append BamHI and NotI restriction sites (Forward: 5' – ACA GGA TCC ATG GTG AGC AAG GGC GAG GAG – 3', Reverse 5' – TGC GGC CGC GTT ATT TGC CTT T – 3'). This PCR product was then ligated into pSNAPf. The SNAPf-mTurquoise2-H2A coding sequence was excised by restriction with NheI and NotI and subcloned into pCDH-EF1-MCS-IRES-Puro to generate pCDH-EF1-SNAP-mTurquoise2-H2A-IRES-Puro (NuclearSNAP). All constructs were verified by DNA sequencing before use.

Estimation of SNAP_{Switch} Concentration. The estimated extinction coefficient of SNAP_{Switch} was determined using the binary system²⁵ Beer-Lambert law: $A_n = \epsilon_1 c_1 l + \epsilon_2 c_2 l$ (Equation 1) where, A_n = absorbance at wavelength n, l = path length (cm), ϵ_m = extinction coefficient of species m at wavelength n ($M^{-1} cm^{-1}$), c_m = concentration of species m at wavelength n (M).

Since both the fluorophore and quencher are conjugated to the same molecule, the concentration of each species was assumed to be the same ($c_1 = c_2 = c$). Using a path length of 0.1 cm, equation 4.1 reduces to: $A_n = 0.1c(\epsilon_1 + \epsilon_2)$ (Equation 2).

The extinction coefficient of each dye at the absorption maximum of the other dye was estimated by measuring the absorbance of a solution with known concentration of sulfoCy5 at 661 nm and of sulfoQSY21 at 646 nm to give $\epsilon_{QSY(646)}$ and $\epsilon_{CY5(661)}$. Using the absorbance of the conjugate at either of these two wavelengths with equation 2 and the extinction coefficients at the absorption maximum of each dye ($\epsilon_{CY5(646)} = 271,000 M^{-1} cm^{-1}$ $\epsilon_{QSY(661)} = 90,000 M^{-1} cm^{-1}$).

Protein Labelling. Transferrin in PBS at 5 mg mL⁻¹ (0.25 mg, 3.1 nmol) was incubated with DIBO-NHS (5 equiv, 7.6 μ g, 15.6 nmol and AF488-NHS (2.5 equiv, 5.0 μ g, 7.8 mol) for 2 hours at 4°C. Unreacted dye was removed using a Zeba Spin column, 7k MWCO buffer exchanged with PBS, following the manufacture's protocols. SNAP_{Switch} was then added (1.5 equiv, 4.6 nmol) and allowed to react overnight at 4°C. Excess SNAP_{Switch} was removed with two Zeba Spin columns.

To label the antibody, Anti-CD44 (50 μ g, 0.33 nmol) was incubated with DIBO-NHS (9.1 equiv, 1.5 μ g, 3.0 nmol) and AF488-NHS (11.7 equiv, 2.5 μ g, 3.9 nmol) for 2 hours at 4°C. Unreacted DIBO and AF488 were removed with a Zeba Spin column. SNAP_{Switch} was then added to the antibody (0.75 equiv,

0.25 nmol) and allowed to react overnight at 4°C before removing unreacted dye with an additional Zeba Spin column.

The degree of labelling (DOL) was estimated by dividing the molar concentration of SNAP_{Switch} approximated using equation 2, by the protein concentration as determined using the absorbance at 280 nm with the Beer-Lambert law and an extinction coefficient for the protein ($\epsilon_{\text{transferrin}} = 87,000 \text{ M}^{-1} \text{ cm}^{-1}$, $\epsilon_{\text{antibody}} = 210,000 \text{ M}^{-1} \text{ cm}^{-1}$). The concentration of AF488 conjugated to the protein was calculated using the Beer-Lambert law, the absorbance at 495 nm and an extinction coefficient of $\epsilon_{\text{AF488}} = 73,000 \text{ M}^{-1} \text{ cm}^{-1}$. Approximate DOL: Transferrin SNAP_{Switch} = 0.36, AF488 = 0.47. Anti-CD44 SNAP_{Switch} = 0.11, AF488 = 0.51.

Oligonucleotide Labelling. The custom 20-mer oligonucleotide modified with dibenzocyclooctyne (DBCO) (Sequence: 5' - TCA GTT CAG GAC CCT CGG CT – DBCO – 3') was purchased from IBA Life Sciences, reconstituted in nuclease free water at a concentration of 600 μM and stored at -20°C. For oligonucleotide labelling, 1.2×10^{-8} mol of the sequence was incubated with SNAP_{Switch} (2 equiv, 24 nmol) or AF488-Azide (1.25 equiv, 12.9 μg , 15 nmol) overnight at 4°C. Unconjugated dye was spun through 7k molecular weight cut-off Zeba Spin columns until free dye no longer permeated throughout the entire resin. Approximate DOL: SNAP_{Switch} = 0.37, AF488 = 0.44.

SNAP Fluorescence Imaging. 3T3-NIH cells were seeded in a clear bottom, black 96-well plate at 5,000 cells per well in 100 μL DMEM supplemented with 20% FBS and 10,000 penicillin/streptomycin one day prior to the experiment. Cells were transfected with 100 ng TfR-SNAP plasmid using 0.3 μL Lipofectamine 3000 and 0.2 μL P3000 reagent per well in Opti-MEM and left overnight. The following day the cells were washed 3 times in serum-free DMEM and incubated with 2 μg transferrin or 0.5 μg Anti-CD44 labelled with SNAP Switch and AF488 for 30 minutes at 37°C. Cells were washed 3 times in FluoroBrite DMEM with 10% FBS and imaged with a 40X air objective.

Transferrin Receptor-SNAP Flow Cytometry. HEK293A cells were seeded in a 24-well plate at 60,000 cells per well in DMEM supplemented with 20% FBS and 10,000 penicillin/streptomycin one day prior to the experiment. Cells were transfected with 500 ng TfR-SNAP or ADR β 2-SNAP plasmid using

Lipofectamine 3000 with 0.3 μL Lipofectamine 3000 and 0.2 μL P3000 reagent per well in Opti-MEM and left overnight. The following day the media was replaced with 250 μL DMEM without serum containing 60 μg transferrin labelled with SNAP-Switch and AF488. Cells were incubated for 30 minutes, washed 3 times with DMEM with 20% FBS and detached by replacing the media with 200 μL citric saline and incubating for 5 minutes. The cells were transferred to a 96-well, V-bottom plate, spun at 250 g for 5 minutes before re-suspending in 200 μL PBS before analysis by flow cytometry.

For analysis, the geometric mean fluorescence intensity of cells with or without transfection was taken as the background. This average of cells only was subtracted from each non-transfected sample while the mean of TfR-SNAP transfected cells was taken from the remaining samples. The ratio of the average, maximum and minimum Cy5 and AF488 signals of the samples in triplicate was then performed.

Lipofectamine 3000 Endosomal Escape Time Course. HEK293 cells were seeded in 24-well plates 1 day prior at 50,000 cells per well in 400 μL DMEM supplemented with 10% FBS and 10,000 penicillin/streptomycin. Cells were transfected with 500 ng CytoSNAP, NuclearSNAP or an empty plasmid (pcDNA3.1) with Lipofectamine 3000 by following the manufacturers protocol. 0.75 μL of Lipofectamine 3000 reagent and 1 μL of P3000 reagent was used per well.

After 16 hours, cells were washed 3 times in DMEM + 10% FBS and transfected again with combinations of unlabeled oligonucleotide and oligonucleotide labelled with SNAP_{Switch}, Cy5 or Alexa Fluor 488. Samples consisted of 500 ng total DNA with 250 ng each of unlabeled and labelled oligonucleotide (also containing an unlabeled fraction) and were transfected using the same amounts of Lipofectamine 3000 and P3000 reagent as the previous transfection. The transfection was performed at 5 time points between 0.5 – 16 hours before washing twice with DMEM + 10% FBS and detaching with 200 μL TrypLE at 37°C for 5 minutes. After detachment, 100 μL 1% bovine serum albumin in PBS was added to each well and the entire content transferred to a 96-well V-bottom plate. Cells were spun at 350 g for 5 minutes and resuspended in PBS before analysis by flow cytometry.

Cells initially transfected with empty plasmid and subsequently with non-fluorescent oligonucleotide at the 4 hour time point were gated on forward versus side scatter log area plot and applied to all samples. Cells subsequently transfected with the Alexa Fluor 488 labeled oligonucleotide at the 4 hour time and positive for this fluorescent signal were used to compensate for excitation of this fluorophore by the 405/552 nm lasers. Cells transfected with NuclearSNAP with and mTurquoise fluorescence as positive or negative by side-scatter versus mTurquoise fluorescence expression and were used to compensate for spillover into the Alexa Fluor 488 channel. Spillover of mTurquoise and Alexa Fluor 488 fluorescence into the Cy5 channel was negligible.

Lipofectamine 3000 Endosomal Escape Imaging.

HEK293 cells were seeded at 20,000 cells per well in an 8 well chamber slide 1 day prior in 400 μ L DMEM supplemented with 10% FBS and 10,000 penicillin/streptomycin. Cells were transfected with 500 ng CytoSNAP, NuclearSNAP or an empty plasmid (pcDNA3.1) with Lipofectamine 3000 by following the manufacturers protocol. 0.75 μ L of Lipofectamine 3000 reagent and 1 μ L of P300 reagent was used per well.

After 16 hours, cells were washed 3 times in DMEM + 10% FBS and transfected again with 3100 ng oligonucleotide labelled with SNAP_{Switch} also containing an unlabelled fraction and were transfected using the same amounts of Lipofectamine 3000 and P3000 reagent as the previous transfection. The cells were incubated for an additional 16 hours before washing the cells twice with cold FluoroBrite with 10% FBS and then left for 10 minutes on ice. The membrane was then stained with wheat germ agglutinin-AF488 at a final concentration of 1 μ g mL⁻¹ for 5 minutes before washing an additional two times in FluoroBrite with 10% FBS.

Supplementary Information

SNAP_{Switch}: A Molecular Sensor to Quantify Endosomal Escape and Cellular Localisation

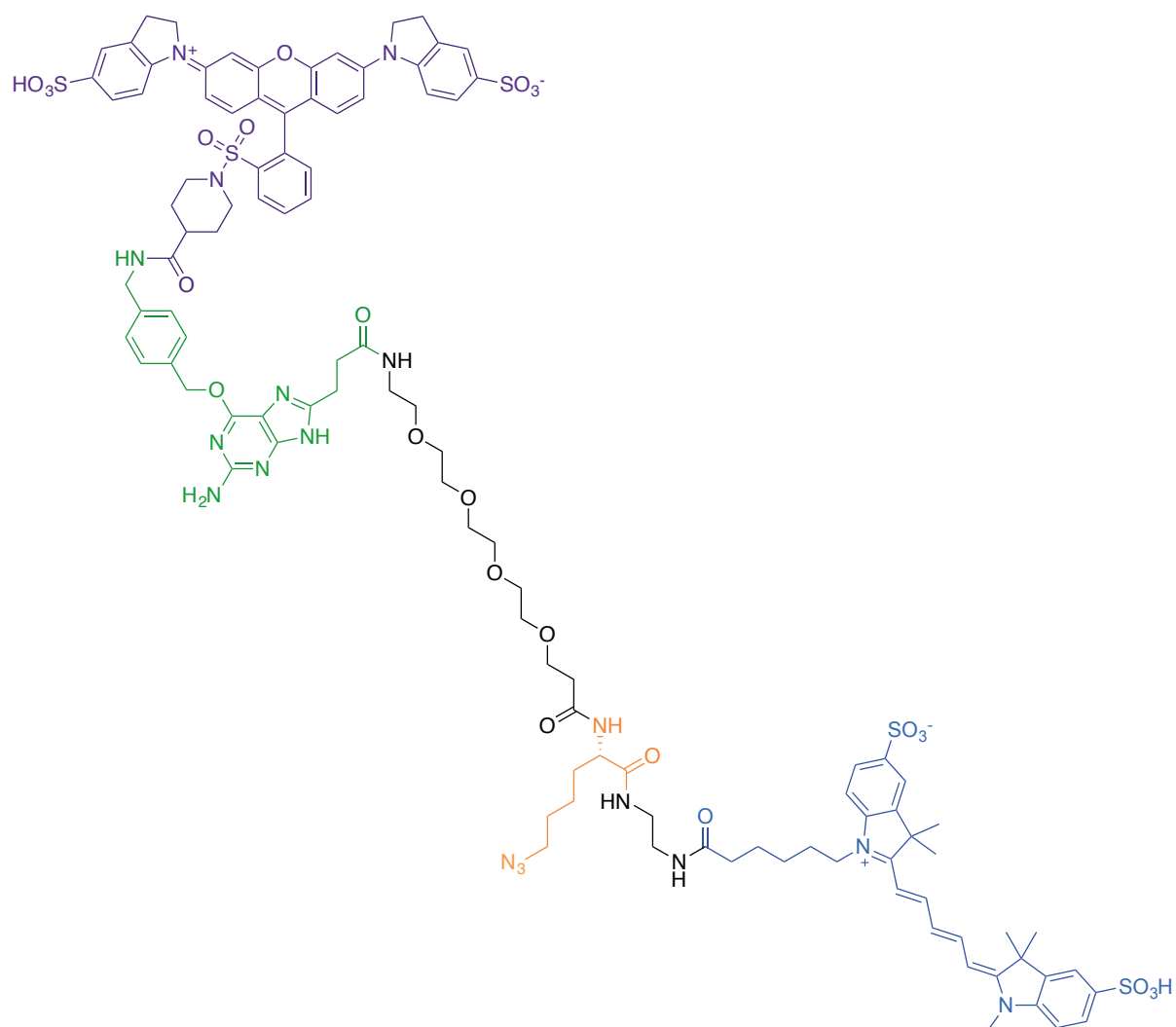
Laura I Selby^{1,2}, Luigi Aurelio¹, Moore Chen¹, Daniel Yuen¹, Bim Graham¹ & Angus P R Johnston^{1,2*}

¹Monash Institute of Pharmaceutical Sciences, Monash University, Parkville, Victoria, Australia.

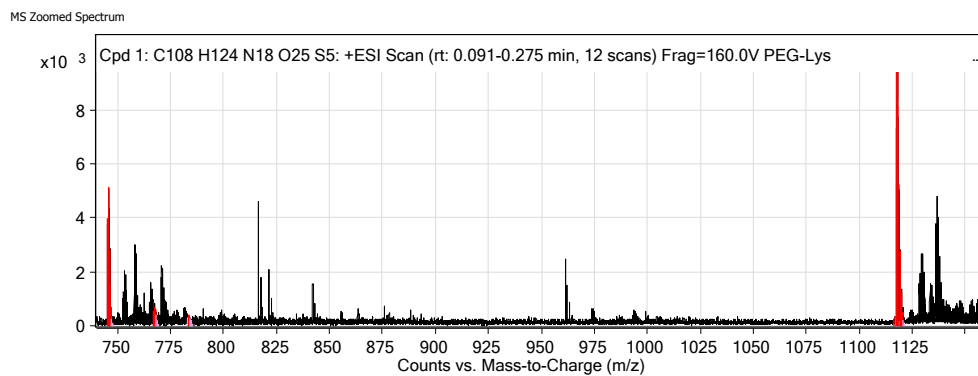
²ARC Centre of Excellence in Convergent Bio-Nano Science and Technology, Monash University, Parkville, Australia.

Correspondence

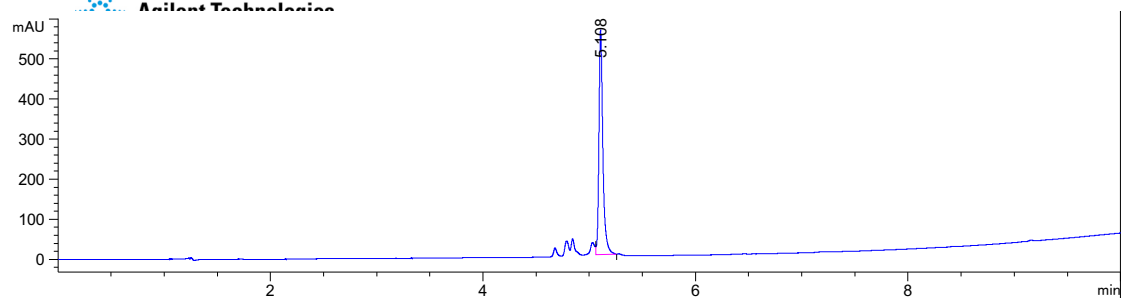
Email: Angus.Johnston@monash.edu



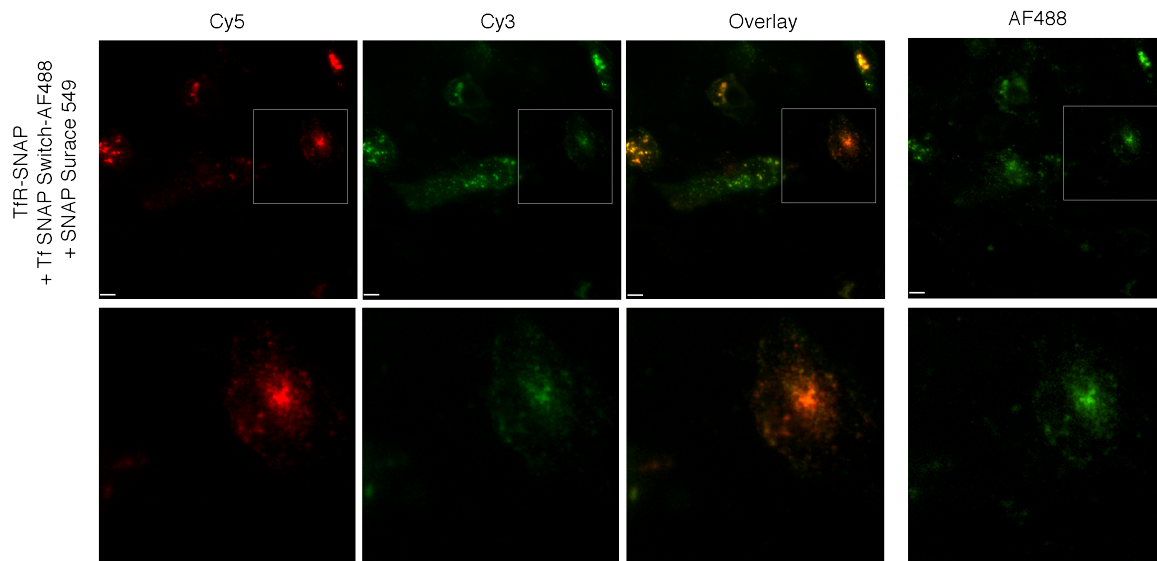
Supplementary Figure 1 – Chemical structure of SNAP_{Switch}. SulfoQSY21 (purple) is conjugated to the side of the benzyl guanine substrate (green) that is transferred to the SNAP-tag. The substrate is linked to an azide (orange) for attachment to the particle or protein of interest through a PEG linker. A sulfoCy5 (blue) fluorophore resides on the side of the substrate that remains with the material after interaction with the SNAP-tag.



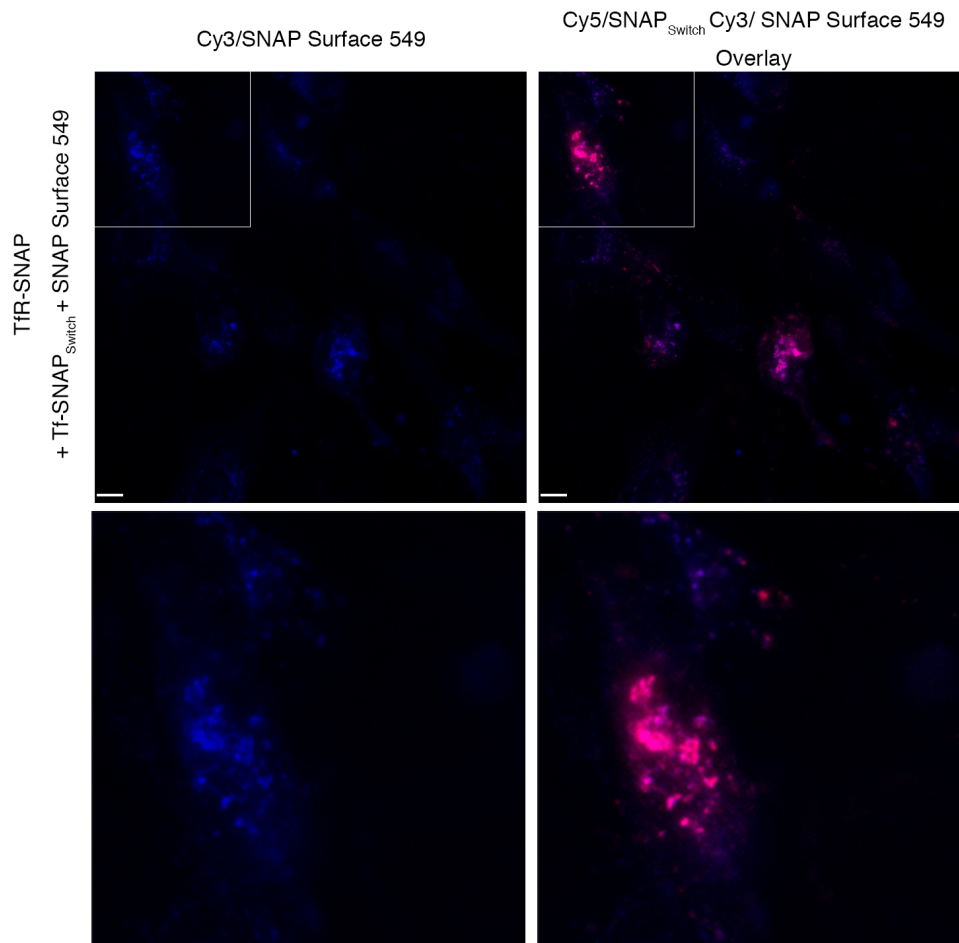
Supplementary Figure 2 – HRMS ESI⁺ spectra with found ions highlighted in red.



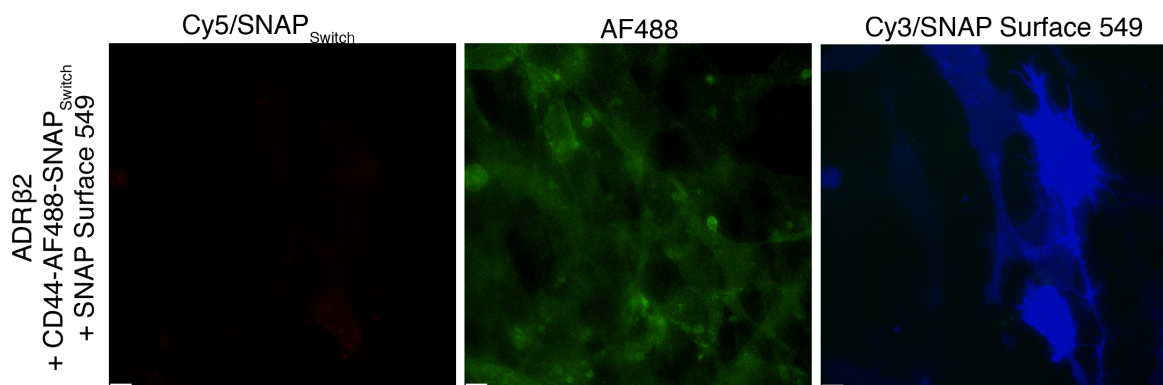
Supplementary Figure 3 – Analytical HPLC trace of SNAP-Switch. UV absorbance by diode array detector at 254 nm.



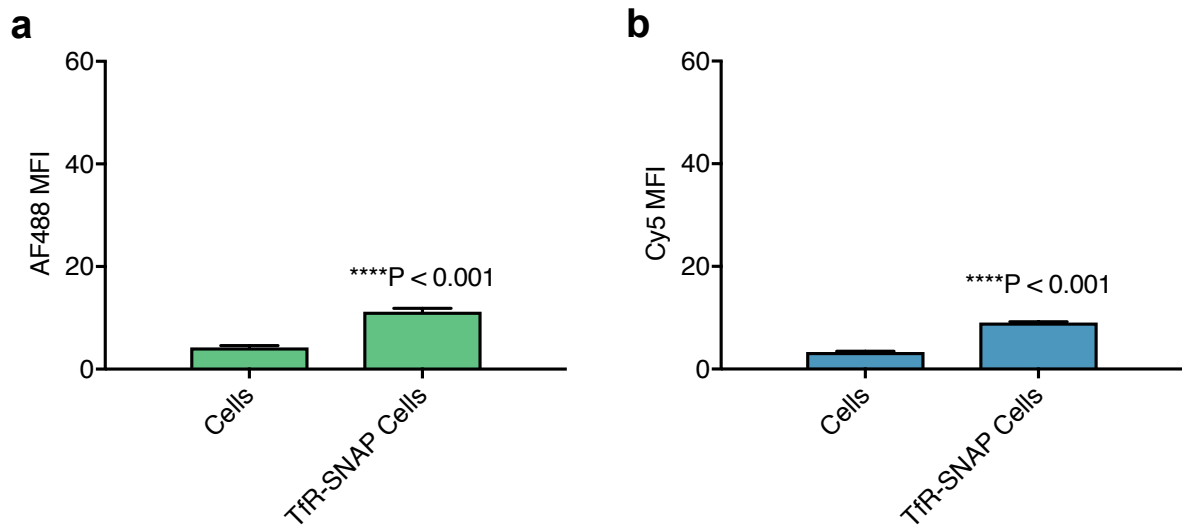
Supplementary Figure 4 – Additional fluorescence microscopy images of transferrin dual labelled with SNAP Switch and AF488. Fluorescence microscopy images of transferrin labelled with SNAP_{Switch} (Cy5, first column, red) incubated for 30 minutes with 3T3-NIH cells transfected to express the SNAP-tag fused to the transferrin receptor (TfR-SNAP), labelled with SNAP Surface 549 (second column, green). The AF488 fluorescence showing the location of transferrin is displayed in the third column. Zoomed views of the boxed areas are shown in the bottom panels. Scale bar = 10 μ m.



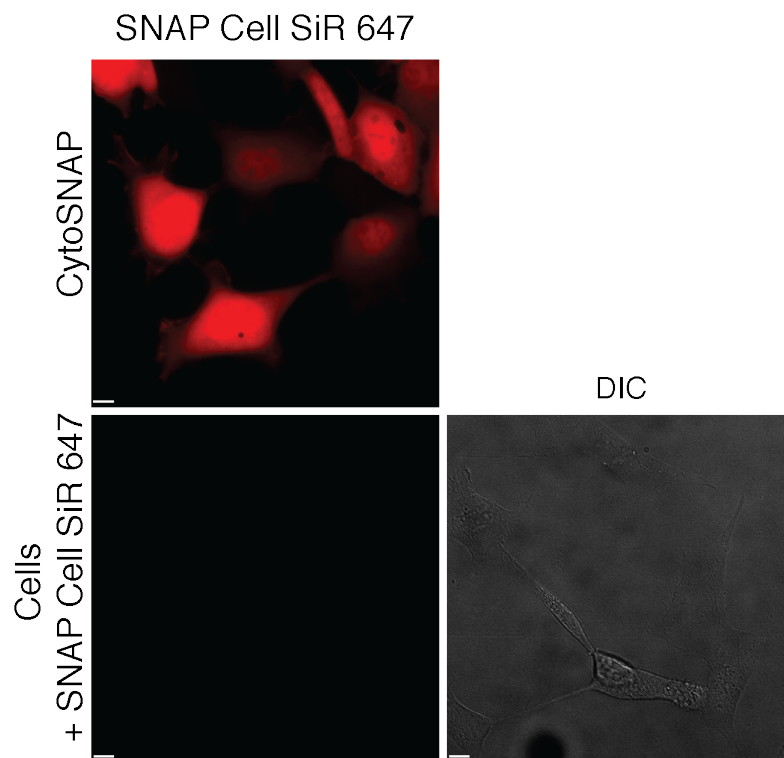
Supplementary Figure 5 – SNAP-tag expression in Tfr-SNAP cells labelled with SNAP Surface 549. Fluorescence microscopy image of SNAP-tag (first panel) of the same location from **Figure 2a** in the main text overlaid with the Tf-SNAP_{Switch} signal (Cy5, second panel). Zoomed views of the boxed areas are shown in the bottom panels. Scale bar = 10 μ m.



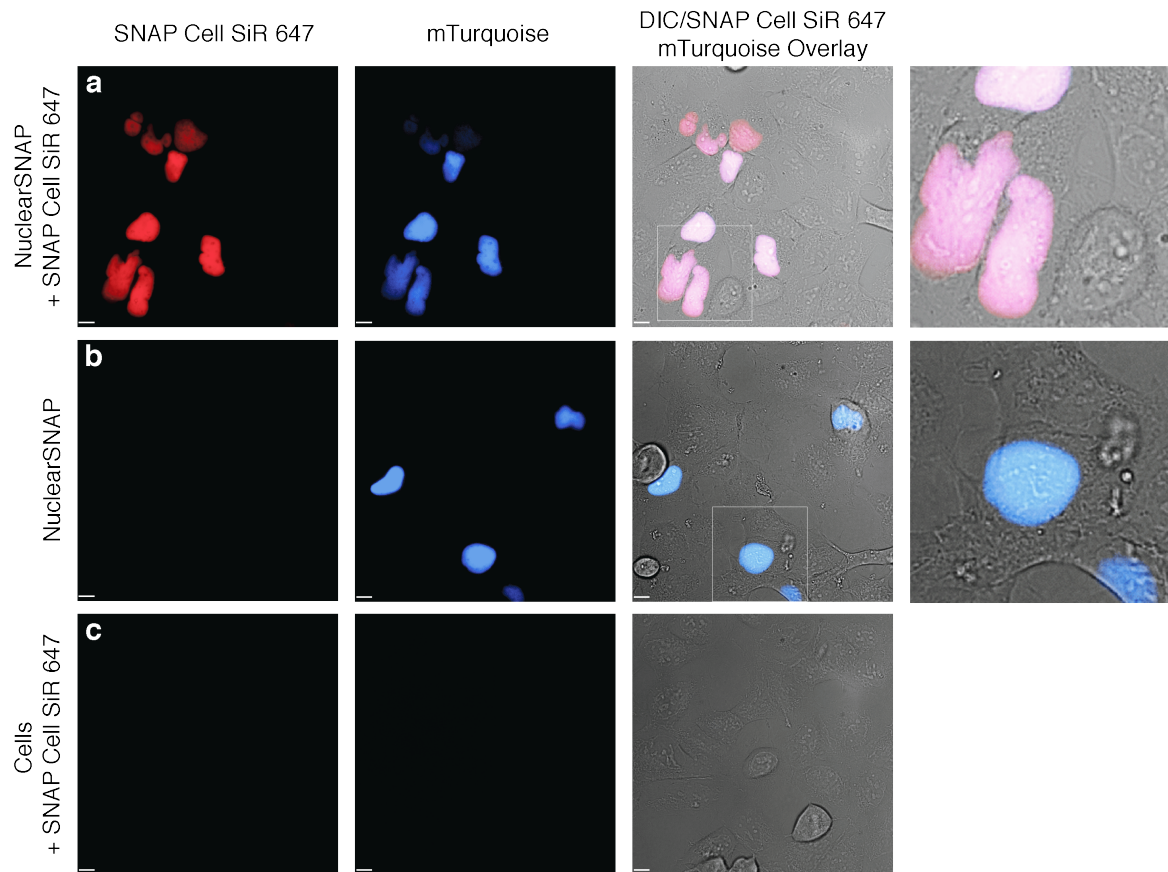
Supplementary Figure 6 – Fluorescence microscopy image of 3T3-NIH cells transfected with beta-2-adrenergic receptor 2 (ADR β 2-SNAP) labelled with SNAP Surface 549 (Cy3, blue), incubated with anti-CD44 dual-labelled with SNAP Switch (Cy5) and AF488 (green). Scale bar = 10 μ m.



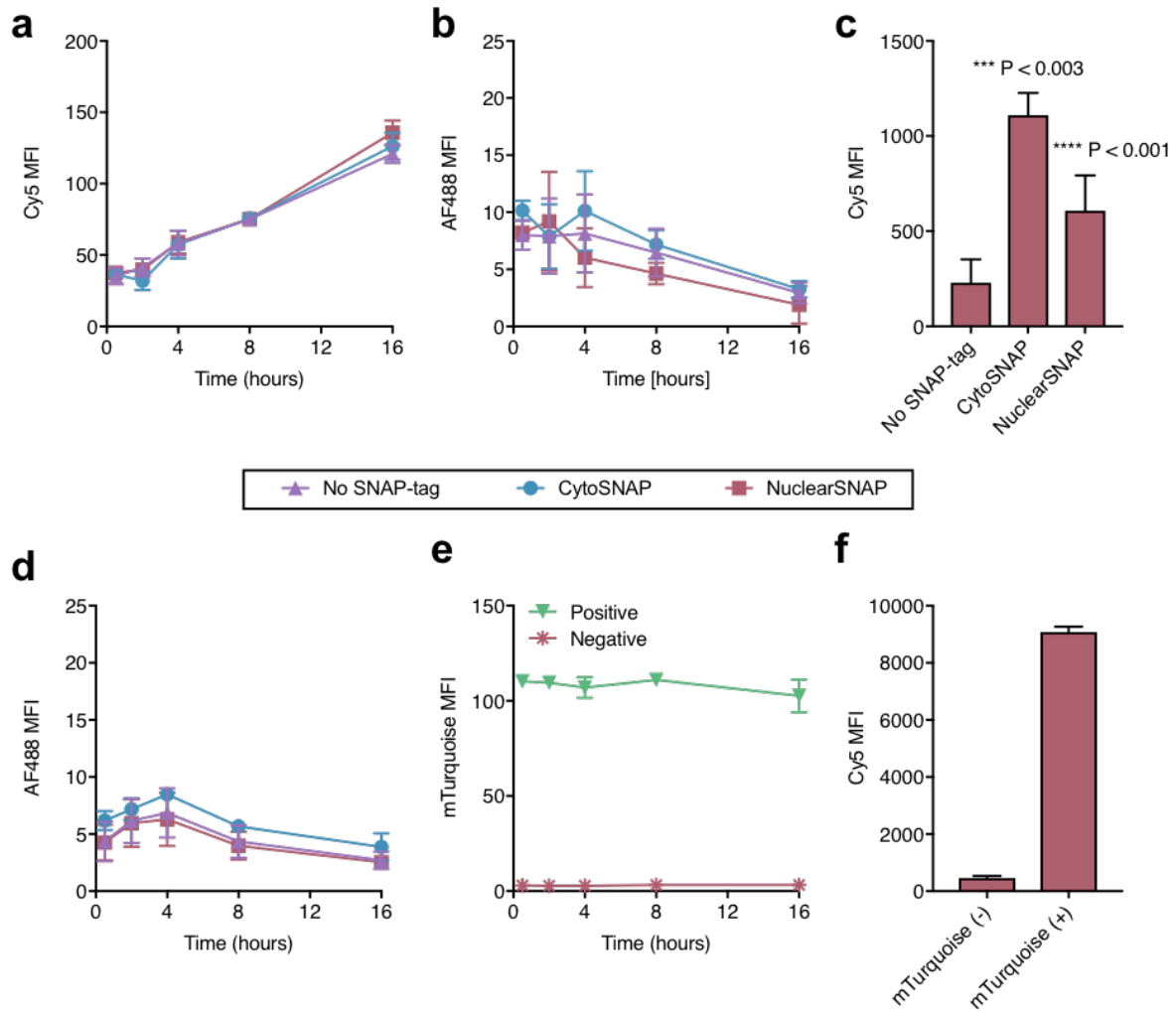
Supplementary Figure 7 – Background fluorescence of HEK293 cells with and without transfection to express TfR-SNAP. The mean fluorescence intensity of the (a) AF488 and (b) Cy5 signal is plotted with error bars representing the standard deviation. ****P < 0.0001 unpaired t-test, n = 3.



Supplementary Figure 8 – Cytosolic SNAP-tag labelling with membrane permeable SNAP Cell SiR 647. HEK293 cells transfected to express SNAP-tag in the cytosol were or non-transfected labelled with 5 μ M SNAP-Cell TMR-Star for 30 minutes at 37°C. Brightness and contrast normalized across the Cy3 channel. Scale bar = 10 μ m.



Supplementary Figure 9 – HEK293 transfected with NuclearSNAP, (a) with and (b) without treatment with SNAP Cell SiR 647. Zoomed views of the boxed areas in (a) and (b) are shown in the rightmost panels. (c) Non-transfected treated with SNAP Cell SiR 647. Brightness and contrast normalised, scale bar = 10 μm .



Supplementary Figure 10 – Delivery of fluorescently labelled oligonucleotides with Lipofectamine 3000 and expression of the SNAP-tag by flow cytometry. **(a)** Cy5 and **(b)** AF488 mean fluorescence intensity of cells transfected with dual-labelled Lipofectamine 3000 complexes formed with Cy5- and AF488-oligonucleotide over 16 hours. **(c)** SNAP-tag labelling with SNAP Cell SiR 647 across all experiments. **(d)** Mean fluorescence intensity of cells transfected with complexes formed with oligonucleotides labelled with AF488 and SNAP_{Switch}. **(e)** mTurquoise and **(f)** SNAP Cell SiR 647 signal of cells gated for positive or negative expression of the mTurquoise in NuclearSNAP transfected cells. Mean of results from two biological replicates in duplicate is plotted with the error bar representing the standard deviation. Significance in **(c)** is determined by unpaired t-test ($n = 4$) by comparing CytoSNAP and Nuclear SNAP to the sample transfected with an empty plasmid.

Chapter 5. Oligonucleotide Switches for Quantifying Endosomal Escape Efficiency

5.1 Summary

Endosomal escape is a critical event in the delivery of therapeutics that are active in the cytosol or in other subcellular locations. There is currently a lack of robust assays to directly detect endosomal escape adding difficulty to the design of nanoparticles engineered for this purpose. The use of the quenched SNAP-tag substrate described in Chapter 4 was demonstrated as a method to detect endosomal escape but requires transfection of the cells to produce an exogenous protein. An ideal escape sensor would respond to a molecule already present within the cytosol such as mRNA. A DNA sensor complementary to the mRNA for the housekeeping gene glyceraldehyde 3-phosphate dehydrogenase (GAPDH) was designed and tested *in vitro*. However, the signal-to-noise ratio was too low for results to be reproducible due to the low copy number of individual mRNA sequences within cells.

5.2 Introduction

Endosomal escape is currently regarded as a major bottleneck in the delivery of therapeutics by nanoparticle systems.^{1,2} To design materials that can effectively transport drugs to the cytosol, robust methods for detecting this event and determining its efficiency are required. Current methods generally fall under one of two categories: leakage or endpoint assays and are covered in greater detail in Chapter 1 and reviewed elsewhere.³

The distribution of small fluorescent molecules such as calcein or labelled dextran within a cell can be used to visualise endosomal escape (**Figure 5.1A**).⁴⁻⁶ Calcein is a membrane impermeable dye that is co-internalised into endosomes when material is taken up by endocytosis. Dye trapped in endosomes experiences a high local concentration which causes self-quenching⁶ and a punctate appearance (**Figure 5.1C**).⁷ Bursting or leakage of endocytotic vesicles causes an even distribution of dye throughout the cytosol and an overall increase in cell fluorescence intensity (**Figure 5.1B**). A major issue with this method is that assigning the cell an “escape” or “no escape” state is subjective.

Endpoint assays measure the overall outcome in the delivery of a certain molecule. For example, delivery of nucleic acids results in either the production^{8,9} or knock down^{10,11} of a specific gene which can then be detected via flow cytometry or microscopy. However, this is an indirect measure of endosomal escape³ as the readout from these assays is obtained after multiple steps following the delivery event such as the transport of the gene to the nucleus and subsequent synthesis of the protein. Both assays are limited in that they only offer a binary indicator that escape has occurred, without providing any information on the efficiency of delivery to the cytosol. A strategy to overcome these issues is to design a fluorescent sensor that is triggered when the endo/lysosomal pathway has been breached. A potential avenue to accomplish this is to engineer the sensor to respond to a molecule found exclusively in the cytosol. Ideally, the sensor would increase in fluorescence as more material escapes, allowing the efficiency of escape induced by a given material to be quantified.

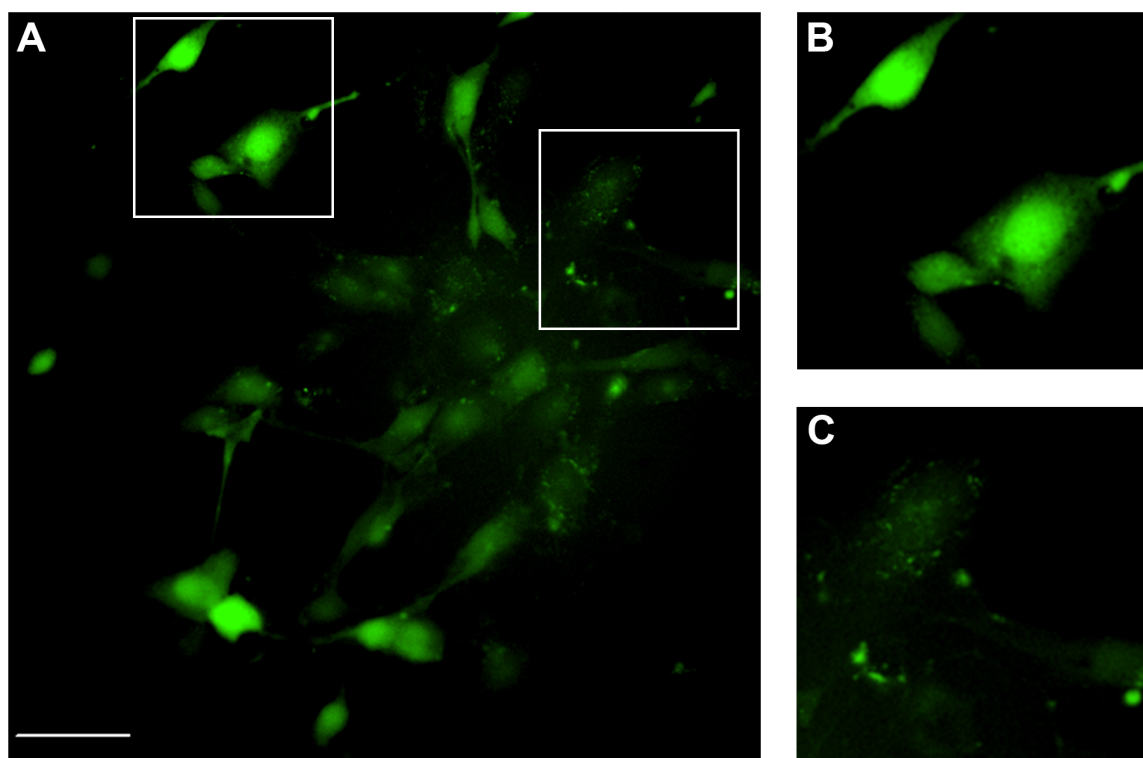


Figure 5.1 – A comparison of punctate and diffuse fluorescence. 3T3-NIH cells co-incubated with endosomal escape inducing nanoparticles and the membrane impermeable dye, calcein. **(A)** A mixture of cells displaying punctate or diffuse fluorescence are present. The highlighted region on the right **(B)** shows diffuse fluorescence while the region on the left shows **(C)** punctate fluorescence. Scale bar = 50 μm .

5.2.1 Cytosolic Response Assays

A rational approach in the design of an improved endosomal escape sensor is to have the probe respond to entities only present in the cytosol. An example of such a target is the glucocorticoid receptor which has already been used to develop assays for the transfer of peptides and proteins to the cytosol. This receptor binds small lipophilic molecules and controls a host of cellular processes including metabolism and development through gene regulation.¹² The protein contains three domains which include a transcription activation region, a DNA-binding domain and ligand-binding domain.¹³ When present in the cytosol, the receptor is complexed with heat shock protein 90 at the ligand-binding domain. In the presence of an agonist such as dexamethasone,¹⁴ heat shock protein 90 is displaced and the receptor undergoes a conformational change, translocates to the nucleus and modifies gene expression.¹⁵

Appelbaum et al. (2012) modified an assay originally developed by Yu et al. (2005)¹⁶ to compare the ability of miniature proteins containing multiple α -helical arginine residues to escape to the cytosol.¹⁷ In this assay, cells were transfected to express a glucocorticoid-green fluorescent protein (GFP) fusion. This resulted in a diffuse GFP signal in both the cytosol and nucleus. Potential candidates for escape were conjugated to dexamethasone and incubated with the transfected cells. If the proteins could access the cytosol, heat shock protein 90 was displaced by the dexamethasone causing translocation to the nucleus and an increase in GFP signal in this location (**Figure 5.2**). Using microscopy and the image analysis software CellProfiler, they calculated the ratio of nuclear to cytosolic GFP signal as a relative indicator of escape ability.

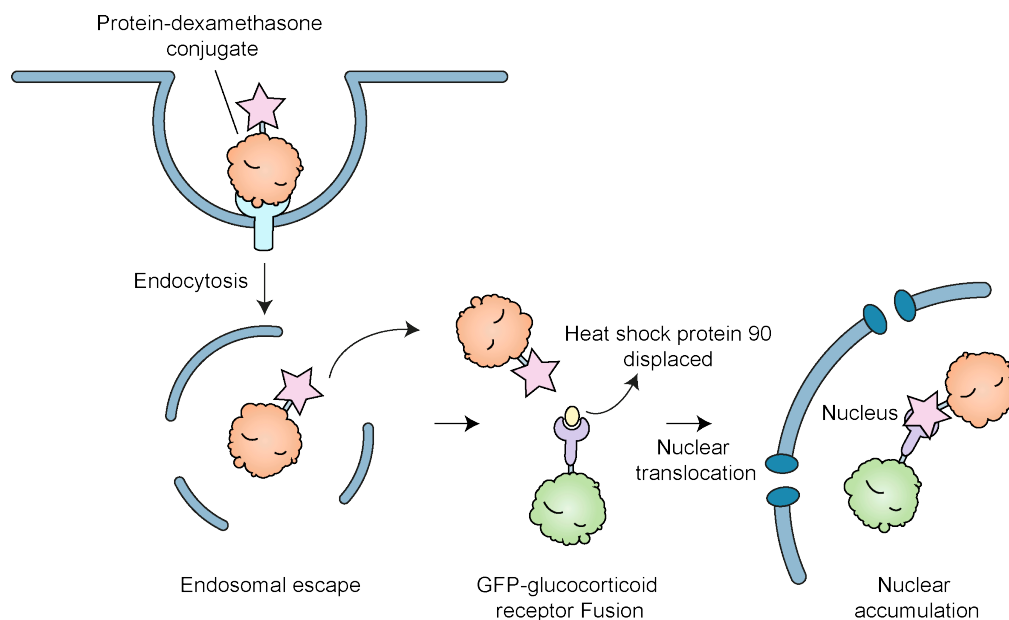


Figure 5.2 – Scheme of the glucocorticoid receptor-based assay to detect the endosomal escape of proteins. Proteins of interest are conjugated to dexamethasone and are taken up by endocytosis into cells transfected to express fusion proteins of the glucocorticoid receptor with GFP in the cytosol. Conjugates capable of escape reach the cytosol where dexamethasone binds to the ligand-binding domain of the glucocorticoid receptor, displacing heat shock protein 90. This causes the GFP fusion protein to translocate to the nucleus and causes an increase in the nuclear GFP signal.

Exogenous substances known to accumulate in the cytosol have also been used as a target to detect escape. The fluorescent molecule coumarin-cephalosporin 4-acetoxymethyl ester (CCF4-AM) is membrane permeable and moves to the cytosol of cells where it is converted to a charged and membrane-impermeable form by cytosolic esterase cleavage of the AM group. The coumarin and cephalosporin components are linked through a lactam group and form a Förster resonance energy

transfer (FRET) pair. The lactam group is a substrate of the enzyme β -lactamase and if it encounters CCF4, the lactam group is cleaved, resulting in an increase in donor signal.¹⁸ Although this system was originally developed for the study of β -lactamase expression,¹⁹ the CCF4-AM substrate has been used to investigate protein delivery to the cytosol in dendritic cells through delivery of CCF4-AM followed by β -lactamase.²⁰ Currently, this assay and the glucocorticoid receptor assay have only been used to measure protein delivery. However, they demonstrate there is potential in using substances localised to the cytosol as effective targets for designing assays to detect endosomal escape.

5.2.2 mRNA as a Cytosolic Recognition Element

Protein synthesis via the translation of messenger RNA (mRNA) is a fundamental cellular process that occurs at ribosomes located both in the cytosol and endoplasmic reticulum. mRNA for specific genes can move to certain regions within the cytosol to assist with localisation of the gene product.²¹ However, many mRNA molecules are uniformly distributed throughout the cytosol. An example of this is the sequence for glyceraldehyde 3-phosphate dehydrogenase (GAPDH).^{22,23} GAPDH takes part in multiple pathways within the cell but is most commonly known for the role it plays in ATP production via glycolysis in the cytosol.²⁴ The mRNA for this protein has traditionally been considered to be a housekeeping gene,²⁵ signifying its critical role for basic cell maintenance and hence, expression in all cells under regular circumstances.²⁶ These properties make mRNA, and specifically the sequence for GAPDH a prime target for recognition by an endosomal escape sensor.

5.2.3 DNA-based Sensors for mRNA Detection

Several methods have been developed for detection of mRNA sequences in a cell. *In situ* hybridisation (ISH) uses DNA oligonucleotide probes complementary to a mRNA sequence, allowing them to hybridise and signal the presence of the molecule. These probes were originally tagged with biotin or radioactive groups for detection but are now labelled with fluorescent dyes (FISH), permitting analysis via fluorescence microscopy or flow cytometry.²⁷ This method has been extended to allow quantification of mRNA through detection of single mRNA molecules using additional probes that hybridise to multiple locations along the target mRNA. All FISH protocols require cells to be fixed and permeabilised to permit

access of the probes to the cytosol.²⁸ In addition, the cells must be thoroughly washed to remove unbound sequences and reduce the background fluorescence.

Molecular beacons were developed as fluorogenic probes that only fluoresce when the target mRNA is encountered and hybridisation has occurred.²⁹ They exploit the native ability of DNA to form hairpin structures due to self-complementarity. The beacon is composed of a single strand of DNA with a fluorophore at one end and a quencher dye at the other. The sequence of base pairs next to the fluorophore is complementary to the those next to the quencher allowing for hybridization (stem sequence). The base pairs in between these two regions (loop sequence) is complementary to the mRNA sequence of interest. Binding of the mRNA sequence to the loop causes a conformational change which results in breaking of bonds within the stem region and subsequent opening of the beacon. Molecular beacons have multiple applications,³⁰ including their use as mRNA detection probes in live-cell experiments.^{31–33} Delivery to the cytosol is possible through permeabilization of the membrane using bacterial toxins such as streptolysin O, microinjection, electroporation and cell-penetrating peptides.³⁴

A more recent development is a nanoparticle-based mRNA detection probe called the “SmartFlare” or “NanoFlare”.^{35,36} This probe consists of an oligonucleotide duplex conjugated to a gold nanoparticle. The conjugated sequence is complementary to an mRNA strand of interest and the non-conjugated sequence is fluorescently labelled. Without the target sequence present, the fluorescent signal is quenched through non-radiative energy transfer with the gold particle.³⁷ If the mRNA target sequence is encountered, the fluorescently labelled sequence is displaced, disrupting the quenching which in turn results in a fluorescent signal. By conjugating two different NanoFlare probes on to one nanoparticle, the authors were simultaneously able to detect both actin and survivin mRNA expression,³⁶ demonstrating the probes specificity. The nanoparticles are commercially available through Merck and exist for a variety of target mRNA sequences for both human and mouse, including GAPDH. The details on how the particles are able to reach the cytosol has not yet been established.

5.2.4 Design of a DNA-based Switch to Quantify Endosomal Escape

The use of nucleic acid hybridisation in sensors has proven itself as a robust method to detect mRNA in a variety of situations. An additional requirement of an endosomal escape sensor using mRNA as a trigger is that it needs to be responsive in live cells, without need for fixing, permeabilising or washing out excess intracellular probes. This requires the probe to behave as a switch. The fluorescence must remain off until the mRNA in the cytosol is encountered, breaking the quenching interaction and allowing the probe to switch on. The endosomal escape sensor design proposed is based on a quenched oligonucleotide duplex that can be attached to a particle or protein of interest via an azide using copper-free click chemistry. If internalised nanoparticles escape into the cytosol, the sensor responds to GAPDH mRNA, resulting in a fluorescent signal (**Figure 5.3**).

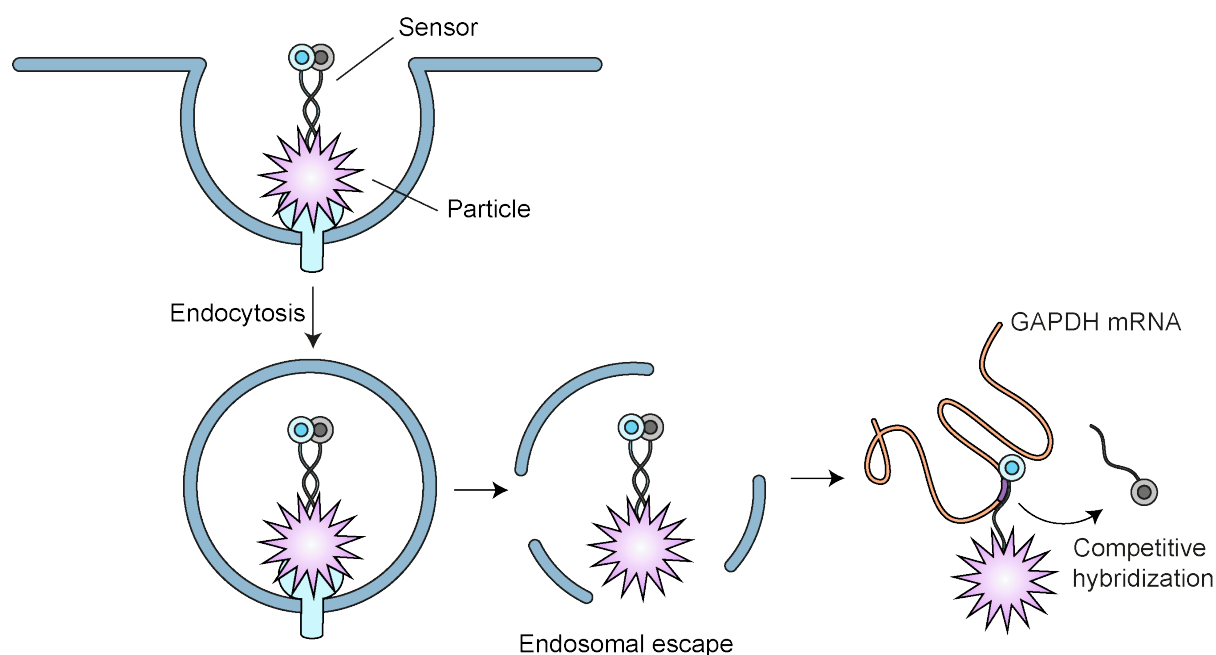
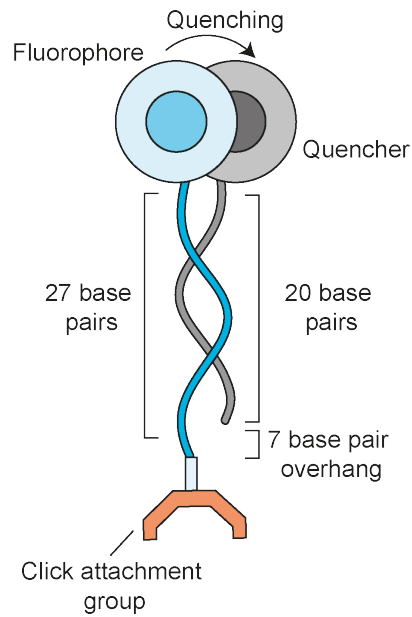


Figure 5.3 – Scheme of the proposed endosomal escape sensor. The sensor is covalently attached to a particle of interest and taken up by the cell. If the particle escapes its endocytic vesicle after internalisation, it will encounter GAPDH mRNA in the cytosol and cause an increase fluorescence intensity.



5.4

Figure 5.4 – Duplex escape sensor scheme. A fluorescently labeled oligonucleotide is quenched through hybridization of a shorter strand tagged with a quencher. GAPDH mRNA can bind to the overhanging sequence of base-pairs and remove the quencher strand through competitive hybridization.

The duplex escape sensor is composed of a 27-mer fluorescently labelled (Cyanine 5 – Cy5) oligonucleotide that is quenched when hybridized to a complementary strand labelled with a quencher dye (BlackHole Quencher 2 – BHQ2) (**Figure 5.4**). The opening of this sensor is based on the concept of toehold-mediated strand displacement. Here, a strand of DNA in a hybridized pair is replaced by a new strand, causing dissociation of the original sequence. This event is predicted to occur in three steps (**Figure 5.5A**). The invading strand must initially bind to a region of complementary base pairs called a toehold. This region is critical as both the forward and reverse rates of single base pair binding are extremely rapid. The original strand is then removed through branch migration of the invading strand down the sequence.³⁸

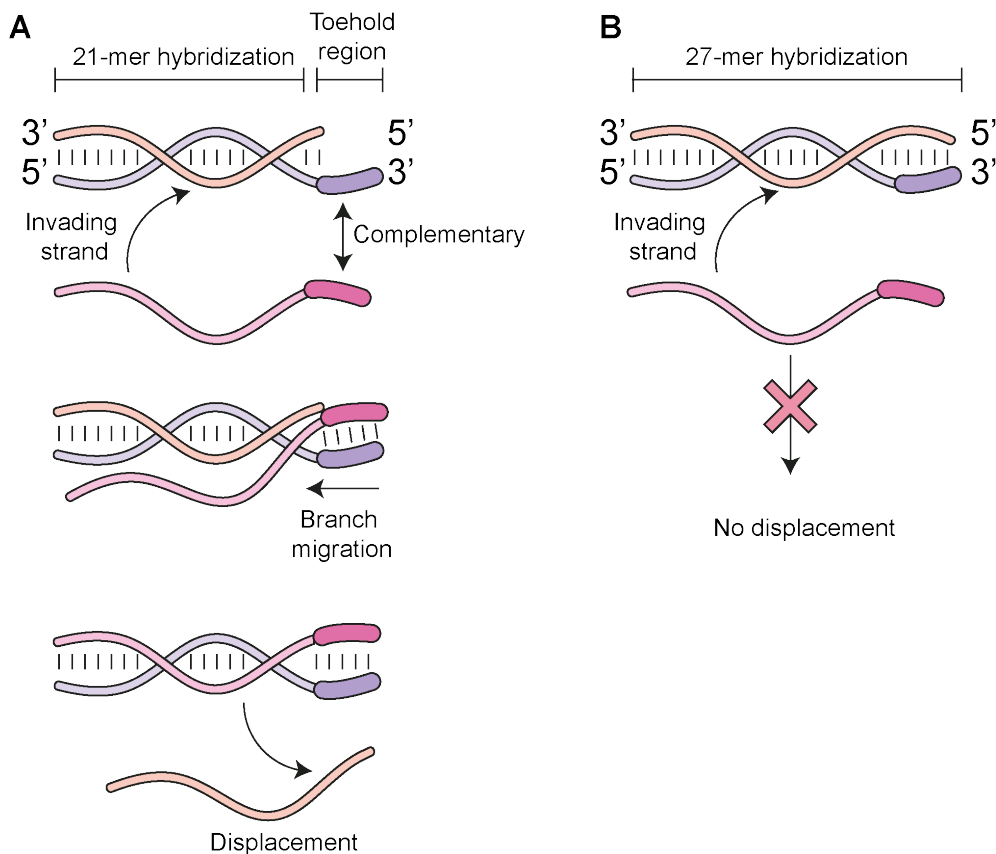


Figure 5.5 – Toehold strand displacement. **(A)** The invading strand binds to a complementary overhang sequence of base pairs (toehold) in the duplex to form an intermediate. The invading strand then gradually displaces the original shorter strand. **(B)** With no toehold region to bind to, the invading strand cannot replace the currently bound strand.

In theory, duplexes containing quencher strands of different lengths should respond differently to the presence of complementary mRNA. For example, a 20-mer quencher strand would leave a 7 base-pair toehold region, allowing for the strand to be competed off by the mRNA. However, a quencher strand that extends fully down the fluorescent strand (27-mer oligonucleotide) should not be removed as there is no toehold to establish the initial intermediate (**Figure 5.5B**). Any increase in fluorescence in the second scenario would then be due to degradation of the sensor and not detection of the mRNA.

5.3 Results and Discussion

5.3.1 Sensor Sequence Design

The duplex escape sensor sequence is designed to bind to a region on the mRNA for the protein GAPDH. As a starting point for the sensor, the 27-base pair sequence used on the commercially available mRNA NanoFlare live mRNA detection probe for mouse GAPDH was obtained from Merck Millipore (**Figure 5.6**). The human sequence for GAPDH varies by one base pair within the 27-mer sequence. This mismatch is at the 5th base position on the 3' end of the sequence where a cytosine (mouse) is substituted with an adenosine (human). The reverse complementarity of these sequences to GAPDH mRNA in the mice was confirmed via a mRNA nucleotide sequence search using the Basic Local Alignment Search Tool (BLAST).³⁹

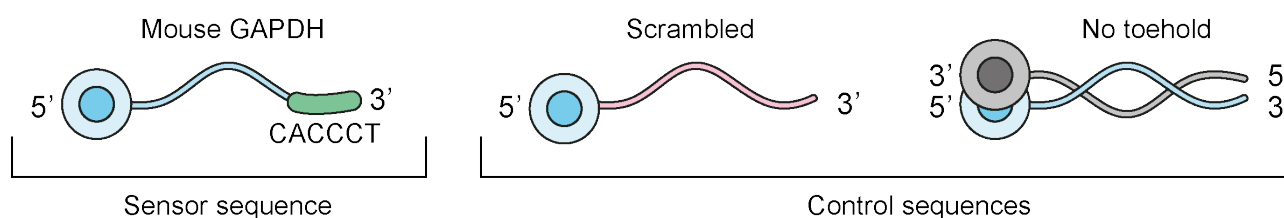


Figure 5.6 – Comparison of the fluorescently labelled sensor and control sequences.

Two control sequences were also designed (**Figure 5.6**). A scrambled sequence with mismatches placed along the entire strand was designed. This scrambled control contains 17 mismatches to mouse GAPDH, 18 mismatches to human GAPDH and both have at least 3 mismatches within the toehold region. The most similar mRNA sequence within the mouse and human genome contain less than 16 base pairs of complementarity. The second control sequence includes a 27-mer quencher sequence which lacks the toehold region required for removal of the quencher strand (as discussed in section 5.2.4).

The potential for degradation of the exogenous nucleic acids by cytosolic nucleases⁴⁰ was also considered. Several base-pair modification strategies have been developed to reduce this susceptibility. Phosphorothioation substitutes the non-bridging oxygen with a sulfur atom on the DNA backbone⁴¹ (**Figure 5.7**) which reduces nuclease degradation by displacement of metal ions present in the active site that are required for its catalytic activity.⁴² The DNA backbone of both the fluorescent and quencher

strand of the duplex sensor was modified to include phosphorothioated bonds down the entire sequence.

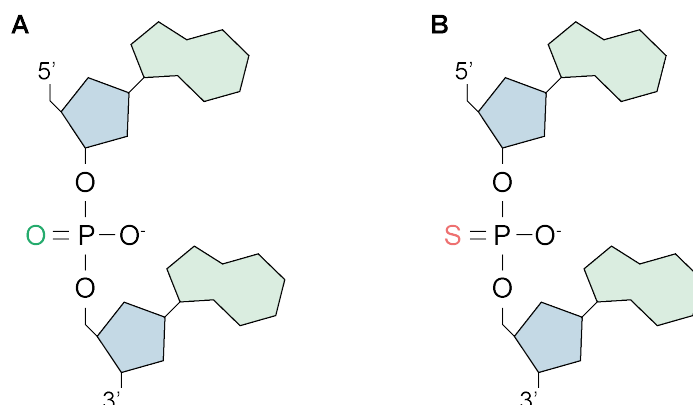


Figure 5.7 – Illustration of a regular and modified DNA backbones. **(A)** Phosphodiester bond as found in regular DNA. **(B)** Phosphorothioate bond, substituted with a sulfur atom to prevent degradation from nucleases.

5.3.2 Duplexed Sensor Complementary Sequence Detection and Stability

The ability of the complementary strand to quench the fluorescent component of the sensor efficiently and the stability of the duplexes was investigated. After addition of the complementary strand to either the GAPDH (**Figure 5.8A**) or scrambled fluorescently labelled strand (**Figure 5.8B**), the fluorescence intensity rapidly decreased to a minimum within 2 minutes. Monitoring the fluorescence at 37°C over 40 minutes showed no non-specific opening of the duplex as the fluorescent intensity remained stable over this period in media containing fetal bovine serum. This demonstrates the stability of the duplexes in conditions similar to experiences in the extracellular environment.

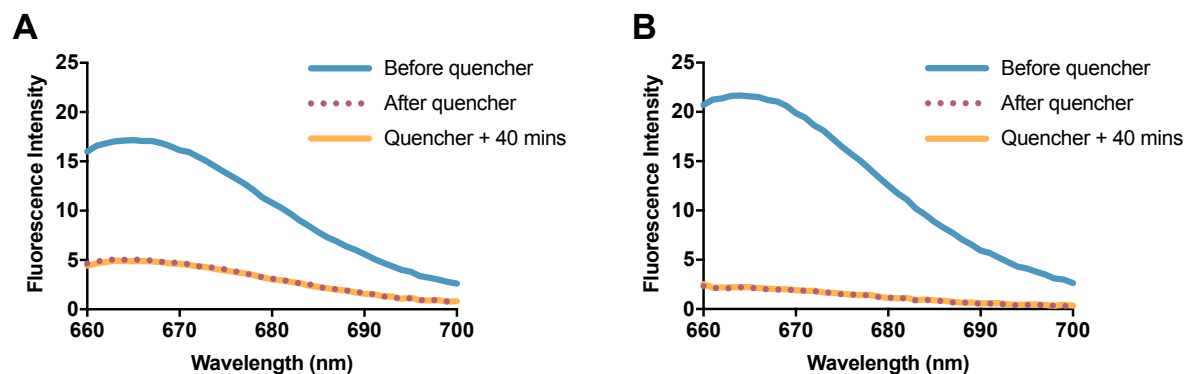


Figure 5.8 – Quenched sensor is stable in the presence of serum. **(A)** 20-mer GAPDH sensor or **(B)** scrambled sequence with complementary quencher in Dulbecco's Modified Eagle Medium (DMEM) supplemented with 10% fetal bovine serum (FBS) at 37°C for 40 minutes.

The response of the quenched sensor and control strands to the target GAPDH sequence was also tested. Addition of the complementary sequence restored fluorescence of the GAPDH sensor strand by approximately 70% when quenched with the 20-mer sequence (**Figure 5.9A**). No return in signal was seen when the GAPDH sensor was quenched with the 27-mer strand and challenged with the complementary sequence (**Figure 5.9B**). This confirms that the lack of toehold region prevents the 27-mer quencher displacement in favour of the GAPDH sequence and is therefore useful as a control to monitor degradation of the duplex *in vitro*. Furthermore, no increase in fluorescence was detected from the 20-mer quenched scrambled sequence when the GAPDH sequence was added (**Figure 5.11C**) which demonstrates the specificity of the sensor and the suitability of this duplex as a second control sequence.

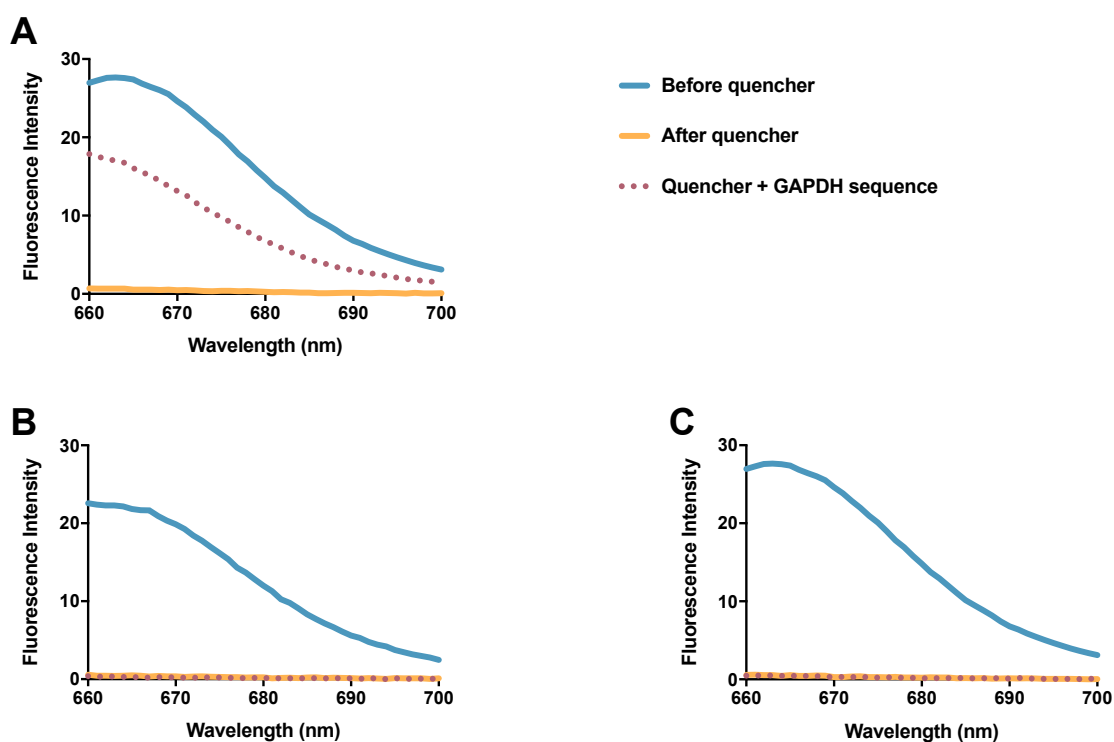


Figure 5.9 – GAPDH sensor responds to the target sequence but the scrambled does not. **(A)** GAPDH sensor quenched with the 20-mer sequence. **(B)** GAPDH sensor quenched with the 27-mer sequence and **(C)** scrambled strand quenched with the 20-mer sequence. In each experiment, 0.2 μ M fluorescent strand was quenched with 3.7 equivalents of quencher sequence in phosphate buffered saline then challenged with 4 equivalents of the GAPDH target strand.

5.3.3 Optimizing Sensor Response

To get a better understanding of how responsive the sensor was, the amount of target sequence required for the largest increase in fluorescent signal was examined. In addition, the amount of

quencher required to completely suppress the fluorescent signal was also investigated. Altering the molar equivalents of quencher strand mixed with the GAPDH sensor showed that 2 equivalents were required to reach the maximum efficiency and a further increase did not improve the amount of quenching (**Figure 5.10A**). In addition, the ability of the GAPDH sensor to respond to the complementary sequence was independent of the amount of excess quencher. Challenging sensor quenched with increasing amounts (1 to 5 equivalents) of the 20-mer strand with 3 equivalents of the GAPDH target sequence had minimal effect on the final fluorescence intensity (**Figure 5.10B**).

By setting the quencher to GAPDH sensor ratio to 2, the effect of the number of equivalents of complementary strand on the return of fluorescence signal was investigated. The fluorescence intensity of the sensor quenched with the 20-mer linearly increased in the presence of GAPDH target sequence until a plateau was observed above 2 equivalents of complementary strand (**Figure 5.10C**). These results suggest that the maximum signal for the sensor was achieved in the presence of 2 equivalents of complementary strand. Consistent with previous observations, minimal return was observed at any concentration of GAPDH target sequence when the sensor was quenched with the 27-mer sequence (**Figure 5.10D**).

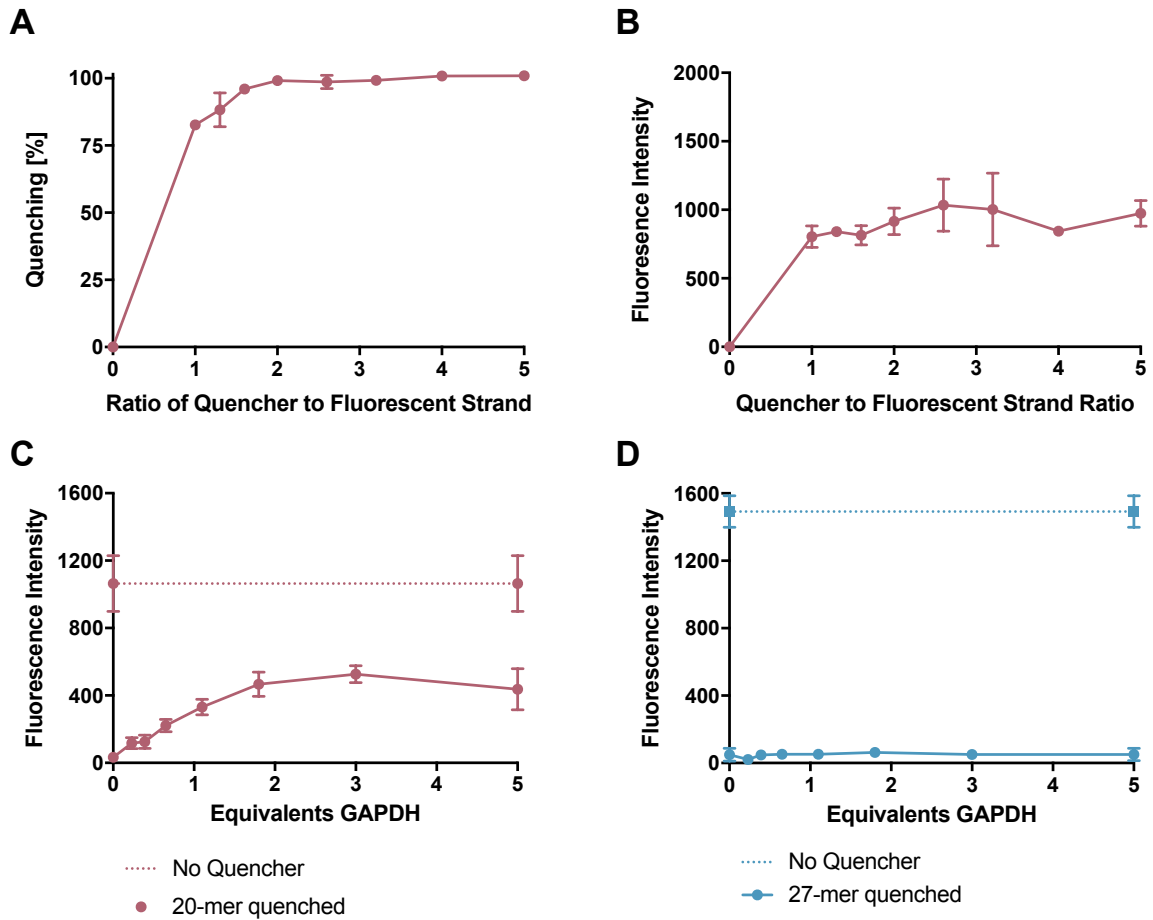


Figure 5.10 – Optimizing the ratio of quencher to fluorescent strand and evaluating the return in fluorescence in the presence of the GAPDH target sequence. **(A)** Quenching efficiency of 37.5 nM GAPDH sensor with increasing amounts of 20-mer quencher strand. **(B)** Return of sensor fluorescence quenched with increasing amounts of 20-mer quencher strand, challenged with 3 equivalents of GAPDH target sequence. **(C)** Return of sensor fluorescence quenched with 2 equivalents of the 20-mer strand and challenged with increasing amounts of the GAPDH target sequence. **(D)** Return of sensor fluorescence quenched with 2 equivalents of the 27-mer strand and challenged with increasing amounts of the GAPDH target sequence. Mean of triplicate results is plotted with the error bars representing the standard deviation.

5.3.4 Duplex Sensor Stability In Vitro

As the duplex escape sensor did not degrade in simulated extracellular conditions (**Figure 5.8**), we next investigated the stability in early-stage trafficking following endocytosis. The GAPDH and scrambled sequences were conjugated to transferrin and incubated with 3T3-WT cells at 4°C to prevent internalisation. The samples were then quenched with the corresponding 20 or 27-mer sequences. Following quenching, the cells were either kept at 4°C to keep the transferrin at the surface or brought up to 37°C for 1 hour to allow internalisation (**Figure 5.11A,B & Figure 5.12A,B**).

Over 85% of the fluorescence signal was quenched for all sequence and quencher combinations (**Figure 5.11C & 5.12C**). The quenching efficiency of samples duplexed with the 27-mer sequence was higher than the 20-mer equivalent (96% vs. 92% for the scrambled sequence and 97% vs. 95% for the GAPDH sequence). In addition, lower efficiencies were observed at 37°C (86% for the scrambled sequence and 85% for the GAPDH sequence quenched with the 20-mer strand). This indicates that some degree of non-specific opening occurs for the 20-mer strands that is not due to the detection of GAPDH once internalised.

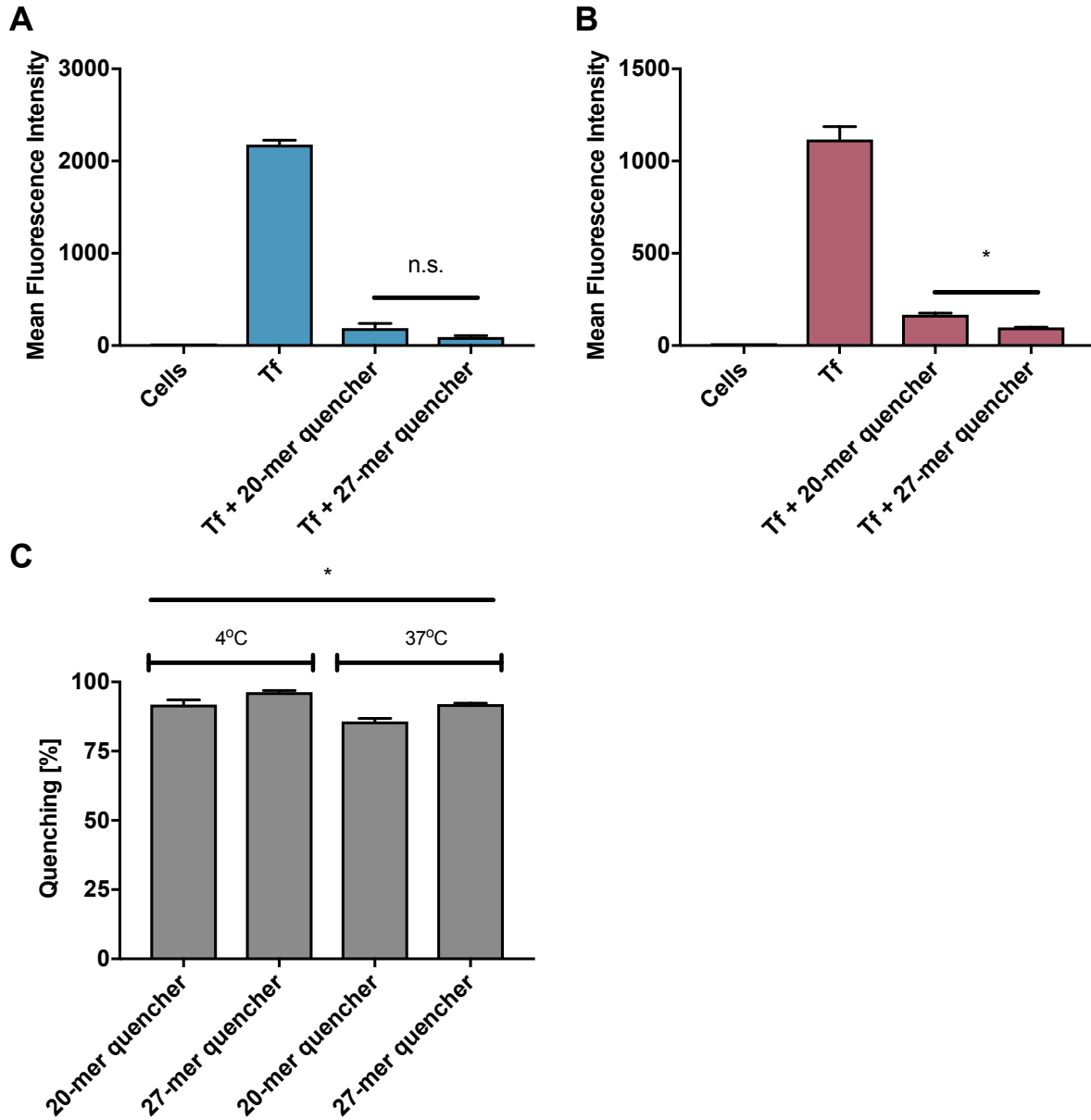


Figure 5.11 – Cellular stability of the scrambled control duplex conjugated to transferrin in 3T3-WT cells by flow cytometry. Oligonucleotide conjugated to transferrin was incubated for 1 hour at (A) 4°C or (B) 37°C. The geometric mean of the results in duplicate from flow cytometry is plotted with the error bars representing the standard deviation. ($P < 0.05$, t-test, $n = 2$). (C) The calculated minimum, maximum and average quenching remaining after 1 hour. ($*P < 0.05$, one-way ANOVA, $n = 3$).

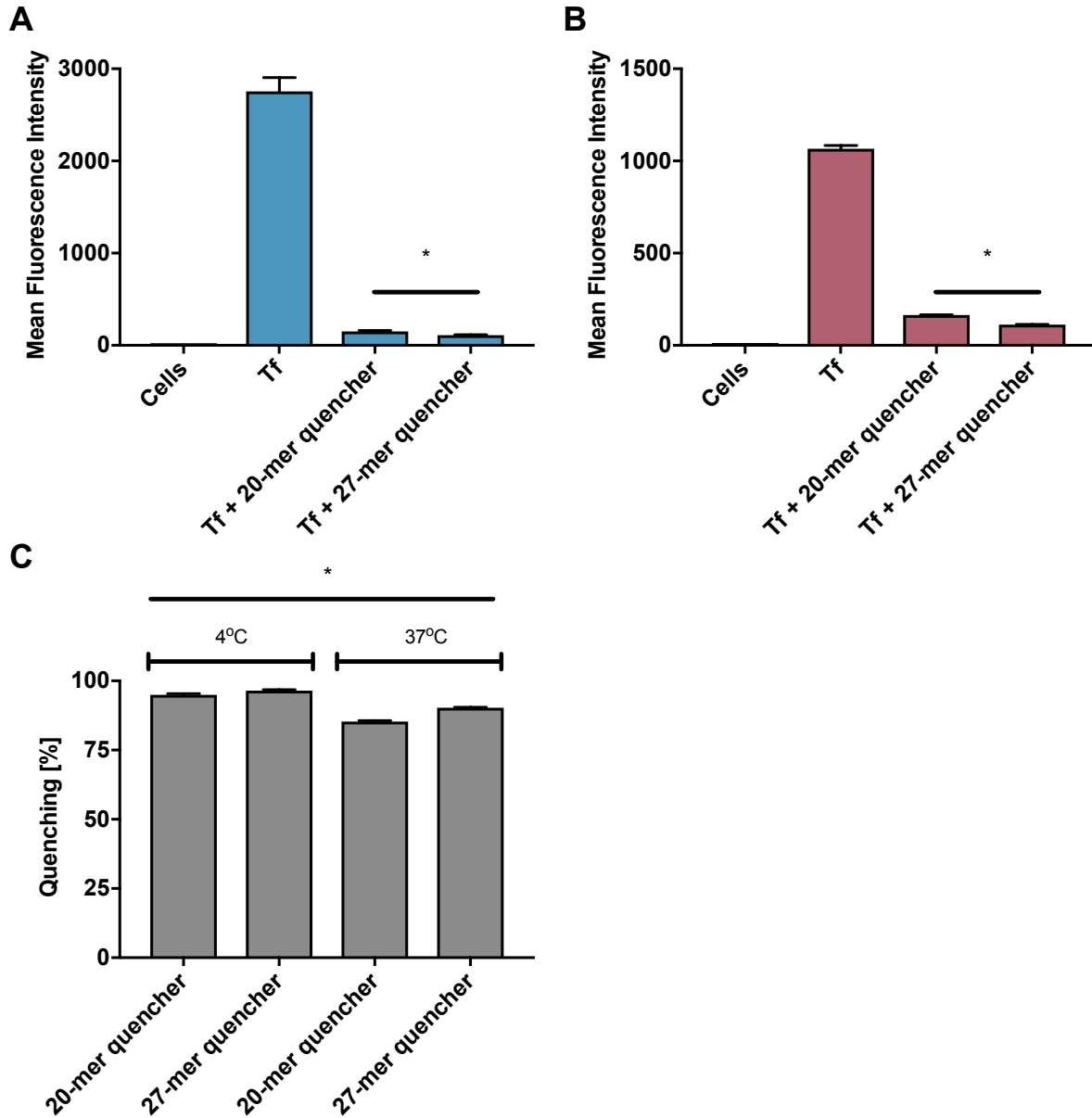


Figure 5.12 – Cellular stability of the GAPDH sensor duplex conjugated to transferrin in 3T3-WT cells by flow cytometry. Oligonucleotide conjugated to transferrin was incubated for 1 hour at (A) 4°C or (B) 37°C. The geometric mean of the results in duplicate from flow cytometry is plotted with the error bars representing the standard deviation. ($P < 0.05$, t-test, $n = 2$). (C) The calculated minimum, maximum and average quenching remaining after 1 hour. ($*P < 0.05$, one-way ANOVA, $n = 3$).

The non-specific opening of the sensor over time was also investigated in later-stage trafficking. While transferrin is returned to the cell surface quickly from recycling endosomes,⁴³ the antibody to the transferrin receptor (OKT9)⁴⁴ is trafficked to lysosomes⁴⁵ instead. Labelling the antibody with both the oligonucleotide sequence and Alexa Fluor 488 allowed the amount of association to be tracked when the sensor is quenched. In addition, this was carried out in HeLa cells (human, epithelial) as they do not contain the target mouse GAPDH sequence. This allows degradation of the sensor to be detected as there is no target sequence to release the quencher strand.

There was no difference in the association of antibody labelled with either scrambled or GAPDH sequences to HeLa cells as the trend of the Alexa Fluor 488 signal over time was similar (**Figure 5.13A**). In addition, hybridization of the quencher strand did not change association (**Figure 5.13A**). Quenching was initially highly efficient as the Cy5 signal of both the scrambled and GAPDH sequences was low compared to the unquenched samples (**Figure 5.13B**). This equated to a quenching efficiency of ~97% for the scrambled and ~100% for the GAPDH sequence. However, the signal increased over time. The Cy5 signal of the quenched samples increased to ~17% of the unquenched sample over 1.5 hours (**Figure 5.13C**). The effect was similar for both the GAPDH sensor and the scrambled sequence. This value is similar to the reduction in quenching efficiency seen in the 20-mer quenched oligonucleotides conjugated to transferrin at 37°C (**Figure 5.11C & Fig 5.12C**). This suggests that both the control and sensor oligonucleotide sequences undergo a comparable degree of non-specific opening when trafficked along the endo-lysosomal pathway.

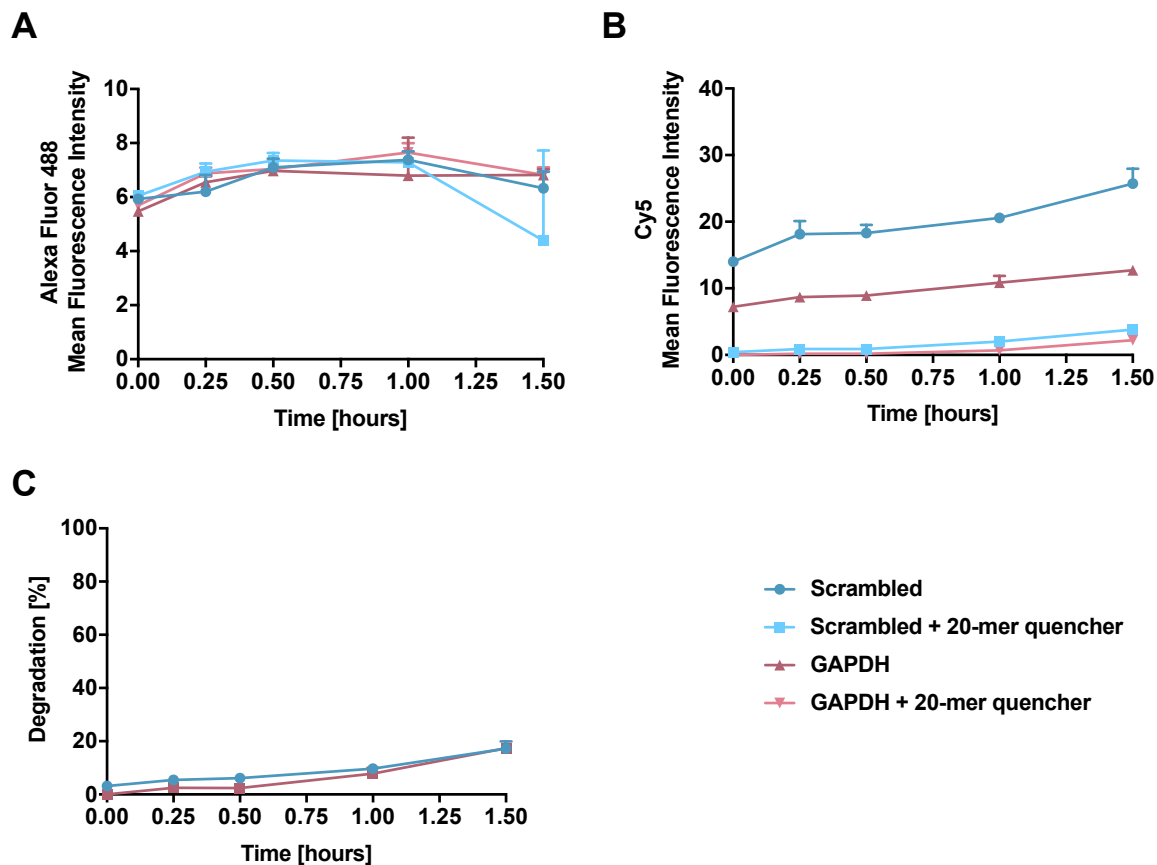


Figure 5.13 – *In Vitro* stability of the sensor and control sequences on an anti-transferrin antibody. Antibody labeled with Alexa Fluor 488 and the sensor or scrambled sequence, quenched with the 20-mer sequence and bound to HeLa cells at 4°C. Excess antibody was washed out and the cells brought up to 37°C over 1.5 hours before analysis by flow cytometry. **(A)** Alexa Fluor 488 mean fluorescence signal over time. **(B)** Mean Cy5 signal from the sensor or scrambled sequence over time and **(C)** The percentage increase in Cy5 fluorescence from the quenched sample over time. The geometric mean of the results in triplicate from flow cytometry are plotted with the error bars representing the standard deviation **(A and B)** or the minimum and maximum percentage calculated all quenched and unquenched samples **(C)**.

5.3.5 *Inducing Endosomal Escape with Lipofectamine 3000*

To test the ability of the escape sensor to detect endosomal escape, a method known to induce endosomal escape is required. Lipofectamine 3000 is a cationic liposome formulation that complexes negatively charged DNA to assist in the delivery of nucleic acids into cells. Oligonucleotides delivered using cationic liposomes are released from intracellular vesicles and into the cytosol.⁴⁶ Internalised Lipofectamine complexes have been reported to avoid trafficking along microtubules, evading transport to lysosomes where degradation occurs.⁴⁷ The degree by which Lipofectamine 3000 complexes could evade lysosomes was investigated by qualitative colocalisation imaging (**Figure 5.14A**). The majority of lysosomal associated membrane protein 1 (LAMP1) did not localize with Lipofectamine complexed with the fluorescent GAPDH sensor strand. The majority of the signal from the GAPDH sensor originated from other areas of the cell, possibly representing escape to the cytosol and trafficking to the nucleus with several punctate structures surrounding this region. The specificity of LAMP labelling was also validated. Fluorescent labelling of punctate structures was only observed when both the primary and secondary antibodies were present (**Figure 5.14B**). When only the secondary antibody was present (Anti-Rabbit Alexa Fluor 488), no labelling was seen (**Figure 5.14C**).

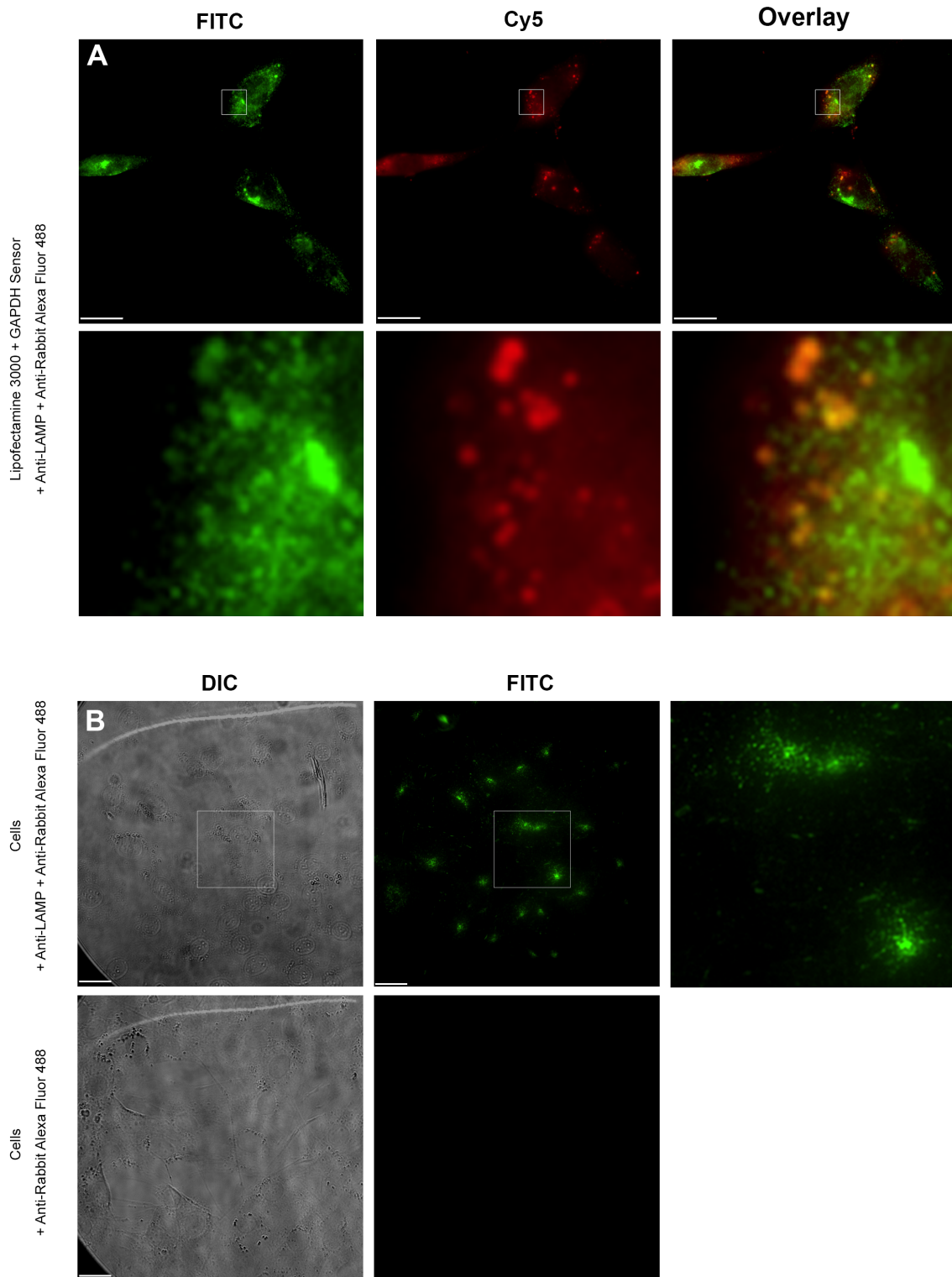


Figure 5.14 – Lipofectamine 3000 localisation with lysosomes. GAPDH sensor sequence was complexed with Lipofectamine 3000 and incubated with 3T3-NIH cells overnight. **(A)** Cells were fixed, permeabilized and stained for lysosomal associated membrane protein 1 (LAMP1) with anti-LAMP1 and goat anti-rabbit Alexa Fluor 488 then imaged with a 40X air objective. The bottom panels show zoomed views of the boxed areas. **(B)** Anti-LAMP staining in 3T3-NIH cells without Lipofectamine 3000. The right most panel shows a zoomed view of the boxed area. **(C)** Anti-rabbit Alexa Fluor 488 alone does not non-specifically label cells. Images in **(B)** and **(C)** were obtained with a 60X silicone objective. Scale bar = 25 μm in all images.

We investigated if free sensor could enter cells without Lipofectamine, as this phenomenon has been documented for phosphorothioated oligonucleotides.⁴⁸ Association of the single stranded GAPDH sequence with 3T3-WT cells significantly increased when delivered with Lipofectamine 3000 compared to the oligonucleotide alone (**Figure 5.15A**), demonstrating the role of Lipofectamine 3000 in this increase. Single stranded sequences may be complexed by Lipofectamine differently to duplexes which might change how they associate with cells. To test this, the GAPDH and scrambled sequences were pre-hybridized with a non-fluorescent 27-mer complementary sequence. For both sequences, the association with the double stranded sample was much higher than for those containing only single stranded oligonucleotides (**Figure 5.15B**). Interestingly, the effect of the complementary strand on association was more pronounced in the scrambled sequence than on the GAPDH sequence.

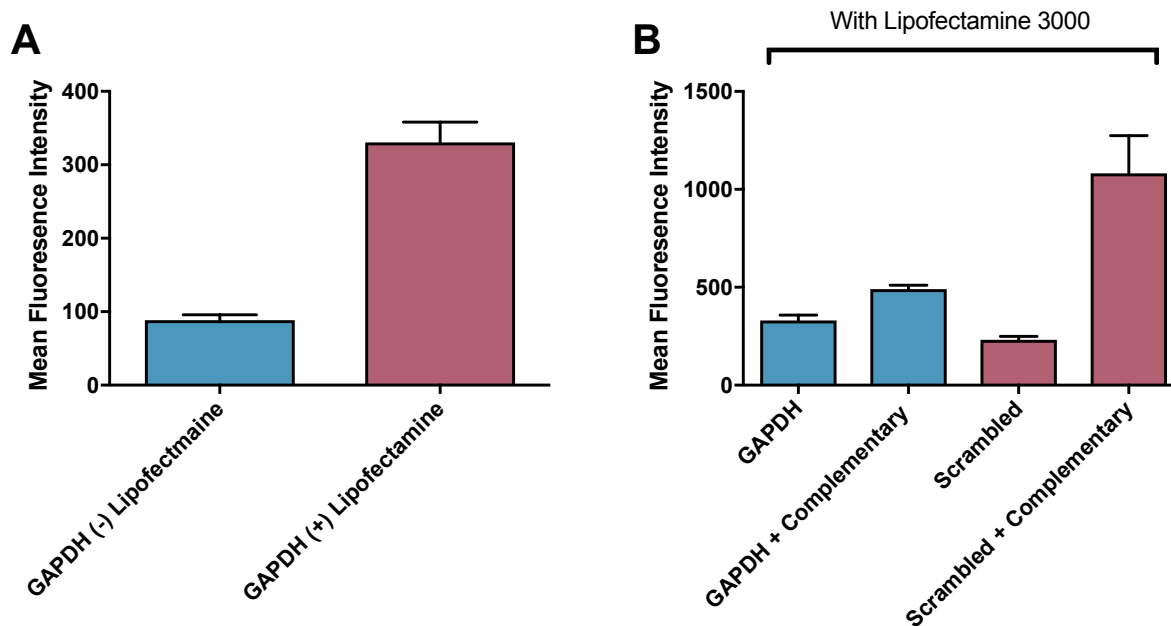


Figure 5.15 – Delivery of oligonucleotides with Lipofectamine 3000 to 3T3-WT cells, analyzed by flow cytometry. **(A)** The association of free and complexed single stranded GAPDH sensor sequence. **(B)** The effect complexes formed with single or double stranded sensor or scrambled sequences. The geometric mean fluorescence intensity of the samples in duplicate from flow cytometry is plotted with the error bar representing the standard deviation.

Next, we examined the ability of the GAPDH sensor to detect delivery to the cytosol by Lipofectamine 3000. The sensor or scrambled sequence was hybridized with quencher strand and then complexed with Lipofectamine. The amount the complexes associated with 3T3-NIH cells was variable as demonstrated by the fluorescence intensity of the unquenched sensor across repeated experiments

(**Figure 5.16A & B**). As this cell line expresses the target sequence, endosomal escape induced by Lipofectamine should cause an increase in the 20-mer but not in the 27-mer quenched samples. However, no significant difference between the 20-mer and 27-mer quenched samples was detected (**Figure 5.16A & B**).

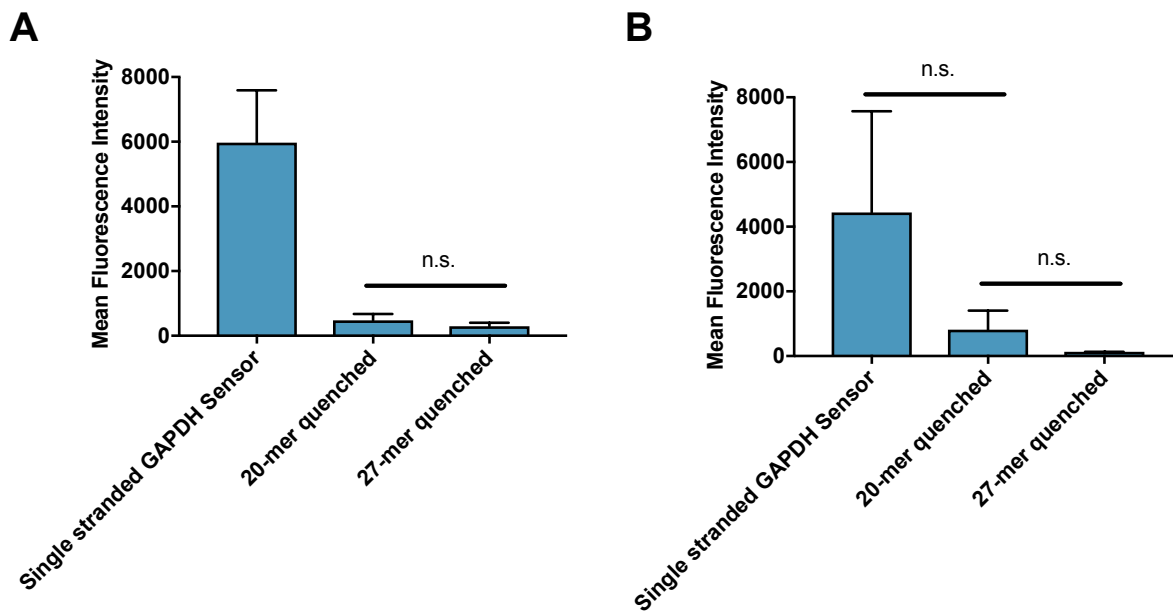


Figure 5.16 – Lipofectamine 3000 delivery of the GAPDH sensor in 3T3-WT cells. (**A**) Free GAPDH or quenched GAPDH sensor complexed with Lipofectamine. (**B**) A repeat of the same experiment. The geometric mean fluorescence intensity of samples in duplicate is plotted with the error bars representing the standard deviation. n.s = not significant by unpaired t-test, $n = 2$ ($P > 0.05$).

To determine if the variability was due to disparities in the uptake of complexes containing quenchers of different lengths, the complexes were labelled with an additional fluorophore. The sensor or scrambled sequence was first hybridized with quencher strand and then complexed by Lipofectamine with an additional non-complementary sequence labelled with Alexa Fluor 488. A similar Alexa Fluor 488 fluorescent signal across all samples showed that the length of the quencher on the sensor did not change association of the complexes with 3T3-NIH cells (**Figure 5.17B**). There was a small difference between the Cy5 signal of the 20-mer and 27-mer quenched sequences with the 27-mer quenched sample being slightly higher (**Figure 5.17A**). To confirm there was no difference being overlooked by the slight variations in association of the complexes, a ratio between the Cy5 and Alexa Fluor 488 signals was calculated but no escape could be detected (**Figure 5.17C**).

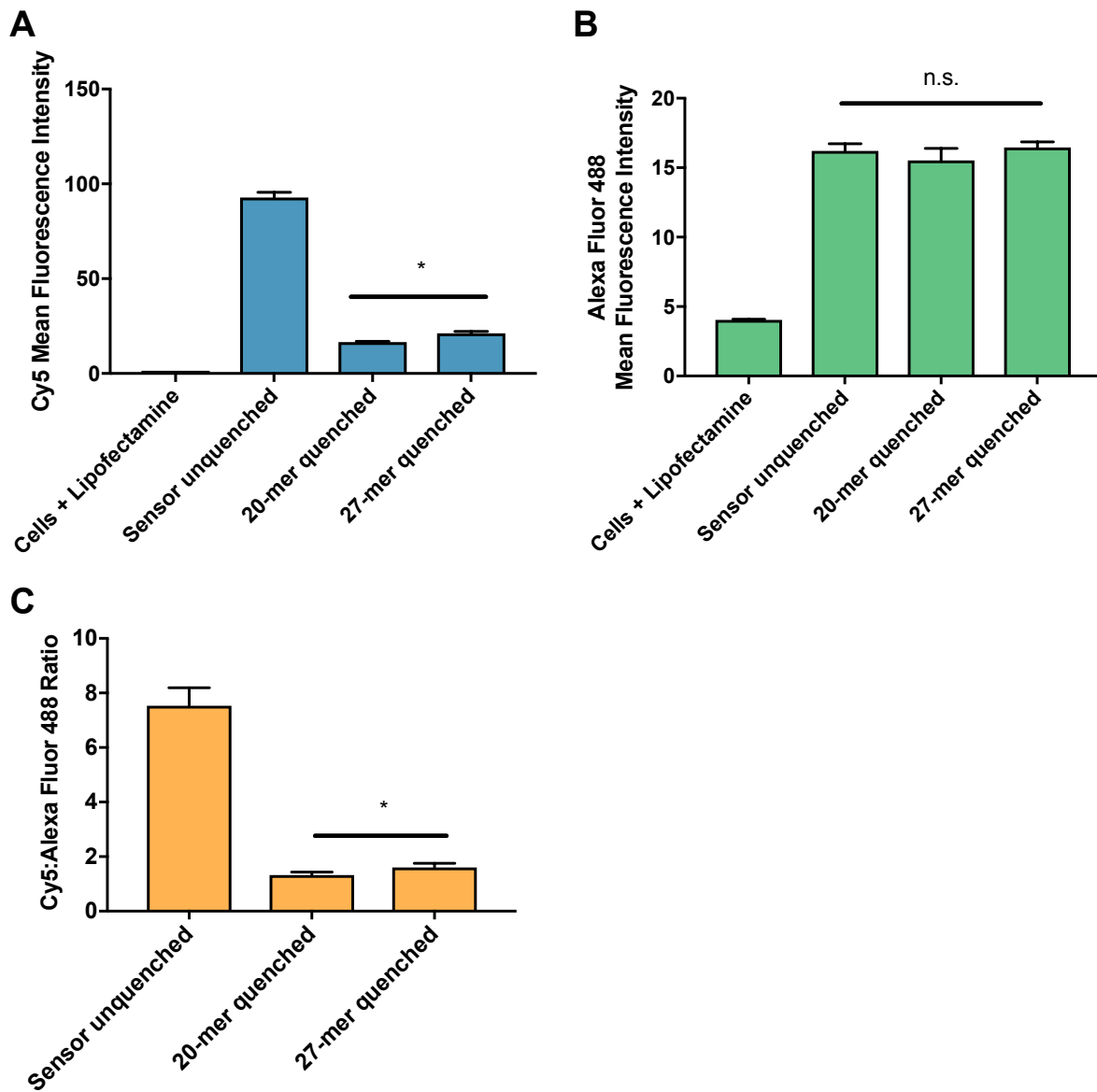


Figure 5.17 – Lipofectamine 3000 delivery of GAPDH sensor to 3T3-NIH cells. Mean fluorescence intensity of the (A) Cy5 or (B) Alexa Fluor 488 signal from GAPDH sensor quenched or unquenched, complexed with non-complementary scrambled sequence labeled with Alexa Fluor 488. The geometric mean fluorescence intensity from flow cytometry is plotted with error bars representing the standard deviation (n.s = not significant ($P > 0.05$) by one-way ANOVA, $n = 3$). (C) The average ratio between the Cy5 and Alexa Fluor 488 signal of each sample type, with the error bars representing the maximum and minimum calculated possible values (* $P < 0.05$, unpaired t-test, $n = 3$).

Microscopy also showed the sensor to be highly variable. Delivery of the unquenched GAPDH sensor to 3T3-NIH with Lipofectamine 3000 resulted in cells with high amounts of fluorescence both diffusely distributed in the cytosol and as punctate vesicles (**Figure 5.18A & Figure 5.19A**). Certain experiments showed no difference between the 20-mer quenched sensor (**Figure 5.18B**) and 27-mer quenched control sequence (**Figure 5.18C**). However, on other occasions there was a difference between the two as fluorescence localised to nuclear structures (**Figure 5.19C**) in the 20-mer quenches sensor was absent in the 27-mer control (**Figure 5.19C**).

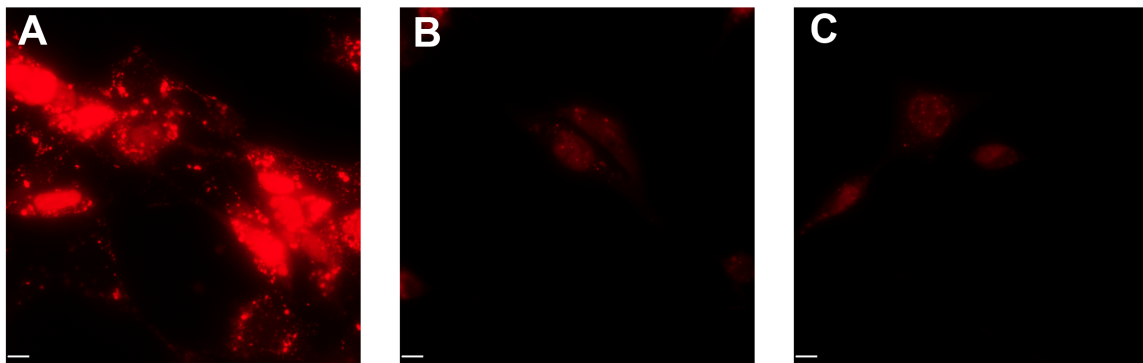


Figure 5.18 – Fluorescence microscopy images of Lipofectamine 3000 delivery of GAPDH sensor. GAPDH sensor hybridized with either (A) unlabeled complementary sequence, (B) 20-mer quencher or (C) 27-mer quencher complexed with Lipofectamine 3000 and incubated in 3T3-NIH cells overnight. Scale bar = 10 μm .

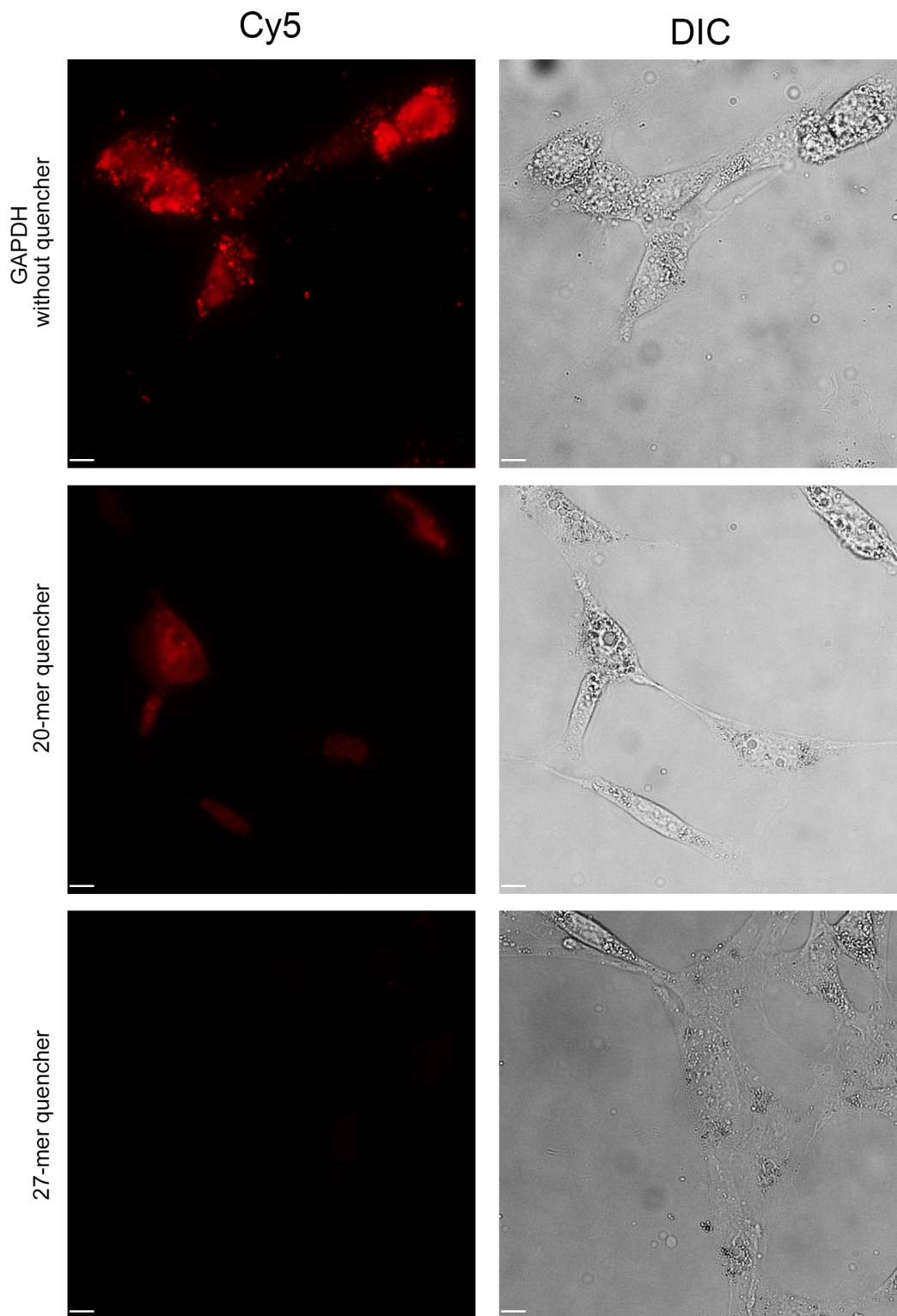


Figure 5.19 – Fluorescence microscopy images of Lipofectamine 3000 delivery of GAPDH sensor. GAPDH sensor hybridized with either (A) unlabeled complementary sequence, (B) 20-mer quencher or (C) 27-mer quencher complexed with Lipofectamine 3000 and incubated in 3T3-NIH cells overnight. Scale bar = 10 μ m.

Collectively, these results suggest that the sensor reliably cannot detect escape induced by Lipofectamine. Even though Lipofectamine produces pronounced expression when delivering plasmid to this cell type, the amount of escape may be too low for an appreciable quantity of replacement of the 20-mer quenched strand with GAPDH mRNA. Alternatively, the level of GAPDH within the cytosol may be too low so that even when escape is high, the change in signal is out competed by the background of the quenched sequences.

5.3.6 *Testing for GAPDH mRNA with Unhindered Cytosolic Access*

The lack in ability of the sensor to detect escape suggests the signal-to-noise ratio of the sensor may be too low. To test this, the sensor was given unhindered access to the contents of the cytosol. This was achieved by adding quenched sensor to lysed cells or to fixed and permeabilised cells. Lysis buffer previously shown to preserve mRNA⁴⁹ was added to cells and lysis was confirmed visually by light microscopy. However, there was no difference between samples with the GAPDH sensor (**Figure 5.20A**), the scrambled sequence (**Figure 5.20B**) or in the intensity of the 20-mer or 27-mer quenched samples. In addition, the percentage the 20-mer signal return of the maximum achievable signal was low (0.9 to 1.8%) and not significantly different compared to either the 27-mer quenched or scrambled controls (**Figure 5.20C**). In addition, there was no difference compared to samples with no cells present. Therefore, the presence of GAPDH mRNA could not be confirmed using the duplex sensor in lysed cells.

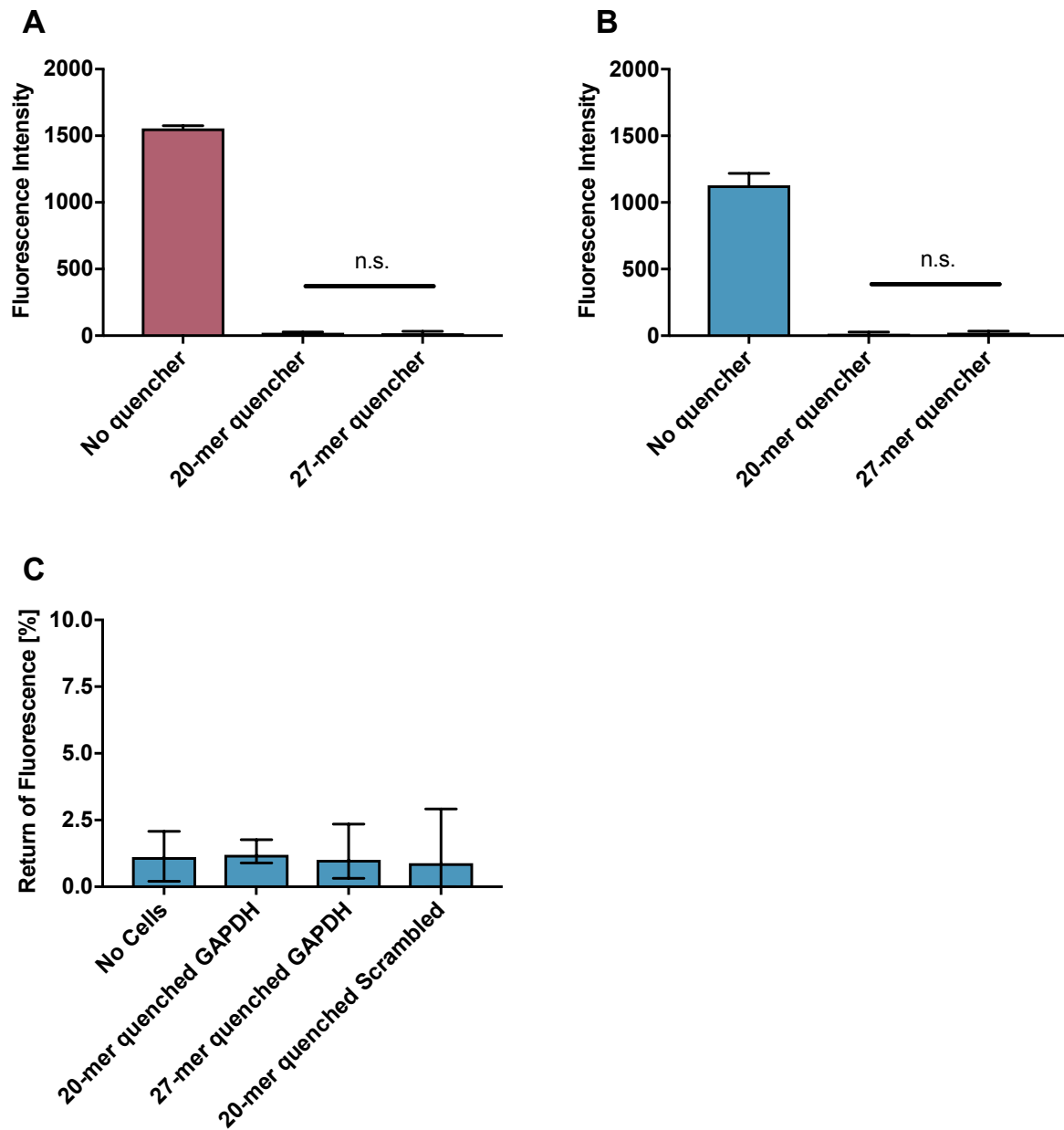


Figure 5.20 – GAPDH mRNA detection in lysed cells. Quenched and unquenched GAPDH or scrambled sequence was added to lysed 3T3-WT cells or lysis buffer without cells. **(A)** GAPDH sensor sequence **(B)** scrambled sequence (n.s = not significant by unpaired t-test, $P > 0.05$, $n = 3$). **(C)** Percentage of Cy5 fluorescence of the quenched samples relative to the unquenched sequences. Lysis performed triplicate. Mean fluorescence intensity is plotted with error bar representing the standard deviation **(A and B)**. The percentage return is plotted as the average, with the upper and lower limits calculated from the data as the error bars **(C)**.

The potential that mRNA degradation was occurring following cell lysis could not be eliminated. To overcome this, the cells were fixed and permeabilised before adding the sensor, similar to the protocol followed for fluorescence *in situ* hybridization, an established method for mRNA detection.²⁸ Addition of unquenched GAPDH sensor sequence to 3T3-WT cells resulted in diffuse fluorescence throughout both the cytosol and nucleus (**Figure 5.21A**) which corresponds to hybridisation of the sequence to GAPDH mRNA. However, no displacement of the quencher occurred as the subsequent fluorescent signal was not detectable in samples incubated with the 20-mer duplex (**Figure 5.21B**). In addition, the scrambled sequence also showed a similar distribution to the GAPDH sensor even though the cells do not contain the target sequence for hybridisation (**Figure 5.21D**). This indicated the sequences are non-specifically sticking to components inside the cell.

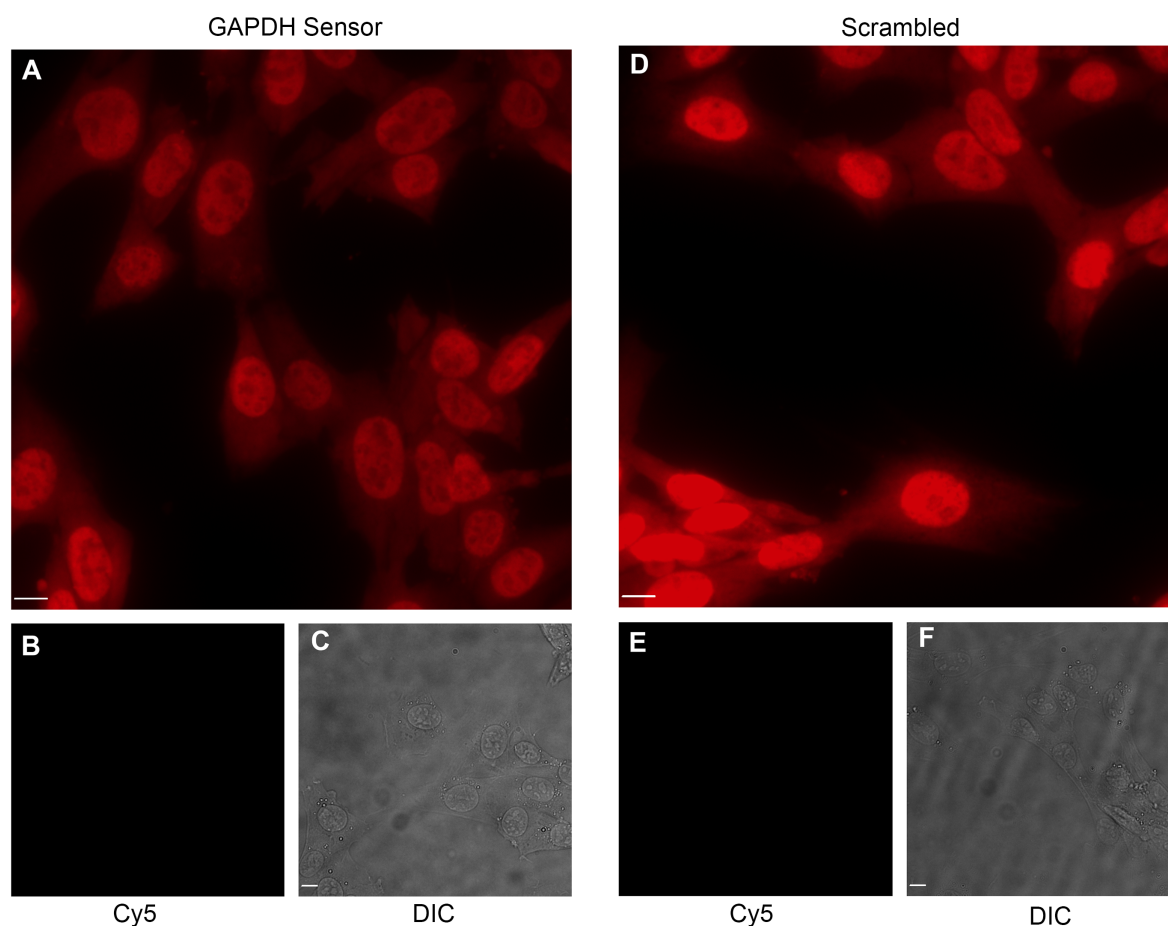


Figure 5.21 – GAPDH sensor and control sequence added to fixed and permeabilised cells. 3T3-WT cells were fixed, permeabilised and incubated with (A) unquenched GAPDH sensor, (B) 20-mer quenched GAPDH sensor, (D) unquenched scrambled sequence or (E) 20-mer quenched scrambled sequence. (C) and (F) shows the position of the cells in (B) and (E) respectively via the differential interference contrast image (DIC). Scale bar = 10 μm .

Fixing the cells may rigidify the mRNA too much to allow the quencher strand to be competed off. Hybridization in FISH protocols do not require strand exchange and as there appears to be hybridization of the unquenched sample this scenario is a possibility. However, the non-specific adherence of the scrambled sequence within fixed cells and the lack of mRNA detection within lysed cells suggests that the mRNA copy number is below detection threshold of the sensor. It is estimated there is approximately 200,000 mRNA copies per mammalian cell.⁵⁰ Of this collection of molecules, approximately 1,300 - 1,800 of these are GAPDH mRNA molecules (in 3T3-NIH and K562 cells).^{51,52} As the optimum sensor response was determined to occur in the presence of 2 equivalents of complementary sequence, it may be that the amount of sensor delivered so that the fluorescent signal is high enough for detection causes a high background signal when quenched. This leads to a poor signal-to-noise ratio and prevents any change in signal when the sensor is in the presence of GAPDH mRNA.

The similarity of our sensor to the commercial NanoFlare mRNA detection system indicates that mRNA copy number may not be the sole reason no response was seen in any of the trialed methods. NanoFlares are reported to contain on average 90 oligonucleotides per particle and are delivered to cells at a final concentration 0.5 – 5 nM³⁵ which equates to between 45 – 450 nM oligonucleotide. The amount of oligonucleotide delivered in the series of Lipofectamine experiment was within this range. While it is difficult to compare the background signal across the experiments as the levels of uptake may be different, it does imply that the signal to noise ratio of the NanoFlares is superior to the duplex escape sensor.

A possible reason for this may be the level of degradation in the duplex sensor observed across the experiments. The NanoFlare is reported to be resistant to break down as the high oligonucleotide loading on the particles causes a negative surface charge which in turn induces a local salt concentration that inhibits enzymatic degradation.⁵³ This suggests that if our sensor was covalently attached to the particle of interest and the degree of labelling was high enough, degradation may be avoided. However, this is not feasible as this level of conjugation would change the physiochemical properties of the material the sensor was attached to.

5.4 Conclusions

The endosomal escape sensor in duplex form was demonstrated to be highly responsive in the presence of its target sequence in solution. It was also shown to be specific as the fluorescence of quenched samples did not increase when a scrambled duplex was challenged with the target sequence. However, the sensor could not detect escape induced with Lipofectamine 3000. The sensor was also unresponsive when unhindered access to the cytosolic constituents was provided by cell lysis or by permeabilising the cell. The proposed issues with the sensor are twofold:

- i) The sensor, even though modified to resist cleavage is subject to degradation along the endo/lysosomal trafficking pathway, decreasing the signal to noise ratio of the sensor.
- ii) This first problem is compounded by the low concentration of GAPDH mRNA within the cell. The copy number is too low for this sensor design to detect the target sequence at the level it is delivered to the cells.

This work highlights the balancing act between sensor supply and the amount of recognition element present. Providing more sensor means an increased background but does not necessarily correspond with a larger signal if the recognition element is limited. To move forward, a cytosolic entity present at a much higher concentration is required. This may require overexpression to be induced, such as the SNAP-tag system described in Chapter 4.

5.5 Materials and Methods

5.5.1 Instrumentation

UV/visible absorbance spectroscopy to determine the concentration of DNA oligonucleotide probes or protein samples was performed on a NanoDrop Spectrophotometer ND-1000. Fluorescence spectra was collected with a Shimadzu RF-5310PC fluorescence spectrophotometer with temperature maintained by an Eyla NTT-2200 Water Bath. Bulk fluorescence intensity values at set excitation/emission were obtained with a PerkinElmer EnSpire Multilabel plate reader.

5.5.2 *Materials*

Custom fluorescently modified oligonucleotide sequences using Cyanine (Cy) and Black Hole Quencher (BHQ) dyes were purchased from Integrated DNA Technologies (IDT) or IBA Lifesciences GmbH. Dulbecco's Modified Eagle's medium (DMEM) (Gibco), fetal bovine serum (FBS) (Gibco) and Penicillin/Streptomycin (Invitrogen) were purchased from Thermo Scientific. Human holo-transferrin, calcein, potassium chloride, Triton X-100 and phosphate buffered saline tablets were purchased from Sigma-Aldrich. Tris hydrochloride was purchased from Fisher Scientific. Goat anti-rabbit Alexa Fluor 488 and Anti-Lysosomal Associated Membrane Protein 1 were purchased from Abcam. Anti-transferrin receptor (human) antibody OKT9 was kindly donated by Dr. Justine Mintern (Bio21 Institute, Melbourne).

5.5.3 *Cell Culture*

Cells were purchased from American Type Culture Collection (ATCC). 3T3 MEF WT (3T3-WT) (ATCC: CRL-2752) and HeLa (ATCC: CCL-2) were maintained in DMEM, high glucose (GlutaMAX) with phenol red, supplemented with 10% FBS and 1% penicillin/streptomycin at 37°C with 5%. 3T3-NIH (ATCC: CRL-1658) were maintained in in DMEM, high glucose (GlutaMAX) with phenol red, 20% FBS and 1% penicillin/streptomycin at 37°C with 5%. The cells were maintained by research assistants, Ewa Czuba (3T3-WT), Moore Chen (3T3-NIH) and Honours student Josh Rennick (HeLa) (Monash University, Melbourne).

5.5.4 *Flow Cytometry*

Flow cytometry was performed on a Stratadigm S1000EXI flow cytometer (Stratadigm, California, USA) using a 488 nm excitation with emission collected in the 515 – 545 nm channel (Alexa Fluor 488) and a 642 nm excitation with emission collected in the 661 – 690 nm channel or a BD FACS Canto II flow cytometer (BD Biosciences, USA) with a 640 nm excitation and emission collected in the 650 – 670 nm channel. FCS2.0 files were exported using BD FACSDIVA (version 6.0, BD Biosciences, USA) or FCS3.0 files were exported using CellCapTure Analysis Software (Stratadigm, California, USA). 1×10^4 events were collected per sample. The cells were gated by forward versus side scatter and analysed in FlowJo (version 10, Tree Star, Oregon, USA).

5.5.5 Fluorescence Microscopy

Images were collected via fluorescence microscopy using a 60X 1.3 NA silicone or a 40X 0.9 NA air objective with a standard “Pinkel” DAPI/FITC/Cy3/Cy5 Filter set (Semrock). Emission was separated and captured using a 414/497/565/653 nm dichroic mirror and a quad-band bandpass emission filter between 503 – 515 nm and 614 – 804 nm. For live cell imaging, CO₂ and temperature controls were used to maintain 5% CO₂, humidity and a temperature of 37°C. All image analysis was performed in Slidebook 6.0 (Intelligent Imaging Innovations, Denver, USA).

5.5.6 Oligonucleotide Sequences

Oligonucleotides were reconstituted in Milli-Q or nuclease free-water to prepare 150 μM or 600 μM stock and stored at -20°C.

GAPDH Target Sequence

The GAPDH complementary sequence for opening the beacon or duplex sensor:

5' – AGGGTGGAGCCAAAAGGGTCATCATCT – 3'

Fluorescent Components of the Duplex Escape Sensor

The sequences for the fluorescent components of the duplex escape sensor are as follows with phosphorothioate bonds represented by a (*) symbol:

Mouse GAPDH sensor sequence

5' – Cy5 – AGATGATGACCCTTTTGGCTCCACCCT – azide – 3'

Mouse GAPDH sensor sequence (phosphorothioated)

5' – Cy5 – A*G*A*T*G*A*T*G*A*C*C*C*T*T*T*G*G*C*T*C*A*C*C*C*T* – azide – 3'

Scrambled control sequence

5' – Cy5 – TCAGTTCAGGACCCTCGGCTTTACGGT – azide - 3'

Scrambled control sequence (phosphorothioated)

5' – Cy5 – T*C*A*G*T*T*C*A*G*G*A*C*C*C*T*C*G*G*C*T*T*T*A*C*G*G*T* – azide - 3'

Quencher Components of the Duplex Escape Sensor

GAPDH 27-mer quencher

5' – A*G*G*G*T*G*G*A*G*C*C*A*A*A*A*G*G*G*T*C*A*T*C*A*T*C*T* – BHQ2 – 3'

GAPDH 20-mer quencher

5' – A*G*C*C*A*A*A*G*G*G*T*C*A*T*C*A*T*C*T* – BHQ2 – 3'

Scrambled control sequence 27-mer quencher

5' – A*C*C*G*T*A*A*A*G*C*C*G*A*G*G*G*T*C*T*G*A*A*C*T*G*A* – BHQ2 – 3'

Scrambled control sequence 20-mer quencher

5' – A*G*C*C*G*A*G*G*G*T*C*C*T*G*A*A*C*T*G*A* – BHQ2 – 3'

5.5.7 Protein Degree of Labelling

The degree of labelling (DOL) of the protein by the oligonucleotide sensor was calculated from the following equation using a correction factor to compensate for the additional absorbance at 280 nm from DNA:

$$\text{DOL} = \frac{[\text{fluorophore}]}{[\text{protein}]} = \frac{(A_{\text{dye}} \times \epsilon_{\text{protein}})}{\epsilon_{\text{dye}}(A_{280} - \text{CF} \times A_{\text{dye}})} \quad (5.1)$$

where,

A_{dye} = absorbance of the sample at absorbance maxima of the dye

$\epsilon_{\text{protein}}$ = extinction coefficient of the protein at 280 nm ($\text{M}^{-1} \text{cm}^{-1}$)

ϵ_{dye} = extinction coefficient of the dye at the absorbance maxima ($\text{M}^{-1} \text{cm}^{-1}$)

A_{280} = absorbance of the sample at 280 nm

CF = correction factor calculated from the absorbance of the fluorescent component alone at 280 nm divided by the absorbance at the maxima

5.5.8 Quenching Efficiency and Return of Fluorescence Equations

To determine quenching efficiency, the mean fluorescence intensity of the cells alone was averaged and subtracted from each sample and then substituted into the following equation:

$$\eta_{quenching} = \left(1 - \frac{I_{quenched}}{I_{unquenched}}\right) \times 100 \quad (5.2)$$

where,

$\eta_{quenching}$ = efficiency of quenching (%)

$I_{quenched}$ = fluorescence intensity of the quenched sample

$I_{unquenched}$ = fluorescence intensity of the unquenched sample

To determine the return in fluorescence signal, the mean fluorescence intensity of the cells alone was averaged and subtracted from each sample and then substituted into the following equation:

$$\eta_{return} = \left(\frac{I_{quenched}}{I_{unquenched}}\right) \times 100 \quad (5.3)$$

where,

η_{return} = return of original signal (%)

$I_{quenched}$ = fluorescence intensity of the quenched sample

$I_{unquenched}$ = fluorescence intensity of the unquenched sample

5.5.9 Sensor Fluorescence in Solution

Obtaining the fluorescent spectra of several of the sensors in media containing FBS was assisted by summer research student May Lai (Monash University, Melbourne) under my supervision.

A typical experiment involved obtaining the background fluorescence spectra by exciting solvent in a 0.5 mL cuvette at the wavelengths of any dyes to be checked. Emission spectra were then obtained for the dye of interest before adding any second sequences and repeatedly measuring the emission over set time intervals.

Duplex quenching efficiency, stability and return of signal in the presence of the complementary strand was assessed. A fluorescence emission spectrum was obtained by excitation at 650 nm with emission measured between 655 – 700 nm with a 5 nm slit width and fast scanning speed. The emission spectrum of GAPDH or scrambled sequence diluted to 0.2 μ M in PBS was obtained before adding 3.7 equivalents of quencher sequence. The emission was measured every 2 minutes after addition of the

quencher to ensure quenching had reached completion before adding 4 equivalents of the complementary strand. An emission spectrum was then obtained every 5 minutes until the fluorescence intensity stabilised.

5.5.10 Duplex Sensor Response Optimization

The amount of quencher strand required to remove the Cy5 signal was optimised using a fluorescence plate reader. GAPDH sensor was initially diluted in PBS to 75 nM. 100 μ L of this solution was then combined with 25 μ L of PBS containing 5 to 0 molar equivalents of quencher in a 96-well clear bottom black polystyrene microplate. 25 μ L of PBS containing 3 equivalents of GAPDH complementary sequence was added to a separate set of wells and analyzed. To determine the dependence of the return in signal on the concentration of complementary strand, 100 μ L of 75 nM GAPDH sensor was mixed with 25 μ L of PBS containing 2 equivalents of quencher for 15 mins before adding 25 μ L of PBS or PBS with 5 to 0 equivalents complementary sequence.

5.5.11 Duplex Escape Sensor on Transferrin in 3T3-WT Cells

The ability of the sensor to stay closed under conditions with no endosomal escape was investigated using the protein transferrin with 3T3-WT cells. 3T3-WT were seeded at 60,000 cells per well in 400 μ L DMEM supplemented with 10% FBS and 1% penicillin/streptomycin one day prior to the experiment. Serum was removed by washing three times with DMEM without FBS. 25 μ L DMEM was added with or without transferrin labelled with sensor for a final concentration of 10 μ g mL⁻¹ to duplicate wells and incubated for 30 minutes at 4°C to allow binding to the cell surface. Following two washes with DMEM, 2 equivalents of the 20-mer or 27-mer quencher added to the appropriate wells and cells were incubated at either 37°C or 4°C for a further hour. To detach the cells, 200 μ L of 10 mM EDTA in PBS was added and left for 10 minutes at 37°C or 4°C followed by 300 μ L 1% BSA in PBS. Cells were then manually scrapped off the plate and transferred to flow cytometry tubes. The tubes were spun at 250g for 5 minutes and the cells were resuspended in 200 μ L of 1% BSA in PBS before analysis by flow cytometry.

5.5.12 Duplex Escape Sensor on Anti-Transferrin Antibody in HeLa Cells

Josh Rennick (Monash University, Melbourne) carried out the experiment under my supervision and I assisted with the experimental design.

Mouse anti-transferrin receptor antibody (OKT9) was first labelled with DIBO by adding 5 equivalents of DIBO-NHS (1 mg mL^{-1}) to the protein ($200 \text{ }\mu\text{g}$, 2 mg mL^{-1}) for 2 hours at 4°C . Excess DIBO was removed using a 0.5 mL Zeba 7k MWCO equilibrated with PBS. The OKT9-DIBO was split and non-phosphorothioated mouse GAPDH sensor or phosphorothioated scrambled sequence was added at 2 equivalents, overnight at 4°C . Excess oligonucleotide was removed using 0.5mL 30k MWCO Amicon Ultra centrifugal filters. The samples were washed until the flow through was clear.

HeLa cells were detached from a T-25 cell culture flask using 0.25% trypsin and then counted. The cells were pelleted by spinning at 400 g for 4 minutes then resuspended in cold DMEM with 10% FBS to a final concentration of 1 million cells per mL. Cells were then transferred into 1.6 mL Eppendorf tubes at $100,000$ cells per tube. OKT9 was added to the cells on ice at a final concentration of $5 \text{ }\mu\text{g mL}^{-1}$ for 30 minutes to allowing binding to the cell surface. Excess OKT9 was removed by washing the cells 3 times with DMEM + 10% FBS by spinning at 350 g for 5 minutes. Cells were then transferred to a 96 well plate at 0, 15, 30, 60 and 90-minute time points and incubated at 37°C . Cells were then spun once in the plate for 5 minutes at 350g , resuspended in PBS and analysed via flow cytometry.

5.5.13 Duplex Escape with Lipofectamine 3000 by Flow Cytometry

3T3-NIH cells were seeded at $50,000$ cells per well in $450 \text{ }\mu\text{L}$ DMEM supplemented with 10% FBS and 1% penicillin/streptomycin 1 day prior to the experiment. A bulk dilution of P3000 ($2 \text{ }\mu\text{L}$ per sample) and Lipofectamine 3000 reagent ($1\text{ }\mu\text{L}$ per sample) was made up in $25 \text{ }\mu\text{L}$ OptimMEM per sample. The P3000 solution was split into Eppendorf tubes and combined with the 250 ng GAPDH or scrambled sensor with or without 3.7 equivalents quencher stand. The diluted Lipofectamine 3000 ($25 \text{ }\mu\text{L}$ per sample) reagent was then added to the tubes and incubated for 5 minutes at room temperature to allow for the complexes to form before adding to the cells and incubating for 4 hours at 37°C . Following incubation, cells were washed 4 times with PBS, detached by adding $150 \text{ }\mu\text{L}$ 0.25% trypsin in PBS for 3 minutes at room temperature, followed by $100 \text{ }\mu\text{L}$ 1% BSA in PBS. The entire volume was transferred

to a 96-well, V-bottom plate and spun at 250 g for 5 minutes, washed once in 150 μ L 1% BSA in PBS, resuspended in PBS and transferred to flow cytometry before analysis by flow cytometry.

5.5.14 Escape of Dual-Labelled Lipofectamine 3000 Complexes

3T3-NIH cells were seeded at 120,000 cells per well in 400 μ L DMEM supplemented with 10% FBS and 1% penicillin/streptomycin 1 day prior to the experiment. Duplexes of the fluorescent strand (50 ng) were formed with 2 equivalents non-fluorescent complementary or quencher strands were formed in OptiMEM with 1 μ L of P3000 per sample for 10 minutes. The duplexes were then complexed with one equivalent of a scrambled sequence labelled with Alexa Fluor 488 (see Chapter 4 for sequence details) using 1.5 μ L Lipofectamine 3000 per sample for 10 minutes before adding to the cells and incubating overnight at 37°C. The following day, cells were washed 3 times with DMEM supplemented with 10% FBS then detached by adding 200 μ L of 0.25% trypsin in PBS. Following detachment, 100 μ L of 1% BSA in PBS was added to each well and the entire volume transferred to a 96-well, V-bottom plate. Cells were spun at 250 g for 5 minutes and resuspended in PBS before analysis by flow cytometry.

5.5.15 Lipofectamine 3000 Imaging

3T3-NIH cells were seeded at 5,000 cells per well in 100 μ L in black, clear-bottom 96-well polystyrene plates or at 40,000 cells per well in 8 well plates one day prior to the experiment. Duplexes of the GAPDH sensor were formed by adding 2 equivalents of non-fluorescent complementary strand in OptiMEM media with 0.2 μ L P3000 reagent per well and incubating for 10 minutes at room temperature. Cells were then transfected with a mass of 100 ng fluorescent strand per well using 0.23 μ L Lipofectamine 3000 per well and following the manufacturers protocols. After incubation overnight, cells were washed 3 times in DMEM with 10% FBS. Cells were imaged live in FluoroBrite with 10% FBS or fixed with 3% paraformaldehyde in PBS for 10 minutes at room temperature.

For permeabilization, cells were washed 3 times with PBS before blocking for 2 hours at room temperature with blocking buffer (3% BSA, 0.2% Triton X-100 in PBS). The primary antibody, polyclonal rabbit Anti-Lysosomal Membrane Associated Protein 1 (LAMP1) was added at 2 μ g mL⁻¹ in blocking

buffer and incubated with the cells overnight at 4°C. The cells were then washed 3 times in washing buffer (0.2% BSA, 0.05% Triton X-100 in PBS), allowing 10 minutes per wash. Goat polyclonal anti-rabbit Alexa Fluor 488 antibody was then added at 1 µg mL⁻¹ in blocking buffer and left to incubate at room temperature for 1 hour. Cells were washed again 3 times with washing buffer for 10 minutes per wash, then once with PBS before imaging in PBS.

To validate the anti-LAMP1 antibody, 3T3-NIH cells were seeded at 40,000 cells per well in 8 well plates one day prior the experiment. Cells were washed once in PBS and then fixed with 3% paraformaldehyde in PBS for 10 minutes at room temperature. Cells were then washed 3 times with PBS before blocking for 2 hours at room temperature with blocking buffer (3% BSA, 0.2% Triton X-100 in PBS). The primary antibody, polyclonal rabbit Anti-Lysosomal Membrane Associated Protein 1 (LAMP1) was added at a concentration of 1 µg mL⁻¹ in blocking buffer and incubated with the cells overnight at 4°C. The cells were then washed 3 times in washing buffer (0.2% BSA, 0.05% Triton X-100 in PBS), allowing 10 minutes per wash. Goat polyclonal anti-rabbit Alexa Fluor 488 antibody was then added at 1 µg mL⁻¹ per well in blocking buffer and left to incubate at room temperature for 1 hour. Cells were washed again 3 time times with washing buffer for 10 minutes per wash, then once with PBS before imaging in PBS.

5.5.16 Cell Lysis

3T3-WT cells were seeded at 10,000 cells/well in 100 µL in black, clear-bottom 96-well polystyrene plates one day prior to the experiment. To lyse the cells, a Tris buffer containing Triton X-100 was used.⁴⁹ Cells were washed once in PBS before adding Tris buffer (10 mM Tris, 150 mM NaCl, pH 7.4) with or without 1% Triton X-100. The fluorescent oligonucleotide sensor (GAPDH and Scrambled) was added at 7.5×10^{-12} mol per well, pre-complexed with 3.7 equivalents of either non-fluorescent or quencher-labelled complimentary strand. The lysed cells were left for 20 minutes before the fluorescence intensity of each well was determined on a fluorescence plate reader.

5.5.17 Cell Fixation and Permeabilization

Cells were seeded at 40,000 cells per well in 400 µL in an 8-well chamber slide one day prior to the experiment. Cells were fixed and permeabilised as described previously (section 5.4.16). Instead of

adding antibody, GAPDH sensor or scrambled sequence at 0.16 nM incubated with or without 2 equivalents of quencher for 15 mins prior were added and incubated with the cells overnight at 4°C. Cells were then washed 3 times with 1X saline-sodium citrate (0.15 M NaCl, 0.015 M sodium citrate, pH 7) at room temperature, 5 minutes per wash and imaged.

5.6 References

1. Shete, H. K., Prabhu, R. H. & Patravale, V. B. Endosomal escape: a bottleneck in intracellular delivery. *Journal of nanoscience and nanotechnology* **14**, 460–74 (2014).
2. Varkouhi, A. K., Scholte, M., Storm, G. & Haisma, H. J. Endosomal escape pathways for delivery of biologicals. *J. Control. Release* **151**, 220–8 (2011).
3. Martens, T. F., Remaut, K., Demeester, J., De Smedt, S. C. & Braeckmans, K. Intracellular delivery of nanomaterials: How to catch endosomal escape in the act. *Nano Today* **9**, 344–364 (2014).
4. Hu, Y. *et al.* Cytosolic delivery of membrane impermeable molecules in dendritic cells using pH responsive core-shell nanoparticles. *Nano Lett.* **7**, 3056–3064 (2007).
5. Zhan, X., Tran, K. K., Wang, L. & Shen, H. Controlled endolysosomal release of agents by pH-responsive polymer blend particles. *Pharm. Res.* **32**, 2280–2291 (2016).
6. Jones, R. A. *et al.* Poly(2-alkylacrylic acid) polymers deliver molecules to the cytosol by pH-sensitive disruption of endosomal vesicles. *Biochem. J.* **372**, 65–75 (2003).
7. Hu, Y. *et al.* Cytosolic delivery mediated via electrostatic surface binding of protein, virus, or siRNA cargos to pH-responsive core-shell gel particles. *Biomacromolecules* **10**, 756–65 (2009).
8. Cheng, C., Convertine, A. J., Stayton, P. S. & Bryers, J. D. Multifunctional triblock copolymers for intracellular messenger RNA delivery. *Biomaterials* **33**, 6868–6876 (2012).
9. Wang, K. *et al.* Structure-Invertible Nanoparticles for Triggered Co-Delivery of Nucleic Acids and Hydrophobic Drugs for Combination Cancer Therapy. *Adv. Funct. Mater.* **25**, 3380–3392 (2015).
10. Dual, A. B. *et al.* Overcoming Endosomal Barrier by Amphotericin B-Loaded Dual pH-Responsive PDMA-b-PDPA Micelleplexes for siRNA Delivery. *ACS Nano* **5**, 9246–9255 (2011).
11. Gallon, E. *et al.* Triblock Copolymer Nanovesicles for pH-Responsive Targeted Delivery and Controlled Release of siRNA to Cancer Cells. *Biomacromolecules* **16**, 1924–1937 (2015).
12. Weikum, E. R., Knuesel, M. T., Ortlund, E. A. & Yamamoto, K. R. Glucocorticoid receptor control

- of transcription: precision and plasticity via allostery. *Nat. Rev. Mol. Cell Biol.* **18**, 159–174 (2017).
13. Bertorelli, G., Bocchino, V. & Olivieri, D. Heat shock protein interactions with the glucocorticoid receptor. *Pulm. Pharmacol. Ther.* **11**, 7–12 (1998).
 14. Frego, L. E. E. & Davidson, W. Conformational changes of the glucocorticoid receptor ligand binding domain induced by ligand and cofactor binding, and the location of cofactor binding sites determined by hydrogen/ deuterium exchange mass spectrometry. *Protein Sci.* **15**, 722–730 (2006).
 15. Zhou, J. & Cidlowski, J. a. The human glucocorticoid receptor: One gene, multiple proteins and diverse responses. *Steroids* **70**, 407–417 (2005).
 16. Yu, P., Liu, B. & Kodadek, T. A high-throughput assay for assessing the cell permeability of combinatorial libraries. *Nat. Biotechnol.* **23**, 746–751 (2005).
 17. Appelbaum, J. S. *et al.* Arginine topology controls escape of minimally cationic proteins from early endosomes to the cytoplasm. *Chem. Biol.* **19**, 819–830 (2012).
 18. Qureshi, S. a. beta-Lactamase: An ideal reporter system for monitoring gene expression in live eukaryotic cells. *Biotechniques* **42**, 91–95 (2007).
 19. Raz, E., Zlokarnik, G., Tsien, R. Y. & Driever, W. β -Lactamase as a Marker for Gene Expression in Live Zebrafish Embryos. *Dev. Biol.* **203**, 290–294 (1998).
 20. Segura, E., Durand, M. & Amigorena, S. Similar antigen cross-presentation capacity and phagocytic functions in all freshly isolated human lymphoid organ-resident dendritic cells. *J. Exp. Med.* **210**, 1035–47 (2013).
 21. Jansen, R. P. mRNA localization: message on the move. *Nat. Rev. Mol. Cell Biol.* **2**, 247–256 (2001).
 22. Park, H. Y., Trcek, T., Wells, A. L., Chao, J. A. & Singer, R. H. An Unbiased Analysis Method to Quantify mRNA Localization Reveals Its Correlation with Cell Motility. *Cell Rep.* **1**, 179–184 (2012).
 23. Lerner, R. S. *et al.* Partitioning and translation of mRNAs encoding soluble proteins on membrane-bound ribosomes. *RNA* **9**, 1123–1137 (2003).
 24. Tristan, C., Shahani, N., Sedlak, T. W. & Sawa, A. The diverse functions of GAPDH: views from different subcellular compartments. *Cell Signal.* **23**, 317–323 (2011).

25. Barber, R. D., Harmer, D. W., Coleman, R. a & Clark, B. J. GAPDH as a housekeeping gene: analysis of GAPDH mRNA expression in a panel of 72 human tissues. *Physiol. Genomics* **21**, 389–95 (2005).
26. Eisenberg, E. & Levanon, E. Y. Human housekeeping genes, revisited. *Trends Genet.* **29**, 569–574 (2013).
27. Buxbaum, A. R., Haimovich, G. & Singer, R. H. In the right place at the right time: visualizing and understanding mRNA localization. *Nat. Rev. Mol. Cell Biol.* **16**, 95–109 (2014).
28. Levsky, J. M. & Singer, R. H. Fluorescence in situ hybridization: past, present and future. *J. Cell Sci.* **116**, 2833–2838 (2003).
29. Tyagi, S. & Kramer, F. R. Molecular Beacons: Probes that Fluoresce upon Hybridization. *Nat. Biotechnol.* **14**, 303–308 (1996).
30. Tan, W., Wang, K. & Drake, T. J. Molecular beacons. *Curr. Opin. Chem. Biol.* **8**, 547–53 (2004).
31. Santangelo, P. J., Nix, B., Tsourkas & Bao, G. Dual FRET molecular beacons for mRNA detection in living cells. *Nucleic Acids Res.* **32**, 1–9 (2004).
32. Bratu, D. P., Cha, B.-J., Mhlanga, M. M., Kramer, F. R. & Tyagi, S. Visualizing the distribution and transport of mRNAs in living cells. *Proc. Natl. Acad. Sci. U. S. A.* **100**, 13308–13 (2003).
33. Chen, M. *et al.* A molecular beacon-based approach for live-cell imaging of RNA transcripts with minimal target engineering at the single-molecule level. *Sci. Rep.* **7**, 1550 (2017).
34. Bao, G., Rhee, W. J. & Tsourkas, A. Fluorescent Probes for Live-Cell RNA Detection. *Annu Rev Biomed Eng* **11**, 25–47 (2009).
35. Prigodich, A. E. *et al.* Nano-flares for mRNA regulation and detection. *ACS Nano* **3**, 2147–52 (2009).
36. Prigodich, A. E. *et al.* Multiplexed nanoflares: mRNA detection in live cells. *Anal. Chem.* **84**, 2062–2066 (2012).
37. Dubertret, B., Calame, M. & Libchaber, a J. Single-mismatch detection using gold-quenched fluorescent oligonucleotides. *Nat. Biotechnol.* **19**, 365–70 (2001).
38. Zhang, D. Y. & Winfree, E. Control of DNA strand displacement kinetics using toehold exchange. *J Am Chem Soc* **131**, 17303–17314 (2009).
39. Altschul, S. F., Gish, W., Miller, W., Myers, E. W. & Lipman, D. J. Basic local alignment search tool. *J. Mol. Biol.* **215**, 403–10 (1990).

40. Lechardeur, D. *et al.* Metabolic instability of plasmid DNA in the cytosol: a potential barrier to gene transfer. *Gene Ther.* **6**, 482–497 (1999).
41. Gan, R. *et al.* DNA phosphorothioate modifications influence the global transcriptional response and protect DNA from double-stranded breaks. *Sci. Rep.* **4**, 1–8 (2014).
42. Eckstein, F. Phosphorothioate Oligodeoxynucleotides: What is Their Origin and What is Unique About Them? *Antisense Nucleic Acid Drug Dev.* **10**, 117–121 (2000).
43. Mayle, K. M., Le, A. M. & Kamei, D. T. The intracellular trafficking pathway of transferrin. *Biochim. Biophys. Acta* **1820**, 264–281 (2012).
44. Sutherland, R. *et al.* Ubiquitous cell-surface glycoprotein on tumor cells is proliferation-associated receptor for transferrin. *Proc. Natl. Acad. Sci. U. S. A.* **78**, 4515–4519 (1981).
45. Weissman, A. M., Klausner, R. D., Krishnamurthy, R. & Harford, J. B. Exposure of K565 cells to anti-receptor monoclonal antibody OKT9 results in rapid redistribution and enhanced degradation of the transferrin receptor. *J. Cell Biol.* **102**, 951–958 (1986).
46. Lappalainen, K., Miettinen, R., Kellokoski, J., Jääskeläinen, I. & Syrjänen, S. Intracellular distribution of oligonucleotides delivered by cationic liposomes: Light and electron microscopic study. *J. Histochem. Cytochem.* **45**, 265–274 (1997).
47. Cardarelli, F. *et al.* The intracellular trafficking mechanism of Lipofectamine-based transfection reagents and its implication for gene delivery. *Sci. Rep.* **6**, 25879 (2016).
48. Stein, C. a *et al.* Phosphorothioate and normal oligodeoxyribonucleotides with 5'-linked acridine: characterization and preliminary kinetics of cellular uptake. *Gene* **72**, 333–341 (1988).
49. Shatzkes, K., Teferedegne, B. & Murata, H. A simple, inexpensive method for preparing cell lysates suitable for downstream reverse transcription quantitative PCR. *Sci. Rep.* **4**, 1–7 (2014).
50. Shapiro, E., Biezuner, T. & Linnarsson, S. Single-cell sequencing-based technologies will revolutionize whole-organism science. *Nat. Rev. Genet.* **14**, 618–630 (2013).
51. Marcus, J. S., Anderson, W. F. & Quake, S. R. Microfluidic single-cell mRNA isolation and analysis. *Anal. Chem.* **78**, 3084–3089 (2006).
52. White, A. K. *et al.* High-throughput microfluidic single-cell RT-qPCR. *Proc. Natl. Acad. Sci.* **108**, 13999–14004 (2011).
53. Seferos, D. S., Prigodich, A. E., Giljohann, D. A., Patel, P. C. & Mirkin, C. A. Polyvalent DNA nanoparticle conjugates stabilize nucleic acids. *Nano Lett.* **9**, 308–311 (2009).

54. Richardson, W. H. Bayesian-based iterative method of image restoration. *J. Opt. Soc. Am.* **62**, 55–59 (1972).
55. Lucy, L. B. An iterative technique for the rectification of observed distributions. *Astron. J.* **79**, 745–749 (1974).
56. Bruce, M. a & Butte, M. J. Real-time GPU-based 3D Deconvolution. *Opt. Express* **21**, 4766–4773 (2013).

Chapter 6. Summary and Future Directions

6.1 Main Findings and Future Directions

6.1.1 Chapter 2: Histogram Deconvolution (HD Flow)

Flow cytometry is routinely used to assess nanoparticle and protein association with cells. The reported mean fluorescence intensity and percentage of cells that have had a response are often an underrepresentation of the true effect of a given treatment. This is due to overlap of the fluorescence histogram of the control cells, containing negative cells, with that of the sample. Chapter 2 demonstrated the application of the Richardson-Lucy deconvolution algorithm to “deblur” flow cytometry data in order to identify positive cells within the sample with increased sensitivity. To validate the method, a data set where the exact values for the percentage of positive cells are known was generated. To achieve this, the percent positive was determined from the fluorescence channel with optimal intensity. The spill over to a second channel where the intensity was lower was then used to artificially simulate overlapped histograms and to validate the method. The algorithm was demonstrated to be more effective than traditional techniques based on thresholding and those available in the commercial flow cytometry software package FlowJo.

Further development of this algorithm will enable parameters such as the number of data bins and the number of iterations to be automatically set by the program. For example, methods have been developed to calculate optimal stopping conditions for this category of deconvolution algorithm.^{1,2} This will simplify HD Flow analysis and make the process more accessible to non-expert users.

6.1.2 Chapter 3: Fluorescent Sensors for Quantifying Internalisation

Quantifying the amount of material transferred from the outside to the inside of cells is critical in improving drug delivery and understanding simple cellular processes. There are currently limited tools to determine the internalisation of a specific molecule or particle. In addition, the current methods are non-specific, preventing the use of multiple fluorescent labels such as in immunophenotyping. The DNA-based specific hybridization internalisation probe (SHIP) is an exception, however its innately large size and negative charge may limit its use on label some materials. Chapter 3 describes the synthesis of a fluorescent internalisation sensor that acts analogous to SHIP but is based on click chemistry. This allows the same specific removal of extracellular fluorescence but drastically reduces

the size of the component attached to the material of interest to the molecular weight of a standard fluorescent label. In this chapter, the ability of the internalisation sensor to quantify the uptake of various sized proteins was demonstrated.

Under conditions where there is no internalisation, ~80% of the surface signal was quenched. This efficiency was superior to the commonly used pH responsive dye pHrodo red (~50%) and similar to that obtainable with anti-dye antibodies (85%).³ Although the amount of quenching was lower than SHIP under the same conditions (~95%), this can be compensated for using a simple equation (Chapter 1) when determining the amount of material internalised. In addition, the decreased size and charge of the click-based sensor compared to SHIP is advantageous when probing uptake and trafficking, despite the lower quenching efficiency.

The remaining sections of Chapter 3 focused on extending the system by modifying the method of conjugation and reconstructing the elements of the sensor on a peptide. Currently, peptide coupling reagents are required to activate the carboxylic acid for reaction on to amines which can lead to protein cross-linking. Although tetrazine-TCO and azide-cyclooctyne reaction pairs have been used simultaneously for labelling purposes *in vitro*,⁴ this chapter showed that the groups were cross reactivate enough to prevent the use of these groups on the same molecule. Future work could address this by modifying the carboxylic acid on the fluorescent component to a succinimidyl ester for reactivity with amines or maleimide for attachment to thiols. Reconstruction of the sensor components on the particular peptide sequences chosen was not possible due to issues with hydrophobicity and steric hindrance. However, it may be possible to use this system to study the internalisation of other sequences by attaching the sensor components to less obstructed residues.

6.1.3 Chapter 4: Following Trafficking and Detecting Endosomal Escape with

SNAP_{Switch}

Enzymatic tagging systems have been developed that allow for the fluorescent labelling of specific subcellular locations in live cells. However, they have not yet been applied to track the localisation of endocytosed content as none of the fluorescent substrates are attachable to a material. Chapter 4

establishes a quenched and attachable SNAP-tag substrate for investigating localisation within cells after uptake by endocytosis. Following synthesis of the conjugate, the system was shown to detect binding on the cell surface and delivery to both the cytosol and nucleus through generation of a fluorescent signal. The switch-on fluorescence of the sensor allows escape to the cytosol and delivery to the nucleus to be tracked over time and represents a significant advance in signalling localisation in live cells. SNAP_{Switch} addresses problems associated with traditional methods for probing localisation by microscopy, such as the difficulty in interpreting results from incomplete overlap of fluorescent signals and also provides an improved option for detecting endosomal escape as the current approaches are generally non-quantifiable.

Given the potential of SNAP_{Switch}, there are several areas where this project could be further developed in order to facilitate its adaptation as a commonplace technique. A priority is the development of cell lines that stably express the SNAP-tag. Currently, a second fluorescent marker is needed to identify cells positive for the SNAP-tag as the cells only transiently express the enzyme. In order to simplify experimental execution and analysis, cell lines with stable expression could be generated using lentiviral transduction.⁵ The genes for SNAP-tag expression in the cytosol and nucleus within Chapter 4 have already been engineered into a lentiviral expression vector. Therefore, they are ready to be transfected, along with lentiviral packaging vectors, into a cell line of choice for integration into the genome.

Exchanging the specific type of quencher and fluorescent dye on the benzylguanine substrate could also be pursued. This has the potential to improve the kinetics of activation and increase the quenching efficiency, as has been demonstrated for non-attachable quenched substrates.⁶ In addition to receptors on the cell surface, other locations can be tagged within the cell such as the mitochondria, endoplasmic reticulum and the Golgi complex. As drug delivery improves, more focus falls on addressing diseases arising from problems within subcellular organelles.⁷ By expressing the SNAP-tag in these locations and using SNAP_{Switch}, the intracellular trafficking and endosomal escape capacity of materials can be probed.

6.1.4 Chapter 5: Identifying Endosomal Escape with an Oligonucleotide Sensor

The ability of a material to induce escape from endosomes following endocytosis is a critical attribute for many drug delivery applications. Existing methods to detect endosomal escape are either subjective as they require observing a diffuse fluorescence appearance within cells, or only provide an overall efficiency of transfection without describing the amount transferred to the cytosol. Chapter 5 attempts to address this by design of an oligonucleotide duplex that exchanges a quencher-labelled strand for mRNA found in the cytosol, allowing the sensor to fluoresce and signal endosomal escape. By using a cytosolic entity to induce a response in the sensor, transfection of the cells can be avoided as was required for the system described in Chapter 4.

Although the sensor was responsive to the target and resistant against responding to incorrect sequences in solution, it was unable to detect endosomal escape *in vitro*. The sensor underwent a degree of degradation within the cell under conditions where no escape was expected. When combined with the low copy number of individual mRNA sequences, this resulted in a poor signal-to-noise and made any change in signal indiscernible above the background fluorescence of the sensor. These problems are avoided in the NanoFlare live cell mRNA detection system as the high degree of labelling of oligonucleotides induces an increased local salt concentration which lowers DNAase association, increasing stability.⁸ However, modification with numerous negatively charged oligonucleotides to provoke this effect will likely impact the properties of the material and is hence not feasible as a method to detect endosomal escape. To design an endosomal escape sensor that does not require prior transfection of the cells will require selection of a target molecule that is present in much higher amounts than a specific mRNA sequence.

6.2 Overall Summary

This thesis describes the design, synthesis and demonstration of systems for the investigation of the cellular processing of materials. These probes represent advances within the sensor field and are able to track internalisation, trafficking and endosomal escape, three key steps essential for efficacious drug delivery by nanomaterials. In addition, the flow cytometric data analysis method developed improves on current evaluation techniques and is relevant to multiple scientific disciplines. Collectively, a set of

tools and methods was developed that will assist in improving our understanding of how cells and nanomaterials interact.

6.3 References

1. Laasmaa, M., Vendelin, M. & Peterson, P. Application of regularized Richardson-Lucy algorithm for deconvolution of confocal microscopy images. *J. Microsc.* **243**, 124–140 (2011).
2. Szolgay, D. & Szirányi, T. Optimal stopping condition for iterative image deconvolution by new orthogonality criterion. *Electron. Lett.* **47**, 442 (2011).
3. Liao-Chan, S. *et al.* Quantitative Assessment of Antibody Internalization with Novel Monoclonal Antibodies against Alexa Fluorophores. *PLoS One* **10**, 1–15 (2015).
4. Karver, M. R., Weissleder, R. & Hilderbrand, S. A. Bioorthogonal reaction pairs enable simultaneous, selective, multi-target imaging. *Angew. Chem., Int. Ed.* **51**, 920–922 (2012).
5. Dull, T. *et al.* A third-generation lentivirus vector with a conditional packaging system. *J. Virol.* **72**, 8463–71 (1998).
6. Sun, X. *et al.* Development of SNAP-tag fluorogenic probes for wash-free fluorescence imaging. *Chembiochem* **12**, 2217–26 (2011).
7. Rajendran, L., Knölker, H.-J. & Simons, K. Subcellular targeting strategies for drug design and delivery. *Nat. Rev. Drug Discov.* **9**, 29–42 (2010).
8. Seferos, D. S., Prigodich, A. E., Giljohann, D. A., Patel, P. C. & Mirkin, C. A. Polyvalent DNA nanoparticle conjugates stabilize nucleic acids. *Nano Lett.* **9**, 308–311 (2009).